FLOW THROUGH SQUARE DUCTS

WITH

ROUGH RIBS

by

Md. ABU TAHER ALI

B.Sc.Eng.(Mech.), M.Sc.Eng.(Mech.)

Thesis submitted for the degree of
Doctor of Philosophy
in the Faculty of Engineering
University of London
and for
the Diploma of Membership of Imperial College

Mechanical Engineering Department
Imperial College
LONDON SW7 2AZ

JULY 1980

ABSTRACT

Turbulent flows through square ducts with one rough wall and two opposite rough walls have been investigated both experimentally and theoretically.

The experimental programme contributed the larger part of the investigation and provided detailed measurements of mean and turbulent characteristics of fully developed flows in square ducts where asymmetry was introduced by making one or two walls rough with square ribs placed transversed to the flow direction and with a constant pitch to height ratio of 10. The height of the ribs was approximately 2% of the duct width. The measurements made use of hot-wire anemometry and were taken at Reynolds number of 3.42×10^5 for the single rough wall and at a Reynolds number of 3.26 for the two rough walls.

The measurements quantify the influence of the rough wall and show that the region of greatest interaction occurs with the single rough wall where it is characterized by strong diffusional transport of turbulent shear stress and kinetic energy away from the rough wall and towards the smooth wall region; this gives rise to an appreciable separation between the planes of zero shear stress and zero velocity gradient. The flows near the walls are in local equilibrium although the influence of adjoing dissimilar walls is evidenced by the variation of log law constants and wall shear stresses near the corners. Secondary flow velocities, generated largely by normal stress gradients, attain values upto 5% of duct centreline velocity and greatly influence the distribution of both mean and turbulent flow properties. The production of turbulence is mainly in the rough wall region where its spectral analysis indicates the absence of any predominant eddy structure and suggests that the small scale motion may be treated as isotropic. The addition of the second rough wall has little effect on the flow structure near the original rough wall.

The theoretical investigation was concerned with the use and evaluation of a two-equation (k-ε) turbulence model capable of solving flows in noncircular ducts with secondary

motion. In the calculation momentum equations together with algebraic equations for Reynolds stresses and modelled equations for k and ε were solved and asymmetry was introduced by applying different wall functions. Flows in symmetric ducts can, with reasonable accuracy, be described by the two-equation turbulence model but the asymmetry of the flow field limits its value. Turubulence modelling of higher order i.e, solving the Reynolds stresses themselves, is required for flows in asymmetric ducts.

ACKNOWLEDGEMENTS

My first and foremost gratitude is to my supervisor Professor J H Whitelaw. His quidance and advice at different stages of research and his encouragements were invaluable in the completion of this thesis.

My thanks are to Professor B E Launder who guided me in the first year of my work and originated the present research. My thanks are also to Dr A D Gosman who maintained constant interest in this work.

I would like to thank Mr C W Rapley who performed the computer runs and provided me with the results of chapter 6.

It has been a pleasure to work with many research students of the Fluids Section at Imperial College. My close association with Dr D Crabb, Dr R J R Johns, Dr A P Salooja and Mr M A Habib has been particularly valuable.

The help of technical staff, in particular Mr F Bell, Mr O Vis, Mr J Laker and Mr J C Pickett of the Machine shop were specially useful to the development of the experimental system.

I would like to thank Miss V L Trout whose speedy and nice typing resulted in the final presentation of this thesis.

I am grateful to the Association of Commonwealth Universities who provided me with the financial support for the major part of the research programme. I am also grateful to Old Centralians Trust and others who provided me with financial support for some months.

I am grateful to my neighbours, the Hauf and Young families, whose friendly association and good wishes have been inspiring. Lastly my thanks are to my wife and children who have shared my disappointments and successes and provided encouragements.

PREFACE

The work described in this thesis is concerned with the fully developed turbulent flow through asymmetric square ducts. The study of the flow was carried out in two stages, the experimental study and the numerical analysis. In the measurements sensing probes used were mainly pitot tubes, yaw-meters and hot wires. The experimental set up and the instrumentation are described in chapter 3 and the measured results are presented and discussed in chapters 4 and 5. Some of the related studies of square duct flows are described in chapter 1 and the influence of different conditions, such as Reynolds number, aspect ratio, asymmetric wall roughness etc., on the flow is discussed and these results are later compared with the present findings and causes of agreement or disagreement are analysed and results are summarized in chapters 4 and 5.

The basis of numerical analysis is described in chapter 2 where available turbulence models and their achievements and limitations are discussed. On the basis of past experience particularly on duct flow analysis described in chapter 1, two-equation (k-ε) algebraic stress model was chosen for the analysis of the present flow system. Calculated results are presented and compared in chapter 6 and is found that asymmetry of the flow condition limits the capability of the model.

To maintain consistency of presentation some important aspects of asymmetric flow system are omitted from the previous chapters and are discussed seperately in chapter 7. The experimental plots which are not discussed but are vital for future reference or to assess experimental uncertainties, are listed separately as Appendix figures.

C O N T E N T S

	Page
ABSTRACT	2
ACKNOWLEDGEMENTS	4
PREFACE	5
CONTENTS	6
LIST OF TABLES	11
NOMENCLATURE	12
CHAPTER 1 INTRODUCTION	
1.1 The Problems considered: Background and Motivation	15
1.2 Objectives	18
1.3 Previous Works	19
1.3.1 Measurements of Turbulent Flow Through Symmetric Ducts	20
1.3.2 Measurements of Turbulent Flow Through Ducts with Dissimilar Walls	31
1.3.3 Theoretical Studies of Duct Flows	38
1.4 Outline of Research	42
1.5 Thesis Outline	43
CHAPTER 2 EQUATIONS, MODELS AND SOLUTION PROCEDURE	
2.1 Introduction: Preliminary Remarks and Equations	45
2.2 Turbulence Models	47
2.3 Choice of Turbulence Model	51
2.4 Equations for Turbulence Kinetic Energy and Dissipation Rate	55
2.5 The Turbulent Wall Functions	56
2.5.1 The Need For Wall Functions	56
2.5.2 The Wall Functions Employed	56
2.6 Finite-Difference Equations	58

		Page
2.7	Solution Procedure	60
2.8	The Accuracy of the Solutions	61
CHAPTER 3	EQUIPMENT AND EXPERIMENTAL PROCEDURE	
3.1	Experimental Programme	63
3.2	The Flow System	64
3.3	Instrumentation and Measuring Technique	
3.3.1	Pressure Instrumentation	65
3.3.2	Hot-Wire Measurements	66
3.3.2.1	Hot-Wire Signal Processing Equipments	66
3.3.2.2	Turbulence Measurement Procedure	67
3.3.2.3	Calibration Rig	69
3.3.2.4	Calibration of the Hot-Wire	70
3.3.3	Secondary Flow Measurements	71
3.3.3.1	Hot-Wire Measuring Technique	71
3.3.3.2	The Yawmeter	73
3.4	Traversing Mechanism and Probe setting	74
3.5	Error Analysis	75
3.6	Preliminary Tests	78
CHAPTER 4	MEASUREMENTS IN A SQUARE DUCT WITH ONE ROUGH WALL	
4.1	Introduction	81
4.2	Presentation of the Measurements	82
4.2.1	Mean Velocity Profiles and Contours	82
4.2.2	Secondary Mean Velocity	87
4.2.3	Friction Factor and Wall Shear Stresses	89
4.2.4	Contours of Turbulence Intensities	91
4.2.5	Reynolds Shear Stress and Kinetic Energy Contours	92
4.2.6	Longitudinal Turbulence Spectra	95

		Page
4.3	Discussion of the Results	96
4.3.1	Mean Velocity Profiles and Contours	96
4.3.2	Secondary Mean Velocity	99
4.3.3	Friction Factor and Wall Shear Stresses	101
4.3.4	Contours of Turbulence Intensities	102
4.3.5	Reynolds Shear Stress and Kinetic Energy Contours	103
4.3.6	Longitudinal Turbulence Spectra	106
4.4	Summary Conclusions	106
4.4.1	Mean Flow Findings	106
4.4.2	Turbulent Flow Findings	107
CHAPTER 5	MEASUREMENTS IN A SQUARE DUCT WITH TWO ROUGH WALLS	
5.1	Introduction	109
5.2	Presentation of the Measurements	109
5.2.1	Mean Velocity Profiles and Contours	110
5.2.2	Secondary Mean Velocity	113
5.2.3	Friction Factor and Wall Shear Stresses	114
5.2.4	Contours of Turbulence Intensities	115
5.2.5	Reynolds Shear Stress and Kinetic Energy Contours	116
5.2.6	Longitudinal Turbulence Spectra	118
5.3	Discussion of the Results	119
5.3.1	Mean Velocity Profiles and Contours	120
5.3.2	Secondary Mean Velocity	121
5.3.3	Friction Factor and Wall Shear Stresses	123
5.3.4	Contours of Turbulence Intensities	126
5.3.5	Reynolds Shear Stress and Kinetic Energy Contours	127

		Page
5.3.6	Longitudinal Turbulence Spectra	129
5.4	Summary Conclusions	130
5.4.1	Mean Flow Findings	130
5.4.2	Turbulent Flow Findings	131
CHAPTER 6	**CALCULATIONS**	
6.1	Introduction	133
6.2	Presentation and Discussion of the Results	133
6.2.1	Axial Mean Velocity Contours	134
6.2.2	Secondary Mean Velocity	135
6.2.3	Distribution of Wall Shear Stress	137
6.2.4	Reynolds Shear Stress and Turbulence Kinetic Energy Contours	138
6.3	Summary	141
6.3.1	Achievements and Limitations	141
6.3.2	Sources of Error	142
6.3.3	Possible Methods of Improvements	144
CHAPTER 7	**GENERAL DISCUSSION**	
7.1	Introduction	146
7.2	Present Work: Its Areas of Importance	146
7.3	Some Aspects of Discrete Rib Roughness	147
7.3.1	Roughness Height	147
7.3.2	Roughness Spacing	148
7.4	Log Law of the Walls	150
7.5	Secondary Mean Velocity	152
7.6	Some Aspects of Asymmetric Flow	154
CHAPTER 8	**CONCLUSIONS**	
8.1	Achievements of the Experimental Work	160
8.2	Achievements of the Theoretical Work	161
8.3	Extension of the Present Work	162

		Page
APPENDIX A	Hot-Wire Response Equations	163
APPENDIX B	Calibration and Correction Procedure of Yawmeters	166
REFERENCES		168
LIST OF FIGURES		182
FIGURES		188

LIST OF TABLES

		Page
1.1a	Symmetric Duct Flows: Measurements of Mean Flow Properties	21
1.1b	Symmetric Duct Flows: Detailed Measurements	27
1.2	Measurements of Turbulent Flow through Ducts with Dissimilar Walls	32
1.3	Theoretical Studies of Rectangular Duct Flows	39
5.1	Ratio of Mean Wall Shear Stress to the Total Flow Resistance of the Duct	124
7.1	Comparison of Flow in Ducts with one Rough Wall	156

NOMENCLATURE

Symbol	Meaning
A	Duct cross sectional area
a	Duct width
B_s	Constant in the 'Law of the wall' for smooth surfaces
B_R	Constant in the 'Law of the wall' for rough surfaces
C_1, C_2, C_3, C_4, C_μ, C_D	Constants used in turbulence model (chapter 2)
C_f	Friction factor
C_{fs}	Friction factor for all smooth ducts
C_{fr}	Friction factor for all rough ducts
C_{fn}	Friction factor for ducts with n rough walls
D_h	Duct hydraulic diameter, 4A/S
E	D.C. voltage from hot wire anemometer
e	A.C. voltage from hot wire anemometer
e	Rib roughness height
e_s	Sand roughness height
F	Weighting factor
f	Frequency
g	Mass flux per unit area
H	Duct height
K	Yaw factor for hot wire
K_1	Longitudinal wave number, $k_1 = 2\pi f/U_1$
k	Turbulence kinetic energy
ℓ	length scale

Symbol	Meaning
n	Number of rough walls
P	Mean pressure
P	Pitch of roughness elements
P_e	Cell Peclet number
Q	Transferable scalar property
R_e	Reynolds number
$S(\Psi)$	Sensitivity of yawmeters
S	Calibration constant of hot wire
S	Duct perimeter
U_i	Mean velocity components, i = 1,2,3
U_c	Duct centreline velocity
U_b	Duct bulk mean velocity
U_s	Secondary velocity
U_τ	Friction velocity, $U_\tau = \sqrt{\tau_w/\rho}$
U^+	Dimensionless velocity, $U^+ = U/U_\tau$
u_i	Fluctuating velocity components, i = 1,2,3
W	Duct width
x_i	Cartesian co-ordinates, i = 1,2,3
x^+	Dimensionless wall distance, $x^+ = xU_\tau/\nu$ or $x^+ = x/e$
α	Angle between mean velocity vector and normal to hot wire
Γ	Exchange coefficeint
γ_i	Secondary flow angle, i = 1,2
δ	Inter-nodal distance
ε	Dissipation rate of kinetic energy
κ	Constant in the 'Law of the wall'
μ	Molecular viscosity
μ_t	Turbulent viscosity

Symbol	Meaning
μ_{eff}	Effective viscosity
ν	Kinematic viscosity
ρ	Density
$\sigma_{t,k}$, $\sigma_{t,\varepsilon}$	Turbulence model constants
τ_w	Average wall shear stress of the duct
τ_s	Smooth wall shear stress
τ_r , τ_R	Rough wall shear stress
ϕ	General variable
ψ	Stream function
Ω	Axial vorticity
Ω	Ohm (electrical resistance)

Subscripts

i,j,k	Components of Cartesian tensor notations
s	Smooth
R,r	Rough
min	Minimum
eff	Effective

Superscripts

$\overline{}$	Time average
~	RMS
^	Instantaneous

C H A P T E R 1

INTRODUCTION

1.1 The Problems Considered: Background and Motivation

Turbulent flows through pipes and ducts are common in engineering practice. They arise in numerous engineering installations involving the transportation of fluids such as, for example, heat exchangers, nuclear reactors, chemical processing plant, air-conditioning systems, rotating machinery etc. Until recently, experimental examination of these flows was confined to comparatively simple cases and, for over three decades, workers have made detailed measurements of fully developed flow in circular pipes and plane channels with symmetric boundary conditions. Studies of similar detail were not, however, made in more complicated geometries such as ducts with dissimilar boundary conditions and curvature. The attention to equilibrium, symmetric flows was clearly sensible since the nature of some of the properties of turbulent flow could most easily be deduced if the flow was symmetric. In practice, however, the assumption of symmetry is often not justified and the study of turbulent flow in such complex geometries is, therefore, necessary and can be achieved experimentally using techniques such as hot wire and hot film anemometry or, in configurations where a non-disturbing method is essential, laser Doppler anemometry.

In the past few years, digital computers, numerical techniques and the development of numerical models of turbulent flow have made it possible to calculate flows of considerable complexity and thereby create a new approach to the design of flow configurations. The experimental study of turbulent flow, in particular, is generally laborious and expensive and so it is valuable to investigate them by calculation. The success in obtaining accurate turbulent flow predictions, however, depends on prescribing a closed set of equations, which will adequately

account for the flow processes of interest, that is of devising a suitable turbulence model for the complex correlations in the conservation equations governing the flow. These assumptions depend on theoretical reasoning and empirical fact which, if accurate enough within the range of interest, will lead to correct predictions of turbulent flows.

For laminar flows the problem is strictly mathematical because the governing differential equations can be written exactly. Thus, with the aid of high speed computers, much progress in the calculation of laminar boundary layers has been made, and satisfactory results have been obtained for many cases. On the other hand, and because of the limited understanding of the turbulent process, the problem of turbulent flow is phenomological as well as mathematical and, exact formulation of boundary layer equations is not possible. The boundary layer equations for such flows contain extra terms involving the time mean of the product of two fluctating velocities known as the Reynolds stress tensor. At present these terms have not been rigorously related to the mean velocity distribution. Although various methods or models for dealing with these extra terms have been proposed and range from the relatively simple Mixing Length Hypothesis of Prandtl (1925) to the solution of conservation equations for third order correlations by Launder and Spalding (1972). The closure problem, ie, of expressing the Reynolds stresses as functions of known variables, increases in difficulty with the complexity of the model. To solve the recirculating turbulent flows, where convection and diffusion of turbulence are important, two-equation models (k-ε for example) have been widely used, and involve the assumption of local isotropy which occurs at high Reynolds number and a generalized Boussinesq effective viscosity concept. In practice all real flows show some degree of anisotropy and the Reynolds stress is less directly connected with the mean velocity field than is required by the notion of the turbulent viscosity. Thus, the possibility of solving equations for the Reynolds stresses arises but at the cost of introducing additional unknown correlations for which additional approximations in terms of known variables are required. To obtain additional information for simplifying or modelling of more unknown correlation terms as a

function of known variables, experimentation is required. The degree of applicability of a turbulence model over different flow conditions and configurations depends on the assumptions it incorporates, and these assumptions are based on experimental observations and physical reasoning. Thus, turbulence modelling for the prediction of turbulent flows, while attractive for the substitution of complex experimentation, requires experimental evidence for its refinement and continuing generalization. Careful choice and arrangement of experiments can provide some of the necessary information to the point where confidence can be placed in predictions, in the absence of empirical facts. In the recent past most detail measurements have related to simple flows and any model devised from them could be expected to display defficiency when applied to more complex flows which arise in engineering practice.

It is against this background that the objectives of the present research have been formulated. The present work on turbulent flow through straight square ducts, with combinations of smooth and rough walls, arises as a natural extension of the work of Hanjalic and Launder (1972a) and Humphrey and Whitelaw (1979). Hanjalic and Launder were particularly concerned with enhancing the diffusion transport of Reynolds stresses in order to test their turbulence model. In this work, by making the duct sqaure cross section the secondary flow effects and their interaction with the turbulence can be enhanced. Again in the present research, measurements in a asymmetric square duct with roughness ratio (roughness height to duct hydraulic diameter) different from Hymphrey and Whitelaw and with a smooth wall opposite to a rough wall and two opposite rough walls is expected to reveal important and new flow characteristics. The study of flow with dissimilar walls is important since flow characteristics may become prominent which are concealed in simple flows by virtue of symmetry or some other constraint.

Flows with dissimilar surface condition appear in many practical situations where technological requirements impose dissimilar boundary conditions, such as in nuclear reactors, by making the surface of rod bundles rough, the heat transfer rate

between the fuel and the coolant can sufficiently be increased with relatively less increase of overall flow resistance.

1.2 Objectives

The above brief discussion suggests a need for information of knowledge of the flow characteristics of square ducts with dissimilar boundary conditions. The objectives of the present research programme are:

(1) To measure the mean flow characteristics of fully developed square duct flow with one rough wall and with two opposite rough walls.

(2) To measure turbulence properties in the same flows to provide insight into their general structure and, more generally, of flows with dissimilar boundary conditions.

(3) To provide data to enable direct testing of hypotheses of turbulence models.

The first objective is intended to provide data for direct practical use. The designer of heat or mass transfer process equipment usually needs informations of the distribution of velocity, temperature, mass fraction etc. Within the flow field and the level of heat flux (or wall temperature), and the shear stress around the boundary surfaces of the duct. Thus the present data, which relate to the distributions of mean flow velocity, wall shear stress, friction factor etc., will fulfil a part of this need. The second objective is to furnish data of various turbulence properties of flows with dissimilar boundary conditions and so aid understanding of the related physical processes. The third objective is related to the provision of data and its use in the assessment and improvement of turbulence models.

In the present experimental programme, fully developed flow is considered, so that dependent flow properties when suitably nondimensionalized become invariant in the mean flow direction. These dimensionless flow properties may thus, be described as functions of two co-ordinate directions in the plane of the duct cross section (ie, the flow becomes two dimensional)

and the hydrodynamic and heat transfer characteristics of the flow are governed by a set of elliptic differential equations.

Turbulent flow in ducts of non-circular cross section, even when the duct is staight and symmetric, exhibits secondary velocities in the plane of the duct cross section and are caused by the anisotropic nature of turbulence. Apart from the action of turbulence, secondary flow can also be induced through body forces (eg, buoyancy forces or centrifugal forces etc.) or through the motion of bounding wall. In the duct with dissimilar walls, the degree of anisotropy of turbulence is expected to be greatly increased and to cause secondary velocities of higher magnitudes than in symmetric ducts. The presence of secondary flows, and for turbulent flow strongly nonumiform effective transport properties, renders the set of partial differential equations governing the flow, highly non-linear. The prediction techniques developed mainly for square and rectangular symmetric ducts by some workers (Hanjalic and Launder (1972b), Laudner and Ying (1973), Naot et al (1974), Tatchell (1975) and Gessner and Emery (1976), for example) are capable of simulating some of the properties, for example Reynolds stress driven secondary velocity, of turbulent flow. The prediction method of Laundner and Ying (1973) has recently been applied to two other geometries, an equilateral triangular duct (Aly et al, 1978) and the flow in triangular rod bundles (Carajileseov and Todreas, 1975) with secondary flow effects which are in general agreement with the expected behaviour. There are, however discrepancies of turbulence quantities and secondary velocities. Nevertheless, there is sufficient encouragment in these predictions to seek a prediction procedure that is capable of application to dissimilar boundary conditions. The present results are compared with the calculated values obtained from a computation method developed from the works of Launder and Ying, Gessner and Emery and Tatchell.

1.3 Previous Works

In this section, a brief review of previous investigations of flow in ducts is presented. The review of the experimental investigation of duct flow is made in two sections,

dealing with ducts with similar walls in section 1.3.1 and those with dissimilar walls in section 1.3.2; the review of the related theoretical studies is provided in section 1.3.3.

1.3.1 Measurements of Turbulent Flow through Symmetric Ducts

The usual practice has been to measure mean flow properties and to determine and make use of correlations of pressure drop and heat transfer data, based on the hydraulic diameter concept. In these investigations, evidence of secondary flow was deduced from the contours of axial mean velocity and distribution of wall shear stress. Some of the available measurements of mean flow properties are listed in table 1.1a while detailed duct flow measurements are listed in table 1.1b.

(a) Measurements of Mean Flow Properties

At the inlet, the flow through a duct shows a plug like profile with thin shear layers confined near the walls and pressure falls sharply due to the rapid growth of boundary layer. Far downstream, the pressure gradient assumes a constant fully developed value. In duct flows secondary motions arise where there is lateral curvature of the main flow and/or gradients in the Reynolds stresses. The former gives rise of pressure driven secondary motion which, generally, occurs in curved duct flows, flows with 'sudden enlargement' or 'suddent contraction' etc., while the later the normal stress driven secondary motion which occurs due to the anisotropy of turbulence. The fully developed turbulent flows through rectangular ducts are commonly characterised by the presence of normal stress driven secondary motion which is generated near the corners and is sensitive to the aspect ratio (ratio of the duct height to the depth) of the duct. For high aspect ratios, the flow away from the corners is two-dimensional and measurement is possible ignoring the side wall effects as reported by Laufer (1951) and Comte-Bellot (1965). For aspect ratios near one, the entire flow is influenced by the corners and so can not be regarded as two-dimensional even across the planes away from the corners. However, the gross charateristics of flow, such as friction factor, Stanton number, in such ducts can be compared with their counterparts in circular ducts.

TABLE 1.1a - Symmetric Duct Flows: Measurements of Mean Flow Properties

AUTHORS, YEAR	FLOW CONFIGURATION	MEASUREMENTS	INSTRUMENTATION	COMMENT
Hoagland (1960)	Rectangular ducts (W/H*= 1,2 and 3) Re= 6.6×10^4, 8.8×10^4 and 6×10^4 respectively.	U_1 contours; U_s contours and secondary stream lines.	Hot-wire anemometer; hot-wire for measuring U_s	U_1 contours bulged towards the corners; $U_s \leq .15U_c$; highest values U_s lay near diagonals; secondary stream lines closed within the octant of the duct.
Hartnett, Koh and McComas (1962)	Rectangular ducts (W/H= 1,3 and 10) $R_e < 3\times10^5$	$\frac{\partial P}{\partial x_1}$ in fully developed flow	Static pressure taps.	Predicted C_f by Deissler and Taylor's method agreed with the measurement for W/H $\geq$ 5.
Leutheusser (1963)	Rectangular ducts (W/H= 1 and 3) $R_e < 9\times10^4$	$\frac{\partial P}{\partial x_1}$; log law profiles of U_1; U_1 contours; distribution of τ_w.	Static pressure taps; Preston tube; pitot tube.	C_f vs R_e lay below eq, 1.1; U_1 contours bulge towards the corners ; variation of τ_w is gradual except near the corner.
Beavers, Sparrow and Lloyd (1971)	Rectangular ducts (W/H= 15.5 to 35) $5\times10^3 < R_e < 3.7\times10^4$	$\frac{\partial p}{\partial x_1}$	Static pressure taps.	$C_f = 0.127\ R_e^{-0.30}$

* W = Width , H = Height

TABLE 1.1a (cont'd)

AUTHORS, YEAR	FLOW CONFIGURATION	MEASUREMENTS	INSTRUMENTATION	COMMENT
Ahmed and Brundrett (1971b)	Developing flow in a square duct $6 < x_1/D_h^* < 26$ $5.9\times10^4 < Re < 1.65\times10^5$	$\frac{\partial p}{\partial x_1}$; U_1 contours; τ_w distribution.	Static pressure taps; pitot tube; Preston tube.	Flow developed more slowly as Re increased; U_1 contours bulged more towards the corners as flow developed.
Thomas and Easter (1972)	Square duct $4.3\times10^4 < Re < 1.9\times10^5$	$\frac{\partial p}{\partial x_1}$; U_1 profiles; distribution of τ_w.	Static pressure taps; sublayer fence and flush mounted hot-wire probe.	C_f is in agreement with eq. 1.1; except near the corners, U_1 profiles follow the log law and τ_w varies only gradually.

x_1 = Distance from the entrance end, D_h = Hydraulic diameter

Nikuradse (1926) first detected the presence of secondary flow in rectangular sectioned ducts but until Hoagland's work (1960) no quantitative data for the secondary velocities was available, although his data were in variance, with the requirement of mass conservation, Hoagland's major contribution lay in devising a method to measure secondary velocity components using hot wire probe. The method is illustrated in section 3.3.3.1 In all the three geometries as mentioned in the table, isovels bulged towards the corner, and maximum secondary velocity, U_s, was 1.5% of duct centre line velocity, U_c, but in most positions of duct cross section U_s was considerably smaller. In each quadrant the secondary flow stream lines defined two cells with opposite sense of circulation seperated approximately by the diagonal. The secondary motion transported momentum into the corner parallel to the diagonal, then away from the corner parallel to the duct walls and finally back to the centre along the paths parallel to the wall bisectors. Accurate determination of secondary velocity components, U_2 and U_3, is difficult, whether they are measured by Hoagland's method or otherwise, because of the smallness of the secondary velocity components relative to the axial mean velocity. Although more recent measurements of secondary velocity are an improvement of Hoagland's they generally fail to satisfy the continuity equation.

Hartnett et al (1962) measured friction factors in rectangular ducts with aspect ratios 1,5 and 10. The friction factor for both the laminar and turbulent flow fields was determined analytically as well as experimentally and the analytic expression for the pressure loss in laminar flow was verified by experiment. In turbulent flow, the analytic method of Deissler and Taylor (1959) was used to calculate the friction coefficient and was in agreement with the measured results for ducts with large aspect ratios. At aspect ratios less than 5 the predicted values of overall friction coefficient were lower than the experimental data, with maximum difference of 12%, from the square duct. It was found that the Blasius law for the coefficient for smooth pipes:

$$C_f = 0.079 Re^{-0.25} \quad \ldots (1.1)$$

accurately predicted the friction coefficient for flow through rectangular ducts of any aspect ratio for Reynolds numbers between 6×10^3 and 5×10^5. The discrepancy in the results of square duct was due to the presence of secondary flow which in the Deissler and Taylor's method was not considered. The authors also correlated pressure drop measure - ments with equation 1.1 for rectangular ducts of aspect ratios between 1 and 169, using data from ten sources prior to 1962.

Leuthesser (1963) measured mean velocity contours, the axial static pressure gradient and the wall shear stress distribution in fully developed flow in ducts with aspect ratios 1 and 3. Friction coefficient data in the Reynolds number range of 3×10^4 to 1×10^5, was approximately 4% below the Blasius circular pipe correlation (eq. 1.1). The wall shear stress distribution, determined from Preston tube measurements, showed only a small variation ($\pm$10%) except in the vicinity of the corners, where it fell rapidly to zero. The fairly uniform distribution of τ_w indicated the existence of secondary flows; without them large variation of τ_w away from the corners would be expected. Isovels of both the square and rectangular sections showed bulging towards the corners, indicating secondary flows moving from the axis towards the corners and then back towards the duct centre line from the mid points of the wall. In spite of the secondary flows, the near wall flow was two-dimensional except near the corners and mean velocity profiles fitted the universal logarithmic law (equation 2.24) with κ and B equal to 0.406 and 5.51 respectively.

Over low Reynolds number range, 5×10^3 to 3.7×10^4 Beavers, Sparrow and Lloyd (1971) measured friction factors in rectangular duct flows which were not well correlated by equation 1.1. Data for six different aspect ratios which were best fitted by

$$C_f = 0.127 R_e^{-0.30} \quad \ldots (1.2)$$

implying a stronger variation with Reynolds number.

Ahmed and Brundrett (1971b) reported developing flow in a square duct and the isovels, initially roughly parallel with the duct walls, exhibited increased bulging towards the duct corners as the flow developed. This development was slower at higher Reynolds number as was confirmed by axial pressure measurements. Ahmed and Brundrett (1971a) suggested that the hydraulic diameter, D_h, was not the most suitable dimension to characterise a noncircular duct since it takes no account of the shape of the duct cross section, a factor which is of great importance in establishing the pattern of secondary flow. For a square duct, for example, of side 'a', the hydraulic diameter is D_h = 'a' but the characteristic diameter used by them is

$$D_L = \tfrac{1}{2} \text{ (Length of side)} + \tfrac{1}{2} \text{ (Length of diagonal)}$$

$$\text{ie.} \quad D_L = 1.207\, D_h \qquad \ldots (1.3)$$

Ahmed and Brundrett argued that the characteristic dimension D_L which included both side and diagonal of a duct, represented the duct shape to some extent and for square, rectangular and triangular cross-section ducts, they claimed improved correlation of friction factor data with equation 1.1 when Reynolds number was based on D_L.

Thomas and Easter (1972) obtained measurements of fully developed flow in a square duct. Their measurements were similar to those of Leuthesser (1963). The friction factor data in the Reynolds number range of 4.3×10^4 to 1.9×10^5 were correlated by the Blasius pip friction law, equation 1.1. The mean velocity profiles from $x_2/a = 0.125$ to 0.875 obeyed the universal log law equation 2.24, with κ and B of 0.418 and 5.45 respectively, in agreement with the values recommended by Patel (1965) for turbulent pipe flow. The wall shear stress distribution was flat over the central two-thirds of the duct wall and fell off towards the corner indicating the presence of secondary flow in the duct cross section.

(b) Detailed Measurements of Duct Flow

In most of the measurements reviewed in part a of this section, the presence of secondary flow and its influence on other flow properties, was evident but the results could not explain what caused them. It was the work of Brundrett and Baines (1964), which first provided a fairly complete explanation of the origin of these secondary flows. They showed that it was the gradients of Reynolds stresses, in the plane of the duct cross section that gave rise to the source of stream wise vorticity. According to Brundrett and Baines, the axial vorticity, Ω_1, equation as derived from Navier Stokes equation, is

$$\underset{\text{I}}{\rho U_2 \frac{\partial \Omega_1}{\partial x_2}} + \underset{\text{II}}{\rho U_3 \frac{\partial \Omega_1}{\partial x_3}} = \underset{\text{III}}{\frac{\partial^2}{\partial x_2 \partial x_3}\left(\rho\overline{u_2^2} - \rho\overline{u_3^2}\right)} - \underset{\text{IV}}{\left(\frac{\partial^2}{\partial x_2^2} - \frac{\partial^2}{\partial x_3^2}\right)\rho\overline{u_2 u_3}} + \underset{\text{V}}{\mu\left(\frac{\partial^2 \Omega_1}{\partial x_2^2} + \frac{\partial^2 \Omega_1}{\partial x_3^2}\right)} \quad \ldots (1.4)$$

where $\Omega_1 = \frac{\partial U_3}{\partial x_2} - \frac{\partial U_2}{\partial x_3}$ and axes notations are as in figure 3.2. From equation 1.4, they deduced that in laminar flow through straight duct, vorticity would not exist and it would arise only in turbulent flow by the gradients of Reynolds stresses ie.

$$\text{Production} = \frac{\partial^2}{\partial x_2 \partial x_3}\left(\rho\overline{u_2^2} - \rho\overline{u_3^2}\right) - \left(\frac{\partial^2}{\partial x_2^2} - \frac{\partial^2}{\partial x_3^2}\right)\rho\overline{u_2 u_3} \quad \ldots (1.5)$$

TABLE 1.1b - Symmetric Duct Flows: Detailed Measurements

AUTHORS (YEAR)	FLOW CONFIGURATION	MEASUREMENTS	INSTRUMENTATION	COMMENTS
Brundrett and Baines (1964)	Square duct $Re = 8.3 \times 10^4$	Secondary velocity vector; contours of $\overline{u_i u_j}$, $(\overline{u_2^2} - \overline{u_3^2})$ and $\frac{\partial^2}{\partial x_2 \partial x_3}(\overline{u_2^2} - \overline{u_3^2})$	Hot wire anemometer; hot wire for measuring U_s.	Source of secondary flow analysed by axial vorticity equation; regions of strong production, convection and and diffusion of Ω_1 identified.
Gessner and Jones (1965)	Square duct; rectangular duct (W/H = 2) $5 \times 10^4 < Re < 5 \times 10^5$	U_1 contours to check symmetry; contours of Reynolds stresses $\overline{u_i u_j}$; secondary velocity components U_2, U_3.	Pitot tube; hot wire anemometer; hot wire for measuring U_s.	U_s/U_c decreased as Re increased; wall shear stress vectors skewed to oppose secondary flow; causes of secondary flow explained by momentum balance.
Tracy (1965)	Rectangular duct (W/H = 6.2)	Profiles of U_1, $\tilde{u}_1$ $\tilde{u}_2$, $\tilde{u}_3$, $\overline{u_1 u_2}$, $\overline{u_1 u_3}$ $\overline{u_2 u_3}$, $(\overline{u_2^2} - \overline{u_3^2})$ and secondary velocity vectors.	Static pressure taps; pitot tube; hot wire anemometer; hot wire for measuring U_s.	Flow was two-dimensional in the central one-third of the duct; secondary flow occurred near the side wall where distribution of $(\overline{u_1^2} - \overline{u_3^2})$ supported its presence.

TABLE 1.1b (cont'd)

AUTHORS (YEAR)	FLOW CONFIGURATION	MEASUREMENTS	INSTRUMENTATION	COMMENTS
Launder and Ying (1972)	Smooth square duct; Rough square duct, discrete roughness with transverse square ribs. ($P/e^* = 7.1$, $e/D_h^* = .075$) Re= 6.9×10^4 and 2.2×10^5	U_1 profiles and contours; U_2 profiles; U_τ distribution; variation of C_f with R_e.	Static pressure taps; pitot tube; hot wire for measuring U_s.	U_1 profiles obeyed log law except near the corners. U_2/U_τ independent of R_e and wall roughness.
Melling and Whitelaw (1976)	Square duct (developing flow) Re= 4.2×10^4	Contours of U_1 and u_1 from $x_1/D_h = 5.6$ to 36.8 Contours of Reynolds stress components $\overline{u_i u_j}$; k and $(\overline{u_2^2} - \overline{u_3^2})$ and U_s velocity vectors at $x_1/D_h = 36.8$	Static pressure taps; laser Doppler anemometer.	With the development of flow u_1 contours bulged more towards the corner than the U_1 contours; away from the corners U_1 profiles obeyed log law variation; friction factor variation showed $C_f = 0.138 \times Re^{-.30}$

* P = Pitch, e = Rib height

The same conclusion was reached by Einstein and Li (1958), although they did not determine the magnitude of the production term. By considering the boundary values of the Reynolds stress tensor $\rho\overline{u_i u_j}$, Brundrett and Baines deduced that production of vorticity must occur within the octant of the duct. To compare the contribution of different terms of equation 1.5, they, using hot wire anemometer, measured normal and shear stress components $\overline{u_i u_j}/U_\tau^2$ and secondary velocity components U_2 and U_3 in an octant of the duct used by Leutheusser (1963). Measurements showed that $\overline{u_2 u_3}/U_\tau^2$ was on the average, substantially smaller than $\frac{\overline{u_2^2}-\overline{u_3^2}}{U_\tau^2}$. Differentiation (by finite difference technique) then showed that the term $(\frac{\partial^2}{\partial x_2^2} - \frac{\partial^2}{\partial x_3^2})\ \frac{\overline{u_2 u_3}}{U_\tau^2}$ was negligible compared with $\frac{\partial^2}{\partial x_2 \partial x_3}(\frac{\overline{u_2^2}-\overline{u_3^2}}{U_\tau^2})$.

Thus the prominent production term in equation 1.5 was the first one and was greatest near the diagonal and the corner ie, in the region where distribution of the contours of U_1/U_c and $\tilde{u}_1/U_c$ was most pronounced. Brundrett and Baines also obtained the convection and diffusion of vorticity in the duct cross section ie, terms (I, II) and V respectively in equation 1.4. They argued that an increase in Reynolds number would lead to increased penetration of the secondary flow into the duct corners but the ratio U_s/U_c would not vary with Reynolds number.

Gessner and Jones (1965) measured secondary velocities by Hoagland's technique in ducts of aspect ratios 1 and 2 and Reynolds numbers between 5×10^4 and 3×10^5. In contrast with the findings of Brundrett and Baines, the results showed a decrease in U_s/U_c, as the Reynolds number increased; Gessner and Jones suggested thatthis was a consequence of increased turbulent mixing tending to reduce gradients in the flow. Measurements of the angle between the wall shear stress vector and the duct axis, complementing the more common measurements of shear stress magnitude, showed an increase from 0^o at the wall midpoints to 4^o at a position near the corner. The skewness of the wall shear stress vector thus opposed the secondary flow from the corner towards the midpoint of of the side wall. Gessner and Jones directed attention to a single isovel in order

to examine the assumption, in the analysis of Deissler and Taylor (1959), that no Reynolds shear stresses could exist on planes normal to an isovel. From their measurements of shear stress they showed that shear stress could exist on planes normal to the isovels. Finally Gessner and Jones made an momentum balance along a secondary flow stream line from which they concluded that the predominant opposing forces were the Reynolds stresses and static pressure gradients; small differences between these forces were considered to cause secondary flow.

Tracy (1965) obtained detail measurements of fully developed turbulent flow in a duct of aspect ratio 6.4. In his experiment stagnation tube was used for the measurements of mean axial velocity and hot wires for turbulence quantities and secondary velocities. His measurements showed that the flow was two-dimensional in the central one-third (actually 0.375 of total duct area) of the duct and three-dimensional in the side wall areas on either side of the central area. He reached at the same conclusion of Brundrett and Baines (1964) about the sources of secondary flow and made measurements in a half of a side wall area. Far away from the side wall, mean velocity curves showed universal log law (equation 2.24) variation with $\kappa = 0.35$ and $B_s = 3.3$ while near the side wall, in variance. With the approach of the side wall maxima of his mean velocity profiles (parallel to the side wall) shifted away from major axis indicating the presence of secondary velocity. From the profiles of $(\overline{u_2^2} - \overline{u_3^2})$ he justified the presence of secondary velocity in the side region where his measurements showed two counter rotating swirls directing fluids towards the corner. Maximum secondary velocity of about 1.8% of duct centre line velocity was recorded close to the side wall.

Launder and Ying (1972) also measured the secondary velocities both in smooth and rough square ducts, by Hoagland's hot wire technique at Reynolds numbers of 6.95×10^4 and 2.2×10^5 and found that in the smooth duct, secondary velocity, decreased as Reynolds number increased and remained constant when the walls were roughened by transverse square ribs. The secondary velocity, when nondimensionalized by average frition velocity, became

independent of both Reynolds number and wall roughness. They concluded that the friction velocity, U_τ, was more appropriate to normalize secondary velocity than U_c and noted that the variation of U_s with Re, reported by Gessner and Jones (1965), was considerably reduced if U_s was normalised by U_τ rather than U_c. The mean velocity profiles showed a logarithmic variation near the wall for both smooth and rough surfaces.

Melling and Whitelaw (1976) made detailed measurements of developing turbulent flow in a square duct by laser Doppler anemometry, thus avoiding possible effect of probe interference. Mean longitudinal and secondary velocities, turbulence intensities, Reynolds shear stresses etc, were measured over duct cross section at a number of stations from x_1/D_h of 5.6 to 36.8 in the developing flow. Their measurements were in much greater detail than those of Ahmed and Brundrett (1971b). Measurements were made in a quadrant of the duct and symmetry between the two octants was checked and found satisfactory. Contours of longitudinal mean velocity and turbulence intensity in the developing range of the flow showed the gradual bulging towards the corner indicative of production of secondary currents. In each stage of development, the bulging of the contours of turbulence intensity, $\tilde{u}_1/U_c$, was much more pronounced than that of mean velocity, U_1/U_c. Clauser plots of the mean velocity profiles showed logarithmic variations except near the corners. Secondary velocity components, U_2 and U_3, were also measured by the laser Doppler technique and showed uncertainties in the mass balance but their vector plot gave a qualitative picture of the secondary current present in the flow field. The authors adjusted the vector diagram by taking the U_2 component from measured value and adjusted U_3 from the continuity equation. Comparing the two diagrams (adjusted and unadjusted) a realistic view of the reliability of the secondary velocity measurements was provided.

1.3.2 Measurements of Turbulent Flow Through Ducts with Dissimilar Walls

Previous measurements in dissimilar ducts are summarised in table 1.2 and, in general, show increased wall shear stress, heat transfer etc, in the presence of rough walls.

TABLE 1.2 - Measurements of Turbulent Flow through Ducts with Dissimilar walls

AUTHORS (YEAR)	FLOW CONFIGURATION	MEASUREMENTS	INSTRUMENTATION	COMMENT
Wilkie D, Cowin M, Burnett P and Burgoyne T (1967)	Rectangular ducts (W/H = 11) ; three rough plates of different sizes of discrete roughness and one smooth plate; duct is made of combination of any two of the above plates.	$\frac{\partial p}{\partial x_1}$	Static pressure taps; pitot tube.	Variation of C_f with Re to verify Hall's transformation.
Asano (1972)	Six square ducts from all smooth to all rough; two arrangements for two rough wall duct; (e_s^*/D_h=.0043,.01,.02) $2x10^4 < Re < 5x10^5$	$\frac{\partial p}{\partial x_1}$; variation of C_f with Re; U_1 contours for three rough wall duct.	Static pressure taps; pitot tube.	Effect of e_s/D_h and number of rough wall on duct flow resistance studied and from the result friction factor correlation proposed for ducts with combination of smooth-rough wall.
Fujita (1978)	Six sqaure ducts as of Asano but discrete round wire roughness; (P/e =10, e/D_h =.02) $1.7x10^4 < R_e < 6.5x10^4$	U_1 profiles and contours; Distribution of smooth wall shear stress; variation of C_f with Re.	Static pressure taps; Preston tube; pitot tube.	U_1 velocity profiles obey log law; U_1 contours bulge towards the corner;with the arrangement of rough wall, smooth wall shear stresses vary. Friction factor correlation proposed by Asnano modified.

* e_s - sand roughness height

TABLE 1.2 (cont'd)

AUTHORS (YEAR)	FLOW CONFIGURATION	MEASUREMENTS	INSTRUMENTATION	COMMENT
Hanjalic and Launder (1972a)	Rectangular ducts; (W/H = 6, 12) one rough wall with discrete, transverse square ribs. (e/D_h = .066, .034 P/e = 10) $1.8x10^4 < Re < 7.7x10^4$	Profiles of U_1; components of turbulence intensities, $\tilde{u}_i$ and Reynolds shear stress, $\overline{u_1 u_j}$; spectra of $\overline{u_i u_j}$; distribution of micro and macro length scales.	Static pressure taps; Stanton and Preston tubes; pitot tube; hot wire anemometer.	U_1 profiles near both the walls showed local equilibrium, zero values of $\frac{\partial U_1}{\partial x_3}$ and $\overline{u_1 u_3}$ do not coincide, integral length scales show less asymmetry than the turbulence velocity correlation.
Humphrey and Whitelaw (1979)	Developing flow in a square duct with one rough wall; discrete sqaure rib roughness. (e/D_h = .99, P/e = 10) $Re = 2.58x10^4$	Contours of U_1, U_3, $\tilde{u}_1$ $\tilde{u}_3$, $\overline{u_1 u_3}$ at positions above the ribs and in between the ribs, over the developing length; variation of C_f with Re.	Static pressure taps; laser Doppler anemometer.	U_1 contours bulge much earlier than smooth duct results; strong secondary motion lies near the side walls; generation of turbulence was identified to be near the rough wall. Near the smooth wall local flow equilibrium was found.

Hall (1962) noted that friction factor data for noncircular ducts of uniform surface roughness agreed well with those of circular pipes provided the hydraulic diameter was used as the characteristic length of the system. As an extension of this observation, he proposed that in ducts composed of different surface roughness (ie, an annulus consisting of a rough core tube in a smooth outer tube), the flow on either side of a surface of the maximum velocity was unaffected by the flow on the other. Some implications of the model are illustrated in figure 1.1, for the case of flow between parallel planes. Referring to figure 1.1, the velocity profile from the smooth surface to the point of maximum velocity in a rough-smooth assembly should, according to Hall's model, be identical to the half profile in flow between two smooth planes, provided the smooth wall shear stress and the longitudinal pressure gradient were the same in each case.

Some experiments by Wilkie et al (1967), undertaken specially to check the degree of correctness of Hall's transformation theory, brought some inconsistencies. The measurements were taken in flow between parallel plates in which neither, one or both of the plates had been roughened with transversed isolated square ribs. The transformed friction factors in the asymmetric assemblies were compared with those measured directly in the symmetric configuration. Differences between the corresponding friction factors of upto 10% were deduced. The Hall transformation assumed implicitly that the positions of maximum velocity and zero shear stress were coincident and Wilkie suggested that, if the position of zero shear stress lay closer to the smooth (or smoother) surface than the position of maximum velocity in an asymmetric arrangement, then the anamolies between transformed and untransformed friction factors could be explained. At that time, no measurements of Reynolds shear stress in unsymmetrically roughened duct were available and the quantitative confirmation of Wilkie's conjecture was later provided by Hanjalic and Launder (1972a). Thus the notions surrounding the Hall transformation were not wholly correct even in flows without secondary currents. In the central region of Wilkie's channels, the strong asymmetry of the surface shear stresses caused considerable dis-

tortion to the mean velocity profile from those occurring in symmetric assemblies. Near the walls of the channel, however, it would seem likely that therewas a region where the flow was not affected by the opposite wall.

Asano (1972) measured in square ducts with six different arrangements of smooth and rough surfaces of the duct walls. Wall surfaces were roughened with sand of three different grain sizes to give the roughness ratio, es/D_h, of values 0.0043, 0.01 and 0.02. Isovel plots for the duct with three rough walls showed bulging towards the corners with the isovels occurring closer to the smooth wall. Asano directed his attention to correlations for the friction factor with the number of rough walls of the duct and proposed the correlation:

$$C_{fn} = \left\{\alpha(4-n)\ C_{fs} + \beta n\ C_{fr}\right\} /4 \qquad \ldots\ (1.6)$$

where n is the number of rough walls, α and β are the constants, C_{fn} is the friction factor for duct with n rough walls and C_{fs} and C_{fr} are the friction factor for duct with all smooth or all rough wall respectively. The constants α^* and β^* were assumed to be the functions of the rough walls of the duct and their equivalent sand roughness.

This equation did not give good prediction for roughness whose equivalent sand roughness deviated from that of his own, as observed later by Fujita (1978). The deviation was thought to be caused by the experimental error and the unsuitable conditions assumed in the process leading to the equations.

Fijita (1978) carried out his ivestigation in square ducts with six different arrangements of smooth-rough walls as Asano but with discrete roughness made by 1 mm diameter round wires placed transverse to the flow direction at 10 mm apart. Smooth wall shear stresses were determined from the Preston tube measurements using Patel's (1965) method of calculation and rough wall shear stresses were obtained by substracting the smooth wall shear stress from the total duct resistance. The distribution of smooth wall shear stress for all the ducts

---

* $\alpha = (4 - \beta n) / (4 - n)$
$\beta = \{5(2 - B) + 0.03\}n - \{0.63 \log (e_s/D_h) + 0.5\}$

showed its higher gradient near the smooth wall corners than the corners having one rough wall, indicative of the presence of weak secondary motion in the rough wall region comparing with that near the smooth wall. Contribution of different wall shear stress to the total duct flow resistance was determined and found to vary with the arrangement of the walls. For the prediction of friction factor for ducts with different number of rough walls Fujita used the correlation of Asano, equation 1.6, but with constants α^* and β^* as functions of the number of rough walls, n, only. This improved the predicted value for higher range of roughness ratio (upto $e_s/D_h = 0.144$). The universal log law profiles for the smooth wall were shown to be valid for the considerably large part of the duct wall ($x_2/a = 0.05$ to 0.50). Isovel plots of all the ducts showed in general bulging towards the corners which was most in the smooth duct.

Hanjalic and Launder (1972a) made a detailed study of asymmetric flow in ducts of high aspect ratio (6 and 12). Asymmetry was introduced by roughening one of the walls with square ribs transverse to the flow direction. Measurements of mean velocity was made with pitot tube and turbulence properties upto fourth order correlation, were measured with hot wires. The smooth wall shear stress was determined with a Stanton tube. Normalised mean velocities near both the walls, rough and smooth, obeyed the universal log law profiles, suggesting local equilibrium. For the rough wall profiles, the authors suggested that the imaginary origin (the imaginary wall, in a discrete rough surface, where velocity was assumed to be zero) be located at 0.4 rib height below the rib root. The main emphasis was to establish the turbulence structure, particularly in the central region of the channel where two dissimilar wall flows (generated by the smooth and rough surfaces) interacted. Evidence of interaction was provided by the profiles of the mean velocity, Reynolds stresses and triple correlations. The results showed that the region of strong interaction was characterised by substantial diffusive transport of turbulent shear stress and kinetic energy

---

* $\alpha = 1.0 + 0.035n$

$\beta = 0.56 + 0.11n$

from the rough wall towards the smooth wall region. This stress transport was the cause for appreciable seperation observed between the planes of zero shear stress and maximum mean velocity. In contrast to the turbulent velocity correlations, both the macro and micro turbulent length scales exhibited nearly symmetric behaviour. The longitudinal integral scales were of the same order of magnitude to those in a smooth channel or in a pipe.

Humphrey and Whitelaw (1979) measured the mean and turbulent flow properties of a developing flow through a asymmetric square duct and thus enhanced the effects of side walls which was absent in Hanjalic and Launder's measurements. One of the duct walls was roughened by fixing square ribs with pitch to height ratio of 10 and a laser Doppler anemometer was used for the measurements. At various stages of flow development, measurements were taken both above the rib and in between the ribs and showed, in general, the effect of sudden contraction and sudden enlargement respectively. The variation of flow characteristics due to these effects was confined mainly to the region near the rough wall. The measurements showed the early appearance (at x_1/D_h = 6.15 comparing with x_1/D_h = 13.2 in Melling and Whitelaw's smooth duct measurements) of secondary motion which progressively increased with the development of flow. At the final stage of development (x_1/D_h = 41.68), the U_3 component of secondary velocity (flow across the rough wall) reached a maximum of 17% of duct centre line velocity and their high values were also present near the smooth wall adjacent to the rough wall. The transverse, turbulence intensity, $\tilde{u}_2$ was not available but, from the high values of $\tilde{u}_3$ alone, the smooth wall region was suggested to be the zone of high degree of anistropy favourable for the generation of secondary motion. The effect of secondary flow on the distribution of flow properties was pronounced. Measurements showed that turbulence was generated near the rough wall and carried away towards the smooth wall in the direction of secondary velocities. Results of the longitudinal velocity component showed that the bulk of the flow was shifted towards the smooth wall (opposite to the rough wall). Although the logarithmic law of the wall was followed near the midplane of both the rough and smooth wall, departure from the universal

behaviour became significant near the corners where side wall strongly affected the flow.

1.3.3 Theoretical Studies of Duct Flows

Until recently theoretical studies of turbulent duct flows received less attention and there is little predicted flow information available for such flow. Some of these works are listed in table 1.3. At early stage of calculation Deissler and Taylor (1959) devised a method, without considering the effect of secondary velocity, for determining axial velocity and heat transfer in fully developed duct flows. Later a more realistic model with secondary flow generation was used by Launder and Ying (1973) and Naot et al (1974) for fully developed flow and by Tátchell (1975) and Gessner and Emery (1976) for developing flow.

In Deissler and Taylor's method of calculation, velocity was assumed to follow a universal profile, equation 2.24, across the wall and the veloicty distribution was found by the method of successive aproximation on the basis of force balance between the local wall shear stress, τ_w, and axial pressure gradient, $\partial P/\partial x_1$. Because secondary flow was neglected, isovels obtained by Deissler and Taylor in triangular and square ducts did not exhibit bulges towards the corners. For the same reason, the wall shear stress distribution showed a greater variation at positions remote from the corners than has been found by experiments. Hartnett et al (1962) attempted to predict their data by this analysis; the friction coefficient as a function of Reynolds number was adequately predicted for aspect ratios greater than 5, but for a square duct the predicted friction factor was upto 12% too low. The discrepancy was due to the greater influence of secondary flows in small aspect ratio ducts.

A method for the prediction of fully developed turbulent flow in square ducts with secondary flow represented, was described by Launder and Ying (1973). They expressed the equations of motion, equations 2.4 to 2.6, in terms of stream function ψ, and axial vorticity, Ω_1, and thereby eliminating pressure term from the general form of equations, where $\partial\psi/\partial x_2 = -U_3$, $\partial\psi/\partial x_3 = -U_2$ and $\Omega_1 = \partial U_2/\partial x_3 - \partial U_3/\partial x_2$. By neglecting or approximating

AUTHORS (YEAR)	FLOW CONFIGURATION	SOLUTION METHODS	COMMENT
Diessler and Taylor (1959)	Square and equilateral triangular duct $2.4 \times 10^5 < Re < 9 \times 10^5$	Graphical Integration and iteration	Secondary velocity not accounted for
Launder and Ying (1973)	Square duct; smooth and rough $Re = 6.9 \times 10^4$ and 2.2×10^5	One equation (k) model; shear stress approximated by algebraic relation with mean velocity gradients; ℓ is prescribed by algebraic relation.	Prediction of smooth wall shear stress distribution is in good agreement. Predictions of U_1 and U_2 contours are in general agreement with the measurements.
Naot D, Shavit A and Wolfshlein M (1974)	Square duct $Re = 8.3 \times 10^4$	Nine equations model.	Predicted contours of U_1, k, $\overline{u_2 u_3}$, $(\overline{u_2^2} - \overline{u_3^2})$ and stream function, Ψ are in general agreement with measurement, but comparing with the precision of other predicted values (Launder and Ying for example) complexity of the model is not justified.
Tatchell (1975)	Developing square duct $5.4 \times 10^4 < Re < 3.5 \times 10^5$	Two (k-ε) equations model. Shear stress approximated algebraically as Launder and Ying.	Predicted contours of U_1 and k show less bulging than the measurements; pressure drop agrees with Ahmed but development of centreline velocity is less than the measurements.
Gessner and Emery (1976)	Square duct	One equation (k) model; prescription of ℓ different from Launder and Ying and so the algebraic relation for shear stresses	Predicted contours of U_1, $\tilde{u}_1$, $\tilde{u}_2$, $\tilde{u}_3$, k, $\overline{u_1 u_2}$ are in general agreement with the experiment.

terms in Reynolds stress transport equation (equation 2.14), Launder and Ying modelled the stresses in duct cross section in terms of mean rate of strain in planes parallel to the duct axis:

$$\overline{u_2^2} - \overline{u_3^2} = C^1 \, k/\varepsilon \left(\overline{u_1 u_2} \, \frac{\partial U_1}{\partial x_2} - \overline{u_1 u_3} \, \frac{\partial U_1}{\partial x_3} \right) \qquad \ldots (1.7)$$

$$\overline{u_2 u_3} = C^1 \, k/\varepsilon \left(\overline{u_1 u_3} \, \frac{\partial U_1}{\partial x_3} + \overline{u_1 u_2} \, \frac{\partial U_1}{\partial x_3} \right) \qquad \ldots (1.8)$$

where C^1 is constant. The shear stress components, $\overline{u_1 u_2}$ and $\overline{u_1 u_3}$, were then modelled with the effective viscosity concept (section 2.2) and ε was calculated from the algebraic relation

$$\varepsilon = C_D k^{3/2}/\ell \qquad \ldots (1.9)$$

where C_D is an empirical constant and ℓ a turbulence length scale. The system of equations was closed at the level of one-equation turbulence model by solving the kinetic energy equation (equation 2.20) and specifying the length scale proposed by Buleev (1963). Predictions of the flow through both smooth and rough ducts gave isovels exhibiting significant bulging towards the duct corners and agreeing well with their measurements (1972). Predicted profiles of one component of secondary velocity, U_2/U_τ, in both ducts showed the same type of distribution as those of measurements but their magnitudes differed from the later. Predicted kinetic energy contours were similar in shape to those reported by Brundrett and Baines (1964) but the magnitudes were substantially lower than those measured. The distribution of smooth wall shear stress was in good agreement with that measured by Brundrett and Burroughs (1967) and friction factor variation with Reynolds number agreed well with the experimental results of Leuthesser (1963), Hartnett et al (1962) and their own rough duct measurements.

The model proposed by Naot et al (1974) was intended to provide a solution for the problem of fully developed turbulent

flow in a square duct. Reynolds stresses were modelled by means of respective transport equations, rather than algebraic relationships and nine governing equations resulted, for the axial velocity, vorticity, stream function and six components of Reynolds stresses, which had to be solved simultaneously. Numerical results yielded isotach patterns which agreed well with Leuthsser's (1963) experimental results although, the degree of isotach distortion was overly emphasized in the vicinity of the wall bisector. Turbulence kinetic energy contours exhibited much less distortion than those measured by Brundrett and Baines (1964) and the predicted and measured values of $(\overline{u_2^2}-\overline{u_3^2})$ were of the same order of magnitudes. Although these predictions showed encouraging trends, further improvement is necessary, to obtain results in both fully developed and developing flow to a sufficient quality to justify the complexity of the model.

Tatchell (1975) used a modified version of the model of Launder and Ying (1973) to predict both fully developed and developing flow in ducts of square cross section. Instead of specifying a length scale distribution as used by Launder and Ying, Tatchell calculated turbulence dissipation, ε, from its modelled transport equation (equation 2.21) in addition to that for k (equation 2.20). Predictions were made with a three-dimensional boundary layer calculation procedure. The primary purpose was to test the procedure rather than the turbulence model and thus no attempt was made to optimise the predictions by adjusting constants in the modelled equations. Tatchell compared his predictions with the measurements of Ahmed (1971a) in a developing flow at Re= 8.8×10^4 as far downstream as $x_1/D_h = 26.2$; these included mean velocity and turbulence kinetic energy. The rate of development of centre line mean velocity was predicted to be slower than measured by Ahmed and that predicted at Re= 3.6×10^4 agreed well upto $x_1/D_h = 25$ with Melling's (1975) measurements at Re= 4.2×10^4. At 90 hydraulic diameter downstream while the centre line velocity and axial pressure gradient attained their nearly fully developed values, the centre line turbulence kinetic energy exhibited significant axial variation. The overall agree-

ment of fully developed flow calculations was good. Contours of mean velocity and turbulence kinetic energy showed bulging towards the corner although there weresome inconsistencies in magngitudes compared with the experimental results of Brundrett and Baines (1964) and Gessner (1964). Predicted directions of secondary velocities were in agreement with those of Brundrett and Baines but their magnitudes differed in some regions by about 100%. In the rough duct measurements of Launder and Ying (1972) the effect of wall roughness was seen to increase the centre line velocity and to raise the level of secondary flows. Both these effects were reflected in the calculations.

The algebraic stress closure developed by Gessner and Emery (1976) is very similar to that of Launder and Ying (1973). As the authors indicated, the approach was based on the pressure-strain model developed by Hanjalic and Launder (1972b) and used the mixing length distribution proposed by Buleev (1963) in a modified form and that agreed with the experimental results of Tracy (1965). Profiles of turbulence intensities, Reynolds shear stress, turbulence kinetic energy and $(\overline{u_2^2} - \overline{u_3^2})$ of experimental results of Gessner (1964) were compared with the predicted ones and found in general agreement.

1.4 Outline of Research

The observations presented in the preceding sections of this chapter showed that there are deficiencies in the measurements of turbulent flow through rectangular duct (particularly ducts with combination of rough-smooth wall) which can be compared to test the turbulence models used in their calculations. Like measurements, calculation details of turbulent duct flow are few. Turbulent flow in low aspect ratio ducts with rough-smooth wall provides a sensitive test for the model because of the asymmetry of the flow configuration and of the magnitude of the secondary velocities and their dependence on accurate prediction of Reynolds stress. By comparing measurements and calculation of quantities such as axial mean and secondary velocities and Reynolds stresses, the turbulence models could be tested, modified and extended to further complex flow geometries used in

present day engineering installations.

Two flows, of considerable theoretical interest, which are, therefore, investigated, ie, the flows in square ducts with one rough wall and two rough walls. The investigation is carried out in two stages: first the measurements and secondly the calculation and the comparison between the two. The experimental programme, which is by far the larger component of the present work, is aimed to provide detailed measurements of the flow field in straight square ducts, with one rough wall and two opposite rough walls. The ducts designed to be square cross section in order to enhance the charateristics of secondary motion and hence its interaction with the other flow properties generated by the dissimilar boundary conditions. In the experimental study, the following variables are mapped in both flows over the entire duct cross section:

$$U_1,\ U_2,\ U_3,\ \tilde{u}_1,\ \tilde{u}_2,\ \tilde{u}_3,\ \overline{u_1u_2},\ \overline{u_1u_3},\ k,\ (\overline{u_1^2} - \overline{u_3^2})$$

and the distribution of wall shear stress is presented over the entire duct wall at the measuring section. In addition, the variation of friction factor with Reynolds number and longitudinal turbulence spectra are also presented.

In the second stage of the investigation, a fully elliptic numerical procedure was used for the calculation of duct flows. The present calculation includes some of the work of Launder and Ying (1973), Tatchell (1975) and Gessner and Emery (1976). The model, before applying to the asymmetric flow configuration, is tested with known experimental results. Finally, the model was used for the calculation of the asymmetric flow configuration in which measurements are made.

1.5 Thesis Outline

The remainder of this thesis is divided into seven chapters whichdeal with the seperate aspects of the problem. In chapter 2, the equations of motion and turbulence models used to solve those equations are presented and discussed. The

selection of turbulence model and solution procedure used in the present calculation are also presented in chapter 2. Chapter 3 describes the flow system and measuring techniques used. An anlaysis of the uncertainties in the measurements are made in section 3.5. Chapter 3 concludes with preliminary tests to check the flow symmetry of the ducts.

Chapters 4 and 5 deal with the measurement results and, in each case, these are dealt in two sections, first with the presentation of results and then with their relationship to previous works. The chapters conclude with a summary of the results.

In chapter 6, the calculated results of square ducts with all smooth, two rough and one rough wall are respectively presented and compared with the measurements. The chapter concludes with the analysis of discrepancies and the suggestions for the improvement of the model.

Chapter 7 starts with a discussion of the areas of importance of the present work. Some general discussions in connection with the characteristics of discrete rough wall and asymmetric turbulence structure are also made in this chapter. The thesis in concluded in chapter 8 with an assessment of the contributions and limitations of the present work. Possible areas for continuing research are also described in the concluding chapter.

C H A P T E R 2

EQUATIONS, MODELS AND SOLUTION PROCEDURE

2.1 Introduction: Preliminary Remarks and Equations

This chapter describes the components of the method used to evaluate the turbulent flows of chapters 4 and 5. Forms of the governing equations of fluid motion applicable to the present flow configuration are discussed together with available turbulence models and solution methods. The choices of turbulence model and solution procedure are justified.

The difficulties involved in solving the conservation equations describing the instantaneous motion of a turbulent flow (as opposed to the same equations for laminar flows) are well known. In paricular, the problems are associated with the fluctuating and small-scale (about 10^3 times smaller than the typical flow dimension) nature of turbulent motions and the consequent requirement of a number of nodes, for adequate numerical solution, in excess of that available with present-day computers. The commonly adopted alternative and that used here, is to work with the time-averaged forms of the conservation equations.

The general forms of the conservation equations for steady, incompressible constant property flow in rectangular coordinates are given by:

Continuity

$$\frac{\partial U_i}{\partial x_i} = 0 \qquad \ldots (2.1)$$

Momentum

$$\rho U_j \frac{\partial U_i}{\partial x_j} = \frac{\partial P}{\partial x_i} + \frac{\partial}{\partial x_j}\left(\mu \frac{\partial U_i}{\partial x_j} - \rho \overline{u_i u_j} \right) + F_i \qquad \ldots (2.2)$$

Transferable scalar quantity

$$\rho U_j \frac{\partial Q}{\partial x_j} = \frac{\partial}{\partial x_j}\left(F_q \frac{\partial Q}{\partial x_j} - \rho\overline{u_j q}\right) + S_q \qquad \ldots (2.3)$$

where capital letters denote average values and small letters instantaneous values. The rectangular coordinates summation convention on repeated indices is applied. F_i and S_q denote additional source terms in equations 2.2 and 2.3 respectively. Generally, however, F_i is the body force arising through gravitational effects and S_q, for the case of enthalpy transport for instance, corresponds to the heat generated by the dissipation of the kinetic energy of the flow.

The above equations can, however, be simplified for the present situation where the flow is fully developed and predominantly in the main flow direction (x_1 - direction in figure 3.2). Derivatives of the velocity components (both mean and instantaneous) in the x_1 - direction are thus zero together with gravitational effects for this horizontal flow. Equations 2.1 and 2.2 can thus be rewritten in expanded form for directions 1,2 and 3 respectively as

Continuity

$$\frac{\partial U_2}{\partial x_2} + \frac{\partial U_3}{\partial x_3} = 0 \qquad \ldots (2.4)$$

Momentum

x_1 - direction

$$\rho U_2 \frac{\partial U_1}{\partial x_2} + \rho U_3 \frac{\partial U_1}{\partial x_3} = \frac{\partial P}{\partial x_1} + \mu\left[\frac{\partial^2 U_1}{\partial x_2^2} + \frac{\partial^2 U_1}{\partial x_3^2}\right] - \rho\left[\frac{\partial \overline{u_1 u_2}}{\partial x_2} - \frac{\partial \overline{u_1 u_3}}{\partial x_3}\right] \qquad \ldots (2.5)$$

x_2 - direction

$$\rho U_2 \frac{\partial U_2}{\partial x_2} + \rho U_3 \frac{\partial U_2}{\partial x_3} = \frac{\partial P}{\partial x_2} + \mu\left[\frac{\partial^2 U_2}{\partial x_2^2} + \frac{\partial^2 U_2}{\partial x_3^2}\right] - \rho\left[\frac{\partial \overline{u_2^2}}{\partial x_2} + \frac{\partial \overline{u_2 u_3}}{\partial x_3}\right] \qquad \ldots (2.6)$$

x_3 - direction

$$\rho U_2 \frac{\partial U_3}{\partial x_2} + \rho U_3 \frac{\partial U_3}{\partial x_3} = \frac{\partial P}{\partial x_3} + \mu \left[\frac{\partial^2 U_3}{\partial x_2^2} + \frac{\partial^2 U_3}{\partial x_3^2} \right] - \rho \left[\frac{\partial \overline{u_2 u_3}}{\partial x_2} + \frac{\partial \overline{u_3^2}}{\partial x_3} \right] \quad \ldots (2.7)$$

similarly the Q equation can be rewritten by neglecting the axially-directed diffusive fluxes as:

Transferable scalar quantity

$$\rho U_2 \frac{\partial Q}{\partial x_2} + \rho U_3 \frac{\partial Q}{\partial x_3} = \frac{\partial}{\partial x_2} \left(\Gamma_q \frac{\partial Q}{\partial x_2} \right) + \frac{\partial}{\partial x_3} \left(\Gamma_q \frac{\partial Q}{\partial x_3} \right) - \left[\frac{\partial}{\partial x_2} (\rho \overline{u_2 q}) + \frac{\partial}{\partial x_3} (\rho \overline{u_3 q}) \right] + S_q \quad \ldots (2.8)$$

2.2 Turbulence Models

In the time-averaged equations for conservation of momentum (eq. 2.2) there is a term involving time-averaged products of velocity fluctuations, $\overline{u_i u_j}$ and in the Q equation, that of the correlation between velocity and the scalar, i.e. $\overline{u_i q}$. These are known as turbulent (or Reynolds) stresses and turbulent fluxes and they are not known appropriately. Thus the problem of closure arises, that is, of relating the turbulent stresses or fluxes to known variables or functions of known variables of the flow. The problem can be overcome, at least in part, by turbulence models where a set of additional equations, either differential or algebraic, enables these quantities to be approximated in terms of calculable quantities. These approximate equations are based on assumptions and physical reasoning, supported by experimental evidence. Numerous turbulence models have been proposed and aimed to solve the particular problem of the individual investigator. The great majority of available models may be grouped under two

catagories:

(a) Turbulent viscosity models and

(b) Turbulent stress models

(a) <u>Turbulent viscosity models</u>

Models in this group are characterised by the assumption that the Reynolds stresses, $\overline{u_i u_j}$, are related to the time-averaged rate of strain tensor by a scalar property of turbulence structure i.e. an apparent turbulent viscosity, μ_t, and can be expressed as:

$$- \rho\overline{u_i u_j}' = \mu_t \left[\frac{\partial U_i}{\partial x_j} + \frac{\partial U_j}{\partial x_i}\right] - \frac{2}{3}\delta_{ij}\rho k \qquad \ldots (2.9)$$

where δ_{ij} is the Kronecker delta tensor which is 1 for $i = j$ and 0 otherwise and k is the kinetic energy of turbulence.

Equation 2.9 is the generalised form of the Boussinesq hypothesis as shown by Hinze (1959). The turbulent viscosity, μ_t, is further assumed to be related to a typical turbulent length scale, ℓ, and characteristic velocity, V_t, by:

$$\mu_t = \rho V_t \ell \qquad \ldots (2.10)$$

Depending on the manner in which V_t and ℓ are determined, different types of viscosity models are in use such as zero, one (k) or two (k-ε) equation models.

Until recently, the most commonly used practical model in predicting turbulent flow was the first one (i.e. Prandtl's mixing length hypothesis) in which ℓ is prescribed algebrically and V_t assumed to be proportional to the mean velocity gradient, $\frac{\partial U_1}{\partial x_2}$, and they are related through expression:

$$\mu_t = \rho \ell^2 \left| \frac{\partial U_1}{\partial x_2} \right| \qquad \ldots (2.11)$$

A more general approach of mixing length hypothesis is based on Prandtl - Kolmogorov formula (Prandtl, 1945, Kolmogorov, 1942) in which it is assumed that V_t is a function of turbulent kinetic energy and that μ_t is related to two turbulent quantities, the turbulent kinetic energy, k and the length scale, ℓ, via the espression:

$$\mu_t = C\mu\rho\ell k^{\frac{1}{2}} \qquad \ldots (2.12)$$

where $C\mu$ is a constant. The turbulent kinetic energy is obtained by solving the transport equation for k which is devised in section 2.4. The length scale may be specified algebrically (Wolfshtein 1967, Runchal 1969) or may be obtained by solving the transport equation for some variable of the form $k^m \ell^n$, for example energy-length scale model, ($k\ell$) (Rodi and Spalding, 1970) and dissipation model ($k^{3/2} \ell^{-1}$) (Jones and Launder 1970). It has been shown that one equation models can be used with reasonable degree of confience only for a limited number of two dimensional boundary layer flows.

The difficulty of prescribing a length scale is overcome by the two equation ($k-\varepsilon$) model employed in the present calculation, wherein ℓ is assumed to be a function of k and ε ($\alpha k^{3/2}/\varepsilon$), thereby removing the need to specify ℓ. The turbulent dissipation rate, ε, is calculated (in addition to k) from its modelled transport equation (equation 2.21). Thus, the turbulent viscosity is represented by the equation:

$$\mu_t = C\mu\rho k^2/\varepsilon \qquad \ldots (2.13)$$

Two equation models have been applied to the calculation of a wide range of two-dimensional boundary layer flows by among others, Rodi and Spalding (1970), N_g (1971) and Jones and Launder (1973) and two dimensional recirculating flows by Lefeuvre (1973), Roberts (1972), Matthews and Whitelaw (1971) and Date (1973). These studies include such diverse flow situations as: wall flows, free shear flows, cross flow in a tube

bank, confined swirling flow with seperation and flow and heat transfer in a twisted tape in a heat exchanger. In general, the performance of the model is good. Mean flow quantities, such as, surface shear stress, veloicty profiles, pressure drop and heat transfer rates are in most cases well predicted. Turbulence quantities, such as k and μ_t show fairly good agreement with measurements.

However, while the turbulent viscosity model and the (k-ε) model in particular, have enjoyed a certain amount of success in predicting the various types of flows described above, they have shortcoming in predicting turbulent flows with secondary motion. It has long been known (Nikuradse 1926) that for fully developed turbulent flow in rectangular ducts, secondary motions exist which are due entirely to the action of turbulent normal stresses (Brundrett and Baines, 1964). For fully developed laminar flows, in contrast, the lateral velocities are zero. The turbulence induced velocities are themselves small (a few percent of mean velocity) but their neglect in calculations can cause significant errors: for example, the friction factor for the flow in a square duct is under estimated by as much as ten percent (Launder and Ying 1973). Consequently, it is important that any calculation procedure for such flows should be capable of predicting these secondary motions, but this can not be done with a turbulence model of the turbulent viscosity type.

(b) Reynolds stress models

Reynolds stress models have been developed as an alternative to the turbulent viscosity approach, so as to deal with the turbulent flow structure more realistically. In these models Reynolds stresses are solved from their differential transport equations and such models have been formulated by, among others, Daly and Harlow (1970), Hanjalic and Launder (1972b) Launder et al (1975) and Naot et al (1972). In this catagory, the Reynolds stresses are obtained from modelled forms of their transport equations, thus obviating the need for a turbulent viscosity assumption, but requiring the solution of a larger

number of equations. The turbulent stresses are, therefore, less directly connected to the mean velocity than implied by the turbulent viscosity assumption.

The disadvantage in pursuing a stress transport model approach in complex flow situations is the uncertainty regarding the appropriate form of the modelled transport equations and the computation work involved in solving the seven strongly coupled differential equations which make up the models; for equations must be solved for six stresses and for ε. Fortunately under certain circumstances, it is possible to reduce the stress equations to algebraic relations. In order do to this, some assumption must be made regarding the convection and diffusion terms. For example, Launder and Ying (1973) chose to neglect these terms entirely for their calculations of fully developed flow in a square duct, and were successful in predicting the turbulent induced secondary motions. Alternatively, the net rate of transport of stress by convection and diffusion may be related to that of turbulence energy (for which a differential equation must be solved); this approach has been adopted by Rodi (1972) and Koosinlin (1974). Bradshaw et al (1967a) have proposed a simpler type of stress model for two-dimensional boundary layer flows, wherein the turbulent shear stress is presumed to be directly proportional to k which is obtained from its modelled transport equation. This model has been successfully extended to external three-dimensional boundary layers, by, among others, Nash (1969) and Bradshaw (1971). However, the presumption that shear stress is proportional to k is valid only for a restricted range of near surface boundary layers and this type of model is, therefore, not suitable for the more complex flow situation studied here.

2.3 Choice of Turbulence Model

The choice of turbulence model for the present flow is dictated by the need to predict the turbulence induced secondary motion without severely extending the existing computing capabilities. Brundrett and Baines (1964) (discussed in section 1.3.1) showed that the source of secondary flow is the difference of the normal stress, $(\overline{u_2^2}-\overline{u_3^2})$ (by comparison, the

other source term, the shear stress in the crossplane of the duct, $\overline{\rho u_2 u_3}$, is neglible). Hence, if the secondary flows are to be predicted, the adopted turbulence model must provide a reasonable simulation of the normal stresses.

As $\overline{u_2^2}$ and $\overline{u_3^2}$ are always of positive sign (i.e, the normal stresses - $\rho\overline{u_2^2}$ and $-\rho\overline{u_3^2}$ are always negative) while the gradients $\frac{\partial U_2}{\partial x_2}$ and $\frac{\partial U_3}{\partial x_3}$ can be both positive and negative, a turbulent viscosity type of model as implied by equation 2.9, can not properly simulate the normal stresses. Hence, a more correct approach to model the normal stresses would be to determine them by way of their transport equations i.e, turbulent stress model. But a model of this type would mean the solution of six Reynolds stress equations in which would appear large strongly coupled source terms. It has been found in the previous works (section 1.3.3) that models of this type (for example, model of Naot et al, 1974) can not predict better results comparing with those predicted by much simpler models, such as Gessner and Emery (1976), Launder and Ying (1973), for which complexity of the model can not be justified. Thus a compromise has been made between the turbulent viscosity and Reynolds stress model and an algebraic stress model similar to Gessner and Emery (1976) has been adopted in the calculation. A brief outline of the model is presented below.

Gessner and Emery started with the Reynolds stress transport equation developed by Hanjalic and Launder (1972b)

$$U_k \frac{\partial \overline{u_i u_j}}{\partial x_k} = -\left(\overline{u_j u_k}\frac{\partial U_i}{\partial x_k} + \overline{u_i u_k}\frac{\partial U_j}{\partial x_k}\right) - 2\nu\,\overline{\left(\frac{\partial u_i}{\partial x_k}\right)\left(\frac{\partial u_j}{\partial x_k}\right)}$$

I(convection) II(generation) III(dissipation)

$$+ \frac{\overline{P}}{\rho}\left(\frac{\partial u_i}{\partial x_j} + \frac{\partial u_j}{\partial x_i}\right) - \frac{\partial}{\partial x_k}\left[\overline{u_i u_j u_k} - \nu\frac{\partial \overline{u_i u_j}}{\partial x_k} + \frac{P}{\rho}\left(\delta_{ik}u_i - \delta_{ik}u_j\right)\right]$$

IV(redistribution) V(diffusion)

... (2.14)

On the basis of arguments and experimental results presented by Hanjalic and Launder and on the basis of boundary layer approximation for fully developed turbulent rectangular duct flow, equation (2.14) was simplified by neglecting convective and diffusive transport effect as the first approximation. By taking dissipation of Reynolds stress to be locally isotropic (in small scale motions) and by using the Hanjalic and Launders (1972b) pressure strain relationship, Gessner and Emery reduced equation 2.14 to algebriac equations from which Reynolds stresses were extraced as follows:

$$\overline{u_2^2} = -C_2 C_4 \frac{k^3}{\varepsilon^2} \left(\frac{\partial U_1}{\partial x_2}\right)^2 + C_3 k \qquad \ldots (2.15)$$

$$\overline{u_3^2} = -C_2 C_4 \frac{k^3}{\varepsilon^2} \left(\frac{\partial U_1}{\partial x_3}\right)^2 + C_3 k \qquad \ldots (2.16)$$

$$\overline{u_1 u_2} = -C_4 \frac{k^2}{\varepsilon} \left(\frac{\partial U_1}{\partial x_2}\right) \qquad \ldots (2.17)$$

$$\overline{u_1 u_3} = -C_4 \frac{k^2}{\varepsilon} \left(\frac{\partial U_1}{\partial x_3}\right) \qquad \ldots (2.18)$$

$$\overline{u_2 u_3} = -2C_2 C_4 \frac{k^3}{\varepsilon^2} \left(\frac{\partial U_1}{\partial x_2}\right) \left(\frac{\partial U_1}{\partial x_3}\right) \qquad \ldots (2.19)$$

where k is the kinetic energy of turbulence and ε is the dissipation rate and C_1, C_2, C_3 and C_4 are empirical constants. The Reynolds stress model represented by equations 2.15 to 2.19 has been adopted in the calculation procedure.

The quantity $\rho C_4 k^2/\varepsilon$ can be identified as a turbulent viscosity μ_t as per equation 2.13, which means that equations 2.17 and 2.18 reduce to a simple viscosity model for Reynolds stresses $-\rho\overline{u_1 u_2}$ and $-\rho\overline{u_1 u_3}$ in axial planes. This is however, not so, for the cross-flow plane Reynolds stresses, $-\rho\overline{u_2^2}$, $-\rho\overline{u_3^2}$ $-\rho\overline{u_2 u_3}$ which to depend on mean strain rates in planes normal to the cross flow plane. It is this cross-planar effect that produces secondary flows in the cross-flow planes.

In the applications of Reynolds stress models to particular geometries by Launder and Ying (1973), Aly et al (1978) and Carajilescov and Todreas (1975), the dissipation rate of turbulence energy ε was calculated from the algebraic relation $\varepsilon = C_D k^{3/2}/\ell$ where C_D is an empirical constant and ℓ a turbulent length scale, the spatial distribution of which must be specified.

Although, Launder and Ying (1973) and Aly et al (1978) obtained some success by calculating ℓ from a formula proposed by Buleev (1963). Carajilescov and Todreas (1975) found it necessary to resort to experimental measurements in order to produce a satisfactory length scale prescription. This needs a complex empirical input which is considered undesirable in the prediction procedure for asymmetric rectangular passage shape and so, following the practice of Tatchell (1975), it was removed in the calculation procedure of the present problem by calculating ε from its modelled transport equation presented in the next section.

The momentum equation (equations 2.5 to 2.7) together with the algebraic equations for Reynolds stresses (equations 2.15 to 2.19) and modelled equations for k and ε form a closed set representing fully developed turbulent flow through square ducts.

In order to be consistent with the aim of obtaining a prediction procedure for general surface conditions, no attempt has been made to optimise the empirical constants, where values have been taken from previous studies (Launder and Spalding, 1972 and Launder and Ying, 1973) and are summarized below:

$$C_2 = 0.0185, \quad C_3 = 0.57, \quad C_4 = 0.09$$

It is recognised that more appropriate values of these constants may well emerge from future comparisons of predictions and experimental data as it becomes available for different passage geometries and surface conditions.

2.4 Equations for Turbulence Kinetic Energy and Disspation Rate

The modelled equation for k was first devised by Kolmogorov (1942) and has since been used by many workers (for example, Launder and Ying (1973), Jones and Launder (1973), Rodi and Spalding (1970). The ε equation was devised by Daly and Harlow (1970) and has been applied by Hanjalic and Launder (1972b), Matthews and Whitelaw (1971) and many others. The above mentioned equations for two-dimensional boundary layer flows at high Reynolds number have the following forms:

k - equation

$$\rho U_2 \frac{\partial k}{\partial x_2} + \rho U_3 \frac{\partial k}{\partial x_3} = \frac{\partial}{\partial x_2}\left[\left(\mu + \frac{\mu_t}{\sigma_{t,k}}\right) \frac{\partial k}{\partial x_2}\right] + \frac{\partial}{\partial x_3}\left[\left(\mu + \frac{\mu_t}{\sigma_{t,k}}\right) \frac{\partial k}{\partial x_3}\right] + \rho(P-\varepsilon) \quad \ldots (2.20)$$

ε - equation

$$\rho U_2 \frac{\partial \varepsilon}{\partial x_2} + \rho U_3 \frac{\partial \varepsilon}{\partial x_3} = \frac{\partial}{\partial x_2}\left[\left(\mu + \frac{\mu_t}{\sigma_{t,\varepsilon}}\right) \frac{\partial \varepsilon}{\partial x_2}\right] + \frac{\partial}{\partial x_3}\left[\left(\mu + \frac{\mu_t}{\sigma_{t,\varepsilon}}\right) \frac{\partial \varepsilon}{\partial x_3}\right] + C_{\varepsilon 1} \rho \varepsilon \frac{P}{k} - C_{\varepsilon 2} \rho \varepsilon^2 / k \quad \ldots (2.21)$$

where, the rate of production of energy, P, is defined by

$$P = -\left[\overline{u_1 u_2} \frac{\partial U_i}{\partial x_2} + \overline{u_2 u_3} \frac{\partial U_2}{\partial x_3} + \overline{u_2 u_3} \frac{\partial U_3}{\partial x_2} + \overline{u_3^2} \frac{\partial U_3}{\partial x_3} + \overline{u_2^2} \frac{\partial U_2}{\partial x_2}\right] \quad \ldots (2.22)$$

Equation (2.22) may be rewritten in terms of μ_t by using equation (2.9). For square duct calculations, where U_2 and U_3 are small (a few percent of axial mean velocity), P can be written as:

$$P = \frac{\mu_t}{\rho}\left[\left(\frac{\partial U_1}{\partial x_2}\right)^2 + \left(\frac{\partial U_1}{\partial x_3}\right)^2\right] \qquad \ldots (2.23)$$

The values of the constants in equations (2.20) and (2.21) are:

$$\sigma_{t,k} = 1.0, \quad \sigma_{t,\varepsilon} = 1.185, \quad C_{\varepsilon 1} = 1.55, \quad C_{\varepsilon 2} = 2.00$$

2.5 The turbulent Wall Functions

2.5.1 The Need for Wall Functions

In boundary layer flows, in an appreciable region near the solid wall the mean and turbulence quantities are solely determined by the viscosity of the fluid, the wall shear stress and the normal distance from the wall. Thus, it is common practice in camparing turbulent flows to use wall functions to match the interior flow with the wall conditions in an effort to avoid the large number of grid nodes that would otherwise be necessary in this region of high gradients. Furthermore, the modelled equations for k and ε given in section 2.4 are valid for only high Reynolds number flows (i.e, flows for which the effect of laminar viscosity on the turbulence may be neglected); the use of wall functions allows the near wall grid nodes to be placed sufficiently far from the wall for the high Reynolds number condition to be satisfied.

2.5.2 The Wall Functions Employed

The region close to the wall is assumed to be of constant shear so that the wall shear stress and velocity variation with the distance normal to the wall, are related by the well known log-law of the wall:

$$U_s^+ = \frac{1}{\kappa} \ln x_2^+ + B_s \quad \ldots (2.24)$$

where

$$U_s^+ = U_1 / U_{\tau s} \quad \ldots (2.25)$$

$$x_2^+ = \frac{\rho x_2 U_{\tau s}}{\mu} \quad \ldots (2.26)$$

$$U_{\tau s} = \sqrt{\tau_s / \rho} \quad \ldots (2.27)$$

and κ and B_s are constants.

If the wall is rough and the flow is fully turbulent, the velocity in the vicinity of the wall is independent of viscosity, in such cases it can be shown that the velocity distribution is given by:

$$U_R^+ = \frac{1}{\kappa} \ln \frac{x_2}{e} + B_R \quad \ldots (2.28)$$

where

$$U_R^+ = U_1 / U_{\tau R} \quad \ldots (2.29)$$

$$U_{\tau R} = \sqrt{\tau_R / \rho} \quad \ldots (2.30)$$

and e is the characteristic roughness height and B_R is a constant depending on the geometric shape and arrangement of the roughness element.

For the smooth duct calculations the values of κ and B_s were taken from Schlichting (1960).

$$\kappa = 0.40$$

$$B_s = 5.5$$

and for the calculation of ducts with one and two rough walls

the values of the constants, κ, B_s, B_R in equations 2.24 and 2.28 were taken from the experimental results stated in sections 4.1 and 5.1 respectively.

Close to the wall, the production and dissipation of turbulence kinetic energy are nearly equal and the diffusion is negligible. Thus the turbulence energy, k, near the wall, was obtained as for the internal nodes with generation and dissipation calculated using the local values of wall shear stress.

The value of ε near the wall was obtained by neglecting transport of ε by convection and diffusion and assuming a length scale that varies linearly with distance from the wall, x_2, (Launder and Spalding, 1972) so that

$$\varepsilon = C_4^{\frac{3}{4}} k/\kappa x_2 \qquad \ldots (2.31)$$

2.6 Finite-Difference Equations

Equations 2.5 to 2.7 together with equations 2.20 and 2.21 may be represented in terms of the single transport equation:

$$\rho U_2 \frac{\partial \phi}{\partial x_2} + \rho U_3 \frac{\partial \phi}{\partial x_3} - \frac{\partial}{\partial x_2}\left(\Gamma_\phi \frac{\partial \phi}{\partial x_2}\right) - \frac{\partial}{\partial x_3}\left(\Gamma_\phi \frac{\partial \phi}{\partial x_3}\right) = S_\phi \qquad \ldots (2.32)$$

where ϕ stands for any of the main dependent variables U_1, U_2 U_3, k and ε; and Γ_ϕ $(\mu + \mu_t/\sigma_{t,\phi})$ and S_ϕ are respectively the corresponding duffusivity and source terms.

An element of cartesian grid system employed in the calculations is shown in figure 2.1. The variables P, U_1, k and ε were calculated at the grid nodes but following modern practice, the cross-flow velocities, U_2 and U_3 were computed at the intervening locations, mid-way between the pressures. This allowed the cross-flow velocities to be readily determined from the driving pressures and made available for the calculation of mass fluxes through the ϕ cell.

The finite-difference equivalent of equation 2.32 was derived, for each grid location, by approximate integration

over imaginary contiguous control volumes surrounding each location, an example of which is shown in figure 2.1. The resulting sets of equations of each variables can be expressed as:

$$C_p \phi_p = C_w\phi_w + C_E\phi_E + C_N\phi_N + C_S\phi_S + S_U \quad \ldots (2.33)$$

where $$C_w = A_w g_w (F_w-1) \quad \ldots (2.34)$$

$$C_E = A_E g_E F_E \quad \ldots (2.35)$$

(similar terms may be valuated in the N-S direction)

and $$C_p = C_w + C_E + C_N + C_S - S_p$$

S_U and S_p are the source term coefficients such that

$$S_\phi \Delta X_1 \Delta X_2 \Delta X_3 = S_U + S_p\phi_p$$

where $S_\phi \Delta X_1 \Delta X_2 \Delta X_3$ is the integration of the source term over the control volume, g_w, g_E etc, are the mass fluxes entering through the control volume face.

The terms F_w, F_E etc, are the weighting factors, dependent on the finite difference scheme used. The present calculations used a hybrid difference scheme based upon central difference scheme assumes a linear variation of ϕ across the control volume; thus F is defined for example, as

$$F_w = (1+2Pe_w^{-1})/2 \quad \ldots (2.36)$$

with Pe, the cell Peclet number, given by

$$Pe = \frac{g_w \delta_w}{\Gamma_w} \quad \ldots (2.37)$$

where Γ_w is the mean of the exchange coefficients at neighbouring nodes and δ_w is the distance between nodes. This scheme is unstable for Pe > 2 as shown by Runchal (1972) and in such circumstances is replaced by an upwind difference scheme which evaluates the diffusion flux from the central difference scheme but the convective flux from the upwind node, thus

$$F_w = 1+Pe_w^{-1} \qquad Pe > 0$$

$$F_w = Pe_w^{-1} \qquad Pe < 0$$

In practice, this hybrid scheme uses the central difference method for $2 < Pe > -2$, and the upwind scheme at all other values. It provides a compromise between accuracy and economy and is stable for all Pe as shown by Runchal (1972).

Departure from the above practices were made in the case of the continuity equation (equation 2.4) which after integration, was combined with the cross-flow momentum equations (strictly a pressure correlation) of the form of equation 2.32 above. Details of the derivation are given in Caretto et al (1972)

2.7 Solution Procedure

For a given computational grid, the finite-difference equations were assembled and solved by two-nested iteration sequences. The outer sequence caused the variables to be updated sequentially and repeated until convergence was achieved, the order being to solve the momentum equations for the cross flow velocities, the continuity equation for pressure (which were then used to bring the velocities into continuity balance), the axial momentum equation for the axial velocity and the turbulence equations for the turbulence parameters. The inner sequence effected the solution of the linearised equations for each variable by a line-iteration of 'ADI' procedure based on the tri-diagonal matrix algorithm.

Convergence of the overall procedure was by no means assured, due to the coupling and nonlinearity of the equations, the former feature being particularly prominent in the Reynolds stress modelling employed in the calculation. In the regions of small coefficients, extra sweeps of the line iteration procedure was applied. The calculations were taken as converged when the sums over the field of the absolute mass and momentum residues were less than a small presribed fraction (usually of the order of 10^{-3}) of the axial mass and momentum fluxes. Results to be presented in chapter 6, were solved in the quadrant (for smooth duct and duct with two rough walls) and the half-section (for duct with one rough wall) of the flow domain and obtained by using 12 x 12 and 12 x 22 staggered grids. More grid lines were provided near the wall in order to reduce the effect of high gradients.

2.8 The Accuracy of the Solutions

The accuracy of the above mentioned solution procedure is affected by the differential equations and by numerical features (i.e, the error in the numerical solution of the finite-difference equations as compared with the exact solution of the differential equations), discussed below:

(a) Errors in the differential equations

These errors arise as a consequence of approximations introduced in deriving the boundary layer form of the equations, and in modelling the turbulence. The level of error is assessed by comparing the final finite-difference solutions with exact solutions, when these are available, or with experimental measurements and such assessments are done in section 6.3.

(b) The Numerical Error

The overall numerical error is composed of three components: the truncation error (as defined below): the iterative error and the computer round-off error.

The truncation error: This error results from representing the true continuous distribution of a quantity in terms of values at

the nodes of a finite difference mesh, with interpolation formulae between them. The magnitude of the error depends on the local grid distribution. The error can be reduced to an acceptable level by, firstly, making the grid non-uniform so as to concentrate nodes in regions of high gradients, and, secondly, performing tests in which the number of grid nodes is systematically increased until solutions with successive grids are the same within an acceptable level.

The iterative error: The iterative error is the difference between the iterative numerical solution and the exact solution of the difference equations. It is a reflexion of the fact that, ultimately, the total number of iterations must be limited for reasons of economy; for, the computing time increases in direct proportion to the number of iterations. A compromise is sought in that the iterative error is reduced to a small acceptable value by performing a sufficiently large number of iterations such that subsequent iterations are shown to cause negligibly small changes in the solution. Errors due to iteration are, therefore, negligible in the solutions.

The round-off error: This error is a result of the limitations on a computing machine to perform all arithmatic operations with a finite number of digits. In practice, the round-off error is reduced to negligible proportion of the overall error by using a sufficiently large number of digits.

In addition to above errors, the smearing of velocity gradients is a commonly found effect of numerical or false diffusion due to upwind differencing which is used whenever the cell Peclet number is greater than two, the value at which central differencing becomes unstable. Peclet numbers greater than two are the result of large grid cells and can only be reduced by grid refinement. Further comments will be made in relation to the present calculation in section 6.3.

C H A P T E R 3

EQUIPMENT AND EXPERIMENTAL PROCEDURE

3.1 Experimental Programme

The experimental programme comprised detailed measurements of mean and turbulent characteristics of the flow in a square duct with two different boundary conditions. In the first case, one wall was rough and the remaining three walls were smooth; and in the second case, the two opposite walls were rough and the remaining two walls were smooth. The mean longitudinal and secondary velocities were obtained. Rough and smooth wall shear stresses were calculated by numerical integration from Clauser plots and the pressure gradient in the duct flow direction was measured. Amongst the fluctuating properties of the flow, longitudinal and transverse turbulence intensities and Reynolds shrear stresses were considered. Distributions of frequency spectra of longitudinal turbulence component were obtained near the rough surface of the single rough wall duct and on the centreline (normal to the rough walls) of the double rough wall duct.

Mean velocities were recorded by the flattened-tip pitot tube while the secondary velocities were measured both by the hot wire and the yaw meter. Measurements of turbulence properties were obtained with single hot wire probes, normal and 45^{0} inclined.

A brief description of the flow system appears in the next section (section 3.2) and is followed by description of the instrumentation and measuring techniques (section 3.3). Traversing mechanism and probe setting method is illustrated in section 3.4 and error analysis and short discussions of preliminary measurements for symmetry check are made in sections 3.5 and 3.6 respectively.

3.2 The Flow System

A schematic diagram of the flow system is shown in figure 3.1. The 150 mm x 150 mm square duct (hydraulic diameter 150) was manufactured from 12.7 mm thick perspex sheet which was flat within ± 0.04 mm. The duct was 5.61 meters long and was made in sections of 1.87 meters; it was fabricated from four rectangular pieces screwed together along their longer sides. A thin layer of silicon rubber seal was applied between the joints to prevent air leakage. One or two of the walls (as the case may be) of the duct was roughened throughout the entirelength, by sticking 3.18 mm square sectioned silver-steel ribs (transverse to the flow direction) with araldite. The ratio of the roughness height to the hydraulic diameter, thus, was approximately 1 to 50 (actually 3.18 to 150.5). The ribs were spaced 31.8 ± 0.05 mm apart to give a pitch to height ratio of 10:1. The ribs were square sectioned rolled bar with smooth edges. Each section of the duct was joined by means of flanges. Dowel pins were used in the flanges to avoid any possible misalignment in the axis of the duct assembly. A bell mouth, with wire screens in its front, was fitted at the entrance end of the duct to obtain a smooth inlet free of large scale of turbulence. In order to maintain cleanliness appropriate for hot wire measurements, the air entered the apparatus through a filter box.

The fan was installed at the discharge side of the duct through a diffuser, so that, the room air was drawn through the duct when the fan was running. The fan was driven by a 25 hp a.c. motor and was coupled through a variable speed hydraulic coupling. There was a butterfly valve at the outlet of the fan and the air velocity through the duct could be controlled both by regulating the speed of the fan and by varying the butterfly valve opening.

To supress mechanical vibrations, the blower and the motor assembly was mounted on flexible rubber mountings. Also, the duct system was connected with the fan inlet through a bellows, which prevented any vibration from the fan assembly being passed on to the duct assembly. Floor vibration was

minimised by rubber isolators. The duct was mounted on a handy-angle frame structure and was free from any significant vibration.

The test section was situated 36 hydraulic diameters downstream of the duct entry. The developing length of 36 hydraulic diameter is usually sufficient to give fully developed velocity profiles in turbulent flow. The linear pressure gradient (figures 4.15 and 5.14) showed that the fully developed flow was achieved at the test section. The isometric view of the test section and its axes notation is shown in figure 3.2.

3.3 Instrumentation and Measuring Technique

3.3.1 Pressure Instrumentation

Static pressure holes, 0.4 mm diameter, were made at 150 mm apart along the centreline of a smooth wall. Later the holes were counter drilled for insertion of 3 mm brass tubing to facilitate manometer connections. Before assembly of the duct walls, the pressure holes were checked for any burrs and were cleaned carefully. Details of the static pressure hole are shown in figure 3.3a.

The stagnation pressure probe used in all measurements was a flattened-tip pitot tube with internal and external tip heights of 0.16 mm and 0.4 mm respectively. The width of the tube at the tip was about 1.65 mm. Pressure probe dimensions are shown in figures 3.3b and 3.3c.

Due to the small tip height (0.16 mm) of the pitot tube used in the measurement, the McMillan (1956) correction factor for the effective displacement of the pitot tube centre towards the region of higher velocities was negligible and so it was not considered in the pitot tube measurements. The low Reynolds number correction illustrated in Bryer and Pankhurst (1971), was applied when pitot tube Reynolds numbers, hU/ν, were less than 200. Here h is the internal height of the pitot tube tip. In addition, the wall effect correction was applied for total head readings near the smooth wall as described in Bryer and Pankhurst (1971).

The mean velocities were inferred from the total and the wall static pressure data from the incompressible Bernoulli's equation,

$$U_m = \sqrt{\frac{2}{\rho}(P_o - P_w)} \qquad \ldots (3.1)$$

where Po and Pw are the stagnation and wall static pressure respectively. The pitot tube was assumed to be sensitive to the longitudinal component of turbulence only, and so further correction was made as follows:

$$U_l = U_m \sqrt{(1 - \frac{\overline{u_l^2}}{U_m^2})} \qquad \ldots (3.2)$$

where U_m is the local measured velocity. During the measurements, wall static pressure, P_w, was assumed to be constant across the measuring section of the duct and was not corrected for turbulence.

Pressure measurements were determined with a band of transducers (Universal Manometer of Furness Control Ltd) and a Solartron Time Domain Analyser (JM 1860). To check the calibration of the transducers, the manometer readings were checked against a liquid micromanometer using a signal from a pitot tube located in the core region of a jet. The pressure was recorded by both the manometers and virtually no difference was noticed between the two readings. The manometer was then calibrated against the output voltage of the transducer which varied linearly with the pressure. The calibration constant was used for the integration process of all manometric readings of the duct measurements. For the measurements of both the static and the total pressure an integration period of 10 seconds was used.

3.3.2 Hot - Wire Measurements

3.3.2.1 Hot - Wire Signal Processing Equipments

In the measurements of turbulence quantities DISA miniature wire probes 55P11 (straight, general purpose type) and 55P12 (45° slanting sensor type), were used as the transducers. The signals were processed by DISA constant

Temperature Anemometers (Type 55A01) along with DISA Linearisers (Type 55D10) and Integrators (Type 55B30). The root-mean-square voltage was measured with a Solartron Digital Voltmeter, and a Solartron Time Domain Analyser (JM1860) was used to measure the DC voltage. Averaging periods for the mean and fluctuating quantities were about 10 seconds and 15 seconds respectively.

The straight general purpose probe (type 55P11) was employed for the measurements of longitudinal fluctuating velocity while the transverse fluctuating velocities and shear stresses were obtained with the single 45^{o} probe (55P12), inclined with the axis of the probe support. The problem of unequal wire sensitivities and wire interference, that arises with the X-probe, was thus avoided, although the probe had to be traversed twice across the duct for each set of readings with the wire successively in the + 45^{o} and - 45^{o} positions. During the measurements DISA probes were used with DISA probe support Type 55H20 which was located within DISA probe mounting tube (Type 55H152), to maintain constant sensor location when the probes were rotated about their own axes.

For the measurements of frequency spectra, a General Radio sound and Vibration Analyser (Type 1564-A) was used along with the DISA Anemometer (55A01) and DISA RMS meter (55D35). Measurements were taken on the Time Domain Analyser with a averaging period of 30 seconds for each frequency, a response from 2.5 Hz to 25 KHz in four decade ranges and it can be set at bandwidths of either $^{1}/_{3}$ octave or $^{1}/_{10}$ (23% or 7% of the mean value respectively). In this investigation, spectral density measurements were taken at $^{1}/_{10}$ octave.

3.3.2.2 Turbulence Measurement Procedure

In the turbulence measurements, the use of the lineariser with the hot-wire-anemometer transformed the standard cooling law for the wire

$$\hat{E}^2 - A = S\ U_{eff}^{n} \qquad \ldots (3.3)$$

into a form

$$\hat{E} = S\ \hat{U}_{eff} \qquad \ldots (3.4)$$

thus removing the exponent n and constant A from the equation 3.3. Here $\hat{E}$ is the instantaneous DC voltage of the anemometer, $\hat{U}_{eff}$ is the instantaneous effective cooling fluid velocity, S is the sensivity of the wire and A is a constant.

For the inclined wires, the effective cooling velocity was taken to be

$$U_{eff} = U(\alpha)\, F(\alpha) \qquad \ldots (3.5)$$

where $\hat{U}(\alpha)$ is the instantaneous velocity vector acting at an angle α with the normal to the wire. The function $F(\alpha)$ depends mainly on the inclination of the wire with respect to the mean flow direction and L/D ratio, where L is the length and D is the diameter of the wire. Several forms for the function $F(\alpha)$ were proposed but in this investigation the most well known function

$$F(\alpha) = (\cos^2\alpha + K^2 \sin^2\alpha)^{\frac{1}{2}} \qquad \ldots (3.6)$$

was chosen for measurements. Here the coefficient K represents the fraction of the velocity component parallel to the wire, that affects the wire cooling. For $L/D = 250$ (used in this investigation), the value of K varied from 0.17 to 0.255 for different wires used during the measurements. The value of K for each wire was determined during its calibration which will be discussed in section 3.3.2.4.

In this investigation the interpretion of the hot-wire signals was based on the assumption of low turbulence intensity (15%) and the equations for the wire cooling were deduced from equation (3.4) as follows:

$$\frac{\sqrt{\overline{u_1^2}}}{U_1} = \frac{\sqrt{\overline{e_o^2}}}{E_o} \qquad \text{for } \alpha = o \qquad \ldots (3.7)$$

In the $x_1 - x_2$ plane, for $\alpha = \pm 45°$

$$\frac{\sqrt{\overline{u_2^2}}}{U_1} = \frac{1}{\sqrt{2}} \left\{\frac{1+K^2}{1-K^2}\right\} \left[\frac{\overline{e_1^2}}{E_1^2}_{\alpha=+45^o} + \frac{\overline{e_2^2}}{E_2^2}_{\alpha=-45^o} - 2 \frac{\overline{e_o^2}}{E_o^2}_{\alpha=o} \right]^{\frac{1}{2}}$$

$$\ldots (3.8)$$

$$\frac{\overline{u_1 u_2}}{U_1^2} = \frac{1+K^2}{4(1-K^2)} \left[\frac{\overline{e_1^2}}{E_1^2}_{\alpha=+45^\circ} - \frac{\overline{e_1^2}}{E_2^2}_{\alpha=-45^\circ} \right] \quad \ldots (3.9)$$

and in the $x_1 - x_3$ plane, for $\alpha = \pm 45^\circ$

$$\sqrt{\frac{\overline{u_3^2}}{U_1}} = \frac{1}{\sqrt{2}} \frac{1+K^2}{1-K^2} \left[\frac{\overline{e_3^2}}{E_3^2}_{\alpha=+45^\circ} + \frac{\overline{e_4^2}}{E_4^2}_{\alpha=-45^\circ} - 2 \frac{\overline{e_0^2}}{E_0^2}_{\alpha=0} \right]^{\frac{1}{2}}$$

$$\ldots (3.10)$$

$$\frac{\overline{u_1 u_3}}{U_1^2} = \frac{1+K^2}{4(1-K^2)} \left[\frac{\overline{e_3^2}}{E_3^2}_{\alpha=+45^\circ} - \frac{\overline{e_4^2}}{E_4^2}_{\alpha=-45^\circ} \right]$$

$$\ldots (3.11)$$

Developments of these equations are outlined in Appendix (A).

Spectral density measurements were performed directly without calibration. The ratio of the correlation of the filtered to that of the total signal yields the correlation spectral density

$$F_u(f) = \frac{\overline{u_1^2(f)}}{U_1^2} \cdot \frac{1}{\Delta f} \quad \ldots (3.12)$$

Here Δf represents the effective bandpass width of the frequency analyser which in the present investigation was 7% of the actual frequency.

3.3.2.3 Calibration Rig

The calibration rig was a low turbulence (0.7%) round jet emerging from a 40 mm nozzle which was connected to a centrifugal fan through a settling chamber filled with alluminium foil honeycomb. The inlet opening of the fan could

be varied by a sliding valve and was covered with a glass fibre filter. The velocity of the jet could be varied from 0 - 40 m/s, nearly equal to the duct centreline velocity (44.75 m/s) and, the wires were calibrated in the same velocity range as in the duct. The hot wire probe support in the calibration rig, could be rotated through a wide range of angles between the probe and the jet axis. The angular position of the probe (with respect to the jet axis) could be read from a 9 cm diameter protractor upto the accuracy of 0.5^{o}. The angular movement of the probe support was used when calibrating the slanting wires and the yawmeters which will be discussed in sections 3.3.2.4 and 3.3.3.2 respectively.

3.3.2.4 Calibration of the Hot Wire

Calibration of the hot wire was carried out in the potential core of the jet. For the normal wires the calibration was carried out by mounting the hot wire probe and pitot tube side by side, parallel to the mean velocity vector and taking pairs of readings for each velocity, one for mean DC voltage of the wire another from the output of Universal manometer. Lineariser initial settings were made according to its instruction manual and further adjustments were made by trial during the calibration process until the linear relation between the hot wire mean voltage (DC) and mean velocity i.e. $E = SU_{eff}$, was obtained. To avoid interference of the flow the pitot tube was drawn aside while recording the hot wire voltage.

For slanting wires the calibration procedure was more involved. First the wire was placed in the jet at an angle 45^{o} with the jet axis and the linear wire voltage response with respect to the air velocity was obtained as described in the case of the normal wire. Since the value of K of the wire remains constant for relatively small range of wire angle with respect to the mean flow direction, it was calibrated near the operating angle. The wire was set at two different angles, 30^{o} and 45^{o}, for each velocity and their corresponding mean voltage was recorded. The constants S and K of the wire were then calculated according to the following equations:

$$S^2 = \frac{2E^2(30) - E^2(45)}{U^2} \quad \ldots (3.13)$$

$$K^2 = \frac{3E^2(45) - 2E^2(30)}{2E^2(30) - E^2(45)} \quad \ldots (3.14)$$

3.3.3 Secondary Flow Measurements

The secondary flow velocities were measured by two different methods, ie, the constant current hot-wire method of Hoagland (1960) and by three holes yawmeters. The results obtained by both methods were in good agreement as seen from figure 4.9, but the scatter of the points obtained from the hot wire was much more than that obtained from the yawmeters. For this reason yawmeters results were considered for calculation and for further measurements of secondary velocity, yawmeters were used. However both the measuring techniques are described here for relative comparison regarding their sensitivity to the secondary flow direction.

3.3.3.1 Hot Wire Measuring Technique

A circuit diagram for the measuring system is shown in figure 3.4a, which is a simple Wheatstone bridge. The hot wire (normal wire) was placed in the duct with the probe axis normal to the axis of the duct at shown in figure 3.4b. The hot wire was set at an angle α (position NN^1) with the assumed direction of flow (line XX^1)* and the Wheatstone bridge was balanced by adjusting the resistance of the variable resistor. The hot wire was then rotated about its own axis to a position on the other side of the assumed flow direction until the bridge was balanced again (position MM^1). The angular position of the hot wire, β, was noted. The bisector of the angle $(\alpha + \beta)$ then gave the true direction of flow.

If the direction of flow makes an angle γ_2 with the duct axis (figure 3.4b). The velocity component U_2 of the

---

* In the test, axial direction was taken as the assumed direction of flow.

secondary velocity, U_s, can be calculated from

$$U_2 = U_1 \tan \gamma_2 \qquad \ldots (3.15)$$

where U_1 is axial velocity which is found from pitot tube measurements.

The accuracy of the measurements, of the secondary flow angle depends on the Wheatstone bridge circuit, the instrument for measuring or comparing the amount of balance in the circuit (it may be a galvanometer or a millivoltmeter), the accuracy of the rotating gear for measuring the angle and a device for measuring the position of the hot wire relative to the axis of the duct. The bridge consisted of two fixed resistors each of 5.6 Ω ± .5% (figure 3.4a), which is nearly equal to the hot wire resistance. Equal resistors were chosen in the circuit to permit best response to small changes in hot wire resistance. Two compensating variable resistors, one O - 20Ω and other O - 1Ω were used to give coarse and fine adjustments respectively. The current to the bridge was supplied from a 1.5v stabilized DC power source through a O - 25Ω resistor. A digital millivoltmeter capable of reading upto O.O1 mv was connected in the circuit (figure 3.4a) to measure the balance of the bridge. A resistor-capacitor (R-C) circuit was installed parallel to the millivoltmeter in order to damp out the fluctuations of millivoltmeter readings due to turbulence and to give a stable reading. Too much damping would make the bridge less sensitive to the flow direction. So as a compromise, some fluctuations were allowed by decreasing the impendence of the R-C circuit and made the bridge as sensitive as possible.

In this measurements DISA normal wire type 55P11 was used. The angular position of the hot wire was measured by the protractor whose vernier scale could read upto O.1°.

3.3.3.2 The Yawmeter

The principle of operation of a yawmeter is based on the fact that the percentage of total pressure of the flow field recorded by the pressure probe depends on the angle of incidence of the flow on the plane of the probe hole; it is a maximum when the flow is normal to the plane of the probe hole and a minimum when parallel to it. The pressure, recovery characteristic ie, the sensitivity to yaw of the probe depends on its apex angle. Multitube yawmeters as shown in figure 3.5, were used in the measurements of secondary flow angles. They were made from stainless steel tube of 0.81 mm OD. and 0.5 mm ID, with an apex angle of 70^{o}. This value was used by Bryer et al (1958) and found satisfactory.

The sensitivity of the yawmeter in incompressible flow can be expressed as

$$S_{(\gamma)} = \frac{P_1 - P_2}{(P_3 - P_0)\,\gamma} \qquad \ldots (3.16)$$

where P_1 and P_2 are the pressures recorded in the camphered tubes (figure 3.5), P_3 is the total pressure recorded by the total head tube of yawmeter, P_o is the atmospheric pressure and γ is the angle of the yawmeter with respect to the flow direction. In practice the most important thing is the magnitude of the pressure difference $(P_1 - P_2)$, which can be detected by the probe and the accuracy with which it can be measured, as these together determine the resolution attainable in the measurement of flow direction. The smallest change of the flow angle $\Delta\gamma$ which can be detected by a yawmeter system can be expressed by the equation

$$\Delta\gamma = \frac{\Delta Pmin}{S(\gamma) \times \frac{1}{2}\rho U_1^2} \qquad \ldots (3.17)$$

where $\Delta Pmin$ is the minimum pressure difference that can be read on the manometer and $S(\gamma)$ is the yawmeter sensitivity. In this investigation two yawmeters were used one for

measuring the U_2 component of velocity and another for U_3 component of velocity; their sensitivities were calculated to be 0.0466 and 0.057 respectively. Furness universal manometer can read pressure upto the accuracy of 0.1 mm of water in the pressure range of 200 mm of water (used in the measurement). The yawmeters in the present system, thus could read angle better than 0.05° at a wind speed of 34.5 m/s (average velocity of the duct). This limit of resolution is adequate in the present measurement.

When a yawmeter is used in a nonuniform flow field its performance is likely to depend on the gradients of velocity, static pressure and total pressure. Across a boundary layer or other shear flow, the static pressure remains practically constant and the velocity changes are accompanied by changes in total pressure. It was found that the yawmeters camphered tubes pressures vary linearly with the total pressure. This property of the yawmeter was employed for the correction of its readings which were influenced by the variation of total pressure of the flow field. The correction procedure of the yawmeter along with its calibration is illustrated in Appendix (B).

The effects of total pressure gradients on the accuracy of yawmeter measurements can be large when the direction of the gradient is from one sensing hole to another. The separation distance between the holes should then be as small as possible; to acheive this two yawmeters were employed so that the yawmeters can be placed in the direction of less total pressure gradient.

3.4 Traversing Mechanism and Probe Setting

The traversing mechanism shown in figure 3.6, was used to place the probe in any desired position of the duct test section. A slider sheet 25 mm x 12.7 mm and 350 mm long was fitted with a smooth wall opposite to the rough wall or one of the rough walls as the case may be, such that the internal surface of both the slider sheet and the duct wall was always in coincidence. To mount the probe traversing gear a 180 mm x 350 mm (12.7 mm thick) perspex sheet was screwed with the slider sheet. A slider sheet traversing

gear was mounted on one of the smooth walls adjacent to the rough wall (the smooth wall where x_2 = o) and was connected with the slider sheet so that it could be moved parallel to the x_2-axis. The probe propelling gear was mounted on the centre of the slider sheet. The sensing probe when fitted with this gear could be propelled in the direction parallel to the x_3-axis. In addition to linear movements in x_2 and x_3 directions, this gear was fitted with a protractor and could rotate about its own axis. In the above arrangement the probe could thus be set at any position and at any angle in $x_1 - x_2$ plane of the duct test section. The linear movements of the gear were performed by the micrometers which could read upto 0.05 mm and the angular movement was measured by a protractor with verniear which could read upto 0.1^{o}.

Extreme care was taken to set the probe as correctly as possible with respect to the wall and parallel to the duct axis. Two travelling telescopes were used and electrical connection was made between the probe and the walls. When the probe support would touch one of the walls (rough or smooth or both rough) the light would glow. The wall distance x_3 of the sensing probe would then be ascertained from the telescope which could travel parallel to the x_3 axis. This could be done by focusing the edge of the wall and the probe centre respectively with the hairline of the telescope and recording their respective readings. Another telescope was mounted on the top of the duct and it could move parallel to the x_2 axis. This telescope was used to place the probe parallel to the duct axis and to determine the wall distance x_2. Both the telescopes had the vernier capable to read upto 0.05 mm. For the aligning difficulty due to the finite dimension of the hairline and the probe tip, accuracy of the measurement upto 0.05 mm could not be expected, however, measurement accuracy upto 0.1 mm is quite safe.

3.5 Error Analysis

In this section a brief account of errors associated with different stage of measurements are given. The errors were introduced in the system of measurements during the calibration of the sensing elements and were later added to these during the final measurements.

The error in the measurement of wall distance is critical for those properties whose gradient near the wall are greatest and most important. As discussed earlier in section 3.4, the sensing probes could be placed in the duct with a uncertainty of $\pm$ 0.1 mm with respect to the wall. This could result in errors of upto 0.25% in mean velocity near the wall. Error in the measurement of distance between successive points was negligble.

During the measurements, the fan speed varied within $\pm$ 1%, due to the variation of both the motor speed and viscosity of oil used in the fluid coupling. This caused a variation of not more than 0.5% in the centreline velocity.

In all pressure measurements (static and total), the maximum transducer error was 0.6% of the measured value. This is smaller than the experimental scatter which can be seen in the plots of mean velocity profiles and static pressure gradients (figures 4.1, 4.15, 5.1 and 5.14). Thus the errors in the slope of Clauser plots (figures 4.3 to 4.5, 5.3 and 5.4) and static pressure gradient arose largely from fitting the data to a straight line and the maximum was around $\pm$ 5% for Clauser plots and $\pm$ 1% for pressure gradients. These errors in the slope of Clauser plots and pressure gradient introduced errors of the same magnitude in the determination of local wall shear stress and average wall shear stress of the duct respectively. It should be noted that average wall shear stresses determined from Clauser plots were 8.5% and 10% higher for the duct with one rough wall and two rough walls respectively than those obtained from their static pressure gradients.

Though the protractors could read upto 0.1°, due to the difficulty in aligning the hot wire with the duct axis it was estimated that the secondary flow angle could at best be measured to an accuracy of 0.2° which was about 40% of the value of the flow angles prevailing in the major part of the flow area. The fluctuations of the millivoltmeter readings were damped out by a R-C (Resistor-capacitor) circuit. The damping made the system less sensitive to the flow direction where variation of $\pm$ 0.2° could hardly be read on the millivoltmeter. Thus the total uncertainty in the measurement

of the secondary flow angle by the hot wire method was about ± 80% of the mean value.

Measurements of secondary flow angles by yawmeters removed the use of protractor and so error in the measurement of angles was eliminated. It was expected that the probe could be aligned safely within ± .1° with the duct axis. In the high pressure range (200 mm of water) transducer error was neglibible. In different position of the duct five sets of readings were taken for each position and it was found that the angles varied within ± 15% of mean value near the walls and ± 5% in the centre region of the duct. In the above readings an integration period of 15 seconds was used. Apart from the above uncertainties, yawmeter readings were sensitive to the total pressure gradient of the flow field in which it was placed, and its effect on the yawmeter readings introduced further uncertainties of about ± 15% near the walls: away from the walls, however, the pressure gradient was small and its effect was negligible.

In the measurements of turbulence properties the assumption of low turbulence intensity in the hot wire cooling law equations (Appendix A) introduced errors of ± 2% for normal wires and ± 5% for slanting wires for typical turbulence level of 15%. For turbulence level above 30% the accuracy rapidly becomes unacceptable. However the error in assuming low tubulence level is secondary if other inaccuracies dominate the result. For example, if the angle between the instantaneous flow and the sensor axis falls below 20° the simple yaw law on which equation 3.6 is established, no longer exists; in a flow of turbulence intensity of about 30% there is a 10% probability of this occurring. Further Gaussian probability distribution indicates the occurrence of 33% instantaneous reverse flow which the hot wire is normally unable to resolve. Thus it is clear that the hot wire results obtained from the equations 3.7 to 3.11, are subject to unacceptable for turbulence levels greater than 30%. In addition to the error inherent in the assumption of low turbulence intensity, linearisation of the hot wire was possible to within ± 0.5% of the actual velocity over the operating velocity range (10-45 m/s).

The value of K was determined by positioning the hot wire at a pair of yaw angles of the value 30° and 45° to the mean flow direction. The measured voltages at the pair of yaw angles yielded solution for both S and K as per equation 3.13 and 3.14. The process was repeated for several sets of velocity in the range 10-40 m/s which produced average values of S and K from a distribution between ± 1.5% and ± 10% of the mean respectively. In the calibration rig the alignment of the hot wire with respect to the jet axis was checked by recording the maximum wire voltage placing the wire in a position normal to the flow direction which was within ± 0.5° of the geometric alignment. The determination of K is sensitive to the precision of yaw setting and a 0.5° error gives an accuracy limitation of 6% of the measured value.

The angle of the hot wire on the supports was measured under a microscope after each rewelding and the probe was accepted for use if the angle fell within ± 0.5° of 45°. This measurement is also important because 3° angle error will give a 10% change in the $\tilde{u}_2/U_c$ or $\tilde{u}_3/U_c$ sensitivity.

Further due to the difficulty of aligning the probe with the duct axis it was expected that the wire could be placed in the duct to within ± 0.1° of the duct axis. Summation of all the errors in the hot wire system at turbulence intensity of 15% gives probable errors of ± 6% for normal wires and ± 15% for slanting wires.

The frequency spectra were measured by passing the signal from a single normal probe through a $1/10$ octave filter of the frequency analyser. The energy content of the output signal was integrated over a time period of 30 seconds. This gave deviation of about ± 15% at lowest measured frequency and ± 2% in the higher frequency range, from the mean value of three readings.

3.6 Preliminary Tests

In order to test the instrumentation and measuring techniques of hot wire described in section 3.3, preliminary measurements of mean velocities and turbulence intensities were

made in a smooth channel. The results were compared with those of Melling (1970), and found satisfactory (the discrepancies were less than 1.5% for mean velocities and 5% for turbulence intensities) within the experimental uncertainties described in section 3.5.

After several preliminary runs of the present flow system, it was found that the flow velocity decreased gradually to about 2% in about 40 minutes. This reduction was caused by the decrease in fan speed due to the increase of temperature of the oil in the fluid coupling. Thus the fan was run for one hour before the moments which led to the measurements.

For single rough wall duct, symmetry for the two half section was, checked. In order to do that readings for mean velocity and longitudinal turbulence intensity were taken in two symmetrical positions, on either side of the duct centre (ie, at $x_2/a = 0.25$ and $x_2/a = 0.75$) as shown in figure 3.7. For mean velocity the maximum variation was less than 2% and for turbulence intensity that was less than 3% of their mean values.

For the duct with two rough walls, symmetry was checked for mean velocity, longitudinal turbulence intensity, $\tilde{u}_1$ and secondary flow angle, γ_2, primarily between the two quadrants of the duct ($x_2/a = 0 - 0.5$ and, $x_3/a = 0 - 0.5$ and $0.5 - 1.0$). The check was done by traversing the probe from one rough wall ($x_3/a = 0$) to another ($x_3/a = 1.0$) for two positions, one at the centre of the rough wall ($x_2/a = 0.50$) and other at $x_2/a = 0.25$. Measurements of mean velocity was also taken at a symmetrical position of the third quadrant of the duct ($x_2/a = 0.75$, $x_3/a = 0 - 0.5$). Plots of measurements are shown in figure 3.8. The maximum variation of mean velocity was less than 1% and that of the turbulence intensity was less than 3% of their mean values. The variation of secondary flow angle, γ_2, was in general much higher, in the range of 50% and more. Greater uncertainty in the measurements of secondary flow angles, particularly for small angles (less than 0.5°) was thought to be the cause of this relatively high variation between the two symmetrical flow fields. The above variations for both the ducts were accepted for symmetry and measurements were

taken in a half and a quarter section of the duct with one rough wall and two rough walls respectively.

C H A P T E R 4

MEASUREMENT IN A SQUARE DUCT WITH ONE ROUGH WALL

4.1 Introduction

The flow in a square duct with one rough wall and three smooth walls, has different flow characteristics from those of a symmetric duct. To represent the results in the region of smooth and rough walls the respective wall friction velocities are used as characteristic velocity scales; similarly $\nu/U_{\tau s}$ and e (rib height) are used as characteristic length scales in the regions close to the smooth and rough wall (where distance from the wall and conditions of the surface are the only important factors) respectively. However, to represent the flow characteristics of the duct, in general, the centre-line velocity, U_c, and hydraulic diameter, D_h, are chosen as the velocity scale and length scale respectively for normalizing the respective parameters of the duct.

Because of the different nature of wall conditions, the extent of each wall region depends upon the Reynolds number and the aspect ratio (height to width) of the duct. Moreover, the interaction of the flows in the mixing zone (which may be described as the region of the flow where an overlapping and mutual interference of the two opposite dissimilar wall regions occurs) has different effects upon the mean and turbulent flow parameters. As a result, turbulent motion exhibits a different degree of asymmetry from the mean motion and zero and stationary values of the various characteristic. Variables, which are usually employed to separate the regions of a complex flow, do not coincide.

In the present investigation, all the measurements were taken at a Reynolds number of 3.42×10^5, where R_e is based upon the duct hydraulic diameter, D_h, and bulk mean velocity, U_b, of the duct.

During the measurements, the temperature of the room air was constant within $\pm$ 2°C.

The next two sections, 4.2 and 4.3 respectively, describe and discuss the measurements of the fully developed flow through a square duct with one rough wall. In section 4.4 the chapter is concluded with a summary of the present flow findings.

4.2 Presentation of the Measurements

This section includes a description of the process data reduction and physical interpretation of the profiles and contours obtained. For ease of presentation, the results are divided into six subsections, three for mean and three for turbulent flow properties.

4.2.1 Mean Velocity Profiles and Contours

Figure 4.1 displays mean velocity profiles from the rough wall at various distances from the side wall ($x_2 = 0$). The point of maximum velocity is marked on each profile. On the plane of symmetry ($x_2/a = 0.5$), the maximum velocity occurs towards the rough wall ($x_3/a = 0.48$) and gradually moves away from it (rough wall) towards the smooth wall ($x_3/a = 1$) as the side wall is approached. This behaviour reflects the influence of secondary motion. In the absence of secondary motion, the maximum mean velocity on the symmetry plane would have been shifted from the centre towards the smooth wall ($x_3/a = 1$), where resistance to the flow is minimum. Near the symmetry plane, strong secondary motion carries fluid of higher momentum from the smooth wall region towards the rough wall and thereby shifts the position of maximum velocity towards the rough wall. An inflexion point is present in each profile and indicates the zone of interaction of the rough wall profile with the smooth wall. On the symmetry plane ($x_2/a = 0.05$), the inflexion point occurs approximately at $x_3/a = 0.80$ and near the side wall, at $x_2/a = 0.05$, it occurs at approximately $x_3/a = 0.94$. This shows that, like the velocity maxima, the points of inflexion shift towards the smooth wall as the side wall is approached. The above observations indicate that the influence of the rough wall over the smooth wall increases from the symmetry plane ($x_2/a = 0.5$) of the duct towards its side wall ($x_2/a = 0$).

The bulk mean velocity of the duct, U_b, is needed to determine the Reynolds number and to allow comparison of some of the present results with those of previous workers. The ratio U_b/U_c is defined by

$$\frac{U_b}{U_c} = \frac{1}{A} \iint_A \frac{U_1}{U_c} \, dA \qquad \ldots (4.1)$$

where A is the duct cross sectional area. The average mean velocity ratios, determined by graphical integration, are numbered, in figure 4.1, from O at the duct centre line ($x_2/a = 0.5$) to N at the duct wall ($x_2/a = 0$). A linear velocity ratio is assumed between the successive stations except between the N-1 station and the wall where, because of the large velocity gradient, the velocity is assumed to be uniform with an estimated value U_N. Representing the area on the graph between the stations i-1 and i by ΔA_i, the bulk mean velocity ratio is calculated from

$$\frac{U_b}{U_c} = \frac{1}{A} \left[\sum_{i=1}^{N-1} \frac{1}{2} \left(\frac{U_{b\,i-1}}{U_c} + \frac{U_{b\,i}}{U_c} \right) \Delta A_i + \frac{U_N}{U_c} \Delta A \right] \qquad \ldots (4.2)$$

and was found to be 0.77.

Figure 4.2 shows mean velocity profiles parallel to the rough wall ($x_3/a = 0$). These were obtained by interpolating the points from figure 4.1. The effect of secondary flow on the distribution of mean veloicty can be confirmed from these profiles. Velocity profiles in the two quadrants (upper quadrant, $0.5 \leq x_3/a \leq 1.0$ and lower quadrant, $0 \leq x_3/a \leq 0.5$) of the duct are different in their physical shape. In the lower quadrant, the profiles show that the mean velocity gradually increases and reaches its maximum on the symmetry plane showing the presence of little or no secondary flow in that region. In contrast, the profiles in the upper quadrant show the presence of strong secondary motion. For example, at $x_3/a = 0.8$, the velocity increases from the symmetry plane ($x_2/a = 0.5$) to a point midway between the side

wall ($x_2/a = 0$) and the symmetry plane; the velocity then decreases towards the side wall. This behaviour of velocity change is prominent near the smooth wall indicating a region of strong secondary velocity.

The distributions of mean velocity are replotted in semilogarithmic coordinates on a Clauser chart ie. U_1/U_c versus $\log [U_c x_3/\nu]$, where the abscissa is proportional to the distance, x_3, from the duct wall. The Clauser chart represents log law velocity profiles of equation (2.24) in the form

$$\frac{U_1}{U_c} = \sqrt{\frac{C_f}{2}} \left[\frac{1}{\kappa} \ln \left(\sqrt{C_f/2} \times \frac{U_c x_3}{\nu} \right) + C \right] \quad \ldots (4.3)$$

with C_f is defined in this case as

$$C_f = \frac{\tau_w}{\frac{1}{2}\rho U_c^2} \quad \ldots (4.4)$$

Figures 4.3 to 4.5 show the profiles plotted in this form for the rough wall and smooth wall ($x_3 = a$ and $x_2 = 0$) respectively. They confirm that, near the walls, the variation of mean velocity is logarithmic. This is clearly seen along the symmetry axis, $x_3/a = 0.5$, in figures 4.3 and 4.4. However as the distance normal to the wall increases, the profiles tend to deviate from the logarithmic variation. Near the symmetry axis, the smooth wall ($x_3 = a$) profiles depart from the logarithmic line, as in the case of symmetric smooth duct flow but away from the symmetry axis ($x_3/a < 0.4$), due to the progressive influence of the rough wall, the smooth wall profiles fall below the logarithmic line as happened in the asymmetric channel flow of Hanjalic and Launder (1972a). This indicates that near the symmetry plane ($x_2/a = 0.5$), the influence of the rough wall over the smooth wall is more in ducts with high aspect ratios than in those with low aspect ratios.

Leutheusser (1963) found that if the local wall shear stress is used to nondimensionalise U_1 and x_3, the universal logarithmic law (equation 2.24) is valid for flow in the

near wall region of square ducts. Like the smooth wall equation, an identical equation (equation 2.28) can be used for the rough wall. Though the present results show the logarithmic variation of mean velocity with distance normal to the wall, they can not be used to verify Leuthesser's (1963) conclusion since the local wall shear stress was not measured directly. In the present study, however, an indirect method was used to find the values of κ, B_S and B_R (in equations 2.24 and 2.28). In this method κ is expressed in terms of the known quantities of the duct and is evaluated graphically in the following way:

$$\int_S \tau_w dS = \rho\kappa^2 \int_S \frac{(U_\tau)^2}{(\frac{}{\kappa})} dS = \frac{\partial P}{\partial x_1} A$$

or

$$\kappa = \left\{ \frac{\partial P}{\partial x_1} A \Big/ \left[\rho \left(U_{\tau/\kappa} \right)^2 ds \right] \right\}^{\frac{1}{2}} \quad \ldots (4.5)$$

where S and A are respectively the perimeter and cross sectional area of the duct. The slope of the Clauser chart, U_i/U_c versus ln $(x_3 U_c/\nu)$ for the rough wall or ln $(a-x_3)U_c/\nu$ for the smooth wall, or ln $(x_2 U_c/\nu)$ for the side wall, is equal to the slope, $U_{\tau/\kappa}$, of the universal profile and hence the term $\int_S (U_{\tau/\kappa})^2$ ds can be found by numerical integration. The pressure gradient has been measured and left hand side of equation 4.5 can be evaluated. Hence κ can be found and the value of B_S and B_R determined from the logarithmic plot. The following were found:

$$\kappa = 0.385, \; B_R = 2.85 \text{ and } B_S = 6.84$$

The value of κ , which is supposed to be a universal constant, is within the existing range of uncertainty. The value of B_R is low and that of B_S high. The value of B_R will improve if the imaginary origin (which will be discussed in section 4.3.1) of the log law profile for the rough wall is shifted above the

rib root ie, the duct wall. With the duct wall as the origin for both the smooth and rough wall, the equations 2.24 and 2.28 can now be rewritten with their proper constants as:

$$U_S^+ = \frac{1}{0.385} \text{In } x_3^+ + 6.84 \qquad \ldots (4.6)$$

$$U_R^+ = \frac{1}{0.385} \text{In } \frac{x_3}{e} + 2.85 \qquad \ldots (4.7)$$

since the value of κ is known, the local friction velocities may be calculated from the slope of the Clauser charts (figures 4.3 - 4.5) and are used to normalize the mean velocities. Universal log law velocity profiles for the rough wall are, thus, plotted in figure 4.6. All profiles, except some near the corner, collapse onto the logarithmic line after about 2 rib heights. Profiles near the corner (x_3/a = 0.1, 0.05 and 0.025) show the gradual increase of the value of the constant B_R in equation 2.23. Universal log law velocity profiles for the smooth wall (opposite to the rough wall), shown in figure 4.7, form a logarithmic line only near the centre ie, at x_2/a = 0.5 and 0.4, other profiles show that the value of B_S in equation 2.24 progressively increases as the side wall is approached. Thus the departure of the profiles from the universal logarithmic line near the smooth wall starts much earlier than that near the rough wall. It can be concluded that, near the symmetry plane, the profiles both near the smooth and rough wall follow a universal logarithmic behaviour. Similar conformity of near wall profiles with universal logarithmic distribution was observed by Hanjalic and Launder (1972a) in their asymmetric channel flow and led them to conclude that the flow was essentially in local equilibrium in spite of the dissimilar stucture prevailing at opposite walls. Diversity of constants in the log law near the corner of the square duct occurs due to the deviation of the flow from two-dimensionality. This fact

was reported both by Melling and Whitelaw (1976) and Humphrey and Whitelaw (1979).

Contours of mean velocity, U_1, are shown in figure 4.8 and were obtained from the mean velocity results of figure 4.1. They display almost no bulging near the rough wall corner ($x_2 = 0$, $x_3 = 0$) but show bulging towards the smooth wall corner ($x_2 = 0$, $x_3 = a$). Unlike the symmetric smooth duct contours, the present contours show no bulging in the centre region of the side wall ($x_2 = 0$). Bulging of the contours, however, occurs in the centre region of the smooth wall (opposite to the rough wall) and in the upper quandrant of the duct, supports the presence of cross stream rotational motion. Near the symmetry plane, the contours in the rough wall region are more evenly distributed than those in the smooth wall region and indicate that there is little or no influence of cross stream motion. Due to the influence of U_3 component of cross stream motion isovels on the symmetry plane ($x_2/a = 0.5$) shift towards the rough wall. This shift is confined near the centre ($0.35 < x_3/a < 0.65$) where influence of wall is little. Near the walls, however, isovels occur closer to the smooth wall than the rough wall in spite of their bulging in the smooth wall region.

4.2.2 Secondary Mean Velocity

The secondary flow angles were measured at the same Reynolds number and positions as the axial velocity field. The angles γ_2 and γ_3, in degrees, are plotted in figures 4.9 and 4.10 respectively. As described in section 3.3.3, the secondary flow angles, γ_2, were measured both by yawmeter and hot-wire to allow comparison of the two methods and their results are plotted in figure 4.9. The maximum angle is about 2.5°. In the majority of flow region, however, the secondary flow angle is less than 0.5° and it should be borne in mind that the absolute accuracy of measurement is about 0.2°. The scatter is maximum near the rough surface and is about 40% to 60% (in some extreme cases about 100%) of the mean value; away from the rough wall the scatter decreases to about 10% to 15%. To minimise the effect of scatter, when determining U_2 and U_3 from equation 3.13 mean curves were drawn through the points in figures 4.9 and 4.10 (in figure 4.9 mean curves were drawn

through the points of yawmeter readings) and the smoothed curves were used for the calculation of U_2 and U_3. The computer plot of the vectors U_2 and U_3 were thus obtained and are shown in figures 4.11 and 4.12 respectively. The two vectors U_2 and U_3 are combined to give total secondary velocity with magnitude

$$U_{Sec} = \sqrt{U_2^2 + U_2^2} \qquad \ldots (4.8)$$

and with direction relative to the x_2 - axis given by

$$\gamma_{Sec} = \tan^{-1} \frac{U_3}{U_2} \qquad \ldots (4.9)$$

From this information, the secondary velocity vector distribution of figure 4.13 was obtained. A secondary velocity vector of length equal to the short horizontal bar shown in the diagram has a magnitude of $U_{sec} = 0.05U_c$ and the maximum secondary velocities were, therefore, less than 5% of U_c. The vector plot of figure 4.13 shows a strong vortex in the upper quadrant of the duct with centre at about $x_2/a = 0.28$ and $x_3/a = 0.74$ and a very weak one near the rough surface. The main vortex directs fluid upwards along the side wall ($x_2 = 0$), along the top wall ($x_3 = a$) towards the duct symmetry plane and downwards. This vortex is responsible for bulging of the mean velocity contours towards the smooth wall corner of the duct and near the symmetry plane, shifting them from the smooth wall towards the core region of the duct. The counter rotating weak vortex near the rough wall transfers fluid from the centre towards the rough wall corner ($x_2 = 0$, $x_3 = 0$) and then along the rough wall towards the duct symmetry plane. This transfer of fluid across any line of the duct cross sectional area, should satisfy the condition for mass balance. Depending upon the precision of measurement in different flow regions, the mass balance is satisfied within different degree of variation. This fact will be analysed and discussed in section 4.3.2 along with the results of other workers. Figure

4.12 shows two distinct zones of U_3: one of positive U_3 (pointing towards the smooth wall, x_3 = a) and the other of negative U_3 and the two zones are separated more or less by the diagonal of the flow area obtained by joining the rough wall corner with the centre of the smooth wall. Three zones of U_2 are noticed in figure 4.11, two zones of positive U_2 (flow away from the side wall, x_2 = 0) near the two walls (rough wall, x_3 = 0 and smooth wall, x_3 = a) and one of negative U_2 covering the main flow area of the duct. In both the corners, however, small zones of negative U_2 are noticed though they are in positive U_2 zones.

4.2.3 Friction Factor and Wall Shear Stresses

The measured friction factor variation with Reynolds number is shown in figure 4.14. The value of average wall shear stress τ_w is obtained from the equation

$$\tau_w = -\frac{Dh}{4}\frac{dP}{dx_1} \qquad \ldots (4.10)$$

and the friction factor is calculated from

$$C_f = \frac{2\tau_w}{\rho U_b^2} \qquad \ldots (4.11)$$

A selection of the static pressure distribution, measured along the duct axis at various Reynolds numbers, is shown in figure 4.15. The axial pressure gradient, $^{dP}/dx_1$, was linear, within the scatter of the data, from about ten diameters down stream of the entrance. The linear pressure gradient indicates that the flow was fully developed in the measuring station which was 36 diameter downstream from the entrance end. The Reynolds number was varied by altering the flow velocity and the centre line velocity, U_c, was recorded for each Reynolds number. The bulk mean velocity U_b for all Reynolds number was assumed to be the same fraction of duct centre line velocity as calculated for

Reynolds number 3.42×10^5. Bulk mean velocity was also calculated for Re = 1.12×10^5 and its ratio with duct centreline velocity was found to be within 2.5% of the value for Re = 3.42×10^5. In figure 4.14, the Blasins friction law for pipes (equation 1.1) is also shown for comparison; the present results are best represented by the relation

$$C_f = 0.0148\ Re^{-0.05} \qquad \ldots (4.12)$$

which is in between the Blasins friction equation for smooth pipes and fully turbulent rough pipe flow where friction factor was found to be almost constant.

Figure 4.16 presents the distribution of wall shear stress normalized by the average wall shear stress calculated by the equation 4.10. As discussed in section 4.2.1, local wall shear stresses were calculated indirectly from the Clauser chart plot. Figure 4.16 shows that the rough wall shear stress increases from the corner towards the symmetry plane where it reaches its maximum. The top wall (x_3 = a) shear stress increases from the corner towards the symmetry plane, reaches it maximum at about $x_2/a = 0.7$ and then decreases. The side wall ($x_2 = 0$) shear stress increases gradually from the rough wall corner towards the centre of the wall and remains nearly constant from $x_3/a = 0.3$ to $x_3/a = 0.5$ and then begins to decrease towards the smooth wall corner. The cross stream motion towards the side wall increases the value of the wall shear stress while that away from the wall decreases its value. For example, from the rough wall corner to $x_3/a = 0.62$, the U_2 component of secondary velocity, in figure 4.11, is towards the side wall, and then it is away from the wall except near the corner; correspondingly the side wall shear stress (figure 4.16) has higher values in the region where flow is towards the wall and it starts to decrease from about $x_3/a = 0.55$ where the U_2 component of secondary velocity changes its direction from towards the wall to away from it. The above phenomenon can also be observed for the top wall in figures 4.12 and 4.16.

4.2.4 Contours of Turbulence Intensities

Figures 4.17, 4.18 and 4.19 show contours of normalized turbulence intensities, $\tilde{u}_1/U_c$, $\tilde{u}_2/U_c$ and $\tilde{u}_3/U_c$ respectively. Before discussing the physical implications of these contours, some comments on consequences of the method of data processing are useful. $\tilde{u}_1/U_c$, $\tilde{u}_2/U_c$ and $\tilde{u}_3/U_c$ were calculated according to the hot wire equations 3.7, 3.8 and 3.10 respectively. They were plotted and smoothed for each station. Values of $\tilde{u}_1/U_c$, $\tilde{u}_2/U_c$ and $\tilde{u}_3/U_c$ were then taken from the graph of corresponding profiles for contour plotting. Typical profiles in figures A4.1 to A4.3 show that the data were of good quality except near the rough wall where scatter was about 10%. All three components of turbulence intensities bulge towards the smooth wall corner confirming the influence of secondary flow on their distribution. Axial turbulence intensities reach their maximum at about 2.25 rib heights (measured from the rib root) and on the symmetry plane of the duct. The maxima of transverse turbulence intensities, $\tilde{u}_2/U_c$ and $\tilde{u}_3/U_c$, occur at about 7 rib heights (figures 4.18 and 4.19) and between the symmetry plane and the side wall at a value of about $x_2/a = 0.3$. Thus, as expected, turbulence is generated near the rough wall. Comparison of the contours in figures 4.17 - 4.19 with the distribution of secondary velocity in figure 4.13 indicates that the turbulence intensities generated near the rough wall region of the duct are convected towards the side wall ($x_2 = 0$) and then along the side wall towards the top wall ($x_3 = a$). Compared with the contours of U_1/U_c (figure 4.8), the bulging of the contours of $\tilde{u}_1/U_c$ (figure 4.17) is more pronounced in the upper quadrant of the duct where secondary velocity is relatively strong. This indicates that the distribution of $\tilde{u}_1/U_c$ is influenced more by the secondary flow than that of U_1/U_c. Contours of $\tilde{u}_2/U_c$ and $\tilde{u}_3/U_c$ show that their distribution is less influenced by the secondary flow than that of $\tilde{u}_1/U_c$. Near the symmetry plane, the gradient of $\tilde{u}_1/U_c$ is nearly uniform in the lower quadrant ($0 < x_3/a < 0.5$) of the duct and decreases in the upper quadrant ($0.5 < x_3/a < 1.0$) while near the side wall it is nearly the same throughout the duct height. Minimum values of $\tilde{u}_2/U_c$ occur on the symmetry plane at about $x_3/a = 0.58$ while those of $\tilde{u}_1/U_c$ shift towards the side wall

(x_2 = 0) and the top wall (x_3 = 0) and occur at about x_3/a = 0.8, x_2/a = 0.3 and those of $\tilde{u}_3/U_c$ move further in the direction of $\tilde{u}_1/U_c$, occuring close to the top wall at x_2/a = 0.15. The contours of $\tilde{u}_2/U_c$ and $\tilde{u}_3/U_c$ show that their gradients are steep near the rough wall and gradually decrease away from the wall. Due to the gradual variation of $\tilde{u}_2/U_c$ and $\tilde{u}_3/U_c$ in most part of the duct cross section, contours representing only slightly different values are widely spaced. Contours of $\tilde{u}_3/U_c$ in figure 4.19 show two maxima of nearly the same magnitude, $\tilde{u}_3/U_c$ = 0.08, one near the rough wall and another near the side wall where the level of intensity due to $\tilde{u}_2/U_c$ is much less, in the range of about 5.5% of U_c. So the degree of, anisotropy in this zone of the side wall is greatest indicating the source of generation of cross stream motion as shown by Brundrett and Baines (1964).

4.2.5 Reynolds Shear Stress and Kinetic Energy Contours

Contours of Reynolds shear stress $\overline{u_1 u_2}/U_c^2$, and $\overline{u_1 u_3}/U_c^2$, turbulent kinetic energy k/U_c^2 and difference between normal stresses, $(\overline{u_2^2} - \overline{u_3^2})/U_c^2$, are drawn in the same way as those of turbulence intensity contours. Typical profiles are shown in figures A4.4 to A4.7. As expected, scatter is greatest near the rough wall where local tubulence intensities were as high as 30%. Contours near the rough wall are, therefore, less precise than those away from it.

Contours of Reynolds shear stress $\overline{u_1 u_2}/U_c^2$ are drawn in figure 4.20. A single line contour of zero shear stress, $\overline{u_1 u_2}/U_c^2$, divides the flow area into three zones. The bulk of the flow has negative shear stress with two small areas of positive shear stress close to the rough and the smooth (x_3 = a) wall. Contours of high negative shear stress, $\overline{u_1 u_2}/U_c^2$, are stretched along the side wall. Contours in the rough wall corner are closely spaced, indicating the high gradient of shear stress. Except near the corners, contours of $\overline{u_1 u_2}/U_c^2$ near the rough wall move nearly along the wall while those near the top wall move across it, indicating that the Reynolds shear stress, $\overline{u_1 u_2}/U_c^2$, remains almost constant along the rough wall while that near the smooth wall

(x_3 = a) varies from the corner towards the symmetry plane. The shear stress near the smooth wall changes its sign from negative near the corner to positive near the symmetry plane. The contour of zero shear stress, $\overline{u_1 u_2}/U_c^2$, originates from the rough wall corner, travels along the rough wall in a wavy pattern towards the central region of the duct and reaches the symmetry plane at about $x_3/a = 0.41$ and, in the upper quadrant, shifts towards the side wall to a value of about 0.3 and runs upwards towards the smooth wall. The distribution of the zero shear stress contours indicates the relative positions of the velocity maxima in the mean velocity profiles plotted parallel to the rough wall in figure 4.2.

The contours of $\overline{u_1 u_3}/U_c^2$ in figure 4.21 show a well defined distribution, in the lower quadrant (except near the corner) of the duct. In this region Reynolds shear stress $\overline{u_1 u_3}/U_c^2$ increases nearly linearly towards the rough wall. Near the rough wall, the shear stress values should tend to a limit given by

$$-\overline{u_1 u_3}/U_c^2 = \tau_r/\rho U_c^2 \qquad \ldots (4.13)$$

which is about 7.5×10^{-3} and is consistent with the measured values of figure 4.21. The value of $\overline{u_1 u_3}/U_c^2$ reaches its maximum in the central region of the duct and increases slowly towards the top wall. This gradual variation of Reynolds shear stress, $\overline{u_1 u_3}/U_c^2$ is particularly pronounced in the region $0.2 < x_2/a < 0.5$. Consequently, the location of the contours in this region are uncertain in that a change in $\overline{u_1 u_3}/U_c$ as small as 5×10^{-5} would move a contour by about 0.1 on the symmetry plane. Two distinct regions of $\overline{u_1 u_3}/U_c^2$, one positive and other of negative, are indicated in figure 4.21. On the whole, the lower quadrant of the duct is the zone of negative shear stress and the upper quadrant positive. Near the side wall, the negative Reynolds shear stress zone is stretched towards the smooth wall by the strong secondary velocity in that region. On the symmetry plane, the contour of zero shear stress shifts towards the rough wall and occurs at $x_3/a = 0.495$ and moves towards the smooth wall as the side wall is approached. The occurance of zero shear

stress and velocity maxima will be discussed in section 4.3.5.

Figure 4.22 shows the distribution of turbulent kinetic energy, k/U_c^2, where k is defined by by $k \equiv \frac{1}{2}(\overline{u_1^2}+\overline{u_2^2}+\overline{u_3^2})$. As expected, the maximum turbulent kinetic energy is near the rough wall and its peak occurs at about 6 rib heights from the wall. Turbulent kinetic energy is evenly distributed near the rough wall. It gradually increases towards the rough wall and, after reaching its peak, decreases quickly near the top surface of the ribs. Near the side wall, kinetic energy generated near the rough wall is carried away towards the smooth wall in the direction of positive U_3; and on the symmetry plane kinetic energy near the smooth wall bulges away from it in the direction of negative U_3, present in that region. A minimum value of turbulent kinectic energy occurs at about $x_2/a = 0.3$, $x_3/a = 0.75$ and is encircled by the closed contours.

Figure 4.23 shows the contours of the difference between the normal stresses $(\overline{u_2^2}-\overline{u_3^2})/U_c^2$. Its zero contours divide the zone of positive and negative $(\overline{u_2^2}-\overline{u_3^2})/U_c^2$ over the cross stream plane of the duct. The side wall bounded by the zero contour is the zone of high value (of the order of 0.2% of U_c) of negative $(\overline{u_2^2}-\overline{u_3^2})/U_c^2$ which increases steadily towards the side wall. Contours of small value (0-0.05% of U_c) of negative $(\overline{u_2^2}-\overline{u_3^2})/U_c^2$ encircled by the zero contour line, are distributed around the duct centre. High values (.1-.2% of U_c) of positive $(\overline{u_2^2}-\overline{u_3^2})/U_c^2$ are distributed near the two opposite walls, rough and smooth. Close to the rough wall, there is a narrow band running nearly parallel to it (except near the corner) where contours of $(\overline{u_2^2}-\overline{u_3^2})/U_c^2$ are closely spaced. Brundrett and Baines showed that the distribution of the turbulence correlation $(\overline{u_2^2}-\overline{u_3^2})$, is mainly responsible for the production of vorticity and the relative magnitude of the other correlation, $\overline{u_2 u_3}$, related in the production term, is much less than $(\overline{u_2^2}-\overline{u_3^2})$. In the present measurement, however, $\overline{u_2 u_3}$, were not measured. In figure 4.23, gradients of $(\overline{u_2^2}-\overline{u_3^2})/U_c^2$ are considerably large near the side wall particularly near the rough wall corner where the value of the production term (equation 1.5) $\frac{\partial^2}{\partial x_2 \partial x_3}(\overline{u_2^2}-\overline{u_3^2})$, are 5 to 10 times higher than those at the central part of the duct and indicate the generation of secondary motion in that region.

4.2.6 Longitudinal Turbulence Spectra

Spectral measurements of $\overline{u_1^2}$ were determined close to the rough wall (x_3/a = 0.04 and 0.08) and at three positions from the side wall (x_2/a = 0.025, 0.25 and 0.5). The frequency spectra of the hot wire signals were converted into the wave number spectra of the longitudinal velocity component by the transformation

$$K_1 = \frac{2\pi f}{U_1} \qquad \ldots (4.14)$$

where f and K_1 are the frequency and wave number respectively. The power spectral densities of the $\bar{u}_1$ component are normalized by its mean square intensity $\overline{u_1^2}$ and are plotted in figure 4.24 as a function of wave number K_1. The absolute value of longitudinal spectral density is given by

$$\phi_{11}(K_1) = \frac{F_{11}(K_i)}{\overline{u_1^2}} \qquad \ldots (4.15)$$

$$\text{so that} \quad \int_0^x \phi_{11}(K_1)\, dK_1 = 1 \qquad \ldots (4.16)$$

All the curves of spectra show that there is no fall-off of energy at low wave numbers, and that the spectral density becomes constant in the range where its distribution is nearly horizontal. At low wave numbers, there is a large amount of turbulent energy particularly near the rough wall. The low frequency part of the spectra, dominated by inertia, is dependent on the large scale structure. Viscous effects are neglible at the largest eddies of the motion which are long lived eddies and are supposed to be highly anisotropic. According to Sternberg (1965) these large amplitude low frequency eddies are responsible for the convection of disturbances.

All the curves in figure 4.24 show monotonic fall-off with the increase of wave number, indicating the absence of any predominant eddy structure that could have been generated by

the rough wall. The region, in which the spectra falls rapidly with increasing wave number, associates with considerable interaction and diffusion. This energy dispersion, which is both inward and outward, is due to the transfer of kinetic energy and pressure energy by lateral velocity fluctuations. The small short lived, high frequency eddies in the inertial subrange are responsible for dissipation of energy and should have a spectral shape given by $F(K_1) \propto K_1^{-5/3}$, as proposed by Kolmogorov, 1962. In the present investigation, the spectral curves at all positions exhibit a $K_1^{-5/3}$ variation spreading over one decade, indicating the presence of inertial subrange of the spectra near the rough wall. The isotropic condition can thus be expected in that range of the spectra in spite of the strong asymmetric boundary condition. The distribution of spectra for a fixed distance from the rough wall, is nearly identical for various values of x_2/a as seen from spectra No 1 and 2, and 4 and 5 in the figure. Near the rough wall corner, as seen from spectra No. 3 and 6, the $K_1^{-5/3}$ variation starts at higher wave numbers than the other curves (curves 1,2,4, and 5). Before the $K_1^{-5/3}$ variation, the spectra of 3 and 6 seem to follow a K_1^{-1} law for nearly one decade. K_1^{-1} variation of spectra was also reported by Hanjalic (1970) near the smooth wall region of his asymmetric channel.

4.3 Discussion of the Results

The aim of this section is to compare the present measurements with some of those reported in the literature review. Sections 4.3.1 to 4.3.6 examine the results presented in the corresponding sections 4.2.1 to 4.2.6 together with those obtained elsewhere mainly by Humphrey and Whitelaw (1979), Fujita (1978), Melling and Whitelaw (1976), Hanjalic and Launder (1972a) and Launder and Ying (1972).

4.3.1 Mean Velocity Profiles and Contours

Figure 4.25 compares the mean velocity plot, U_1/U_c, of Humphrey, Fujita and the present investigation. In Humphrey's work mean velocity was normalized by the bulk mean velocity, U_b.

From the ratio of bulk mean velocity to centreline velocity of his (Humphrey's) experiment, the results have been renormalised by the duct centre line velocity and replotted with the present results. As expected, the influence of walls (rough wall in particular) in Humphrey's experiment is more prominent than the present investigation. This is because of lower Reynolds number and larger rib height ratio, $^{e}/Dh$ (Humphrey - $Re=2.58 \times 10^{4}$, $^{e}/Dh = 0.099$; present experiment $Re=3.42 \times 10^{5}$, $^{e}/Dh = 0.0212$, where e is the rib height and Dh is the hydraulic diameter of the duct). In Humphrey's work there were insufficient points in the velocity profiles to locate the point of inflexion and the position of maximum velocity. However, careful observation shows some sign of inflexion in his profiles and the maxima of his profiles progressively shift towards the smooth wall as the side wall is approached, which happened in the present case.

Fujita's results are taken from his graphical presentation and are replotted. The Reynolds number was low ($Re = 6.4 \times 10^{4}$) but the ratio $^{e}/Dh$ was about the same ($^{e}/Dh = 0.02$) as the present case. His ribs were made of round wires of 1 mm diameter as against the square ribs (3.18 mm x 3.18 mm) used here. On the symmetry plane, the velocity maxima of Fujita's profiles occur towards the smooth wall (approximately at $^{x_3}/a = .55$) and the position of the velocity maxima remains more or less constant for other profiles at various values of $^{x_2}/a$. However, the point of inflexion exists in Fujita's profiles and its occurance in the veloicty profiles is the same as the present case ie, as the side wall coming closer the point inflexion moves towards the smooth wall ($x_3 = a$).

Several investigators in the past worked on the ribbed rough surfaces and concluded that the origin for the log law profile was not ideal either at the rib root or at the rib crest. In order to improve the universality of the profile of ribbed rough wall, it was argued by Perry and Joubert (1963), Berger and Whitehead (1977), Hanjalic and Launder (1972a) and others, that the origin may be shifted by introducing an additive constant in the argument of the logarithmic term in equation 2.28. Most authors have chosen this constant to fit the profile to

Nikuradse's (1932) value of the slope of 0.40, but some also the value of 0.418 recommended by Patel (1965). In order to provide a basis for comparison this technique has also been adopted in the present work and the value of 0.40 has been adopted for the slope since it is nearer that found from the present tests. The rough wall profiles in the present investigation can thus be represented by the equation

$$U_R^+ = \frac{1}{0.40} \ln (x_3/e - 0.25) + 3.30 \quad \ldots (4.17)$$

and some of the rough wall velocity profiles are plotted in this form in figure 4.26. The profiles collapse onto the logarithmic line from 1.6 rib height e, above the rib root. The reference origin in the present experiment thus fall between the rib root and the rib crest. In the present experiment the displacement of the reference origin from the rib root is relatively small compared with the displacements found by other workers for varying geometries. Displacements have been reported both above the roots ie, by Perry and Joubert (1963), Lin et al (1966) and Battermann (1966) and below the roots ie, by Hanjalic and Launder (1972a), Lawn (1971) and Berger and Whitehead (1977).

Isovels of the present investigation are compared in figures 4.27a and 4.27b with those of Humphrey and Fujita respectively. The three isovels in general bulge towards the smooth wall corner ($x_2 = 0$, $x_3 = a$) and on the symmetry plane, they bulge away from the smooth wall ($x_3 = a$), but the extent to which they bulge differs. The isovels of Humphrey differ markedly from those of the other two in that, close to the side wall ($x_2 = 0$), Humphrey's isovels bulge away from it which does not happen in the other two cases. In the rough wall region, the Humphrey's isovels occur at a distance from the rough wall which is much greater than that at which the same value of isovels occur in the other two experiments. For example, on the symmetry plane, isovels for $U_1/U_c = 0.60$ occur at $x_3/a = 0.18$ in Humphrey's experiment and at $x_3/a = 0.10$ and $x_3/a = 0.105$ in the present and Fujita's experiments respectively. This is expected because of higher rough wall resistance (due to more rib height) on mean flow in Humphrey's experiment than the other two investigations. The isovels in the present

work closely resemble those reported by Fujita. Near the rough wall, agreement between the two sets of results is good. For example, Fujita's isovels for U_1/U_c = 0.5 and 0.6 are almost coincident with those of the present results. Isovels for U_1/U_c = 0.70 are almost coincident except near the smooth wall corner where that of the present work bulges more towards the corner. Further from the rough wall, the difference between the relative positions of the identical isovels of the two experiments increases gradually resulting in the occurance of the present isovels further away from the top wall than those of Fujita, indicating the presence of a stronger vortex in the upper quadrant of the present duct than that in Fujita's one.

4.3.2 Secondary Mean Velocity

The distribution of the U_3 component of secondary velocity in figure 4.12 is compared with that of Humphrey in figure 4.28 which is the only available secondary flow data for a duct geometry similar to that of the present experiment. For qualitative comparison, the measurements of Brundrett and Baines (1964), Gessner and Jones (1965), Launder and Ying (1972) and Melling and Whitelaw (1976) are also discussed here. The large uncertainty in all the available results limits the possibility of detailed comparison. In the laser-Doppler anemometry measurements, considerable uncertainty arose in determining the secondary velocity from small differences between two comparative large voltages which are sensitive to small changes in the orientation of the fringe pattern. The hot-wire anemometry measurements are subject to an uncertainty arising from the direction, γ, of the secondary velocity component in equation 3.15, but additional errors can arise from probe interference. The yawmeter technique is subject to uncertainty due to the pressure gradient of the flow field and more probe interference than the hot-wire because of the bulky shape and size of the yawmeter. An indication of the error in secondary velocity measurements can be found from the continuity equation in the plane normal to the mean flow direction. Humphrey's U_3 measurements (at x_1/Dh = 41.68) in figure 4.28 show high values of positive U_3 in the region of the side wall which can also be seen in the present work in figure 4.12.

Humphrey's measurements show positive U_3, except for a small zone near the rough wall where small negative values of U_3 occur. In Humphrey's measurements, a very high value of U_3, about 17% of duct centreline velocity, was observed near the side wall and may be compared with the present value of about 4%. Due to the large rib height (about 10% of Dh) the effects of "sudden contraction" and "sudden expansion" were accountable near the rough wall of Humphrey's duct and those created favourable conditions for the production of high values of U_3 in addition to the anistropic condition of the duct. Launder and Ying found that the flows to and from the wall for component U_2 agreed within 10% at $x_2/a = 0.20$ and 0.50 but at $x_2/a = 0.80$ the flow from the wall was five times as large as towards the wall. The secondary velocities of Gessner and Jones consistently showed a flow away from the wall about 20% greater than towards it. Melling's measurements showed that, at $x_3/a = 0.232$, the flow away from the wall for the component U_3 was more than seven times that towards it. Brundrett and Baines did not consider uncertainties and the extent to which the continuity equation was satisfied, but from their vector plot, it was found that the flow towards the wall due to U_3 at $x_3/a = 0.8$, was about twice as large as that away from it. In the present investigation (figure 4.11) the mass flow due to U_2 at $x_2/a = 0.45$ is 1.3 times greater away from the wall than towards it; at $x_2/a = 0.30$ and 0.20, the mass balance is satisfied within 15% but at $x_2/a = 0.10$ the mass flow towards the wall is about 3.5 times as large as away from it. In figure 4.12, the mass flow due to U_3 is balanced within 20% near the centre region of the duct but the mass flow towards the wall increases as both the rough or smooth wall is approached. In fact, close to the walls almost all the mass flow due to U_3 is found to be towards the wall. In the experiment, secondary flow angles γ_2 and γ_3 were measured by two yawmeters (discussed in section 3.3.3) and near the wall both the yawmeter results yield more mass flow towards it. In spite of possible discrepancies, all measurements of secondary flow clearly show a movement of fluid towards the corners of the duct irrespective of symmetry.

4.3.3 Friction Factor and Wall Shear Stresses

Figure 4.14 shows Fujita's curve for friction factor versus Reynolds number (for a duct with one rough wall) along with the curve for the present case. Fujita calculated the friction factor from the equation

$$C_f = \frac{2Dh\,\partial P/\partial x_1}{\rho U_b^2} \qquad \ldots (4.18)$$

His values are divided by four to allow the comparison of figure 4.14. The slope of Fujita's curve shows more dependence on Reynolds number than the present results. The different shape of the roughness element may be the cause of different rate of friction factor variation with Reynolds number. Fujita took his measurements in a lower Reynolds number range ($\sim 10^4$) than the present experiment ($\sim 10^5$), however the curves suggest that, for the same Reynolds number, Fujita's duct gives more resistance to the flow than the present one.

Figure 4.29 compares the distribution of smooth wall shear stresses with those of Fujita. For the purpose of comparison, local wall shear stresses are normalized by the average shear stress of the corresponding wall. The average wall shear stress is calculated by graphical integration from

$$\bar{\tau}_s = \frac{1}{S}\int_s \tau_s\, ds \qquad \ldots (4.19)$$

where S is the length of the duct wall under consideration. Qualitatively, the physical shape of the curves for both the results are nearly the same but their relative magnitudes are much different. Near the smooth wall corner ($x_2 = 0$, $x_3 = a$), Fujita's curve show higher wall shear stress for both walls (side wall and top wall) than the present result and near the rough wall corner ($x_2 = 0, x_3 = 0$), Fujita's results show a smaller value of wall shear stress. On the symmetry plane the smooth wall shear stress in Fujita's duct is less than the present one. Fujita in his experiment found that the contribution of rough wall shear stress

is 64.4% of the total wall shear stress; in the present results this value is found to be 65.8%. Contributions of smooth wall shear stresses, however, differ considerably between the two results: in terms of a percentage of total wall shear stress, they are as follows: side wall 12.47%, top wall 9.32%. Corresponding values from Fujita are 11.5% and 12.6%. The difference in smooth wall shear stress, both in its distribution and magnitude, is probably due to the different nature and magnitude of secondary motion generated in two different flow fields. However, it should be remembered that the present wall shear stresses were not measured directly and in Fujita's experiment no secondary flow measurements were obtained.

4.3.4 Contours of Turbulence Intensities

Contours of longitudinal and transverse turbulence intensities $\tilde{u}_1/U_c$ and $\tilde{u}_3/U_c$, are compared with those of Humphrey in figures 4.30 and 4.31 respectively. The overall level of the turbulence intensity in Humphrey's duct was greater than in the present one due to his greater rib height ratio, e/Dh. Gessner indicated a reduction in $\tilde{u}_1/U_c$ of nearly 20% when the Reynolds number was double from 1.5×10^5 to 3×10^5 but this was not confirmed by Melling's (1975) results. Near the rough wall, the contours of $\tilde{u}_1/U_c$ in figure 4.30 show close agreement with those of Humphrey. In both cases, the contours near the rough wall are nearly parallel to it and move upwards as the side wall is approached. In Humphrey's experiment, the maximum $\tilde{u}_1/U_c$ occurred at about 1.9 rib heights against 2.25 rib heights here. In both cases, $\tilde{u}_1/U_c$ contours bulge towards the smooth wall corner of the duct. In Humphrey's experiment, a small zone of high $\tilde{u}_1/U_c$ was present near the side wall and was not found in the present contours. The present $\tilde{u}_1/U_c$ contours, near the symmetry plane, bulge more away from the smooth wall than Humphrey's and their minima shift towards the side wall occurring at about $x_2/a = 0.3$ as against $x_2/a = 0.5$ in Humphrey's case. In the upper quadrant of the duct the variation of $\tilde{u}_1/U_c$ is gradual. A small error in measurements would shift the location of the contours considerably thereby changing its overall shape. For example, on the symmetry plane, the contour of $\tilde{u}_1/U_c = 0.055$ occurs at $x_3/a = 0.69$ and, with a 3% increase in value it would occur at $x_3/a = 0.765$.

In view of the experimental uncertainties arising in both Humphrey's laser-Doppler anemometer measurements and the present hot-wire anemometer measurements the difference between the sets of contours in the sensitive zones are probably not significant. Figure 4.31 shows that contours of $\tilde{u}_3/U_c$ are different from those of Humphrey's results where the maximum $\tilde{u}_3/U_c$ appears to occur just over the rib top and decreased gradually away from the rough wall. In between the symmetry plane and the side wall, a maximum value of $\tilde{u}_3/U_c$ is found near the top wall and is not present in the present contours. In both cases, however, the minimum value of $\tilde{u}_3/U_c$ occurs near the top wall. The closed contours of $\tilde{u}_3/U_c$ spread over most part of the side wall of Humphrey's duct compared with its small part of the present duct, and the gradients of $\tilde{u}_3/U_c$ (in the direction of x_2 - axis) in Humphrey's experiment are steeper than the present results indicating the influence of side wall on the distribution $\tilde{u}_3$ in Humphrey's duct is more pronounced than that in the present one.

4.3.5 Reynolds shear stress and Kinetic Energy Contours

Figure 4.32 shows that the contours of $\overline{u_1 u_3}/U_c^2$ of Humphrey and the present investigation are very similar in the lower quadrant except near the rough wall corner and in the vicinity of the rough wall. From the symmetry plane, the contours run nearly parallel to each other towards the rough wall corner. In Humphrey's contours there is a zone of negative shear stress, $\overline{u_1 u_3}/U_c^2$, near the smooth wall corner bounded by the zero shear stress contour which is not found in the present contours. In addition, the relative magnitude of shear stress, $\overline{u_1 u_3}/U_c^2$, are much less (4 to 8 times) in Humphrey's experiment.

The distribution of shear stress contours in figures 4.20 and 4.21 suggests that to represent the axial mean velocities of figures 4.1 and 4.2, the Reynolds shear stress $\overline{u_1 u_2}$ and $\overline{u_1 u_3}$ can be modelled by an effective viscosity:

$$-\rho\overline{u_1 u_2} = \mu_{eff} \frac{\partial U_1}{\partial x_2} \qquad \ldots (4.20)$$

$$-\rho\overline{u_1 u_3} = \mu_{eff} \frac{\partial U_1}{\partial x_3} \qquad \ldots (4.21)$$

In the lower quadrant of the duct $\frac{\partial U_1}{\partial x_3}$ (figure 4.1) is positive everywhere and hence $\overline{u_1 u_3}$ (figure - 4.21) is negative and of increasing magnitude towards the rough wall because of the increase of $\partial U_1/\partial x_3$ in that direction. Similarly in the upper quadrant of the duct except near the side wall where the status of the lower quadrant is continued, $\frac{\partial U_1}{\partial x_3}$ is negative implying a positive value of $\overline{u_1 u_3}$ and of increasing magnitude towards the smooth wall. Again in the upper quadrant of the duct, the contours of $\overline{u_1 u_2}/U_c^2$ (figure 4.20) and the mean velocity profiles (figure 4.2) fulfil the condition of equation 4.20. For example, (in figure 4.2) at $x_3/a = 0.90$ $\partial U_1/\partial x_2$ is positive from the side wall to approximately $x_2/a = 0.25$ where it is zero and afterwards $\partial U_1/\partial x_2$ is negative upto the symmetry plane where its value becomes zero. Accordingly, the Reynolds shear stress, $\overline{u_1 u_2}$, is negative from the side wall to $x_2/a = 0.29$ where it is zero and then becomes positive and again decreased to near zero on the symmetry plane. Near the rough wall the experimental scatter of $\overline{u_1 u_2}/U_c^2$ is upto 30% as can be seen in figure A4.4 and hence contours near the rough wall are not as reliable as in the other part of the duct where the scatter is less than 10%. Despite these experimental imperfections the contours of $\overline{u_1 u_2}/U_c^2$ from top wall to $x_3/a = 0.20$, can be explained in terms of equation 4.20. Contours of $\overline{u_1 u_2}/U_c^2$ near the rough wall spread along the wall in a wavy pattern indicating a small periodic variation of its value for various values of x_2/a and the mean velocity gradients $\partial U_1/\partial x_2$ are nearly constant. U_1/U_c profiles (figure 4.2) at $x_3/a = 0.1$ and 0.15, cross the zero shear stress, $\overline{u_1 u_2}/U_c^2$, contours three times and this can not be readily explained by the shape of U_1/U_c profiles.

According to equation 4.20 and 4.21 the position of zero shear stress and that of zero velocity gradient should be coincident but figures 4.1 and 4.21 and 4.2 and 4.20 show that they do not coincide. Figure 4.33 presents the contours of zero shear stresses, $\overline{u_1 u_2}$ and $\overline{u_1 u_3}$, and zero velocity gradients $\partial U_1/\partial x_3$ and $\partial U_1/\partial x_3$: curves 1 and 2 show that the planes of maximum velocity and zero shear stress, $\overline{u_1 u_3}$, are not coincident. The position of zero shear stress lies closer to the smooth wall ($x_3 = a$) than the maximum veloicty and moves further from the maximum velocity

position towards the smooth wall as the side wall ($x_2 = 0$) is approached. This feature of noncoincidence of zero shear stress and zero velocity gradiant was also observed in aysmmetric flows of Humphrey and Whitelaw (1979) and Hanjalic and Launder (1972a) where the positions of zero shear stress also lay closer to the smooth wall than those of the maximum velocity. The plane of zero velocity gradient, $\partial U_1/\partial x_3$, of Humphrey's duct is shown in figure 4.32 along with his shear stress, $\overline{u_1 u_3}$, contours. In Beguier's (1965) dissimilar wall jet experiment also positions of zero shear stress did not coincide with those of zero velocity gradient at different downstream positions of the jet. Thus is appears that, asymmetric flows are associated with noncoincidence of zero shear stress and zero velocity gradient. In the upper quadrant of the duct curves 3 and 4 show nearly the same characteristic as curves 1 and 2. The maximum velocity occurs closer to the side wall than the zero shear stress, $\overline{u_1 u_2}$ and, as the top wall is approached, the distance between them increases. On the symmetry plane, however, the zero velocity gradient, $\partial U_1/\partial x_2$ and, zero shear stress, $\overline{u_1 u_2}$, are nearly coincident as the rate of change of velocity gradient $\partial U_1/\partial x_2$ is more gradual. In the lower quadrant of the duct, the zero shear stress, $\overline{u_1 u_2}$ contour moves down towards the rough wall and then runs along it towards the side wall while the zero velocity gradient in that region occurs nearly on the symmetry plane.

Because of the noncoincidence of planes of zero shear stress and zero velocity gradient there is a region between these where $\overline{u_1 u_3}$ and $\partial U_1/\partial x_3$ or $\overline{u_1 u_2}$ and $\partial U_1/\partial x_2$ have the same sign and, hence the production term of turbulence kinetic energy is negative. That is, the turbulent flow field is losing energy to the mean flow. Since a considerable portion of the turbulent energy is dissipated in the same region, the energy is supplied by the diffussion from the surrounding flow regions. Large diffussion in the region of negative generation was reported by Hanjalic.

4.3.6 Longitudinal Turbulence Spectra

The shapes of spectral curves for $\phi_{11}(K_1)$ in figure 4.24 are nearly the same as those of Hanjalic who also observed that the spectra do not fall off at low wave numbers, indicating that spectral density becomes constant at low frequencies. The same nature of behaviour of spectral density at low wave number was also found as Comte-Bellot (1965), Clark (1968) and Hussain's (1975). In Hanjalic's results, the $K^{-5/3}$ region of the spectral curves $\phi_{11}(K_1)$ stretched over one and a half decades whereas, in the present investigation, it stretches over just under one decade. In the present data, the lowest measured frequency of 2.5 Hz corresponds to a wave number whose reciprocal is roughly ten times the width of the duct. The existence of such large eddies, elongated in the streamwise direction with a length considerably larger than the flow width, has also been reported by Hanjalic and in other boundary layer and channel flows. The interpretation of the spectra at such small frequencies, in a duct flow, is rather imprecise because of the possible interference of mean flow fluctuations. The scatter of the points at low frequencies is considerably higher. This is attributed to the fact of possible interference just mentioned above, larger time scale and narrow frequency band of the analyser (used in the measurement) at low frequencies.

4.4 Summary Conclusions

In sections 4.2 and 4.3 measured results have been presented, compared with those of other workers and discussed. The summary conclusions are presented below:

4.4.1 Mean Flow Findings

(1) Near the rough wall, all velocity profiles, except those near the corners, collapse onto a single logarithmic curve of slope $1/\kappa$ at about 1.6 rib heights above the surface. The reference origin of the logarithmic curves is shifted above the rib roots. As could be expected, the smooth surface exerts less influence on the flow near the rough surface than vice versa.

(2) Near the smooth surface there is a significant region of velocity profile, away from the corners, which accords with

the law of the wall. Thus as far as the mean flow properties are concerned, the fluid within this region is in local equilibrium in spite of dissimilar surface conditions. This fact is important for it means that in the rough-smooth duct, a traditional Clauser chart may be used to obtain the shear stress at the smooth surface. Near the corners, logarithmic variation of mean velocity is obeyed but with varying constants of the logarithmic law. This is due to the departure of flow from two-dimensionality in that region.

(3) The influence of the rough wall over the smooth wall is a minimum on the symmetry plane where velocity profiles diverge above the logarithmic line as in symmetric duct flow and, increases towards the side wall where due to its increased effect the smooth wall profiles fall below the logarithmic line.

(4) The main secondary vortex is situated near the smooth wall and a considerably weaker one near the rough wall. The influence of the main vortex on the distribution of both mean and turbulent properties of the duct is considerable.

(5) The distribution of wall shear stress is strongly influenced by the surface conditions of the surrounding walls.

4.4.2 Turbulent Flow Findings

(1) The dissimilar wall conditions impose a strong asymmetry upon the turbulent flow field, which is more pronounced than the asymmetry of the mean motion.

(2) Each wall dominated the turbulent structure in the nearby region. Hence, two major flow regions, with distinct distributions of the turbulence parameters, may be distinguised, being approximately separated by the plane of zero shear stress.

(3) The region governed by the rough surface, occupies a greater part of the duct area. In the major part of this region, the turbulence quantities are distributed evenly. Near the side wall the effect of secondary flow on its distribution is more pronounced. Turbulence quantities in this region are carried in the direction of secondary flow, towards the smooth wall.

(4) Near the symmetry plane, the flow region governed by the opposite smooth wall is extended upto the centre of the duct. The extent of its domination, however, diminishes sharply as the side wall is approached.

(5) A considerable portion of the duct core region is characterised by mutual influence and interaction between the walls of different character.

(6) The noncoincidence of the position of zero shear stress and maximum velocity results in a region of flow where the production of turbulent energy, $-\overline{u_1 u_3}\ \partial U_1/\partial x_3$, is negative; that is, there is an energy transfer from the turbulent flow field to the mean flow. This sink of turbulent energy is compensated by the strong diffusion in that region.

(7) The spectra of $\overline{u_1^2}$, measured closed to the rough wall, display a $K^{-5/3}$ variation over a considerable range of wave number space, covering about one decade and suggests that isotropic flow exists in that frequency range in spite of strong asymmetric boundary conditions.

C H A P T E R 5

MEASUREMENTS IN A SQUARE DUCT WITH TWO ROUGH WALLS

5.1 Introduction

The flow characteristics of a square duct with two opposite walls and two smooth walls may be expected to exhibit symmetric behaviour about the axes of symmetry of the corresponding walls. As in the previous measurements with one rough wall, the wall friction velocities of the respective walls are used as the characteristic velocity scale, and $\nu/U_{\tau s}$ and e (rib height) are used as the characteristic length scale in the regions close to the smooth and rough wall respectively. The centre line velocity and the hydraulic diameter of the duct are used to represent the flow characteristics of the whole cross sectional area of the duct.

In the previous duct the two opposite dissimilar flow regions advanced face to face and mutually interfered with a distinct zone of interaction and mixing while in the present duct the interaction of the dissimilar flow regions is more gradual. The interaction of dissimilar flow regions has different effects upon the mean and turbulent flow parameters. As a result, turbulent parameters of the flow exhibit different degrees of variation from the mean motion as found in symmetric flows.

5.2 Presentation of Measurements

In the present duct the measurements were taken at Reynolds number of 3.26×10^5, based on the hydraulic diameter (150 mm) and average velocity of the duct and the same variables were measured as in the previous measurements. The results are presented in the next section (section 5.2) in the same sequence as in section 4.2. In section 5.3, the results are discussed along with those of the previous measurements and of other

workers mentioned in the literature review. The discussion examines the change of flow characteristics near the rough wall and consequently throughout the entire duct cross sectional area due to the introduction of one more rough wall in the previous flow condition.

5.2.1 Mean Velocity Profiles and Contours

Figure 5.1 represents the mean velocity profiles at various distances from the smooth wall and indicates the velocity maxima. The profiles are all symmetric about the rough wall symmetry plane, $x_3/a = 0.5$. In the centre region of the duct, the velocity maximum occurs on the rough wall symmetry plane and as the smooth wall is approached, gradually shifts towards the rough wall and moves furthest from the symmetry plane at about $x_2/a = 0.15$; it then moves towards the symmetry plane again with further approach towards the smooth wall. The gradient of velocity profiles near the rough wall is large around the midplane of the rough wall ($x_2/a = 0.5$) where the influence of the smooth wall is least and, due to the increasing influence of the smooth wall, their value gradually decreases as the smooth wall is approached. The velocity profiles of figure 5.1 were used to calculate the bulk mean velocity of the duct by graphical integration as outlined in section 4.2.1 and yeilded a ratio of bulk mean velocity to duct centreline velocity of 0.724.

Figure 5.2 shows the velocity profiles plotted parallel to the rough wall. They were obtained by interpolating the points from figure 5.1. Additional measurements were taken near the smooth wall (from $x_2/a = 0.005$ to 0.0225) to determine the smooth wall shear stress distribution as accurately as possible from a Clauser chart plot. The effect of the secondary flow may also be deduced and shows that the secondary motion (figure 5.12) carries fluid of low momentum from the smooth wall towards the centre of the duct with reduction in axial velocity from that in the absence of secondary velocity there. On the mid plane of the smooth wall, the velocity gradient is steep near the wall, decreases sharply at about $x_2/a = 0.025$ and remains nearly constant for a considerable distance from about

x_2/a = 0.075 to 0.33. Away from the mid plane, the constant gradient range of the velocity profiles decreases quickly with distance from the wall and away from the mid plane of the smooth wall. Near the rough wall ($x_3/a \lesssim 0.2$), the profiles indicate a point of inflexion which moves towards the smooth wall as the profiles approach the rough wall. Near the point of inflexion the velocity gradient becomes zero or nearly zero; it then increases and again decreases to zero on the mid plane of the rough wall. This is due ot the influence of secondary velocity on the distribution of mean velocity. The contour of inflexion point is drawn in figure 5.12; in its vicinity, the secondary velocity carries high momentum fluid from the central region of the duct towards the rough wall resulting in the increase in velocity and hence the inflexion point in the mean velocity profiles.

To examine the behaviour of the mean velocity in the near wall region and consequently to calculate the wall shear stress, its distribution is replotted on Clauser chart co-ordinates ie, U_1/U_c Vs log $[U_c x_3/\nu$ or $U_c x_2/\nu]$. Profiles are plotted for both the rough and smooth wall on figures 5.3 and 5.4 respectively. They indicate that the variation of mean velocity is logarithmic near both walls but that, near the symmetry axes ($x_2/a = 0.5$, $x_3/a = 0.5$), the profiles tend to move above the logarithmic line as distance from the wall increases. As the profiles for both walls approach the corner ($x_3 = 0$, $x_2 = 0$), they tend below the logarithmic line due to the mutual influence of one wall over the other. The same phenomenon was reported by Ying (1971) and Fujita (1978). From the slopes of the profiles in figures 5.3 and 5.4 and the measured pressure gradient in the duct, the value of κ (eq. 2.24) was calculated by graphical integration as illustrated in section 4.2.1 and found to be 0.392. The value of B_s and B_R were then calculated to be 4.94 and 3.9 respectively. The universal log law equations 2.24 and 2.28 for smooth and rough wall respectively can thus be rewritten as

$$U_s^+ = \frac{1}{0.392} \ln x_2^+ + 4.94 \qquad \ldots (5.1)$$

$$U_R^+ = \frac{1}{0.392} \ln x_3/e + 3.9 \qquad \ldots (5.2)$$

With the known value of κ, the local friction velocity was calculated from the slope of the graphs (figures 5.3 and 5.4) and used to normalise the mean velocity U_1. The universal log law velocity profiles for the rough wall are thus plotted in figure 5.5. All the profiles other than those near the corner, collapse onto the logarithmic line after 2 rib heights. Profiles near the corner (for example x_2/a = 0.05 and 0.10) show a gradual increase of the value of the constant B_R in equation 2.28. Similarly, the universal log law velocity profiles near the smooth wall are plotted in figure 5.6 and are similar to the rough wall profiles except near the corner (x_3/a = 0.15 , 0.1 and 0.05) where a variation in the log law constants is required. Near the corner the variation of the constants in the log law is similar for both the walls, rough and smooth.

Contours of mean velocity, U_1/U_c are shown in figure 5.7 and are obtained from the mean velocity results of figure 5.1. They are more uniformly distributed near the rough wall than near the smooth wall. Near the rough wall the contours run nearly parallel to the wall and indicate little or no bulging towards the corner. This parallel property of the isovels extends beyond the diagonal indicating the greater influence of the rough wall over the flow area. Unlike the symmetric duct flows, the mean velocity contours show no bulging in the central region of the rough wall and instead, due to the influence of the U_3 component of secondary velocity (figure 5.11), the contours in this region shift towards the wall. For example, the isovel U_1/U_c = 0.8 occurs at x_3/a = 0.215 on x_2/a = 0.20 which on the symmetry plane (x_2/a = 0.5) shifts towards the rough wall occurring at x_3/a = 0.175. Contours near the smooth wall behave quite differently from those near the rough wall. In the central region of the smooth wall the isovels bulge away from the wall, as in symmetric duct flow, indicating the presence of secondary flow there. Due to the above facts of shifting the isovels towards the rough wall and bulging away from the smooth wall, some isovels occurs closer to the rough wall than the smooth wall in spite of the greater rough wall resistance. For

example, on the centre of the rough wall, the isovel of 0.875 occurs at $x_3/a = 0.23$ while that on the centre of the smooth wall occurs at $x_2/a = 0.25$.

5.2.2. Secondary Mean Velocity

As in the previous duct, yawmeters were used to measure the secondary flow angles and all measurements were recorded at the same Reynolds number and positions at which measurements of axial velocity were taken. Figures 5.8 and 5.9 show angles γ_2 and γ_3 with a maximum value of about 4.5^o and most in the region of 0.5^o. The larger angles were generally present near both the walls, rough and smooth, where the scatter is largest and of the order of $\pm$ 50%, away from the walls the scatter decreases to around $\pm$ 15%. To minimise the effect of scatter during the calculation of U_2 and U_3 from the equation 3.13, γ_2 and γ_3 in figures 5.8 and 5.9 were smoothed. The computer plot results of the vectors of U_2 and U_3 are presented in figures 5.10 and 5.11. In figure 5.11 half of the measurement points were ommitted to avoid overlapping of the vectors U_3. As illustrated in section 4.2.2 vectors U_2 and U_3 were combined to give the direction and magnitude of the secondary velocity U_{sec} and are shown in figure 5.12 where it is found that the maximum value of the secondary velocity in the entire flow field is less than 6% of U_c and the strong vortex near the smooth wall with its centre located at about $x_2/a = 0.13$ and $x_3/a = 0.36$. The presence of single vortex instead of two counter rotating vortices which are normally found in symmetric duct, influences the distribution of mean and turbulent flow properties differently from those of symmetric ducts. High values of secondary velocities are distributed around the vortex and near the walls, The magnitude of secondary velocity decreases towards the centre and reduces to a minimum there. The secondary velocity present in the flow field directs the fluid from the centre towards the corner, then upwards along the smooth wall and finally along the smooth wall midplane back towards the centre. The vortex near the smooth wall is responsible for the bulging of the mean velocity contours (figure 5.7) in that region.

The secondary velocity vectors near the corner direct more fluid towards the smooth wall than towards the corner which causes the bending of the isovels in figure 5.7 to be shifted above the diagonal. In figure 5.10 the distribution of the vector U_2 shows two distinct zones; one of positive U_2 (flow away from the smooth wall) and the other of negative U_2; the two zones are separated by a line at $x_3/a = 0.355$ running parallel to the x_2 - axis ie, from the rough wall upto $x_3/a = 0.355$ all flow due to U_2 are towards the smooth wall and from $x_3/a = 0.355$ upto the symmetry plane ($x_3/a = 0.5$) all flow due to U_2 is away from the wall, In figure 5.11 all positive U_3 (flow away from the rough wall) are found to be distributed near the smooth wall only while negative values of U_3 of comparatively smaller magnitude are distributed over the bulk of the flow.

5.2.3 Friction Factor and Wall Shear Stresses

The variation of friction factor, C_f, with Reynolds number is shown in figure 5.13. Friction factor was calculated from the axial pressuregradient of the duct, as illustrated in section 4.2.3. Figure 5.14, which became linear considerably upstream of the measuring station and, confirmed that the flow was fully developed. As in the previous measurements, the centre line velocity, U_c, was recorded for each Reynolds number and the bulk mean velocity, U_b, was assumed to be the same fraction of centre line velocity for all Reynolds number as calculated for Reynolds number of 3.26×10^5. In the range of Reynolds number of the present measurements the value of friction factor remains almost constant at a value of about 1.5×10^{-2}, which is higher than that obtained in the previous duct but below that of fully turbulent rough pipe flow.

The distribution of normalised wall shear stress is presented in figure 5.15, which shows that the rough wall shear stress increases from the corner towards the centre and reaches its maximum there. The smooth wall shear stress also increases from the corner towards the centre and reaches its maximum at about $x_3/a = 0.35$ before slowly decreasing towards the centre. The secondary velocity towards the wall increases the value of

the wall shear stress while that away from the wall tends to decrease its value. This fact can be observed by comparing the distribution of wall shear stress and secondary velocity in figures 5.15 and 5.12 respectively.

5.2.4 Contours of Turbulence Intensities

Figures 5.16 to 5.18 show the contours of normalized turbulence intensities $\tilde{u}_1/U_c$ and $\tilde{u}_2/U_c$ and $\tilde{u}_3/U_c$ respectively and were obtained as described in section 4.2.4. Experimental points are shown in figures A5.1 to A5.3. Figure A5.1 shows that the maximum scatter of the $\tilde{u}_1/U_c$ points near the rough wall was less than 3% of the local mean value and was even less near the centre of the duct. The quality of $\tilde{u}_2/U_c$ and $\tilde{u}_3/U_c$ results was good ($\simeq$ 4%) except near the walls where the scatter revealed 10% of the mean value. Figure 5.16 shows that the longitudinal turbulence intensity, $\tilde{u}_1/U_c$, reaches its maximum at about 2.35 rib heights (measured from the rib root) on the mid plane of the rough wall and then decreases gradually towards the centre maintaining the equally spaced distribution of the contours suggesting itsnearly constant gradient across the rough wall. Contours of $\tilde{u}_1/U_c$, run nearly parallel to the rough wall, when they approach the smooth wall, they are carried away from the rough wall in the direction of secondary velocities and spread along the smooth wall. In contrast to the rough wall, contours near the smooth wall are widely spaced and a small error in the measurement of $\tilde{u}_1/U_c$ in this region would shift the contours considerably. In figure 5.17 closed loop contours of $\tilde{u}_2/U_c$ extend over the entire rough wall region where on the symmetry plane $\tilde{u}_2/U_c$ reaches its maximum at about 3.8 rib heights and then decreases towards the centre. Near the mid-plane of the rough wall, the distribution of $\tilde{u}_2/U_c$ contours is fairly uniform. Close to the smooth wall, contours of $\tilde{u}_2/U_c$ are closely spaced. Away from the wall contours of $\tilde{u}_2/U_c$ are widely spaced as the contours of $\tilde{u}_1/U_c$. Near the rough wall $\tilde{u}_3/U_c$ contours in figure 5.18 also show a closed loop pattern which is confined in the central region of the wall. The maximum value of $\tilde{u}_3/U_c$ occurred at about 4.25 rib heights and unlike

$\tilde{u}_1/U_c$ and $\tilde{u}_2/U_c$, its maximum is shifted from the midplane of the rough wall to a value of around $x_2/a = 0.4$. In the central region of the rough wall, the variation of $\tilde{u}_3/U_c$ is much more gradual than those of $\tilde{u}_1/U_c$ and $\tilde{u}_2/U_c$. Close to the smooth wall another peak of $\tilde{u}_3/U_c$ of nearly equal magnitude to that near rough wall is also noticed. Elongated closed loop contours surrounding the peak cover most part of the smooth wall. In the rough wall region the order of magnitude of $\tilde{u}_2/U_c$ is nearly the same while that of $\tilde{u}_1/U_c$ is about 1.5 times higher. Close to the smooth wall the order of magnitude of $\tilde{u}_3/U_c$ is about 1.5 times that of $\tilde{u}_2/U_c$ (except near the corner where their magnitudes are nearly the same). Despite the different order of their magnitudes and different rate of variation in different wall regions of the duct, all the intensities emerge into nearly the same order of magnitude in the centre of the duct. This type of behaviour of turbulence intensities was reported earlier by many workers in boundary layer flows.

5.2.5 Reynolds Shear Stress and Kinetic Energy Contours

Contours of Reynolds shear stress $\overline{u_1 u_2}/U_c^2$ and $\overline{u_1 u_3}/U_c^2$, turbulence kinetic energy k/U_c^2 and the turbulence correlation, $(\overline{u_2^2} - \overline{u_3^2})/U_c^2$, are shown in figures 5.19 to 5.22 respectively. Data points for the above quantities are shown in figures A5.4 to A5.7. Close to the rough wall, the maximum scatter for $\overline{u_1 u_3}/U_c^2$ and k/U_c^2 is less than 10% of the mean value and in the central region of the duct is of the order of 4%. The scatter of data for $\overline{u_1 u_2}/U_c^2$ (figure A5.1) is around 40% near the rough wall and 5% near the centre. The scatter of the data for $(\overline{u_2^2}-\overline{u_3^2})/U_c^2$ (figure A5.7) is greatest with values of around 80% of mean value near the rough wall.

Contours of negative Reynolds shear stress, $\overline{u_1 u_2}/U_c^2$ (figure 5.19) are distributed almost uniformly in the region bounded by the zero contour line and the smooth wall. The positive shear stress of comparatively smaller magnitude is present in a small region close to the rough wall. Near the midplane of the rough wall the zone of positive shear stress extends towards the centre.

The zero shear stress contour moves from the centre towards the rough wall and along the wall towards the corner. Similarly most of the negative shear stress contours run from the smooth wall midplane towards the rough wall and then converge towards the corner, indicating its gradual variation (with respect to x_2 - axis) near the rough wall (except near the corner) comparing with its variation in other flow regions. Away from the corner, the contours near the smooth wall are diverted away by the secondary velocity, from the corner back towards the midplane of the smooth wall and thus form closed loop concentric contours centred around the maximum value which lies on the midplane of the smooth wall. Closed contours near the symmetry plane ($x_3/a = 0.5$) indicate a single hump in its variation across the smooth wall which gradually moves towards the wall ($x_2 = 0$) and finally disappears as the rough wall is approached.

Contours of $\overline{u_1 u_3}/U_c^2$ in figure 5.20 show a near equally spaced distribution throughout the rough wall region, indicating the linear variation of shear stress across the rough wall. The zone of constant gradient shear stress, $\overline{u_1 u_3}/U_c^2$, is largest near the midplane of the wall. Away from the midplane, the contours bulge towards the corner and the zone of constant gradient shear stress is reduced with the approach of the smooth wall. Close to the smooth wall the contours change their direction from towards the corner to away from it and spread along the smooth wall. Zero shear stress, $\overline{u_1 u_3}/U_c^2$, contours moves from the symmetry plane ($x_3/a = 0.5$) towards the rough wall and back towards the symmetry plane with progressive approach of the smooth wall. The zero shear stress contour divides the flow area into two zones of shear stress of opposite sign. Positive shear stress is present in a small area bounded by the zero shear stress contour and the midplane of the smooth wall, while the negative shear stress is distributed over the bulk of the remaining flow area.

The contours of turbulence kinetic energy, k/U_c^2, in figure 5.21, show a fairly uniform distribution over the entire flow area. The maximum value of turbulence kinetic energy occurs near the rough wall at about 3.3 rib heights and decreases gradually towards the centre.

Near the rough wall midplane, the contours of k/U_c^2 are equally spaced indicating its linear variation there and run parallel to the wall until the smooth wall is approached where they bulge towards the corner and finally are convected away by the secondary velocity along the smooth wall. Contours of k/U_c^2 near the smooth wall are more widely spaced compared with the distributions near the rough wall. The distribution of contours indicates that most of the turbulence kinetic energy is generated near the rough wall and some of it is carried away by the secondary velocity towards the smooth wall midplane. Near the centre, the distribution of turbulence kinetic energy is nearly symmetric in both the wall directions. For example, the contour of $k/U_c^2 \times 10^3 = 6$, meets the rough wall midplane at $x_3/a = 0.37$ and the smooth wall midplane at $x_2/a = 0.365$.

The distribution of contours of $(\overline{u_2^2}-\overline{u_3^2})/U_c^2$ is shown in figure 5.22. Contours of positive $(\overline{u_2^2}\overline{u_3^2})/U_c^2$ are enclosed by its zero value contours. Two small regions of positive value of $(\overline{u_2^2}-\overline{u_3^2})/U_c^2$ are located near the smooth wall, one near the corner and the other on its midplane. Traces of positive $(\overline{u_2^2}-\overline{u_3^3})/U_c^2$ are also noticed on the midplane of the rough wall. Contours of negative value of $(\overline{u_2^2}-\overline{u_3^2})/U_c^2$ are distributed over bulk of the flow area. Contours of high value of negative $(\overline{u_2^2}-\overline{u_3^2})/U_c^2$ are stretched along the smooth wall. In the major part of the flow region the difference between the normal stresses is much smaller compared with its magnitude near the walls and on the centre of the duct its value approaches to zero. Production of vorticity, $\frac{\partial^2}{\partial x_2\,\partial x_3}(\overline{u_2^2}-\overline{u_3^2})$, in the corner and smooth wall region is about 5 to 8 times higher than that in the other part of the duct, indicating the generation of secondary velocity in those regions.

5.2.6 Longitudinal Turbulence Spectra

In the previous measurements the distribution of longitudinal turbulence spectra was studied only near the rough wall and it was found that the spectral distributions were almost identical for various distance from the smooth wall. Thus in the present measurements the spectral distribution of $\overline{u_1^2}$ was

studied on the symmetry plane ($x_2/a = 0.5$) at various distance from the rough wall. The same method of transformation and normalization of spectra is used as in the results of section 4.2.6.

Figure 5.23 shows the distribution of normalized spectra of $\overline{u_1^2}$ as a function of wave number K_1 at various rough wall distances. In the vicinity of the wall the spectral curves show a characteristic shift towards the higher wave number as the rough wall is approached, a clear indication of the decrease of the scale of energy containing eddies with the approach of the wall. This is consistent with larger shear, caused by the presence of the ribs, destroying larger eddies. This shift is shown in figure 5.23 by redrawing spectra no. 2 with the same axes as spectra no. 1. Away from the wall ($0.16 \lesssim x_3/a \lesssim 0.3$), the curves collapse onto one which suggests a rather uniform longitudinal scale of eddies in that region. In the centre of the duct, the spectra again show a shift towards higher wave numbers indicating a decrease of the scale of energy containing eddies there. Spectra no. 1 and 2 show monotonic fall-off with the increase of wave number, indicating the absence of any predominant eddy structure in the region close to the wall. In contrast to this, spectra no. 3 to 6 show a small hump in the low wave number range of each of the curves. The hump indicates the presence comparatively large amount of energy containing eddies in that wave number range. In spite of the variation of the size of the energy containing eddies at different wall distance, all the spectral curves in the figure show $K^{-5/3}$ variation of $F(k_1)$ at higher wave number, indicating nearly isotropic condition in that frequency range. As the wave number becomes even larger, $F(k_1)$ decreases under the action of kinematic viscosity at a faster rate still. At very high values of wave number it should be (according to Heisenberg, 1948) observed that $F(k_1)$ varies as K^{-7}. K^{-7} variation of $F(k_1)$ at the highest measured values of K_1 is also found in the present measurement.

5.3 Discussion of the Results

In this discussion, the results are compared with those of other workers and attention is given to the change of

different flow characteristics in the present duct from those of the duct with one rough wall, thus, the influence of one wall over the flow characteristics of the other is assessed.

5.3.1 Mean Velocity Profiles and Contours

Figure 5.24 allows comparison of the present mean velocity profiles with Fujita's results for his duct with two opposite rough walls. On the midplane of the smooth wall ($x_3/a = 0.5$) Fujita's profiles show progressively higher value of U_1/U_c as the smooth wall is approached and away from the midplane, show progressively smaller values. These discrepancies are consistent with differences in the secondary velocities in the two ducts which will be discussed later in section 5.3.2. Isovel plotś of both sets of measurements are shown in figure 5.25a. From the bulging of Fujita's isovels, it can be deduced that two counter rotating vortices exist with the one near the rough wall influencing more flow area. In contrast, the present isovels show no bulging near the rough wall and, due to the U_3 velocity component, the isovels near the rough wall midplane occur much closer to the wall than those of Fujita. For example, on the midplane of the rough wall, the 0.8 isovel occurs at $x_3/a = 1.74$ in the present case and at $x_3/a = 2.07$ in Fujita's measurement. Near the smooth wall, however, the isovels of Fujita's measurement occur closer to the wall (smooth); for example the same isovel of 0.8 occurs on smooth wall midplane at $x_2/a = 0.1$ in Fujita's measurement and at $x_2/a = 0.16$ in the present measurements. Thus the vortex near the smooth wall is stronger in the present case. The same type of discrepancy between the present investigation and Fujita's work was also noticed in the measurement of section 4.3.1.

The ratio of the roughness height to duct hydraulic diameter (e/Dh) and the ratio of roughness height to pitch (e/p) were the same for Fujita and the present work but the shape of the roughness element which was round in Fujita's duct and square in present duct. In addition, Fujita's Reynolds number of 6.5×10^4 was significantly lower than the value of 3.3×10^5 used here. The differences in the two sets of results can,

therefore, be limited to the two experimental differences.

Figure 5.25b compares the present isovels with those of the duct with one rough wall. The distribution of the isovels near the rough wall remains nearly the same for both the ducts except in the fact that the present isovels occurs closer to the rough wall, this is consistent with larger shear caused by the opposite rough wall. In contrast to the rough wall, the distribution of isovels near the smooth wall differs considerably, where the bulging of the isovels of the present duct was not observed in the previous duct.

The mean velocity results allowed the determination of the Von Kárman constant, κ, which ranged from 0.385 to 0.392 and may be compared with values of 0.35 to 0.44 reported by other workers, før example Hinze (1962). Determination of κ depends on the precision of the slope of the charts which is around $\pm$ 5%. As in section 4.3.1 log law velocity profile for the rough wall is replotted in figure 5.26 with a new origin located at 0.15 rib height above the rib root as represented by the equation:

$$U_R^+ = \frac{1}{0.4} \ln (x_3/e - 0.15) + 3.9 \qquad (5.3)$$

Profiles in the figure collapse onto the logarithmic line from 1.9 rib height measured from the new origin. The shift of the new origin in this case is 40% less than the previous result. As regards the imaginary origin of the discrete rough surface no definite conclusion has not yet been made. From the experimental findings of the previous workers and the present measurements it seems that the position of the imaginary origin depends on the physical shape of the roughness elements and the surrounding boundary conditions which influence the flow.

5.3.2 Secondary Mean Velocity

In this section the nature of mass unbalance due to secondary velocity is analysed and, from that the possible error of yaw meter readings is deduced; the effect of Reynolds number on secondary velocity is also discussed.

In the present results the deviation from the mass balance due to secondary velocity increases as the walls are approached; for example at $x_2/a = 0.4$ (figure 5.10) mass flow due to U_2 is 1.1 times which increases to 5.4 times at $x_2/a = 0.05$, higher towards the wall than away from it, similarly at $x_3/a = 0.4$ (figure 5.11) mass flow towards the rough wall which is about the half than away from it, progressively increases as the wall is approached and near the wall nearly all the flow is towards it. From the analysis of the above mass balance and that of section 4.3.2, it seems that away from the wall yawmeters give reasonably good readings (comparing with the quality of data by previous workers discussed in section 4.3.2) but, near the wall they consistently give higher mass flow towards it. Yawmeter readings are greatly influenced by the pressure gradient of the flow field (discussed in section 3.3.3.2) which is greatest near the wall and that away from the wall decreases sharply. During measurements correction for pressure gradient has been applied. Apart from the pressure gradient yawmeter readings are also inluenced by the mutual interference of the wall and the probe and, that probably causes higher flow velocity towards the wall. In the present measurements no attempts have been made to make corrections for interference of the probe. Near the rough wall, however, secondary flow is influenced by the local effect of flow reattachment (discussed in section 7.3.2) indicating all flow towards the wall.

From the analysis of the isovels in sections 4.3.1 and 5.3.1 it was deduced that two vortices were present in Fufita's ducts, one near the smooth wall and other near the rough wall while, one stronger vortex was found near the smooth wall of the present work. The roughness ratio (e/D_h) of both the investigations was the same but the Reynolds number of the present work ($\sim 10^5$) was much higher than that used by Fujita ($\sim 10^4$). It seems from the above findings that with the increase of Reynolds number the vortex near the rough wall transfers towards the smooth wall resulting in a strong vortex there. At present, however, no such detailed measurements for secondary flow in asymmetric ducts, are available for comparison and to ascertain

the effect of Reynolds number on it. Even for symmetric ducts there is controversy about the effect of Reynolds number on the magnitude of secondary velocity. Brundrett and Baines (1964) and Hoagland (1960) reported that normalized secondary velocity, U_s/U_C is independent of Reynolds number while according to Gessener and Jones (1965) and Ying (1971) secondary current, U_s/U_C, decreases with increase in Reynolds number.

5.3.3 Friction Factor and Wall Shear Stresses

In this section, friction factor, C_f, and wall shear stress are compared with Fujita's results and the contribution of different wall shear stress to the total duct resistance is discussed and finally friction factors for asymmetric ducts are predicted.

Figure 5.13 shows that Fujita's curve for friction factor versus Reynolds number (for ducts with two rough walls) is almost coincident with the present result. For ducts with smooth and rough walls it is true that the more the number of rough walls, the larger the resistance to the mean flow. If C_{fs} and C_{fr} are assumed to be the friction factor for smooth and rough ducts respectively, then on the basis of proportionate contribution of each wall to the flow resistance, the friction of a duct with n rough wall and (4-n) smooth walls, can be expressed as

$$C_{fn} = \left\{(4-n)\ C_{fs} + n\ C_{fr}\right\}/4 \qquad \ldots\ (5.4)$$

To verify the above correlation the values of C_{fs} and C_{fn} are taken from Fujita's results and these are:

$$C_{fs} = 0.0765\ R_e^{-0.25} \qquad \ldots\ (5.5)$$

$$C_{fr} = 0.0314 \qquad \ldots\ (5.6)$$

Dashed lines in figure 5.13 represent the results calculated by equation 5.4 which are 18 to 30% higher than the experimental results.

Figure 5.27 compares the smooth wall shear stress with that of Fujita. The nature of distribution of wall shear stresses is nearly the same in both the measurements where shear stresses increase from the corner towards the centre and reach their maximum at about $x_3/a = 0.35$ and then gradually decrease, towards the centre. Fujita's measurements show higher value near the corner and lower near the centre. For comparison, the ratio of the mean wall shear stress of each wall to the total flow resistance of the duct with different number of rough wall surface is listed below in table 5.1 along with the values of Fujita's work.

TABLE 5.1

Ratio of mean wall shear stress to the total flow resistance of the duct

		Fujita Re= 9.5×10^4	Present meas. Re= 3.5×10^5
Si S_2 □ R	S_1	12.6%	9.32%
	S_2	11.5%	12.47%
	R	64.4%	65.8%
S □ R	S	7.7%	6.4%
	R	42.3%	43.6%
S R □	S	8.5%	-
	R	41.5%	-
S R_1 □ R_2	S	6.1%	-
	R_1	31.1%	-
	R_2		-

In the present measurements the percentage of rough wall shear stress becomes comparatively higher in table 5.1. This is inconsistent with Fujita's finding of increased rough wall shear stress with the increase of Reynolds number. It is clearly seen from the table that the degree of the contribution of a wall to the total flow resistance of a duct, considerably changes due to the variation of the surrounding walls, even though the wall in consideration is equally smooth or rough. Due to this different degree of contribution of the wall to the total flow resistance of the duct, equation 5.4 could predict friction factor only approximately. The error in equation 5.4 comes from the assumptions of $\bar{\tau}_s/\bar{\tau}_s^1 = 1$ and $\bar{\tau}_r/\bar{\tau}_r^1 = 1$ ($\bar{\tau}^1$ and $\bar{\tau}$ denotes average wall shear stress of symmetric and asymmetric ducts and subscripts s and r are for smooth and rough wall respectively) which are not suitable as seen from table 5.1. Based on the experimental facts two factors $a = \bar{\tau}_s/\bar{\tau}_s^1$ and $b = \bar{\tau}_r/\bar{\tau}_r^1$, are introduced in equation 5.4 and thereby improving the calculated values of C_{fn}. With the factors a and b equation 5.4 can be expressed as

$$C_{fn} = \left\{ a(4-n)C_{fs} + bnC_{fr} \right\} /4 \qquad \ldots (5.7)$$

The factors a and b are really functions of Reynolds number and the number and the arrangement of the rough walls, but they are here approximated by the function of n only. As approximate equations for a and b, the linear equation in terms of n

$$a = 1.0 + 0.036n \qquad \ldots (5.8)$$

$$b = 0.59 + 0.103n \qquad \ldots (5.9)$$

are proposed based on figure 5.28. The numerical constants in both the equations are chosen to satisfy the conditions that $a = 1.0$ for $n = 0$ and $b = 1.0$ for $n = 4$. In figure 5.28, $\bar{\tau}_s/\bar{\tau}_s^1$ and $\bar{\tau}_r/\bar{\tau}_r^1$ are plotted against the number of rough walls along with the results of Fujita. The curves in the figure reveals that in ducts with combination of rough-smooth surfaces, the smooth wall shear stresses increase above their all smooth values

while the rough wall shear stresses decrease from their all rough values and these variations are inversely proportional to the number of corresponding walls present in the duct. Chain lines in figure 5.13 represent the values of C_{fn} obtained from equation 5.7 and are within $\pm$ 5% of the experimental results, suggesting much improvement of equation 5.4. Though this method is derived from the results of discrete wall roughness gives a fairly good prediction when compared with the results of sand roughened ducts of Asano (1972).

5.3.4 Contours of Turbulence Intensities

In this section the distribution of turbulence intensities, $\tilde{u}_1/U_c$, $\tilde{u}_2/U_c$ and $\tilde{u}_3/U_c$, are mainly compared with the previous measurements and their sources of generation are assessed. For the purpose of comparison figures 4.17 to 4.19 and 5.16 to 5.18 are redrawn in figures 5.29b to 5.31 respectively.

Figure 5.29b shows that the opposite rough wall influences the distribution of $\tilde{u}_1/U_c$ in the same way as U_1/U_c (figure 5.25b) but more strongly. Near the rough wall, the magnitude and the nature of distribution of $\tilde{u}_1/U_c$ remains nearly the same except that their contours occur closer to the wall of the present duct, for example, $\tilde{u}_1/U_c \times 10^2 = 13$ contour occurs on the midplane of rough wall at $x_3/a = .15$ while that in the previous duct occurs at $x_3/a = 0.23$. Near the midplane of the smooth wall the distribution of $\tilde{u}_1/U_c$ is modified greatly from the previous results showing a gradual variation there. In figure 5.29a contours of $\tilde{u}_1/U_c$ are also compared with those of smooth duct results of Melling and Whitelaw (1976). In the smooth duct, the bulging of the contours covers nearly the whole wall area while that in the present duct is confined near the central region of the smooth wall where their values are about 10% higher than those of the smooth duct and in the rough wall region their values are about 80% higher.

Figures 5.30 and 5.31 show that near the rough wall the peaks of $\tilde{u}_2/U_c$ and $\tilde{u}_3/U_c$ shift their position and occur on the rough wall midplane of the present duct, but in the major part of the flow region their overall distributions remain nearly

the same. In the rough wall region the magnitudes of $\tilde{u}_2/U_c$ remain nearly unchanged while those of $\tilde{u}_3/U_c$ increase by about 17% which decrease gradually towards the centre of a minimum of 10%. Near the midplane of the smooth wall the distribution of $\tilde{u}_2/U_c$ is greatly modified showing more gradual variation there. Irrespective of the different rate of variation of their magnitudes near the walls, all the turbulence intensities near the centre are increased by about 10%.

In the present geometry generation terms for $\overline{u_1^2}/2$ and $\overline{u_2^2}/2$ and $\overline{u_3^2}/2$ are given by

$$G\left(\frac{\overline{u_1^2}}{2}\right) = -\overline{u_1^2}\frac{\partial U_1}{\partial x_1} - \overline{u_1 u_2}\frac{\partial U_1}{\partial x_2} - \overline{u_1 u_2}\frac{\partial U_1}{\partial x_3} \quad \ldots (5.8)$$

$$G\left(\frac{\overline{u_2^2}}{2}\right) = -\overline{u_1 u_2}\frac{\partial U_2}{\partial x_1} - \overline{u_2^2}\frac{\partial U_2}{\partial x_2} - \overline{u_2 u_3}\frac{\partial U_2}{\partial x_3} \quad \ldots (5.9)$$

$$G\left(\frac{\overline{u_3^2}}{2}\right) = -\overline{u_1 u_3}\frac{\partial U_3}{\partial x_1} - \overline{u_2 u_3}\frac{\partial U_3}{\partial x_2} - \overline{u_3^2}\frac{\partial U_3}{\partial x_3} \quad \ldots (5.10)$$

and are used here to correlate some of the observations presented for the normal stresses (ignoring pressure redistribution and turbulent diffusion). Positive values of $\partial U_1/\partial x_3$ and negative values of $\overline{u_1 u_3}$ over most of the rough wall region combine to produce fairly high levels of, generations of $\overline{u_1^2}/2$ there. Similarly close to the smooth wall, the term $\overline{u_1 u_2}\ \partial U_1/\partial x_2$ is responsible for the generation of $\overline{u_1^2}/2$ but of smaller magnitude. $\overline{u_2 u_3}$ was not determined in the experiment, but high negative values of $\partial U_2/\partial x_2$ and $\partial U_3/\partial x_3$ near the rough wall indicate the generation of $\overline{u_2^2}/2$ and $\overline{u_3^2}/2$ in that region. Near the smooth wall, high values of u_3/U_c and negative values $\partial U_3/\partial x_2$ suggest the presence of high positive values of $\overline{u_2 u_3}$ there.

5.3.5 Reynolds Shear Stress and Turbulence Kinetic Energy Contours

Nondimensionalised Reynolds shear stresses, $\overline{u_1 u_2}/U_c^2$, $\overline{u_1 u_3}/U_c^2$, turbulence kinetic energy, k/U_c^2 and $(\overline{u_2^2}-\overline{u_3^2})/U_c^2$ contours of the present duct are compared with those of the previous one

and for this figures 4.20 to 4.23 and 5.19 to 5.22 respectively are redrawn in figures 5.32 to 5.35.

Contours of $\overline{u_1 u_2}/U_c^2$, $\overline{u_1 u_3}/U_c^2$ and k/U_c^2 (figures 5.32 to 5.34) of both the ducts, show nearly the same type of distribution in most part of the duct flow area except near the central part of the smooth wall where they all differ from the previous distributions and, all contours of the present duct, are in general of higher magnitude and, more closely spaced indicating higher gradients across the walls. Near the rough wall of the present duct the average increase of the value of $\overline{u_1 u_2}/U_c^2$ and $\overline{u_1 u_3}/U_c^2$ and k/U_c^2 is about 35%, 20% and 12% respectively. Near the smooth wall midplane the values of $\overline{u_1 u_3}/U_c^2$ and k/U_c^2 remain nearly the same (except in the fact that there the distribution of $\overline{u_1 u_3}/U_c^2$ is changed providing a small space for its positive closed loop contours) while the magnitudes of $\overline{u_1 u_2}/U_c^2$ contours are greatly increased which is consistent with higher mean velocity gradients, $\partial U_1/\partial x_2$, of figure 5.2 as compared with those of figure 4.2. Contours of zero shear stress, $\overline{u_1 u_3}$, and velocity maxima (obtained from figure 5.1) in figure 5.33 show that they nearly coincide for major part of the duct but, near the smooth wall the later deviates from the former and occurs nearer to the rough wall. Hence in the present duct the zone of negative production of turbulence kinetic energy (discussed in section 4.3.5) is confined only close to the smooth wall. In contrast to the previous contours the distributions of $(\overline{u_2^2}-\overline{u_3^2})/U_c^2$ contours (figure 5.34) of the present duct are different in most part of the flow area except close to the smooth wall where they spread along the wall for both the ducts. In the previous duct, only positive values of $(\overline{u_2^2}-\overline{u_3^2})/U_c^2$ are present near the rough wall where its both positive and negative values are present in the present duct and more flow area is occupied by the contours of negative $(\overline{u_2^2}-\overline{u_3^2})/U_c^2$.

5.3.6 Longitudinal Turbulence Spectra

On the midplane of the rough wall the spectra of $\overline{u_1^2}$ are compared with those in the previous duct and integral length scales are deduced.

For the purpose of comparison spectra No 1 and 4 of figure 4.24 are redrawn in figure 5.36 with spectra No 1 and 2 of figure 5.23. Figure 5.36 shows that, at $x_3/a = 0.4$ spectra of both the ducts are nearly identical but at $x_3/a = .08$, spectra of the previous duct shows higher values at the low frequency range but at higher frequency range spectra of both the ducts become almost identical. As most of the Reynolds stresses are associated with larger eddies, higher values of $\overline{u_1^2}$ spectra at low wave numbers indicate higher normal stress in that region of the previous duct. In figure 5.29b at $x_3/a = 0.5$ and $x_3/a = .08$ ie, at the place where spectra measurements were taken, higher value of $\tilde{u}_1/U_c$ is noticed in the previous duct. Some spectra (spectra No 3 to 6) in figure 5.23 show a maximum at 5 wave numbers which corresponds to frequency of about 20Hz. In Crabb and Whitelaw's (1977) work of flow over two-dimensional rib, maximum of this nature was also observed in their spectra but at higher frequency of about 200Hz.

From the horizontal asymptote of the spectra, $F_{11}(K_1)$, at low wave numbers, some estimates of the longitudinal integral scales can be made from the transformation

$$L_1 = \frac{\pi}{2} \lim_{K_1 \to 0} \frac{F_{11}(K_1)}{\overline{u_1^2}} \qquad \ldots (5.11)$$

The results obtained from the above transformation are plotted in figure 5.37 where integral scales are nondimensionalised by duct hydraulic diameter. The integral scales show the gradual increase of its value away from the wall and remain nearly constant between $0.2 \lesssim x_3/a \lesssim 0.4$ and then decreases gradually towards the centre, indicating the presence of larger eddies in between the wall and the centre.

5.4. Summary Conclusions

The measured results in a duct with two rough walls have been presented and discussed in sections 5.2 and 5.3. Summary conclusions are presented below:

5.4.1 Mean Flow Findings

(1) Near the rough and smooth walls, nearly all the mean velocity profiles collapse onto a single logarithmic line. Near the corners, however, the profiles show logarithmic variation but with increasing values of constant B of the log law equation as happened in the flow of Chapter 4.

(2) The influence of the opposite wall on the log law profile of the rough wall is significant in that the change of opposite wall from smooth to rough causes a vertical shift of the logarithmic curves with increasing value of B_R in equation 2.28 from 3.3 to 4.5.

(3) As in the previous duct the influence of one wall over the profiles at the opposite walls is smallest near the symmetry planes, and increases progressively towards the corners.

(4) Measurements show that the wall shear stress of a smooth surface is increased in the presence of a rough surface while that of the rough is reduced in the presence of the smooth. These results confirm that the flow structure in each zone is different from what it is in a passage with the relevant single roughness on the complete surface.

(5) Both with two and one rough wall, strong secondary flow vortices were observed near the smooth wall while only traces of vortices were detected near the rough wall. It seems that, at high Reynolds number ($R_e = 3.4 \times 10^5$), secondary flow is suppressed in the rough wall region. At the lower Reynolds number ($R_e = 6.4 \times 10^4$) of Fujita, vortices do appear to exist near the rough wall.

(6) The nature of the isovels near the rough wall is only slightly influenced by the surface condition of the opposite wall while that in the smooth wall region changes considerably.

Near the smooth wall bulging of the isovels is prominent in the present flow but not with single rough wall.

5.4.2 Turbulent Flow Findings

(1) The effect of dissimilar wall conditions on the distribution of turbulent flow characteristics is much more pronounced than on the mean flow properties.

(2) The turbulent flow field can be divided into the four regions indicated below which are influenced to different extents by the change of wall conditions.

(a) The change influenced by the rough walls comprises about 60% of the flow area where in general, the distributions of turbulence intensities, Reynolds shear stresses and turbulent kinetic energy, remain nearly the same and their magnitudes increase (12%-35%) with the exception of $\tilde{u}_1/U_c$ whose values decrease there.

(b) In contrast to the rough wall, distribution of turbulence quantities ($\tilde{u}_1/U_c$, $\tilde{u}_2/U_c$, $\overline{u_1 u_3}/U_c$ etc) near the smooth wall is greatly modified but their values are only slightly increased (5% to 10%).

(c) In spite of the different degree of variation for different turbulence quantities in the above two regions, their distribution near the corner remains nearly the same, as all the contours converge or tend to converge towards the corners.

(d) Near the centre the change is smallest where all the turbulence quantities are increased by about 10%.

(3) The position of maximum velocity and zero shear stress, $\overline{u_1 u_3}$ coincide each other for most of the duct flow area in contrast to the previous measurements where velocity maxima always occurred closer to the rough wall than the zero shear stress. In the present duct, noncoincidence of velocity maxima and zero shear stress occurs only in a small zone close to the smooth wall.

(4) Spectra measurements of $\overline{u_1^2}$ reveal that a smaller number of large eddies are present near the rough wall of the present flow, confirming the lower value of $\tilde{u}_1/U_c$ stated in 2(a).

However, at higher frequencies the spectra display a $K^{-5/3}$ variation indicating isotropy in that frquency range as observed in one rough wall flow.

C H A P T E R 6

CALCULATIONS

6.1 Introduction

This chapter presents the results calculated for fully developed turbulent flows in rough-smooth and smooth square ducts which may be compared with the measurements and calculations of previous investigations of smooth ducts discussed in chapter 1. The two-equation (k-ε) turbulence model was employed in the calculation method in conjunction with an algebraic stress model similar to that of Gessner and Jones (1976) and Tatchell (1975) and presented in chapter 2.

The study had two main objectives. First, the evaluation of the two-equation model and the solution procedure of chapter 2, for comparatively simple and well-documented turbulent flow situations of symmetric ducts as described in chapter 1 and secondly, the test of the model in the further complex flow field to include the asymmetric flow situation with strong secondary vortex as observed in chapters 4 and 5. From the analysis of the results of both symmetric and asymmetric ducts the generality of the model is assessed, the causes of error are evaluated and possible methods of improvement are suggested.

6.2 Presentation and Discussion of the Results

In view of the above objectives, the different flow parameters of all the three ducts, such as mean axial and secondary velocities, wall shear stress and Reynolds shear stresses, are presented in different sections in the squence: smooth duct, duct with two rough walls and duct with one rough wall and from the comparison with the respective duct measurements the success and limitations of the two-equation model are evaluated at the end of the chapter.

6.2.1 Axial Mean Velocity Contours

Figure 6.1a shows the calculated contours of axial mean velocity in smooth square ducts and also the measurements of Melling and Whitelaw (1976) and Brundrett and Baines (1964). The calculated contours of U_1/U_c show convergence towards the corner, in general agreement with the measurements. They are, however, closer to the walls than the measured ones and this is due to the higher velcocity gradients predicted near the walls. The calculations were made at a higher Reynolds number (3.66×10^5) than the measurements ($\simeq 10^4$) and this difference is, at least in part, responsible for the discrepancies. The calculated contours are closer to those of Brundrett and Baines ($Re = 8.3 \times 10^4$) than those of Melling and Whitelaw (4.2×10^4) because of the closeness of Reynolds numbers. In the measurements of Melling and Whitelaw symmetry of the isovels was checked and found to be satisfactory; in the calculation, the symmetry condition was imposed. In figure 6.1b, a similar comparison is made with the prediction of Launder and Ying (1973) and Naot et al (1974). The present contours of U_1/U_c are closely similar to those of Launder and Ying in most respects. The algebraic stress models of both solution methods were based on the same reasoning; the main difference was that the length scale was obtained here by solving the modelled equation for ε, whereas it was prescribed algebraically by Launder and Ying. The advantages of the use of the two-equation model for fully developed symmetric flows are, therefore, small. The predicted U_1/U_c contours of Naot et al (1974) occur much closer to the walls and diverge more towards the corner than the present contours. Compared with the experimental results of Brundrett and Baines, the present results are in better agreement than those of Naot et al where nine equations were solved simultaneously. Thus it is seen that if properly simulated, the comparatively simple stress models can give better results with greater economy.

Contours of axial mean velocity, U_1/U_c, are shown in figure 6.2, for flows in the square duct with two opposite rough walls and can be compared with the measurements presented

in section 5.2.1. The isovels are seen to be very similar in the rough wall octant of the duct, where they are nearly coincident or run close to each other. Isovels in this octant show no bulging towards the corner, instead, they occur closer to the rough wall as the symmetry plane ($x_2/a= 0.5$) is approached and thereby indicate the influence of U_3 component of secondary velocity (figure 6.5) on their distribution. The smooth wall octant of the duct shows discrepancies between the two isovels. On the midplane of the smooth wall, the measured isovels bulge away from the wall while the calculated ones show no bulging and occur closer to the wall. This is due to the under prediction of secondary velocity in that region.

In figure 6.3, the calculated isovels of the duct with one rough wall, are compared with the measurements of section 4.2.1, and show, in general, greater asymmetry due to the rough wall than the experimental results. On the symmetry plane, the maximum of U_1/U_c occurs at $x_2/a= 0.75$ which in the experiment occurs close to the duct centre. In the rough wall quadrant of the duct, the bulging of the calculated isovels is prominent as against no bulging of the measured results and this difference is in accordance with the distribution of secondary velocity (figure 6.6). Near the smooth walls ($x_2= 0$ and $x_3= a$) the calculated isovels occur closer to the walls and show higher velocity gradients than the measured isovels. Higher velocity gradients near the smooth wall of this duct and the duct with two rough walls indicate higher smooth wall shear stress which has been predicted (figures 6.8 and 6.9).

6.2.2 Secondary Mean Velocity

In figure 6.4, the secondary velocity vectors calculated for flows in smooth ducts, are compared with the measurements of Brundrett and Baines (1964). The figure shows good agreement between the two results which show two identical counter-rotating voritices in the duct quadrant, directing fluid towards the corner, and along the walls and finally along the symmetry planes back towards the duct centre. The measurements of Brundrett and Baines show that the maximum secondary velocity is about 1.4% of duct centreline velocity, U_c, while that in

the calculation is found to be about 1%. In similar measurements, Melling and Whitelaw (1976) found the maximum of U_s/U_c to be about 1.25%. In spite of the underprediction, the secondary velocities show higher values near the symmetry axes and their direction indicate the transfer of more fluid towards the duct centre than the experiments of both Brundrett and Baines and Melling and Whitelaw.

Figure 6.5 compares the secondary velocity vectors of the calculations and measurements of the square duct with two rough walls. In the figure the calculated vectors confirm overall agreement with the measurements as both the vector plots show a single clockwise rotation (except in the corner, where the calculation shows a localized vortex). There are, however, some differences in the magnitudes and location of the vortex. The magnitudes of the calculated secondary velocities are on the average 40% of the measurements and the centre of the vortex is located nearly on the diagonal of the duct and spread nearly all over the quadrant of the duct. In the experiment the vortex is located near the smooth wall and its influence, in contrast to the calculation, diminishes towards the rough wall midplane where the measured magnitudes are lower than the calculated ones. Near the rough wall, minimum values of secondary velocities are obtained from the calculation but their highest values are recorded in the measurements. The reasons for the high values of secondary velocities are discussed in the next paragraph.

In figure 6.6, the vector plots of the secondary velocity in the duct with one rough wall show, two counter-rotating vortices in each quadrant of the duct. On the average the predicted secondary velocities are about 50% of the measured values. The measured secondary velocities are greatest near the top smooth wall (x_3 = a) where their calculated values are smallest. Near the symmetry plane, measured vectors are always directed towards the rough wall while the calculated vectors direct towards the centre from the two (rough and smooth) opposite walls. These differences in their distribution are reflected on the distribution of the isovels discussed in section 6.2.1. Near the rough wall of both the asymmetric ducts measurements show flow towards the rough wall only, without indicating

any flow away from it until x_3/a= 0.15, but in the calculation no such flow is obtained. Though measurements in this region are affected by the high level of turbulence and probe interference, repeated observations confirmed the flow towards the wall. Measurements were taken in between the ribs. Experiments by other workers, for example, Mantle (1966), on discrete rough surfaces similar to the present roughness showed that reattachment of the flow takes place at about 7 rib heights downstream the rib. This local effect of flow reattachment was not considered in the calculation except the general roughness parameter which was introduced in the calculation through the law of the rough wall. Hence no such secondary flow, directing only towards the rough wall, should be expected in the calculation and has been obtained.

6.2.3 Distribution of Wall Shear Stress

The calculated distribution of wall shear stress of the smooth duct is compared with the measurements of Fujita (1978) and Brundrett and Burroughs (1967) in figure 6.7. The figure shows the qualitative agreement with the curves increasing from the corner towards the symmetry plane, reaching their maxima about midway between the corner and the midplane and decreasing gradually towards the centre. Near the corner, the wall shear stress is underpredicted by about 10% and near the centre is overpredicted by 4%.

In the duct with two rough walls, the values of calculated smooth wall shear stress in figure 6.8, is about 80% higher than the measured values and those of the rough wall are around 14% lower. Near the rough wall, the calculated secondary velocity (figure 6.5) is reduced to a minimum creating a condition similar to laminar flow and thus the rough wall shear stress instead of being uniform in the central part of the wall as seen in the measurements, increases uniformly upto the centre of the wall.

As in the two rough wall duct, smooth wall shear stresses in one rough wall duct are overpredicted, as shown in figure 6.9. Local wall shear stress profiles of the top smooth

wall (x_3= a) show that the calculated values are about twice the measured values and those of the side wall(x_2 = 0) are about 30% higher. Despite higher predictions, the distributions of smooth wall shear stresses are, in general, in accord with the experimental data. Predicted results show that rough wall shear stress increases sharply near the corner and after reaching its maximum at about x_2/a = 0.2 gradually decreases towards the centre of the wall. Measurements of rough wall shear stresses of both the rough ducts show the similar distribution i.e, they increase from the corner nearly at the same rate and exhibit plateaus extending over the central half of the duct wall, but the distributions of their calculated values differ between the two rough ducts and this is linked with the predicted distribution of secondary velocity near the rough wall of the respective ducts (figures 6.5 and 6.6). The average wall shear stress of the double and single rough wall duct were predicted to be 13% and 16% lower than the respective duct measurements but that for the smooth duct was accurate within ±1% of the experimental results of Melling and Whitelaw (1976).

6.2.4 Reynolds Shear Stress and Turbulence Kinetic Energy Contours

Figures 6.10 and 6.11 present the predicted contours of Reynolds shear stresses, $\overline{u_1 u_2}$ and $\overline{u_1 u_3}$, for flows in a smooth square duct and compare them with the measurements of Melling and Whitelaw (1976). The distribution of the contours of both stresses are in good agreement with the measurements but tend to be underpredicted. The open contours, which occupy the greater part of the flow area, were underpredicted by 20% while closed ones by about 50% in spite of higher Reynolds number (3.66×10^5 as against 4.2×10^4 of Melling and Whitelaw) used in the calculation. Contours of turbulence kinetic energy, k, of the smooth duct are compared in figure 6.12a with the experimental results of Melling and Whitelaw (1976) and Brundrett and Baines (1964). Measured and calculated contours of k are similar in their distribution, as they all bulge towards the corner, although the predicted values of k are around 50% of the experimental results. Figure 6.12b compares the present

contours with calculations of Launder and Ying (1973) and Naot et al (1974). The present contours are of the same order of magnitude of those of Launder and Ying who show more bulging, similar to the measurements of Melling and Whitelaw of figure 6.12a. The calculated turbulence kinetic energy contours of Naot et al show least bulging although their magnitudes are 30% higher than the other two predictions presented in the figure.

Calculated contours of the Reynolds shear stress, $\overline{u_1 u_2}$, of the duct with two rough walls, are presented in figure 6.13 and compared with the measurements of section 5.2.5. For the major part of the flow area all the contours run nearly parallel to the smooth wall and finally converge towards the corner. The contour of zero $\overline{u_1 u_2}$, lies mainly on the midplane of the rough wall, satisfying the symmetry condition, close to the rough wall, however, it deviates from the midplane and runs very close to the rough wall which is practically not feasible, because according to figure 6.13, zero contour lies below the rib crest and this happened in the calculation because of the fact stated at the end of section 6.2.2. Near the rough wall the magnitudes of predicted shear stress, $\overline{u_1 u_2}$ are of the same order of the measured ones while those near the smooth wall are 30% lower. In the smooth wall octant of the duct, the measurements show closed contours of $\overline{u_1 u_2}$ indicating a hump in its variation across the smooth wall, and the calculations show nearly parallel contours, indicating its gradual decrease across the wall. Comparing with the $\overline{u_1 u_2}$ contours, $\overline{u_1 u_3}$ contours in figure 6.14 show better agreement with the measurements. In the rough wall octant of the duct, contours of both the results are nearly identical in magnitude and distribution. In the smooth wall octant of the duct the predictions show the convergence of all the contours towards the corner while measured contours are diverted away and spread along the smooth wall. A zero $\overline{u_1 u_3}$ contour is predicted to occur on the symmetry plane (except near the wall) while measurements show its clear deviation from the symmetry plane towards the rough wall and thus providing a zone of positive shear stress, $\overline{u_1 u_3}$, which in the calculation is found to be almost nonexistent. As with the Reynolds shear stress

contours figure 6.15 allows comparison for the contours of turbulence kinetic energy. Like the measurements, calculated contours run along the rough wall and converge towards the smooth wall. All over the flow regions the magnitudes of the calculated turbulence kinetic energy are nearly the same as those of the experimental results. However, some differences are noticed near the centre and the rough wall. Near the centre, the measurements show symmetric distribution of turbulence kinetic energy while calculations shows its asymmetry. Near the rough wall, measured contours show their peak at about 3.3 rib heights above the wall but the highest value of turbulence kinetic energy is predicted on the top of the rib.

Calculated contours of the Reynolds shear stresses, $\overline{u_1 u_2}$ and $\overline{u_1 u_3}$, of the duct with one rough wall, are compared in figures 6.16 and 6.17 with the corresponding measurements. Although, direct comparison of the above two stresses is inappropriate, their contours are in qualitative agreement particularly near the walls parallelto the planes of the respective stresses. Near the side wall ($x_2 = 0$) $\overline{u_1 u_2}$ contours of both the results spread along the wall where their magnitudes are nearly the same. Discrepancies are prominent near the symmetry plane ($x_2/a = 0.5$) and these are in consistence with the distribution of mean velocity of the respective results as can be seen by comparing figures 6.3 and 6.16. Figure 6.17 shows a fair agreement of the calculated shear stress, $\overline{u_1 u_3}$, with the measurements. As in $\overline{u_1 u_2}$ contours, here again the differences are linked with those of the mean velocity distribution (figures 6.3 and 6.17). In the rough wall quadrant of the duct all the calculated contours run parallel to the rough wall and near the side wall converge towards the corner instead of bulging away from it as happened in the measurements. Positive values of shear stress, $\overline{u_1 u_3}$, occur near the top smooth wall ($x_3 = a$) and run nearly parallel to it. Near the rough wall, the predicted values of shear stress, $\overline{u_1 u_3}$, are about 1.5 times higher than the measured values while those near the smooth wall are about double. A similar comparison is made in figure 6.18 for turbulence kinetic energy. Near the rough wall the calculated contours are about 15% higher and they spread along the rough wall and finally with

the approach of the side wall converge towards the rough wall corner. On the symmetry plane the gradient (in the direction perpendicular to the rough wall) of turbulence kinetic energy is lower than the measurements as the contours spread over more flow area. Near the side wall, the influence of secondary flow on the distribution of kinetic energy as found in the measurements, is not at all revealed in the calculation. Calculated contours of $\overline{u_1 u_3}$ and k show that the zone of influence of the rough wall is about two-third the duct flow area while their measured counterparts show that the zone is little over half the duct flow area and this extension of rough wall zone is confined only near the side wall.

6.3 Summary

It has been seen in the previous section that the calculation procedure of chapter 2 has gained success in predicting turbulent flows in square ducts, to a degree proportional to the symmetry conditions of the flow and that has been demonstrated by the agreement between the measured and calculated velocity field of the respective ducts. The results of section 6.2 are summarized in three parts: firstly the achievements and limitations of the present calculation procedure is evaluated, secondly sources of errors are analysed and finally possible methods of improving the present calculation procedure are discussed.

6.3.1 Achievements and Limitations

The results discussed in section 6.2 clearly reveals that the present algebraic stress model and solution method has achieved success in predicting flows in symmetric square ducts but its predicting capability decreased with the increase in asymmetry of the flow. The results of the smooth duct are in excellent agreement with the measurements. A sensitive test, however, is the prediction of two similar counter rotating vortices of secondary velocity spreading over the octants of the duct and that has been achieved with reasonable accuracy. Agreement on other flow parameters such as mean velocity, Reynolds stress etc is also good. In the duct with two rough walls, the

agreement in the rough wall octant is good but discrepancies occur in the smooth wall octant where the two different flow fields interact. In spite of the discrepancies in the zone of interaction, the nature of distribution of the flow properties is, in general, the same as the experimental findings and the outcome is encouraging. In the duct with one rough wall, the prediction shows much greater asymmetry than the measurements and two counter rotating vortices of secondary velocity have been predicted instead of the one found in the measurements. In the measurements, the influence of secondary velocity on the distribution of different flow properties, such as, U_1, $\tilde{u}_1$, $\overline{u_1 u_2}$ etc, is found to be prominent particularly near the smooth walls and that in the calculation is almost non-existent.

6.3.2 Sources of Error

From the discussion of section 6.2 it is found that the discrepancies generally occur in the asymmetric part of the flow and are due to the limitations of the algebraic stress model in a significantly asymmetric flow. In the calculation, flow was assumed two-dimensional which was not true near the rough wall where it varied from rib to rib and was strictly three-dimensional symmetric cyclic flow. In the algebraic stress model the neglect of the transport effect of convection and diffusion of the stresses was reasonable for symmetric smooth duct flows where secondary velocities rarely exceed 1% of maximum mean velocity but in asymmetric duct flows where secondary velocities are in the range of 3-5%, the above mentioned effects were significant and the neglect of those terms caused inaccuracies in the calculations. In a asymmetric flow, the zone of interaction of the two dissimilar flow fields results in strong diffusion (discussed in section 4.3.5) and non-coincidence of zero shear stress and zero velocity gradient (figures 4.33 and 5.20) and these facts were not considered in the present calculation scheme. Thus in rough-smooth ducts, the effect of rough wall on the entire flow field is unlikely to be fully accounted for in the prediction by simply replacing the smooth wall log law by the rough wall log law in the wall functions as was done in the present prediction. Further, log law equations used in the calculations, were true only near the central region of the walls, near the corners, they

vary considerably (as can be seen from figures 4.6, 4.7, 5.5 and 5.6). Thus in the calculations wall functions were also not prescribed properly.

Apart from the inadequate prescription of the present model for asymmetric flows, the discrepancies of the predictions were also due to the numerical constants used in the calculation procedure. In the past, different workers used different numerical constants in order to fit their predictions with certain flow geometry amongst them are the various turbulent Prandtl/Schmidt number and other constants depending on the algebraic relations used in the calculation. All sources indicate that turbulent Prandtl/Schmidt numbers are of the order of unity: nonetheless, specific estimates differ considerably: values ranging from 0.5 to 2.0 have been suggested and used. In deed, these may even be functions of various flow parameters and not constants as is generally assumed.

In the present calculation methods tests were carried out with 12 x 12 and 16 x 16 staggered grids for the smooth duct and showed very little difference; the predicted values of friction factor and mean velocity differed by less than 1% between the two cases. For rough smooth ducts, however, no such test for grid independence were performed and the same grid spacings of the smooth duct (12 x 12 for a quadrant and 12 x 22 for a half section) were used. Grid independence tests for the smooth duct may be insufficient for rough smooth duct where in the smooth wall region, in spite of higher velocity gradient, interaction of two dissimilar flows makes the flow field more complex, requiring finer grids (compared with symmetric ducts) which were not provided in the present calculation method. The use of relatively coarse grids near the smooth walls of the rough-smooth ducts smeared the kinks of the mean velocity profiles as found in the measurements (figure 4.1). For comparison a representative profile is shown in figure 6.19. In the calculation of Ying's (1971) rough duct, the decrease of the value of B_R in equation 2.28 resulted in the increase of the secondary velocity towards the corner. In the present calculation scheme such test was carried out for smooth duct and results were found to be insensitive to the value of B_s and no test was made for the rough wall.

Thus the sources of discrepancy, for asymmetric flows in particular, lie both in algebraic stress model and the numerical scheme.

6.3.3 Possible Methods of Improvement

From the analysis of the sources of error in the present calculation scheme it is clear that improvements are necessary. The algebraic equations of Reynolds shear stress used in the present model should be extended to take into account of the 'residual' stresses occured due to the noncoincidence of zero shear stress and zero velocity gradient as discussed in section 7.6. In order to do this, provision should be made in the calculation scheme to change the existing shear stress equations to the form of equation 7.7 near the zero or near zero velocity gradient zone where the 'residual' stresses occur or to use Launder's (1968) model. Launder (1968) proposed a second order mixing length model of Prandtl by taking into account the gradient of length scale. Applied to the transport momentum, the relationship may be written in terms:

$$-\rho\overline{u_1 u_3} = C_c \mu_t \left[\frac{\partial U_1}{\partial x_3} + C_a \ell \frac{\partial \ell}{\partial x_3} \frac{\partial^2 U_1}{\partial x_3^2} \right] \quad \ldots (6.1)$$

and is similar form of equation 7.7. Here C_c and C_a are constants and ℓ is the length scale to be prescribed. Use of the above equation in the asymmetric plane channel of Hanjalic (1970) brought about some anamolies due to the fact that the contribution of the second order term in the above equation was large near the walls where it was not desired, while it was small in the central region where its effect was needed. This deficiency could perhaps be overcome by specifying different length scale distribution and may be used in the present flow situation. Alternatively which is more involved, is by retaining the con vective and diffusive terms of the Reynolds stresses, their transport equations may be modelled for high Reynolds number

according to Hanjalic and Launder (1972b) and solved with the other equations. Further, numerical constants used in the turbulence model are based on the smooth walls and a more careful examinations is necessary for the rough walls. The provision of more grid lines particularly near the walls is expected to result in better accuracy of the prediction.

C H A P T E R 7

GENERAL DISCUSSION

7.1 Introduction

The background and objectives of the present research programme have been discussed in the introductory chapter of the thesis. The scope of this chapter is to describe the areas of importance of the present work and some important aspects of asymmetric flow and discrete rough wall. In a rough-smooth duct assembly, the character of the rough wall, such as the physical shape, the arrangements and density of the roughness elements, greatly influences the flow field in its own region as well as the flow regions of the other wall and consequently determines the whole flow structure of the duct. In the past different types of roughness elements were used as the roughness parameter and their influences on the flow were studied. In this chapter, discussion is limited to aspects of small ($e/D_h \leq 10^{-1}$) rib-type roughness as used in the present experiments. The discussion also includes the general flow characteristics arising from the interaction of the different flow regions and the change of the secondary velocity field from that of the symmetric duct.

7.2 Present Work: Its Areas of Importance

The problem of achieving very high rates of heat transfer or conversely very low rates of heat transfer at low cost, is the aim of large proportion of engineering heat or mass-transfer problem in turbulent flow. When the aim is to disminish heat exchange, the flow is usually of the thin-shear layer type over the majority of the region of interest, as for example, the external cooling of gas turbine blades by the injection of relatively cool by pass air through slots or holes in the blade inclined at a small angle with the surface. The majority of engineering problems of heat-transfer in turbulent flow, however,

may be linked with the aim of promoting heat transfer-heat exchanger in the widest sense. In these cases, a variety of complicating features may be present. Particularly on the gas stream side of a heat exchanger, it may be desirable to create flow separation to raise the level of effective thermal conductivity of the gas near the wall. Alternatively, vortex motion may be imparted to ducted flow with the two-fold aim of raising the overall level of heat-transfer coefficient and of promoting more uniform distribution of heat transfer. The insertion of twisted tapes or coiling or bending of flow passages are methods that are commonly used to induce strong secondary motions in flow stream. Even where the flow is predominantly parallel to the duct axis, weak (comparing with the induced motions mentioned above) secondary motions will nearly always be present as a result of the anisotropic turbulent stress field. Although, these velocities rarely exceed 5% of the axial mean velocity (figures 6.4 to 6.6)), they affect the flow structure as a whole and consequently the pattern of heat transport. Selective roughening of the duct walls is the common method of promoting turbulence and thereby increasing the heat transfer capability of the surface but admits more complex flow structure, as seen in the present work and previous works of Humphrey and Whitelaw (1979), Fujita (1978), and Hanjalic and Launder (1979a), for example.

7.3 Some Aspects of Discrete Rib-Roughness

7.3.1 Roughness Height

In a turbulent flow near the wall, turbulence is directly influenced by the character of the wall. For a smooth wall this effect occurs through the action of viscous stresses while, for a rough wall, through the action of forces resulting from the flow around the roughness elements, provided these elements project sufficiently beyond the viscous sublayer of the smooth wall. The thickness of the viscous sublayer is of the order of $x_2^+ = 5$. Outside this thin viscous sublayer inertial effects become increasingly important with respect to the viscous effects until, at a distance from the wall of approximately

x_2^+ = 40, the flow becomes fully turbulent with dominating inertial effects and negligible direct viscous effects on the main flow. Thus, the transition from the importance of viscous to inertial effects, takes place between $5 < x^+ < 40$ where viscous and turbulence inertial effects on the main flow are of the same order of magnitude; this region is known as the transition or buffer region. In view of the above flow properties near the smooth wall, it is clear that the surface is termed fully rough only when the heights of the roughness elements are of the order of x_2^+ =40 or more and that, in the flow situations of chapters 4 and 5, corresponds to less than one millimeter. The height of the roughness elements used in the experiment was 3.18 mm. In addition to the height of the roughness elements in relation to the laminar sublayer thickness, the effects of roughness on flows through ducts depend on its relative height with respect to the duct hydraulic diameter i.e, e/D_h, called relative roughness. For tightly space roughness elements, such as coarse sand grains glued on the surface, the single roughness parameter, e/D_h, can be used to express the nature of rough surface but for discrete rib type roughness the spacing between the ribs is most important other than the height of the ribs and discussed below.

7.3.2 Roughness Spacing

For a smooth surface, a significant part of the fluid resistance and heat transfer resistance occurs in the region near the wall. The thickness of the viscous sublayer and the molecular properties of the fluid determine the magnitude of resistances to the transport of heat and momentum. Conditions for a roughened surface are different, in that the high shear stress in the fluid is the result of form drag on the roughness elements. This form drag is evidently due to the generation, spreading and subsequent dissipation of vortices from the wake and separation zones behind each element which is the source of voriticty, and the longitudinal frequency with which such of vorticity occur is therefore of significance in controlling the turbulence structure and energy dissipation phenomena. This fact

strongly suggests that other than height, the longitudinal spacing of the roughness elements is the roughness dimension that is of greatest importance in rough duct flow and would thus offer the most likely basis of correlating friction loss data in such ducts. Thus the parameter involving the height and spacing of the roughness elements, i.e, their ratio, P/e, is most useful in describing the rough wall characteristics.

Realizing the fundamental significance of the pitch of the roughness element in the expenditure of flow energy; it thus, becomes apparent that three different types of flow phenomena may occur near the wall as shown in figure 7.1, and the type which occurs in a given situation will depend primarily on the value of pitch to height ratio, P/e.

If the wall roughness elements are spaced far apart (P/e >7), the individual elements will act as isolated bodies on which are exerted drag forces by the flowing fluid. The vortex behind each element are completely developed and dissipated at the reattachment point (generally seven rib heights behind the upstream rib) and grows in thickness before reaching the next element as shown in figure 7.1b. The apparent friction factor would, therefore, result from the form drag on the roughness elements in addition to the friction drag on the wall surface between the reattachment point and the next element.

The second type of flow results when the roughness elements are placed at a distance approximately equal to the vortex length, P/e ≃ 7 or less, as shown in figure 7.1c, so that the zones of separation and vortex generation associated with each element are not completely developed before the next element is encountered. This type of flow can termed wake interference flow where the friction drag of the wall is obliterated, and the entire region near the wall is replete with intense and complex vorticity and turbulent mixing.

Another type of flow results when the roughness elements are so close together that the flow essentially skims the crests of the roughness elements (figure 7.1d). In the grooves between the elements there will be regions of stagnation fluid containing stable vortices. The bulk of the flow will be over a pseudo-wall composed of roughness crest and the upper parts of

the groove vortices. This type of flow might be termed either quasi-smooth flow or skimming flow and this type of roughness is termed as 'd' type roughness. Much of the energy loss in such flow can probably be attributed to the maintanance of the groove vortices.

From the above discussion, it is clear that the roughness parameter, P/e used in the experiment falls into the first catagory where the flow reattachment takes place before encoutering the next rib. For the influence of other parameters of discrete rib type roughness, such as width, physical shape or helix angle of the roughness elements readers are referred to Wilkie (1966b) and Whitehead (1976).

7.4 Log Law of the Walls

The measurements of chapters 4 and 5 show the considerable influence of surroundings on the value of B in equations 2.24 and 2.28 while that of κ remains nearly constant. Hinze (1962) thought that the difference in the values of κ and B in the log law equations, reported by various investigators, were due to the departure from assumed Reynolds number similarity of the respective flow fields. For this Hinze (1962) re-examined the old data obtained by Nikuradse (1933) and in spite of scatter of the data detected a trend of the values of κ and B as a function of Reynolds number. The general trend as for the parameter κ is to decrease with increasing Reynolds number both for smooth and rough pipes with a tendency to level off at κ = 0.357 for Re $\geq 10^6$. The general trend of the values of B is to decrease with increasing Reynolds number in the case of smooth wall, but no such trend was found due to the large scatter of the data in the case of rough wall. In the above pipe flow measurements of Hinze no secondary flow was present but, as noted earlier, the effect of side walls on the value of B (at the same Reynolds number) is prominent, presumably due to the presence of the strong secondary motion there. It is thought that the extent of the log law region is affected by the secondary flow, being thinner in parts of the wall where this flow is directed towards the wall and thicker in parts where this flow is away from the

wall as can be seen in figures 4.7 and 5.6.

The resistance to flow offered by the rough walls is larger than that offered by the smooth walls and consequently the laws of friction for rough walls are of great practical importance but can not yet be defined uniquely because of the fundamental difficulty that the number of parameters describing the roughness is large owing to the great diversity of geometric forms and their arrangements. The velocity gradient near the rough wall is less steep than that near the smooth wall and the log law region shifts further from the wall than without roughness. Further, due to roughness, the log law profile of mean velocity shifts downwards from those of the smooth wall. To see clearly the connexion between the velocity distributions near the smooth and rough walls, it is useful to replot the results for the rough wall in the form of smooth wall log law equation 2.24. Thus, the log law equation for the rough wall (equation 2.28) can be written in the form

$$\frac{U}{U_\tau} = \frac{1}{\kappa} \ln \frac{x_3 U_\tau}{\nu} + B_s - \frac{\Delta U_1}{U_\tau} f\left(\frac{\kappa U_\tau}{\nu}\right) \qquad \ldots (7.1)$$

where $\Delta U_1 / U_\tau$ is the measure of vertical shift of the rough wall profile from the smooth one and a universal function of $\kappa U_\tau / \nu$ for the considered roughness configuration. From the work of some investigators, for example Hamma (1954), $\Delta U_1 / U_\tau$ and $\kappa U_\tau / \nu$ (for $\kappa U_\tau / \nu > 55$) can be related through the equation

$$\frac{\Delta U_1}{U_\tau} = \frac{1}{\kappa} \ln \frac{\kappa U_\tau}{\nu} + A \qquad \ldots (7.2)$$

where $\kappa = 0.41$ but values of A differ for various types of roughness. For high values of $\kappa U_\tau / \nu$ the first term on the right hand side of equation 7.2 becomes predominant, and $\Delta U_1 / U_\tau$ becomes proportional to $U_\tau \kappa / \nu$ with a constant of proportionality equal to $1/\kappa$. To compare the shift of the rough wall profiles results of the present measurements of both rough and smooth

walls of both the rough-smooth ducts are replotted in figure 7.2. The figure shows the value of shift i.e, $\Delta U_1/U_\tau$ to be equal to 18.5 and 17.2 for one and two rough walls duct respectively. For similar type of roughness and for the same value of $U_\tau\kappa/\nu$ ($\simeq$ 1000) Moore's (1951) measurements showed the similar magnitude of vertical shift ($\Delta U_1/U_\tau$ = 17) for the rough wall profile. For the same value of $U_\tau\kappa/\nu$ ($\sim$ 1000) Hamma's (1954) wire screen roughness gave less value of $\Delta U_1/U_\tau$ (~ 15) because of different roughness configuration. Thus the general view of the displacement of the rough wall log law velocity profile is also applicable in the asymmetric flow, at least in the central region of the duct walls.

Perry and Joubert (1963) argued that the effect of roughness on the velocity profile is, like viscosity, confined only to a thin region adjoining the surface and proposed a unique logarithmic law for both smooth and rough surface in the form of equation 2.24 with $B_R = B_S$ but the kinematic viscosity ν in x_2^+ being replaced by a modified viscosity νe so that $\nu e = f(\kappa U_\tau/\nu)$. For generality and comparison of 'modified' viscosity, νe, one should recall the concept of 'sand grain roughness' of Nikuradse (1933).

7.5 Secondary Mean Velocity

As mentioned in section 1.3.1, Brundrett and Baines made an analysis of the origin of secondary flow from axial vorticity equation 1.4. From the symmetry condition of smooth square duct they also showed that the generation term (equation 1.5) is zero along the wall midplanes and corner bisectors creating eight zones of counter rotating vortices. From the above reasoning of flow symmetry it can be suggested that one vortex should be present in each of half sections of one rough wall duct and in each of quadrants of two rough wall duct. The above mentioned votices in the rough-smooth ducts of the present measurements have, however, been observed. But the isovels of Fujita with similar boundary conditions indicate the presence of a vortex in the rough wall region in addition to one in the smooth wall region. Near the discrete rib-type rough wall the

distribution of secondary velocity is greatly influenced by the relative rib spacing, P/e, and the position of the sensing probe with respect to the rib. Flow over the three types of rib spacing is shown in figure 7.1 wherefrom the expected orientation of secondary velocity could be inferred. For example, Humphrey and Whitelaw's (1979) measurements (P/e = 10) over the rib and between the ribs showed all flow away from the wall and towards the wall in the respective positions near it. Away from the wall, however, the local effect of rib on secondary velocity becomes negligible.

From the modified turbulence kinetic energy equation, Hinze (1967) gave a qualitative analysis of the generation of secondary velocity. As the viscous terms in the kinetic energy equation (eq. 2.20) are of importance only close to the wall where generation of secondary velocity is negligible as also argued by Brundrett and Baines (1964), they are neglected when applying the equation not too close to the wall. Equation 2.20 is then written in the form

$$U_2 \frac{\partial k}{\partial x_2} + U_3 \frac{\partial k}{\partial x_3} = - \overline{u_1 u_2} \frac{\partial U_1}{\partial x_2} - \overline{u_1 u_3} \frac{\partial U_1}{\partial x_3} - \epsilon \quad \ldots (7.3)$$

In a steady-state flow through ducts, the total production of turbulence energy must be balanced by total dissipation of the whole flow region. Thus, in a confined flow, for localized regions of excess turbulence generation, there must be localized regions of excess dissipation and the generation of secondary velocity is due to this different level of energy. When in a localized region, the production of turbulence energy is much greater (or smaller) than the dissipation, there must be a transport of turbulence-poor fluid into (outwards) this region and a transport of turbulence-rich fluid outwards (into) this region.

The above argument can be verified by considering a localized region where there is excess production or dissipation. Near the midplane of the rough wall region of the present

ducts

$$\left|\frac{\partial k}{\partial x_2}\right| << \left|\frac{\partial k}{\partial x_3}\right|$$

and can be neglected and $\frac{\partial k}{\partial x_3} < 0$, further on the symmetry plane ($x_2/a = 0.5$)

$$U_2 = 0 \quad \text{and} \quad \overline{u_1 u_2} = 0$$

Thus U_3 will be either positive or negative (positive indicates flow away from the rough wall) depending on whether production i.e, $-\overline{u_1 u_3}\frac{\partial U_1}{\partial x_3}$, is smaller or greater than dissipation. In the region concerned production is greater than dissipation indicative of negative U_3 which has been observed in the experiment.

7.6 Some Aspects of Asymmetric Flow

It has been seen in chapters 4 and 5 that the mean velocity profiles are greatly influenced by the secondary velocities whose distribution depend on Reynolds number. It should be noted too that mean velocity profiles are also dependent on wall shear stresses which again vary with Reynolds number at different rates: higher for rough wall and lower for smooth wall and are modified further by secondary velocity (sections 4.2.3, 4.3.3, 5.2.3 and 5.3.3). This different rates of variation lie in the fact that the shear stress at the rough surface increases as the square of the velocity, whereas at smooth surface varies roughly as $U^{7/4}$. The ratio τ_r/τ_s should thus be proportional to $U^{1/4}$ in the absence of other effects but this is not so for square ducts where influence of the side wall is prominent as seen in the measurements. The effect of Reynolds number on asymmetric flow is thus more pronounced than on symmetric flow because of the different rates of variation of wall shear stress mentioned above and variation of secondary velocity which with increase of Reynolds number not only changes in magnitude but also in dis-

tribution pattern (section 5.3.2) which in symmetric flow does not usually happen.

In asymmetric ducts with high aspect ratios secondary velocity becomes zero on the symmetry plane where the asymmetry of the mean velocity profiles becomes proportional to the ratio τ_r/τ_s only and, since it varies with $U_1^{\frac{1}{4}}$, profiles become insensitive to Reynolds number at high values*. So for high aspect ratio channels, asymmetry of flow is mainly a function of the rough wall which determines the shear stress τ_r. But with decreasing aspect ratio secondary velocity begins to spread from the corner towards the duct centre where at certain aspect ratio (close to 1) the flow looses the two-dimensional characteristics and can no longer be represented by the wall shear stress effect only. For comparative study of the effect of Reynolds number, roughness ratio and aspect ratio of ducts, some of the asymmetric flow results are summarised in table 7.1. The table shows that the asymmetry of the mean velocity in channels with one rough wall is a function not only of the ratio e/D_h but also of the aspect ratio of the channel. For camparatively low aspect ratio channels the position of maximum velocity is not as near to the smooth wall as for the higher ones. Axial velocities in asymmetric square ducts are mainly influenced by the secondary velocities and the occurance of velocity maxima depends on their distribution and not on the roughness ratio of the duct as happened in asymmetric channels.

From the measurements of smooth wall boundary layer by Klebanoff (1954) and rough wall boundary layer by Corrsin and Kistler (1954) it is found that the ratio between the relative turbulence intensities for a rough wall boundary layer and those for a smooth wall boundary layer is roughly equal to the ratio between the corresponding friction velocities. In the measurement of rough smooth duct flows, however, no such relation between turbulence intensities and wall shear stress, even at the midplanes of the walls, was obtained, obviously due to the influence of rough wall on the flow regions

---

* In the low Reynolds number range (Re = $2\text{-}8\times10^4$) Hanjalic and Launder (1968) found the velocity maximum to be shifted towards the smooth wall with the increase of Reynolds numebr and invariant with Reynolds number at about Re = 8×10^4

TABLE 7.1 - Comparison of Flow in Ducts with one Rough Wall

Investigators	Wilkie et al			Hanjalic and Launder		Aytekin and Berger		Humphrey and Whitelaw	Fujita	Present Measure-ments
	1	2	3	1	2	1				
Channel Height a (mm)	13.87	14.02	14.18	28.0	54.0	100.0	184.0	40.0	50.0	150.0
Aspect Ratio	11.0	11.0	11.0	10.71	5.56	3.0	1.63	1.0	1.0	1.0
Hydraulic Diameter D_h (mm)	25.43	25.68	25.95	51.22	91.5	150.0	228.0	40.0	50.0	150.0
Roughness Height e (mm)	.152	.307	.476	3.18	3.18	7.0	7.00	3.95	1.0	3.18
Pitch to Height Ratio P/e	10	10	10	10	10	7.2	7.2	10	10	10
e/D_h	.006	.012	.018	.062	.035	.047	.031	.099	.02	.0212
e/a	.011	.022	.033	.114	.059	.07	.038	.099	.02	.0212
x_{3m}/a*	.672	.711	.757	.828	.761	.70	.606	~.495	.55	.482
x_{3o}/a*	-	-	-	.869	.806	.755	.636	.58	-	.495
Re	$2x10^4$ - $2x10^5$			$8x10^4$		~$3.4x10^5$		$2.58x10^4$	$6.4x10^4$	$3.42x10^5$

* x_{3m} = value of x for maximum velocity

x_{3o} = value of x for zero shear stress

of the smooth wall. Even though, in the regions of both the rough and smooth ($x_3/a = 1$) walls of one rough wall duct, a similarity between the Reynolds shear stress ($\overline{u_1 u_3}$) distribution and the turbulence kinetic energy distribution may be observed confirming the Von Kárman's similarity hypothesis concerning the structure of turbulence there. The distribution of the ratio $\overline{u_1 u_3}/k$ is given in figure 7.3 where it is nearly constant at value of about 0.28 across the large portion of the respective wall regions (rough wall and opposite smooth wall) of one rough wall duct. With the approach of the side wall, however, this value decrease slightly but with considerable increase of the rough wall region while the smooth wall region ceases to show any similarity. Similar value of $\overline{u_1 u_3}/k$ is observed in Hanjalic's (1970) asymmetric channel flow while $\overline{u_1 u_3}/k = 0.16$ was observed in Hinze's (1959) boundary layer and $\overline{u_1 u_3}/k = 0.14$ in Laufer's (1954) pipe flow measurements.

This similarity property is useful in analysing some of the turbulent flows. Bradshaw et al (1967a) solved the better known equation of turbulence kinetic energy and converted it into an approximate equation for $\overline{u_1 u_3}$ by prescribing a unique algebraic equation relating the shear stress and turbulence energy. For the purpose of demonstration $\overline{u_1 u_3}/k$ was taken as constant. With this assumption the method has been used successfully for the prediction of turbulent boundary layer flow in various conditions. Because of the direct relationship between the shear stress and kinetic energy, this method in its present form is not suitable for the prediction of flows where the shear stress changes signs. Further $\overline{u_1 u_3}$ distribution in two rough wall duct and other shear stress component $\overline{u_1 u_2}$ do not show such distinct region of similarity as discussed below.

In the duct with two rough walls comparatively less part of the wall region suggests the above mentioned similarity as can be seen from figure 7.4. Profiles of $\overline{u_1 u_3}/k$ at $x_2/a = 0.15$ for both the ducts show no constant regions of $\overline{u_1 u_3}/k$ but decrease linearly from the rough wall towards its zero value position. To compare the similarity between $\overline{u_1 u_2}$ and k, profiles of $\overline{u_1 u_2}/k$ are plotted parallel to x_2 - axis for both the ducts as shown in figures 7.5 and 7.6 where they show such similarity only near the

rough wall i.e, from rough wall to $x_3/a = 0.5$ and covering roughly the central part ($0.15 \lesssim x_2/a \lesssim .5$) of the wall but the values of $\overline{u_1 u_2}/k$ vary considerably, from 0 near the rough wall to about 0.3 near the symmetry plane ($x_3/a = .5$) In figure 7.5 beyond $x_3/a = 0.4$, no similarity between $\overline{u_1 u_2}$ and k is present.

In turbulent shear flows, it is generally known that the sum of terms representing the production of turbulence kinetic energy is positive implying a transfer of energy from the mean motion to the turbulence flow field. This contributes to a state of equilibrium for the flow as the turbulence kinetic energy passed to smaller and smaller scales, eventually being transformed into heat by dissipation. It is however shown in section 4.3.5 that flows with asymmetric mean velocity distribution may display localized areas in which the production term is negative implying the existence of zones of opposing shear created by the displacement of the plane of zero shear stress from that of zero velocity gradient. In this zone of energy reversal, the Reynolds stress is of opposite sign to the mean velocity gradient, and momentum transport by turbulence can not be described by conventional gradient modelling. Nevertheless, Launder (1968), Beguier (1969) and Hinze (1970) have from, the double structure concept first proposed by Townsend (1956), proposed a modified relationship. The shear stress is decomposed into two parts: a gradient type term which express the action of small eddies and a term which being proportional to the curvature of the mean velocity profile implying the action of large eddies. Thus shear stress in this zone is expressed as

$$\overline{u_1 u_3} = \frac{\mu_t}{\rho} \frac{\partial U}{\partial x_3}_1 - \overline{u_1 u_3}^* \qquad \ldots (7.4)$$

where $\overline{u_1 u_3}^*$ is the residual stress due to large scale eddies where $\frac{\partial U_1}{\partial x_3} = 0$. Since the derivative of the mean velocity profile is quasi-linear near the velocity extremum, it can be written, after Beguier (1969), as

$$\left(\frac{\partial U_1}{\partial x_3}\right)_B = lm \left(\frac{\partial^2 U_1}{\partial x^2_3}\right)_A + \left(\frac{\partial U_1}{\partial x_3}\right)_A \quad \ldots (7.5)$$

between points A $\left\{\frac{\partial U_1}{\partial x_3} = O\right\}$ and B $(\overline{u_1 u_3} = O)$, lm being the length of the displacement zone shown in figure 7.7. Since $\left(\frac{\partial U_1}{\partial x_3}\right)_A = O$ and it is supposed that $\overline{u_1 u_3}^*$ is constant between A and B, which seems to be a good physical approximation, it is then obtained from the condition at the point B

$$-(\overline{u_i u_3})^*_{AB} = -\frac{\mu_t}{\rho} lm \left(\frac{\partial^2 U_1}{\partial x^2_3}\right)_A \quad \ldots (7.6)$$

and $$-\rho(\overline{u_1 u_3})_{AB} \simeq \mu_t \left(\frac{\partial U_1}{\partial x_3}\right)_{AB} - \mu_t\, lm \left(\frac{\partial^2 U_1}{\partial x^2_3}\right)_A \quad \ldots (7.7)$$

The physical explanation of the energy reversal is intimately related to that of the observed experimental displacement. Gee and Bradshaw (1962) suggest that, for the wall jet, 'pockets of fluid having negative shear stress will frequently penetrate into the wall layer where the mean velocity gradient is positve, and thus give a total contribution to the shear stress which is opposite in sign to that produced by the mean velocity gradient, Spectral measurements of Beguier (1969) in the energy reversal zone of asymmetric plane jet shows negative contribution at low wave number zone. The zone of displacement then, results from the asymmetrical lateral diffusion of large eddies from one side of the extremum of mean velocity profile to the other. In the displacement region, these large eddies would impose the sign of the shear stress which they had carried with them.

C H A P T E R 8

CONCLUSIONS

The present research objectives have been achieved and the findings are summarised at the end of chapters 4, 5 and 6. So a brief review is made here to draw together the main points. A brief discussion of the possible extension of the present work is also made in this chapter.

8.1 Achievements of the Experimental Work

The detailed measurements of the flow structure in square ducts with dissimilar boundary conditions revealed both well-known and not-so-known features. Measurements have shown that near the smooth wall and over a extensive region near the rough wall, the mean and turbulent flow fields appear to be indistinguishably different from those which arise in symmetric flows. The central region of the flow where two dissimilar wall dominated flow regimes interact is, generally, characterised by non-coincidence of zero shear stress and zero velocity gradient which does not occur in symmetric flows and can not be described in conventional way. The secondary flow field generated in the asymmetric flow condition is quite different from the symmetric duct and its influence on the overall flow structure is considerable. Due to its effect, the distribution of flow properties even at the midplane of the rough wall is different from similar measurements of channel flow where no secondary motion is present. In spite of the asymmetry, the mean flow velocity near the walls, both rough and smooth, maintains its log law properties but with variation of constant B in the log law equations suggesting the influence of the side walls. In the rough-smooth flow assembly the contribution of smooth wall shear stress is greater than that if it were all smooth and converse

is true for the rough wall. The rough wall dominates the major part of the flow area where turbulence flow structure maintains its similarity.

It is hoped that the experimental programme provides the details of turbulent flow structure to a level at which it is possible to model the flow. Its results can guide theoretical research in two ways: firstly they provide a set of reference data against which the prediction capabilities of various turbulence models can be tested and by analysis of their differences, the model can be improvised. Secondly, the data provide guidelines as to the most reasonable closing approximations in the chosen set of transport equations.

8.2 Achievements of Theoretical Work

The primary success of the theoretical research is the provision of a turbulence model which can predict with reasonable accuracy the hydrodynamic properties of symmetric square ducts and succeeds to some extent in predicting the influence of dissimilar boundary conditions on the symmetric flow fields. The present research programme, thus, makes a step to calculate asymmetric flow with strong secondary motion.

Comparison between the calculations and experiments have been described in chapter 6 which includes details profiles and contours of mean and turbulent flow properties in square ducts with similar and dissimilar boundary conditions. These results show that the calculations are, generally, in reasonable agreement with the measurements. In all cases, trends have been correctly predicted although detailed examinations have, on occasions, revealed substantial numerical differences. Various reasons have been discussed to account for the observed discrepancies which include numerical smearing, certain assumptions used in the turbulence model and inadequate specification of boundary conditions. Possible methods of improvement of the present model have been suggested at the end of chapter 6 to overcome the above mentioned errors.

8.3 Extension of the Present Work

The study of turbulent flow through ducts with dissimilar wall conditions has been undertaken by a few workers in the past and has been presented in the present thesis. Due to the limited amount of measurements performed in asymmetric flows, several questions, as regards the characteristics of these types of flow, are yet to be answered. As a direct result of the present work, the following suggestion can be made for the continuation of the research in dissimilar flow fields.

(1) Asymmetric duct flows, with secondary velocity, show great variation in the distribution of mean and turbulent flow properties with change of Reynolds number possibly due to changes of the secondary velocity distribution. This change in asymmetric duct flow is more pronouced than in symmetric flows, but systematic detailed measurements have not yet been made of the effect of Reynolds number. Thus, measurements similar to the present ones, should be undertaken to study the effect of Reynolds number in an asymmetric flow field.

(2) Similar to above, the research in the aysmmetric flow field should be extended to include the effects aspect ratio of the duct. Measurements in asymmetric flow fields, are available either at high aspect ratio or at square duct but no such data is available between aspect ratio 5 to 1 where changes of flow structure with aspect ratio are significant, as can be seen in symmetric ducts.

(3) From an engineering standpoint, the urgent need is to extend the present work to include measurements of the mean and turbulent temperature field in strongly asymmetric non-isothermal flows.

APPENDIX A

Hot Wire response Equations

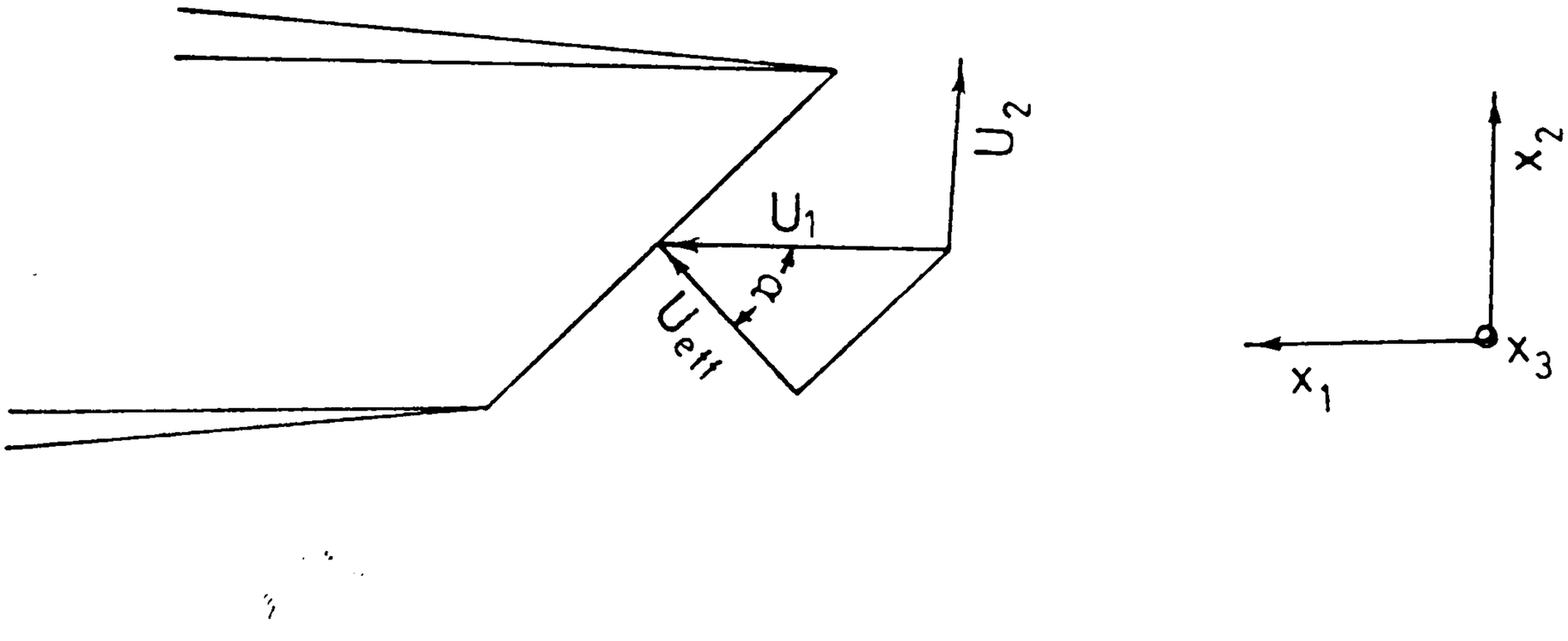

As discussed in section 3.3.2.2, the linearised response equation for the hot wire in low turbulence flow field (15% or less) can be written as

$$\hat{E}_1 = S\hat{U}_{eff} = S\hat{U}_1 F \qquad \ldots (A\text{-}1)$$

where $\hat{E}_1$ is the instantaneous mean voltage, $\hat{U}_1$ is the instantaneous mean velocity and F is the function which depends on the wire parameters such as its length to diameter ratio and its angle with the mean flow direction.

Squaring and taking the first differential, equation (A-1) becomes

$$2E_1\,\partial E_1 = S^2\left[F^2 2U_1\,\partial U_1 + U_1^2 2F\,\partial F\right]$$

or

$$\frac{E_1\,\partial E_1}{S^2} = F^2 U_1\,\partial U_1 + U_1^2 F\,\partial F$$

or

$$\frac{\partial E_1}{E_1} = \frac{\partial U_1}{U_1} + \frac{\partial F}{F} = \frac{\partial U_1}{U_1} + \frac{1}{F}\,\frac{\partial F}{\partial \alpha}\,\partial\alpha$$

For low turbulence level $\delta\alpha = -\frac{\delta U_2}{U_1}$

therefore $$\frac{\partial E_1}{E_1} = \frac{\partial U_1}{U_1} - \frac{1}{F}\frac{\partial U_2}{U_1}\frac{\partial F}{\partial \alpha} \quad \ldots (A\text{-}2)$$

As mentioned in section 3.3.2.2 the function F is taken to be

$$F = (\cos^2\alpha + K \sin^2\alpha)^{\frac{1}{2}}$$

where K is a coefficient.

Squaring and differentiating F with respect to α and putting in equation (A-2) we get

$$\frac{\partial E_1}{E_1} = \frac{\partial U_1}{U_1} + \frac{\partial U_2}{U_1}\frac{(1-K^2)\sin 2\alpha}{2(\cos^2\alpha + K^2\sin^2\alpha)} \quad \ldots (A\text{-}3)$$

For $\alpha = +45^\circ$, Equation (A-3) becomes

$$\frac{\partial E_1}{E_1} = \frac{\partial U_1}{U_1} + \frac{\partial U_2}{U_1}\frac{(1-K^2)}{(1+K^2)}$$

Here ∂E_1, ∂U_1 and ∂U_2 represent the incremental change of their respective mean value. Squaring and averaging equation (A-4), the final equation for the calculation of turbulence is obtained as follows:

$$\frac{\overline{e_1^2}}{E_1^2} = \frac{\overline{u_1^2}}{U_1^2} + \frac{1-K^2}{1+K^2}\frac{\overline{u_1 u_2}}{U_1^2} + \frac{(1-K^2)^2}{(1+K^2)}\frac{u_2^2}{U_1^2} \quad \ldots (A\text{-}5)$$

similarly for $\alpha = -45^\circ$, equation (A-2) will be

$$\frac{\overline{e_2^2}}{E_2^2} = \frac{\overline{u_1^2}}{U_1^2} - 2\frac{1-K^2}{1+K^2}\frac{\overline{u_1 u_2}}{U_1^2} + \frac{(1-K^2)^2}{(1+K^2)}\frac{\overline{u_2^2}}{U_1^2} \quad \ldots (A\text{-}6)$$

For $\alpha = 0^{o}$, equation (A-3) yields

$$\frac{\overline{e_o^2}}{E_o^2} = \frac{\overline{u_1^2}}{U_1^2} \qquad \ldots \text{(A-7)}$$

Finally the following evaluation equations can be obtained from equations (A-5), (A-6) and (A-7).

(a) In the $x_1 - x_2$ plane, for $\alpha = \pm 45^{o}$

$$\frac{\overline{u_2^2}}{U_1^2} = \frac{1}{2}\,\frac{(1+K^2)}{(1-K^2)}\left[\frac{(\overline{e_1^2})}{(\overline{E_1^2})}_{\alpha=+45_1} + \frac{(\overline{e_2^2})}{(\overline{E_2^2})}_{\alpha=-45^{o}} - 2\,\frac{(\overline{e_o^2})}{(\overline{E_o^2})}_{\alpha=o}\right] \qquad \ldots \text{(A-8)}$$

$$\frac{\overline{u_1 u_2}}{U_1^2} = \frac{1+K^2}{4(1-K^2)}\left[\frac{(\overline{e_1^2})}{(\overline{E_1^2})}_{\alpha=+45^{o}} - \frac{(\overline{e_2^2})}{(\overline{E_2^2})}_{\alpha=-45^{o}}\right] \qquad \ldots \text{(A-9)}$$

(b) In the $x_1 - x_3$ plane, for $\alpha = \pm 45^{o}$

$$\frac{\overline{u_3^2}}{U_1^2} = \frac{1}{2}\,\frac{(1+K^2)}{(1-K^2)}\left[\frac{(\overline{e_3^2})}{(\overline{E_3^2})}_{\alpha=+45^{o}} + \frac{(\overline{e_4^2})}{(\overline{E_4^2})}_{\alpha=-45^{o}} - 2\,\frac{(\overline{e_o^2})}{(\overline{E_o^2})}_{\alpha=o}\right] \qquad \ldots \text{(A-10)}$$

$$\frac{\overline{u_1 u_3}}{U_1^2} = \frac{1+K^2}{4(1-K^2)}\left[\frac{(\overline{e_3^2})}{(\overline{E_3^2})}_{\alpha=+45^{o}} - \frac{(\overline{e_4^2})}{(\overline{E_4^2})}_{\alpha=-45^{o}}\right] \qquad \ldots \text{(A-11)}$$

APPENDIX B

Calibration and Correction Procedure of Yawmeter

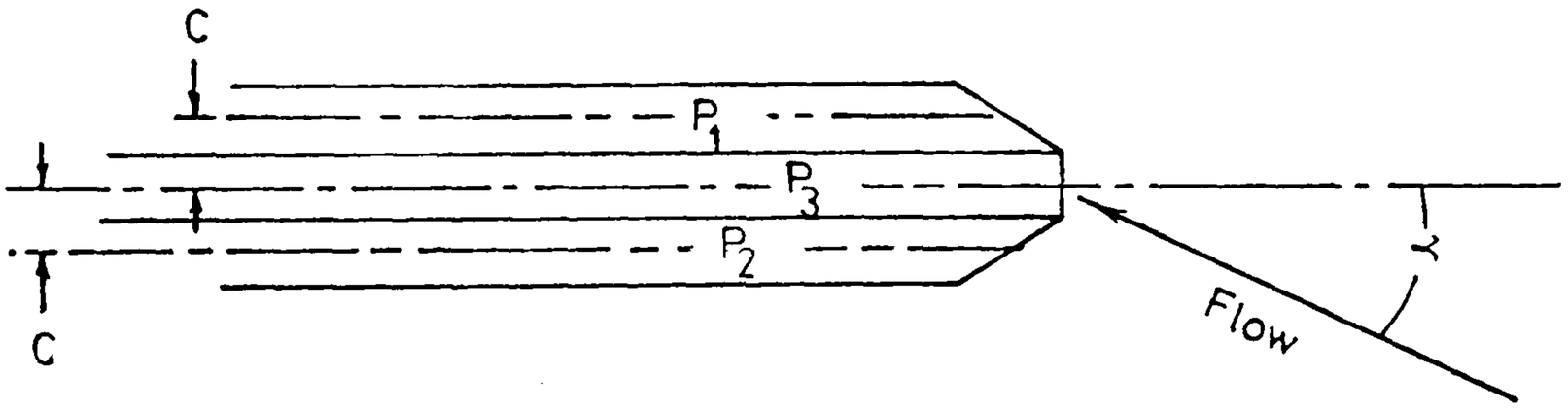

If a yawmeter is placed in a flow field its pressure recorded by the different sensing tubes varies with the flow direction γ. If P_1, P_2 and P_3 are the pressures recorded by the respective tubes shown in the above figure, the ratio $(P_1 - P_2) \div \{P_3 - (P_1 + P_2)/2\}$ varies linearly with the flow angle γ. This variation remains linear within the flow angle of approximately $\pm 20^\circ$.

During the process of calibration the yawmeter was placed in the calibration rig with certain angle (within 20°) with the flow direction. The velocity of the flow was maintained constant while the yawmeter's angular position was varied. For each angular position of the yawmeter the pressure of the different tubes (tubes 1, 2, and 3) were recorded. The pressure ratio $(P_1 - P_2) \div \{P_3 - (P_1 + P_2)/2\}$ was then plotted on a plane graph paper against the angular position γ. This plot gave the calibration of the yawmeter as shown in figure A3.1

It was discussed in section 3.3.3.2 that the pressure of the camphered tubes varies linearly with the total pressure of the flow field. When the yawmeter is placed in a shear flow its recorded pressures are influenced by the total

pressure gradient of the flow field. For the small dimension of the yawmeter tip (in this experiment 0.5 mm between the tube centres) the pressure gradient can be assumed to be linear. The pressure gradient at each yawmeter position was determined from the slope of the total pressure curve. If G is the pressure gradient at the position of the yawmeter and C is the centre distance between the tubes, then the corrected pressures of the camphered tubes would be

$$P_1' = P_1 \pm CG \qquad \ldots (B\text{-}1)$$

$$P_2' = P_2 \pm CG \qquad \ldots (B\text{-}2)$$

where P_1' and P_2' represent the corrected pressure of P_1 and P_2 respectively. If the camphered tube is placed in the direction of higher total pressure with respect to the total head tube (total head tube centre was taken as the reference centre of the yawmeter) then the factor CG will be subtracted from and in the reverse case it will be added with the actual pressure P_1 or P_2 to get the corrected pressure P_1' or P_2' respectively.

REFERENCES

Ahmed, S. and Brundrett, E. (1979a) Characteristic lengths for for non-circular ducts. Int. J. Heat and Mass Transfer 14,157.

Ahmed,S. and Brundrett, E. (1971b) Turbulent flow in non-circular ducts. Part I: Mean flow measurements in the developing region of a square duct. Int. J. Heat and Mass Transfer, 14,365.

Aly, A.M.M., Trupp, A.C. and Gerrard, A.D. (1978) Measurement and prediction of fully developed turbulent flow in an equilateral triangular duct. J.Fluid Mechanics 85,57.

Asano, Y. (19?_, Friction coeffiecient of flow through square duct with different rough surfaces. Trans. JSME 38,3223.

Aytekins, A and Berger, F.P. Turbulent flow in rectangular ducts with low aspect ratios having one rough wall. An unpublished report.

Baumann, E and Rehme, K. (1975) Friction correlations for rectangular roughness. Int. J. Heat and Mass Transfer 18,1189.

Beavers, G.S., Sparrow, E.M. and Magnuson, R.A. (1970) Experiments on hydrodynamically developing flow in rectangular ducts of arbitrary aspect ratio. Int. J. Heat and Mass Transfer, 13,689.

Beavers, G.S., Sparrow, E.M. and Lloyd, J.R. (1971) Low Reynolds number turbulent flow in large aspect ratio rectangular ducts. Trans. ASME, J. Basic Eng. 93,296.

Béguier, M.C. (1965) Mesures des tensions de Reynolds dans un écoulement dissymétrique en régime turbulent incompressible. J. de Mecanique. 4,319.

Bequier, M.C. (1969) Ecoulement plans dissymetriques en regime turbulent incompressible. C.R. Acad. Sc., Paris 268,69.

Berger, F.P. and Whitehead, A.W. (1977) Fluid flow and heat transfer in tubes with integral square rib roughening. J. Br. Nucl. Energy Society 16,153.

Bergles, A.E. (1969) Surveyand Evaluation of Techniques to augment convective heat and mass transfer. Progress in heat and Mass Transfer 1,331.

Bettermann, D. (1966) Contribution a l'etude de la convection forcee turbulente le long de plaques rugueses. Int. J. Heat and Mass Transfer 9,153.

Bradshaw, P. and Ferris, D.H. (1965) The spectral energy mixing layer. Aero. Res. Council

Bradshaw, P., Ferriss, D.H. and Atwell, N.P. (1967a) Calculation of boundary layer development using turbulent energy equation. J. Fluid Mechanics 28,593.

Bradshaw, P. (1967b) The turbulence structure of equilibrium boundary layers. J. Fluid Mechanics 29,625.

Bradshaw, P. (1967c) Inactive motion and pressure fluctuations in turbulent boundary layers. J. Fluid Mechanics 30,241.

Bradshaw, P. (1967d) Conditions for the existence of an inertial subrange in turbulent flow. Aero. Res. Council RM 3603.

Bradshaw, P. (1971) Calculation of three-dimensional boundary layers. J. Fluid Mechanics 46,417.

Bradshaw, P., Dean, R.B. and McEligot, D.M. (1973) Calculation of interacting turbulent shear layers: Duct flow. Trans. ASME, J. Fluid Engineering 95,214.

Bradshaw, P. (Editor) (1976) Topics in Applied Physics, Vol.19, 'Turbulence', Spring-Verlag.

Brighton, J.A. and Jones, J.B. (1964) Fully developed turbulent flow in annuli. Trans. ASME, J. Basic Engineering 86,835.

Brundrett, E. and Baines, W.D. (1964) The production and diffusion of vorticity in duct flow. J. Fluid Mechanics 19,375.

Brundrett, E. and Burroughs, P.R. (1967) The temperature inner law and heat transfer for turbulent air flow in vertical square duct. Int. J. Heat and Mass Transfer 10,1133.

Bryer, D.W., Walshe, D.E. and Garner, H.C. (1958) Pressure probes selected for three-dimensional flow measurements. Aero. Res. Council, RM 3037.

Bryer, D.W. and Pankhurst (1971) Pressure-probe methods for determining wind speed and flow direction. National Physical Laboratory, H.M.S.O.

Buleev, N.I. (1963) Theoretical model of the mechanism of turbulent exchange in fluid flows. AERE Translation 957.

Burk, E. (1969) Influence of Prandtl number on heat transfer and pressure drop of artificially roughened channels. Wärme und Stoffübertragung 2,87.

Carajilescov, P. and Todreas, N. (1976) Experimental and analystic study of axial turbulent flows in an interior sub-channel of a bare rod bundle. Trans. ASME, J. Heat Transfer 98,262.

Carlson, L.W. and Irvine Jr., T.F. (1961) Fully developed pressure drop in triangular shaped ducts. Trans. ASME,

Carreto, L.S., Gosman, A.D., Patankar, S.V. and Spalding, D.B. (1972) Two numerical procedures for steady three-dimensional flows with recirculation. Proc. 3rd Int. Conf. on Numerical Methods in Fluid Mechanics 2,60.

Cebeci, T. (1973) Eddy-viscosity distribution in thick axisymmetric turbulent boundary layers. Trans. ASME, J. Fluid Engineering 95,319.

Champagne, F.H., Sleicher, C.A. and Wehrmann, O.H. (1967) Turbulence measurements with inclined hot-wires. Part 1 and Part 2. J. Fluid Mechanics 28,153.

Champagne, F.H., Harris, V.G. and Corrsin, S. (1970) Experiments on nearly homogeneous turbulent shear flow. J. Fluid Mechanics 41.131.

Chou, P.Y. (1945) On the velocity correlations and the solutions of turbulent fluctuations. Quart. Appl. Mathematics 3,38.

Clark, J.A. (1968) A study of incompressible turbulent boundary layers in channel flow. Trans. ASME, J. Basic Engineering 90,455.

Clauser, F.H. (1954) Turbulent boundary layer in adverse pressure gradient. J. Aero. Science 21,91.

Comte-Bellot, G. (1965) Ecoulement turbulent entre deux parois paralleles. Publ. Scientifiques et Techniques du Ministere de L'Air, No.419.

Comte-Bellot, G. (1976) Hot-wire anemometry. Annual Review of Fluid Mechanics 8,209.

Corrsin, S. and Kistler, A.L. (1954) The free-stream boundaries of turbulent flows. NACA TN3133.

Corrsin, S. (1973) Comments on transport equations in turbulence. The Physics of Fluids 16,157.

Crabb, D, Durão, D.F.G. and Whitelaw, J.H. (1977) Velocity characteristics in the vicinity of a two-dimensional rib. Proc.of the Fourth Brazilian Congress of Mech. Eng. B3,419 also Imperial College, Mech. Eng. Dept. Report FS/77/9

Curr, R. M., Sharma, D. and Tatchell, D.G. (1972) Numerical predictions of some three-dimensional boundary layers in ducts. Computer Methods in Applied Mechanics and Engineering 1,143.

Daly, B.J. and Harlow, F.H. (1970) Transport equations of turbulence. The physics of Fluids 13,2634.

Date, A.W. (1973) Prediction of friction and heat transfer characteristics of flow in a tube containing twisted tape. Imperial College, Mech. Eng. Dept. Report HTS/73/15.

Deissler, R.G. and Taylor, M.F. (1959) Analysis of turbulent flow and heat transfer in non-circular passages. NACA TR R-31.

Dekeyser and Béquier, C. (1979) Asymmetrical heated plane jet with two counter gradient diffusion zones. 2nd symposium on Turbulent shear Flows, Imperial College, 1.1.

Delleur, J.W. and McManus, D.S. (1959) Secondary flow in straight open channels. 6th Midwestern Conf. on Fluid Mechanics, 81.

Dipprey, D.F. and Sabersky, R.H. (1963) Heat and momentum transfer in smooth and rough tubes at various Prandtl numbers. Int. J. Heat and Mass Transfer 6,329.

Doenecke, J. (1964) Contribution á l'etude de la convection forcée turbulentente le long de plaques rugueuse. Int. J. Heat and Mass Transfer 7,133.

Durst, F. (1968) On turbulent flow through annular passages with smooth and rough cores. PhD. Thesis, University of London.

Dvorak, F.A (1969) Calculations of turbulent boundary layers on rough surfaces in pressure gradient. AlAA Journal 7,1752.

Eckert, E.R.G. and Irvine, Jr. T.F. (1957) Incompressible friction factor, transition and hydrodynamic entrance-length studies in ducts with triangular and rectangular cross sections, 5th Midwestern Conf. on Fluid Mechanics, 122.

Edwards, F.J. and Sheriff, N. (1961) The heat transfer and friction characteristics for forced-convection heat flow over a particular type of rough surface. Int. Heat Transfer Conference, Univ. of Colorodo.

Edwards, F.J. (1964) The correlation of forced-convection heat transfer data from surfaces with large scale roughness. Intst. of Mech. Engrs. Thermodynamics and Fluid Mechanics Convention, Paper 22

Einstein, H.A. and Li, H. (1958) Secondary currents in straight channels. Trans. Am. Geophs. Union 39,1085.

Escudier, M.P (1966) The distribution of mixing length in turbulent flows near walls. Imperial College, Mech. Eng. Dept. Report TWF/TN/1.

Eskinazi, S. and Erian, F.F. (1969) Energy reversal in turbulent flows. The physics of Fluids 12,1988.

Fage, A. (1936) On the static pressure in fully developed turbulent flow. Proc. Roy. Society of London, Series A 155,576.

Fournel, E. (1952) On a method of improving heat exchange by forced convection. AERE Translation 659.

Frenkiel, F.N. (1956) Effects of wire length in turbulence investigations with hot wire anemometer. Aero. Quarterly 5,1.

Fujita, H. (1978) Turbulent flows in square ducts consisting of smooth and rough planes. Research report, Faculty of Eng. Mie University 3,11.

Furuya, Y. and Fujita, H. (1967) Turbulent boundary layer on wire-screen roughness. Bulletin JSME 10 , No.37,77.

Furuya, Y. and Fujita, H. (1967) Effect of surface roughness on the velocity defect law. The Physics of Fluids 10,S155.

Furuya, Y., Miyata, M. and Fujita, H. (1976) Turbulent boundary layer and flow resistance on plates roughened by wires. Trans. ASME, J. Fluid Engineering 98,635.

Gee, M.T. and Bradshaw, P. (1962) Turbulent wall jet with and without an external stream. Aero. Res. Council, RM 3252.

Gessner, F.B. and Jones, J.B. (1961) A preliminary study of turbulence characteristics of flow along a corner. Trans. ASME, J. Basic Engineering 83,657.

Gessner, F.B. (1964) Turbulence and mean flow characteristics of fully developed flow in rectangular channels. PhD. Thesis, Purdue University.

Gessner, F.B. and Jones, J.B. (1965) On some aspects of fully developed turbulent flow in rectangular channels. J. Fluid Mechanics 23,689.

Gessner, F.B. (1973) The origin of secondary flow in turbulent flow along a corner. J. Fluid Mechanics 58,1.

Gessner, F.B. and Emery, A.F. (1977) A length-scale model for developing turbulent flow in a rectangular duct. Trans. ASME, J. Fluid Engineering 99,347.

Gessner, F.B. and Emery, A.F. (1976) A Reynolds stress model for turbulent corner flows. Part 1: Development of the model. Trans. ASME, J. Fluid Engineering 98,261.

Gessner, F.B. and Po, J.K. (1976) A Reynolds stress model for turbulent corner flows. Part 2: Comparison between theory and experiment. Trans. ASME, J. Fluid Engineering 98,269.

Goldstein, S. (1936) A note on the measurement of total head and static pressure in a turbulent stream. Proc. Roy Society of Aeronautics 155,570.

Gomelauri, V. (1964) Influence of two-dimensional artificial roughness on convective heat transfer. Int. J. Heat and Mass Transfer 7,653.

Gosman, A.D., Pun, W.M., Runchal, A.K., Spalding, D.B. and Wolfshtein, M. (1969) Heat and Mass Transfer in Recirculating Flows. Academic Press.

Gosman, A.D. and Rapley, C.W. (1978) A prediction method for fully developed flow through non-circular passages. Imperial College, Mech. Eng. Dept. Report FS/78/18.

Hall, W.B. (1962) Heat transfer in channels having rough and smooth surfaces. J. Mech. Eng. Science 4,287.

Hama, F.R. (1954) Boundary layer characteristics for smooth and rough surfaces. Trans. Soc. Nav. Archit. Mar. Engr., NY62,333.

Han, J.C., Glicksman, L.R. and Rohsenow, W.M. (1978) An investigation of heat transfer and friction for rib-roughened surfaces. Int. J. Heat and Mass Transfer 21,1143.

Hanjalić, K. (1970) Two-dimensional asymmetric flow in ducts. PhD. Thesis, University of London.

Hanjalić, K. and Launder, B.E. (1972a) Fully developed asymmetric flow in plane channel. J. Fluid Mechanics 52,301.

Hanjalić, K. and Launder, B.E. (1972b) A Reynolds stress model of turbulence and its application ot thin shear flows. J. Fluid Mechanics 52,609.

Harlow, F.H. and Nakayama, P.I. (1967) Turbulence transport equations. The Physics of Fluids 10,2323.

Hartnett, J.P., Koh, J.C.Y. and McComas, S.T. (1962) A comparison of predicted and measured friction factors for turbulent flow through rectangular ducts. Trans. ASME, J. Heat Transfer 84,82.

Heisenberg, W. (1948) Zur statistischen théorie der turbulenz. Z. Physics 124,628.

Hicken, E. (1972) Temperature distribution in air in a square channel with partial heated sides. Wärme und Stoffübertragung 5,121.

Hinze, J.O. (1967) Secondary currents in wall turbulence. The Physics of Fluids 10,S122.

Hinze, J.O. (1970) Dutch J. Applied Science Research 22,163.

Hoagland, L.C. (1960) Fully developed turbulent flow in straight rectangular duct-secondary flow, its cause and effect on the primary flow. PhD. Thesis, Dept. of Mech. Eng., Massachusetts Institute of Technology.

Hollingworth, P.D. (1967) Accurate measurements of gas flow direction using hot wire anemometer. CEGB Report RD/B/N892.

Huey, L.J. (1978) A yaw-insensitive static pressure probe. Trans. ASME, J. Fluid Engineering 100,229.

Hymphrey, J.A.C. (1978) Flow through ducts with curavture and roughness. PhD. Thesis, University of London.

Hymphrey, J.A.C. and Whitelaw, J.H. (1979) Turbulent flow in a duct with roughness, 2nd symposium on Turbulent Shear Flows, Imperial College, 17.7.

Hurd, C.W., Chesky, K.P. and Shapiro, A.H. (1953) Influence of viscous effects on impact tubes. Trans. ASME, J. Applied Mechanics 20,253.

Hussain, A.K.M.F. and Reynolds, W.C. (1975) Measurements in fully developed turbulent channel flow. Trans. ASME, J. Fluid Engineering 97,568.

Jones, W.P. and Launder, B.E. (1970) The prediction of laminarisation with a two-equation model of turbulence. Imperial College, Mech. Eng. Dept. Report BL/TN/A/40 also Int. J. Heat and Mass Transfer 15,301.

Jones, W.P. and Launder, B.E. (1973) The calculation of low Reynolds number phonomena with a two-equation model of turbulence, Int. J. Heat and Mass Transfer 16,1119.

Jonson, V.K. and Sparrow, E.M. (1966) Experiments on turbulent-flow phenomena in eccentric annular ducts. J. Fluid Mechanics 25,65.

Kacker, S.C. (1971) Estimation of Friction factors of rough surfaces from pressure distribution around a roughness element. CEGB Report RD/B/N1967.

Kacker, S.C. (1973) Some aspects of fully developed turbulent flow in non-circular ducts. J. Fluid Mechanics 57,583.

Kacker, S.C. (1973) Discussion of prediction of flow and heat transfer in ducts of square cross-section. Proc. Inst. Mech. Engineers 187,D147.

Kárman, Th.Von (1934) Turbulence and skin friction. J. Aero. Sciences 1,1.

Kárman, Th.Von (1937) The fundamentals of the statistical theory of turbulence. J. Aero. Sciences 4,131.

Kestin, J. and Richardson, P.D. (1962) Heat transfer across turbulent, incompressible boundary layers. Int. J. Heat and Mass Transfer 6,147.

Kettle, D.J. (1954) The design of static and pitot tubes for subsonic speeds. J. Roy. Aero. Society 58,835.

Kjellström, B. and Hedberg, S. (1966) On shear stress distributions for flow in smooth or partially rough annuli. Aktiebolaget Atomenergi Report AE-243.

Klebanoff, P.S. and Diehl, Z.W. (1952) Some features of artificially thickened fully developed turbulent boundary layers with zero pressure gradient. NACA Report 1110.

Klebanoff, P.S. (1955) Characteristics of turbulence in a boundary layer with zero pressure gradient. NACA Report 1247.

Kline, S.J., Reynolds, W.C., Schraub, F.A. and Runstadler, P.W. (1967) The structure of turbulent boundary layers. J. Fluid Mechanics 30,741.

Klinksiek, W.F. and Piecrce, F.J. (1973) A finite difference solution of the two-and three-dimensional incompressible turbulent boundary layer equations. Trans. ASME, J. Fluid Engineering 95,445.

Kolmogorov, A.N. (1942) Equations of turbulent motions of an incompressible turbulent fluid. Izv. Akad. Nauk. SSSR, Ser. Physics vol. VI, 56.

Kolmogorov, A.N. (1962) A refinement of previous hypothesis concerning the local structure of turbulence in a viscous incompressible fluid at high Reynolds number. J. Fluid Mechanics 13,82.

Koosinlin, M.L. (1974) Turbulent transport properties in swirling two-dimensional boundary layers. PhD. Thesis, University of London.

Kovasznay, L.S.G. (1967) Structure of turbulent boundary layer. The Physics of Fluids 10,S25.

Kovasznay, L.S.G. (1970) The turbulent boundary layer. Annual Review of Fluid Mechanics 2,95.

Laufer, J. (1951) Investigation of turbulent flow in a two-dimensional channel. NACA Report 1053.

Laufer, J. (1954) The structure of turbulence in fully developed pipe flow. NACA Report 1174.

Launder, B.E. (1968) The Prandtl - Kolmogorov model of turbulence with the inclusion of second order terms. Imperial College, Mech. Eng. Dept. Report BL/TN/2.

Launder, B.E. (1971) An improved algebraic modelling of the Reynolds stresses. Imperial College, Mech. Eng. Dept. Report TM/TN/A/9.

Launder, B.E. and Ying, W.M. (1972) Secondary flows in ducts on. J. Fluid Mechanics 54,289.

Launder, B.E. and Ying, W.M. (1973) Prediction of flow and heat transfer in ducts of square cross-section. Proc. Inst. Mech. Engineers 187,73.

Launder, B.E. and Spalding, D.B. (1972) Mathematical models of turbulence. Academic Press.

Launder, B.E., Reece, G.J. and Rodi, W. (1975) Progress in the development of a Reynolds stress turbulence closure. J. Fluid Mechanics 68,537.

Lawn, C.J. and Hamlin, M.J. (1968) Velocity measurements in roughened annuli. CEGB Report RD/B/N1278.

Lawn, C.J. (1970) Application of turbulence energy equation to fully developed flow in simple ducts. CEGB Report RD/B/N1575.

Lawn, C.J. (1971) The use of eddy viccosity model to predict the heat transfer and pressure drop performance of roughened surfaces. CEGB Report RD/B/N1980

Lefeuvre, R. (1973) Laminar and turbulent forced convection processes through in-line tube banks. PhD Thesis, University of London.

Leutheusser, H.J. (1963) Turbulent flow in rectangular ducts. Proc. ASCE, J. Hyd. Division 89, HY-3,1.

Ligget, J.A., Chiu, C.L. and Miao, L.S. (1965) Secondary currents in a corner. Proc. ASCE, J. Hyd. Division 91, HY-6,99.

Lyall, H.G. (1967) Transformation of rough surface data using the true position of the surface of no shear. CEGB Report RD/B/N922.

Lyall, H.G. (1971) Measurement of flow distribution and secondary flow in ducts composed of two interconnected sub-channels. Symposium on Internal Flows, University of Salford.

Mantle, P.L. (1966) A new type of roughened heat transfer surface selected by flow visualization techniques. Proc. 3rd Int. Heat Transfer Conference 1,45.

Maslen, S.H. (1958) Transverse velocities in fully developed flows. Quart. Appl. Math. 16,173.

Matthews and Whitelaw, J.H. (1971) The prediction of film cooling in the presence of recirculating flows with a two-equation turbulence model. Imperial College, Mech. Eng. Dept. Report HTS/71/31.

Mathieu, J. (1961) Contribution a l'etude aérothernique d'un jet plan évoluant en presence d'un paroi. Publ. Scientifiques et Techniques du Ministere de l'Air, no.374.

McMillan, F.A. (1954) Viscous effects on flattened pitot tubes at low speeds. J. Roy. Aero. Society 58,837.

McMillan, F.A. (1956) Experiments on pitot tubes in shear flow. Aero. Res. Council R and M 3028.

Melling, A. (1970) The laser Doppler shift technique and hot wire anemometry. M.Sc./DIC Report, Mech. Eng. Dept., Imperial College.

Melling, A. (1975) Investigation of flow in non-circular ducts and other configurations by laser Doppler anemometry. PhD. Thesis, University of London.

Melling, A. and Whitelaw, J.H. (1976) Turbulent flow in a rectangular duct. J. Fluid Mechanics 78,289.

Moore, W.L. (1951) An experimental investigation of the boundary bayer developement along a rough surface. PhD. Dissertation, State University of Iowa.

Morris, H.M. (1955) Flow in rough conduits. ASCE Transactions 120,373.

Morris, H.M. (1959) Design method for flow in rough conduits. Proc. ASCE, J. Hyd. Division 85, HY-7,43.

Morris, A.W. (1963) The generation of secondary vorticity in an incompressible fluid. Trans. ASME, J. Applied Mechanics 30,525.

Naot, D., Shavit, A. and Wolfshtein, M. (1972) Fully-developed turbulent flow in square channel. Report TME154, Mech. Eng. Dept., Technion, Haifa.

Naot, D., Shavit, A. and Wolfshtein, M. (1973) Two point correlation model and redistribution of Reynolds stresses. The Physics of Fluids 16,6.

Naot, D., Shavit, A. and Wolfshtein, M. (1974) Numerical calculation of Reynolds stresses in a square duct with secondary flow. Wärme und Stoffübertragung 7,151.

Nash, J.F. (1969) The calculation of three dimensional turbulent boundary layers in incompressible flow. J. Fluid Mecahanics 37,625.

Nash, J. F. (1972) Explicit scheme for the calculation of three dimensional turbulent boundary layers. Trans. ASME, J. Basic Engineering 94,131.

Nee, V.W. and Kovasznay, S.G. (1969) Simple phenomenogical theory of turbulent shear flows. The Physics of Fluids 12,473.

Ng, K.H. (1971) Predictions of turbulent boundary-layer developments using a two-equation model of turbulence. Imperial College, Mech. Eng. Department Report HTS/71/2.

Nicol, A.A. and Medwell, J.O. (1964) Velocity profiles and roughness effects in annular pipes. J. Mech. Eng. Science 6,110.

Nikuradse, J. (1926) Untersuchungen über die Geschwindigkeitsverteilung in turbulenten Strömungen. VDl Forschungsheft 70,1229.

Nikuradse, J. (1932) Gesetzmabigkeiten der turbulenten Strömung in glatten rohren. VDl-Forsch. 356.

Nikuradse, J. (1933) Strömungsgesetze in rauhen Rohran. VDl-Forsch. 361. Also Laws for flow in rough pipes NACA TM1292 (1950).

Nunner, W (1958) Heat transfer and Pressure drop in rough tubes. AERE Translation 786.

Olivari, D. (1976) Effects of the wire supports on the frequency response of hot wire anemometer. Vonkárman Institute of Fluid Dynamics TN118.

Palmer, M.D. and Keffer, J.F. (1972) An experimental investigation of an aysmmetrical turbulent wake. J. Fluid Mechanics 53,593.

Patel, V.C. (1965) Calibration of Preston tube and limitation on its use in pressure gradients. J. Fluid Mechanics 23,185.

Perkins, H.J. (1970) The formation of streamwise vorticity in turbulent flow. J. Fluid Mechanics 44,721.

Perry, A.E. and Joubert, P.N. (1963) Rough wall boundary layer in adverse pressure gradients. J. Fluid Mechanics. 17,193.

Perry, A.E., Schofield, W.H. and Joubert, P.N. (1969) Rough wall turbulent boundary layers. J. Fluid Mechanics 37,383.

Perry, A.E. and Morrison, G.L. (1971) Static and dynamic calibration of constant temperature hot wire system. J. Fluid Mechanics 47,765.

Perry, A.E. and Abell, C.J. (1977) Asymptotic similarity of turbulence structures in smooth and rough walled pipes. J. Fluid Mechanics 79,785.

Phillips, O.M. (1969) Shear flow turbulence. Annual Review of Fluid Mechanics 1,245.

Prandtl, L. (1925) Bericht über untersuchungen zur ausgebildeten turbulenz. ZAMM 5,136.

Prandtl, L. (1945) Über ein neues formelsystem für die ausgebildete tubulenz. Nachr. Akad, Wiss., Gottingen, IIA,6.

Rapier, A.C. (1963) Forced convection heat transfer in passages with varying roughness and heat flux around the perimeter. Thermodynamics and Fluid Mechanics Convention, Proc. of Inst. of Mech. Engrs., London 178. Pt 3.

Rehimi, K. (1973) Simple method of predicting friction factors of turbulent flow in non-circular channels. Int. J. Heat and Mass Transfer 16,933.

Reynolds, W.C. (1976) Computation of turbulent flows. Annual Review of Fluid Mechanics 8,183.

Roberts, L.W. (1972) Turbulent Swirling flows with recirculation. Imperial College, Mech. Eng. Dept. Report HTS/72/3.

Rodi, W. (1970) Basic equations for turbulent flow in cartesian and cylindrical co-ordinates. Imperial College, Mech. Eng. Dept. Report BL/TN/A/36.

Rodi, W. and Spalding, D.B. (1970) A two-parameter model of turbulence and its application to free jets. Wärme und Stoffübertrangung 3, 85.

Rodi, W. (1972) The prediction of free turbulent boundary layers by the use of a two-equation model of turbulence. Imperial College, Mech. Eng. Dept. Report HTS/72/24.

Rodi, W. (1975) A new method of analysing hot wire signals in highly turbulent flow and its evaluation in round jet. DISA Information No. 17.

Runchal, A.K. (1969) Transfer processes in steady two-dimensional separated flow. PhD. Thesis, University of London.

Runchal, A.K. (1972) Convergence and accuracy of three finite-difference schemes for a two-dimensional conduction and convection problem. Int. J. Num. Method in Engineering 4,541.

Sams, E.W. (1952) Experimental investigation of average heat transfer and friction coefficients for air flowing in circular tubes having square thread type roughness. NACA RM E52D17.

Savage, D.W. and Myers, J.E. (1963) The effect of artificial structure roughness on heat and momentum transfer. AIChE Journal 9,694.

Schlichting, H. (1960) Boundary Layer Theory. McGraw-Hill

Schulze, W.M., Ashby, Jr. G.C. and Erwin, J.R. (1952) Several combination probes for surveying static and total pressure and flow direction. NACA TN 2830.

Sheriff, N. and Gumley, P. (1966) Heat-transfer and friction properties of surfaces with discrete roughness. Int. J. Heat and Mass Transfer 9,1297.

Simpson, R.L. (1973) A general correlation of roughness density effects on the turbulent boundary layer. AlAA Journal 11,242.

Spalding, D.B. (1972) A novel finite-difference formulation for differential expression involving both first and second derivatives. Int. J. Num. Method in Engineering 4,551.

Stephens, M.J. (1970) Investigation of flow in a concentric annulus with smooth outer and rough inner wall. Part 1. Transverse rib type roughness. CEGB Report RD/B/N1535.

Sternberg, J. (1965) The three-dimensional structure of the viscous sublayer. Agardograph 97.

Tatchell, D.G. (1975) Convection processes in combined three-dimensional boundary layers. PhD. Thesis, University of London.

Tennekes, H. and Lumley, J.H. (1972) A First Course in Turbulence. MIT Press, Cambridge, Mass.

Thailland, A. and Mathieu (1967) Jet parietal. J. de Mecanique 6,103.

Thomas, D.L. and Easter, P.G. (1972) Measurement of wall shear stress in a duct of square cross-section. CEGB Report RD/B/N2477.

Townes, H.W. and Sabersky, R.H. (1966) Experiments on the flow over rough surface. Int. J. Heat and Mass Transfer 9,729.

Townsend, A.A. (1956) The structure of Turbulent Shear Flows. Cambridge University Press, Cambridge.

Townsend, A.A. (1961) Equilibrium layers and wall turbulence. J. Fluid Mechanics 11,97.

Tracy, H.J. (1965) Turbulent flow in three-dimensional channel. Proc. ASCE, J. Hyd. Division 91, HY-6,9.

Ueda, T. and Harada, I. (1964) Experiments on heat transfer on surfaces with transverse fins for flow direction. Bulletin JSME 7,759.

Vollmers, H. and Rotta, J.C. (1977) Similar solutions of the mean velocity, turbulent energy and length scale equation. AlAA Journal 15,714.

Wallace, J.M., Eckmann, H. and Brodkey, R.S. (1972) The wall region of turbulent shear flow. J. Fluid Mechanics 55,65.

Walker, V. and Wilkie, D. (1967) The wider application of roughened heat transfer surfaces as developed for advanced gas cooled reactors. Inst. Mech. Engrs. London. Paper 26.

Watson, M.A.P. (1970) The performance of a square rib type of heat transfer surface. CEGB Report RD/B/N1738.

Webb, R.L., Eckert, E.R.G. and Goldstein. (1971) Heat transfer and friction in tubes with repeated-rib roughness. Int. J. Heat and Mass Transfer 14,601.

Wheeler, A.J. and Johnstone, J.P. (1973) An assessment of three-dimensional boundary layer prediction methods. Trans. ASME, J. Fluid Engineering 95,415.

Whitehead, A.W. (1976) The effects of surface roughening on fluid flow and heat transfer. PhD. Thesis, University of London.

Wilkie, D. (1966a) Forced convection heat transfer from surfaces roughened by transverse ribs. Proc. 3rd Int. Heat Transfer Conference 1,1.

Wilkie, D. (1966b) Calculation of heat transfer and flow resistance of rough and smooth surfaces contained in a single passage. Proc. 3rd Int. Heat Transfer Conference 1,20.

Wilkie, D., Cowin, M., Burnett, P. and Burgoyne, T. (1967) Friction factor measurements in a rectangular channel with walls of identical and non-identical roughness. Int. J. Heat and Mass Transfer 10,611.

Wolfshtein, M. (1967) Convection processes in turbulent impinging jets. PhD. Thesis, University of London.

Wu, J.C. and Sugaranam, A. (1978) Method for numerical solution of turbulent flow problem. AlAA Journal 16,948.

Yaglom, A.M. (1979) Similarity laws for constant pressure and pressure gradient turbulent wall flows. Annual Review of Fluid Mechanics 11,505.

Ying, W.M. (1971) Fully developed flow with swirl in non-circular ducts. PhD. Thesis, Univeristy of London.

Yound, A.D. and Mass, J.N.A. (1936) The behaviour of a pitot tube in a transverse total pressure gradient. Aero. Res. Council R and M 1770.

LIST OF FIGURES

1. Ilustration of Hall's transformation

2.1 Part of the grid showing the co-ordinate system and grid notations

3.1 Schematic diagram of the flow system

3.2 Isometric view of the duct section and axis notations

3.3 Detailed view of static pressure hole, pitot tube and pitot tube mouth

3.4 (a) The Wheatstone bridge circuit
(b) The measurement of secondary flow angle

3.5 Detailed view of yawmeters used for measurements of secondary flow angles γ_2 and γ_3

3.6 Traversing mechanism

3.7 Symmetry check of U_1/U_c and $\tilde{u}_1/U_c$ for the duct with one rough wall

3.8 Symmetry check of U_1/U_c, $\tilde{u}_1/U_c$ and γ_2 for the duct with two rough walls

4.1 Mean velocity profiles across the rough wall

4.2 Mean velocity profiles parallel to the rough wall

4.3 Clauser chart plot for the rough wall ($x_3 = 0$)

4.4 Clauser chart plot for the smooth wall ($x_3 = a$)

4.5 Clauser chart plot for the side wall

4.6 Logarithmic plot of mean velocity near the rough wall

4.7 Logarithmic plot of mean velocity near the small wall

4.8 Contours of mean velocity, U_1/U_c

4.9 Distribution of secondary flow angle γ_2

4.10 Distribution of secondary flow angle γ_3

4.11 Distribution of U_2/U_c vectors

4.12 Distribution of U_3/U_c vectors

4.13 Distribution of secondary velocity vectors, U_s/U_c

4.14 Friction factor V_s Reynolds number

4.15 Pressure gradient along the duct axis

4.16 Distribution of local wall shear stress

4.17 Contours of $\tilde{u}_1/U_c x10^2$

4.18 Contours of $\tilde{u}_2/U_c x10^2$

4.19 Contours of $\tilde{\tilde{u}}_3/U_c x10^2$

4.20 Contours of $\overline{u_1 u_2}/U_c^2 x10^3$

4.21 Contours of $\overline{u_1 u_3}/U_c^2 x10^3$

4.22 Contours of $k/U_c^2 x10^3$

4.23 Contours of $(\overline{u_2^2}-\overline{u_3^2})/U_c^2 x10^3$

4.24 Spectra of $\overline{u_1^2}$ near the rough wall

4.25 Comparison of mean velocity profiles

4.26 Logarithmic plot of mean velocity near the rough wall with origin shifted above the rib root

4.27 Comparison of U_1/U_c contours

4.28 Contours of $U_3/U_c x10^2$ of Humphrey

4.29 Comparison of smooth wall shear stress

4.30 Comparison of $\tilde{\tilde{u}}_1/U_c x10^2$ contours

4.31 Comparison of $\tilde{u}_3/U_c x10^2$ contours

4.32 Comparison of $\overline{u_1 u_3}/U_c^2 x10^3$ contours

4.33 Contours of zero shear stress and zero velocity gradient

5.1 Mean velocity profiles across the rough wall

5.2 Mean velocity profiles parallel to the rough wall

5.3 Clauser chart plot for the rough wall

5.4 Clauser chart plot for the smooth wall

5.5 Logarithmic plot of mean velocity near the rough wall

5.6 Logarithmic plot of mean velocity near the smooth wall

5.7 Contours of mean velocity U_1/U_c

5.8 Distribution of secondary flow angle, γ_2

5.9 Distribution of secondary flow angle, γ_3

5.10 Distribution of U_2/U_c vectors

5.11 Distribution of U_3/U_c vectors

5.12 Distribution of U_s/U_c vectors

5.13 Variation of friction factor with Re

5.14 Pressure gradient along the duct axis.

5.15 Distribution of local wall shear stress

5.16 Contours of $\tilde{u}_1/U_c \times 10^2$

5.17 Contours of $\tilde{u}_2/U_c \times 10^2$

5.18 Contours of $\tilde{u}_3/U_c \times 10^2$

5.19 Contours of $\overline{u_1 u_2}/U_c^2 \times 10^3$

5.20 Contours of $\overline{u_1 u_3}/U_c^2 \times 10^3$

5.21 Contours of $k/U_c^2 \times 10^3$

5.22 Contours of $(\overline{u_2^2}-\overline{u_3^2})/U_c^2 \times 10^3$

5.23 Spectra of $\overline{u_1^2}$ on the rough wall midplane

5.24 Comparison of mean velocity profiles

5.25 Comparison of U_1/U_c contours

5.26 Logarithmic plot of mean velocity near the rough wall with origin shifted above the rib root

5.27 Comparison of smooth wall shear stress

5.28 Relation between the ratios of $\overline{\tau}_s/\overline{\tau}'_s$ and $\overline{\tau}_r\ \overline{\tau}'_r$

5.29 Comparison of $\tilde{u}_1/U_c x10^2$ contours

5.30 Comparison of $\tilde{u}_2/U_c x10^2$ contours

5.31 Comparison of $\tilde{u}_3/U_c x10^2$ contours

5.32 Comparison of $\overline{u_1 u_2}/U_c^2 x10^3$ contours

5.33 Comparison of $\overline{u_1 u_3}/U_c^2 x10^3$ contours

5.34 Comparison of $k/U_c^2 x10^3$ contours

5.35 Comparison of $(\overline{u_2^2}-\overline{u_3^2})/U_c^2 x10^3$ contours

5.36 Comparison of $\overline{u_f^2}$ spectra near the rough wall

5.37 Profile of logitudinal integral scales

6.1 Comparison of U_1/U_c contours in smooth ducts

6.2 Comparison of U_1/U_c contours in a duct with two rough walls

6.3 Comparison of U_1/U_c contours in a duct with one rough wall

6.4 Comparison of secondary velocity vectors in a smooth duct

6.5 Comparison of secondary velocity vectors in a duct with two rough wall

6.6 Comparison of secondary velocity vectors in a duct with one rough wall

6.7 Comparison of wall shear stress distribuion of smooth ducts

6.8 Comparison of wall shear stress distribution of a duct with two rough walls

6.9 Comparison of wall shear stress distribution of a duct with one rough wall

6.10 Comparison of $\overline{u_1 u_2}/U_c^2 x10^3$ contours in a smooth duct

6.11 Comparison of $\overline{u_i u_3}/U_c^2 x10^3$ contours in a smooth duct

6.12 Comparison of turbulence kinetic energy contours in smooth ducts

6.13 Comparison of $\overline{u_1 u_2}/U_c^2 x10^3$ contours in a duct with two rough walls

6.14 Comparison of $\overline{u_1 u_3}/U_c^2 x10^3$ contours in a duct with two rough walls

6.15 Comparison of $k/U_c^2 x10^3$ contours in a duct with two rough walls

6.16 Comparison of $\overline{u_1 u_2}/U^2 x10^3$ contours in a duct with one rough walls

6.17 Comparison of $\overline{u_1 u_3}/U^2 x10^3$ contours in a duct with one rough wall

6.18 Comparison of $k/U_c^2 x10^3$ contours in a duct with one rough wall

6.19 Comparison of mean velocity profile in a duct with one rough wall

7.1 Variation of flow pattern with P/e

7.2 Law of the wall for rough and smooth walls in rough-smooth ducts.

7.3 Profiles of $\overline{u_1 u_3}/k$ in a duct with one rough wall

7.4 Profiles of $u_1 u_3/k$ in a duct with two rough walls

7.5 Profiles of $u_1 u_2/k$ in a duct with one rough wall

7.6 Profiles of $u_1 u_2/k$ in a duct with two rough walls

7.7 Diagram showing the planes of zero velocity gradient and zero shear stress

APPENDIX FIGURES

A 3.1 Calibration curve for the yawmeters

A 4.1 Profiles of $\tilde{u}_1/U \times 10^2$

A 4.2 Profiles of $\tilde{u}_2/U_c \times 10^2$

A 4.3 Profiles of $\tilde{u}_3/U_c \times 10^2$

A 4.4 Profiles of $\overline{u_1 u_2}/U_c^2 \times 10^3$

A 4.5 Profiles of $\overline{u_1 u_3}/U_c^2 \times 10^3$

A 4.6 Profiles of $k/U_c^2 \times 10^3$

A 4.7 Profiles of $(u_2^2-u_3^2)/U_c^2 \times 10^3$

A 5.1 Profiles of $\tilde{u}_1/U_c \times 10^2$

A 5.2 Profiles of $\tilde{u}_2/U_c \times 10^2$

A 5.3 Profiles of $\tilde{u}_3/U_c \times 10^2$

A 5.4 Profiles of $\overline{u_1 u_2}/U^2 \times 10^3$

A 5.5 Profiles of $\overline{u_1 u_3}/U_c^2 \times 10^3$

A 5.6 Profiles of $k/U_c^2 \times 10^3$

A 5.7 Profiles of $(u_2^2-u_3^2)/U_c^2 \times 10^3$

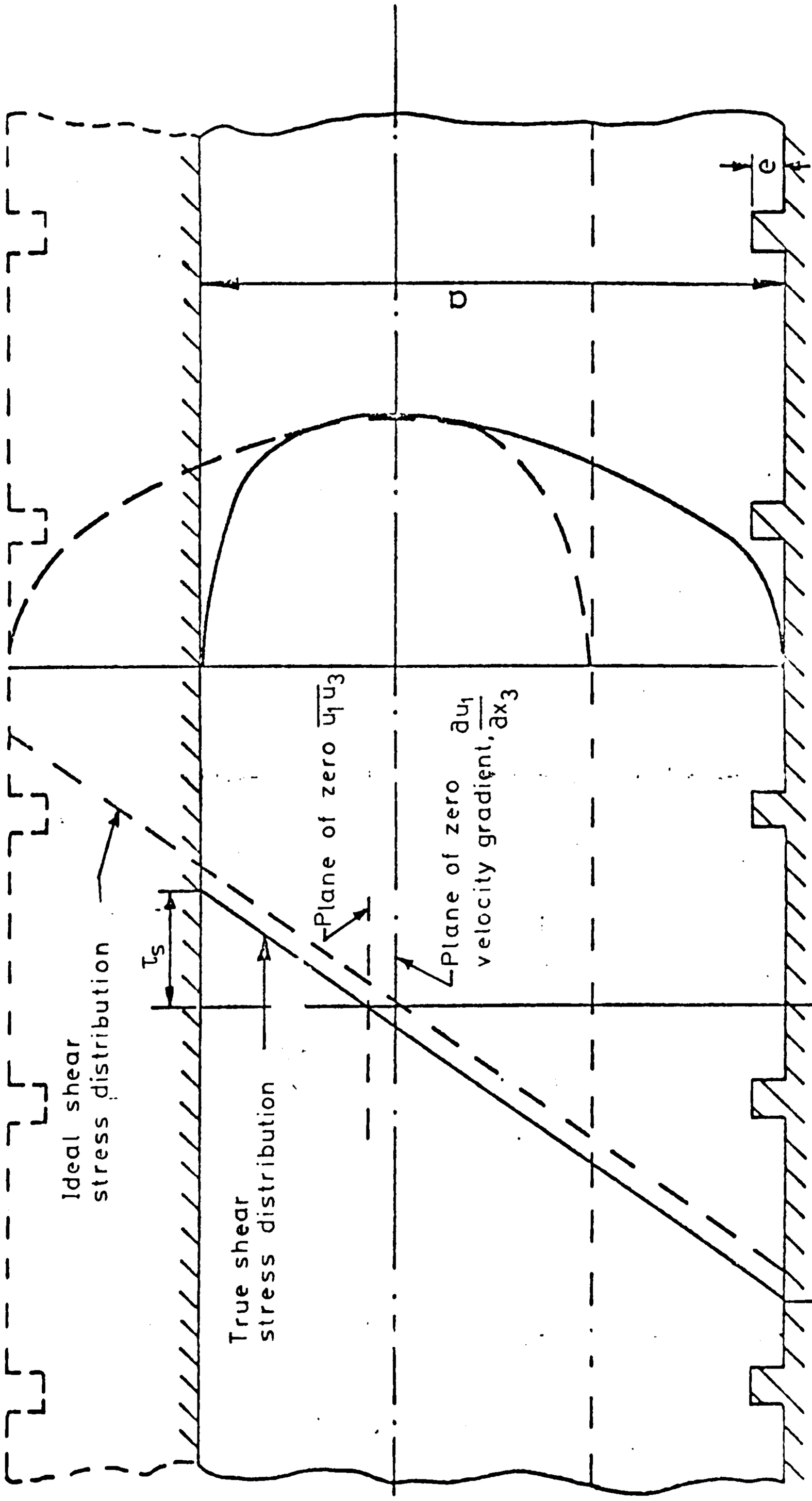

Fig.1'1 Illustration of Hall's transformation.

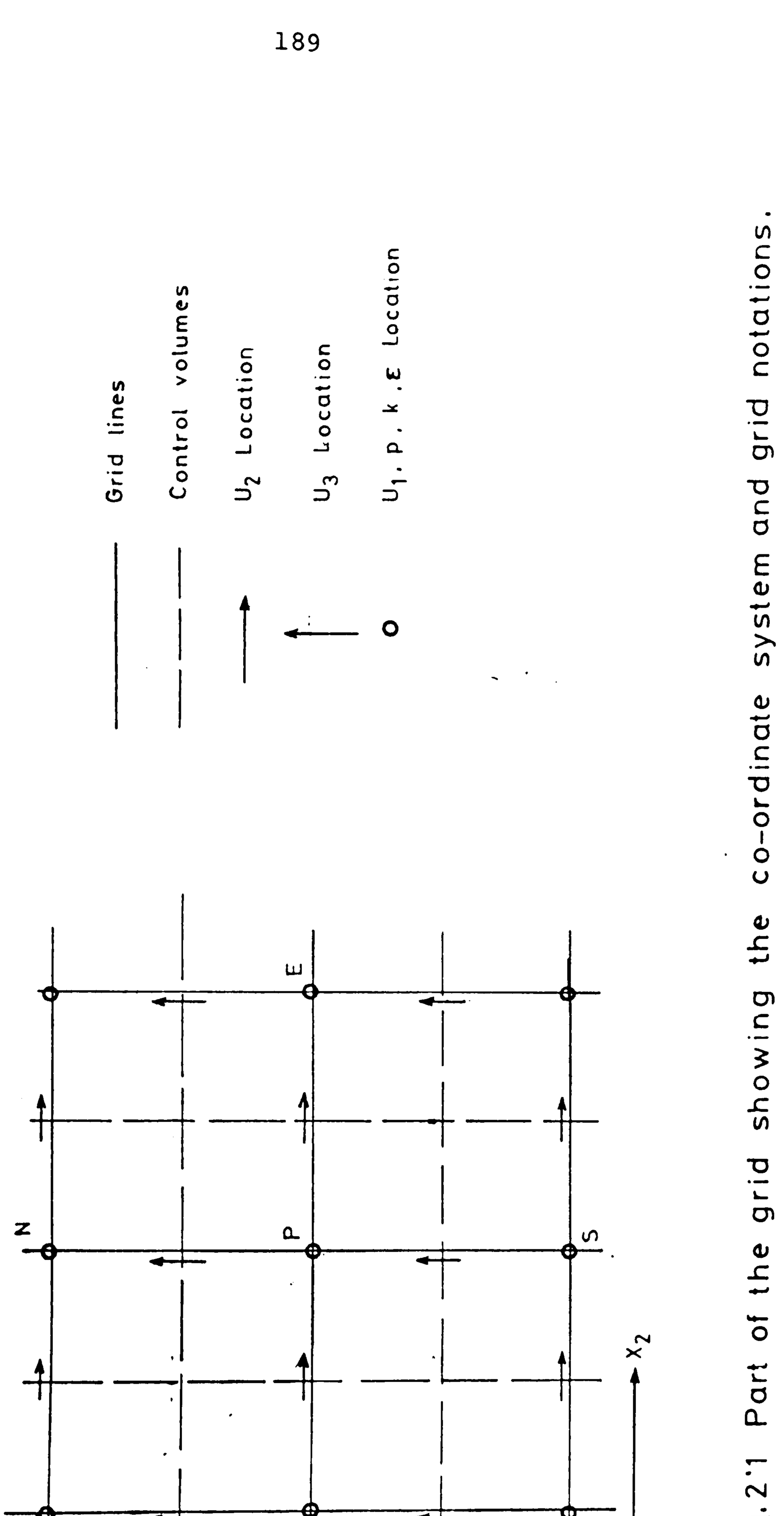

Fig. 2'1 Part of the grid showing the co-ordinate system and grid notations.

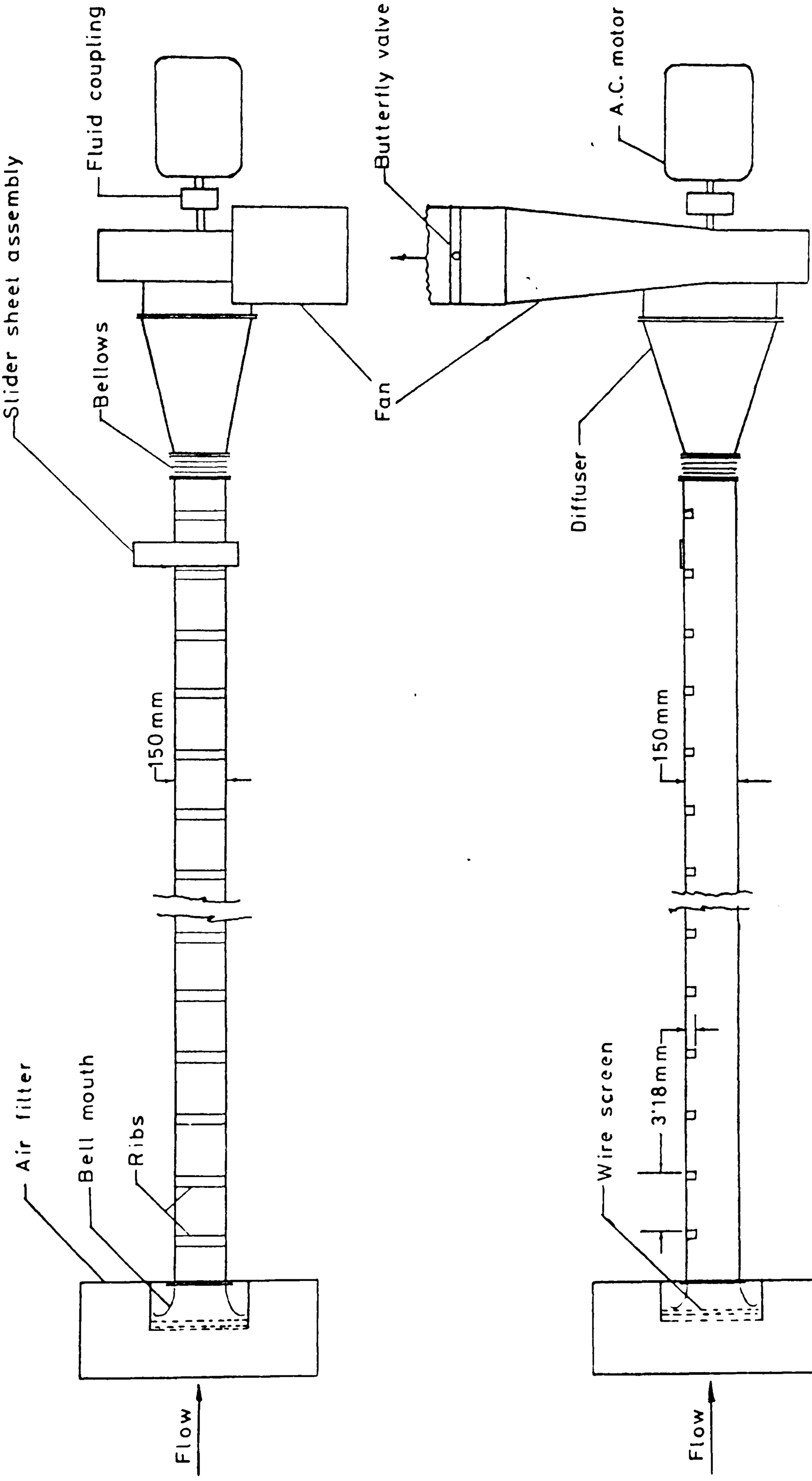

Fig. 3·1 Schematic diagram of the flow system.

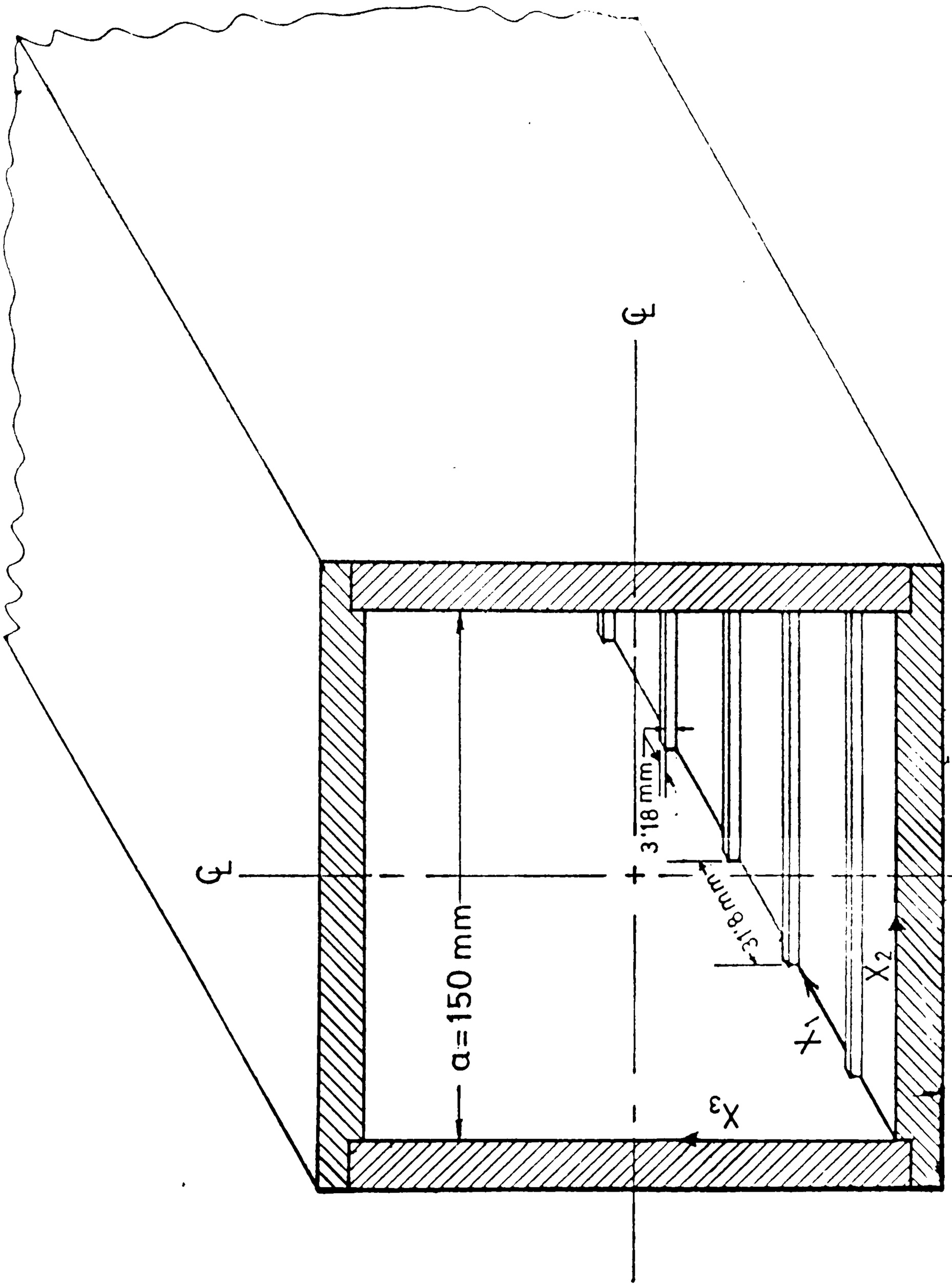

Fig. 3'2 Isom
and

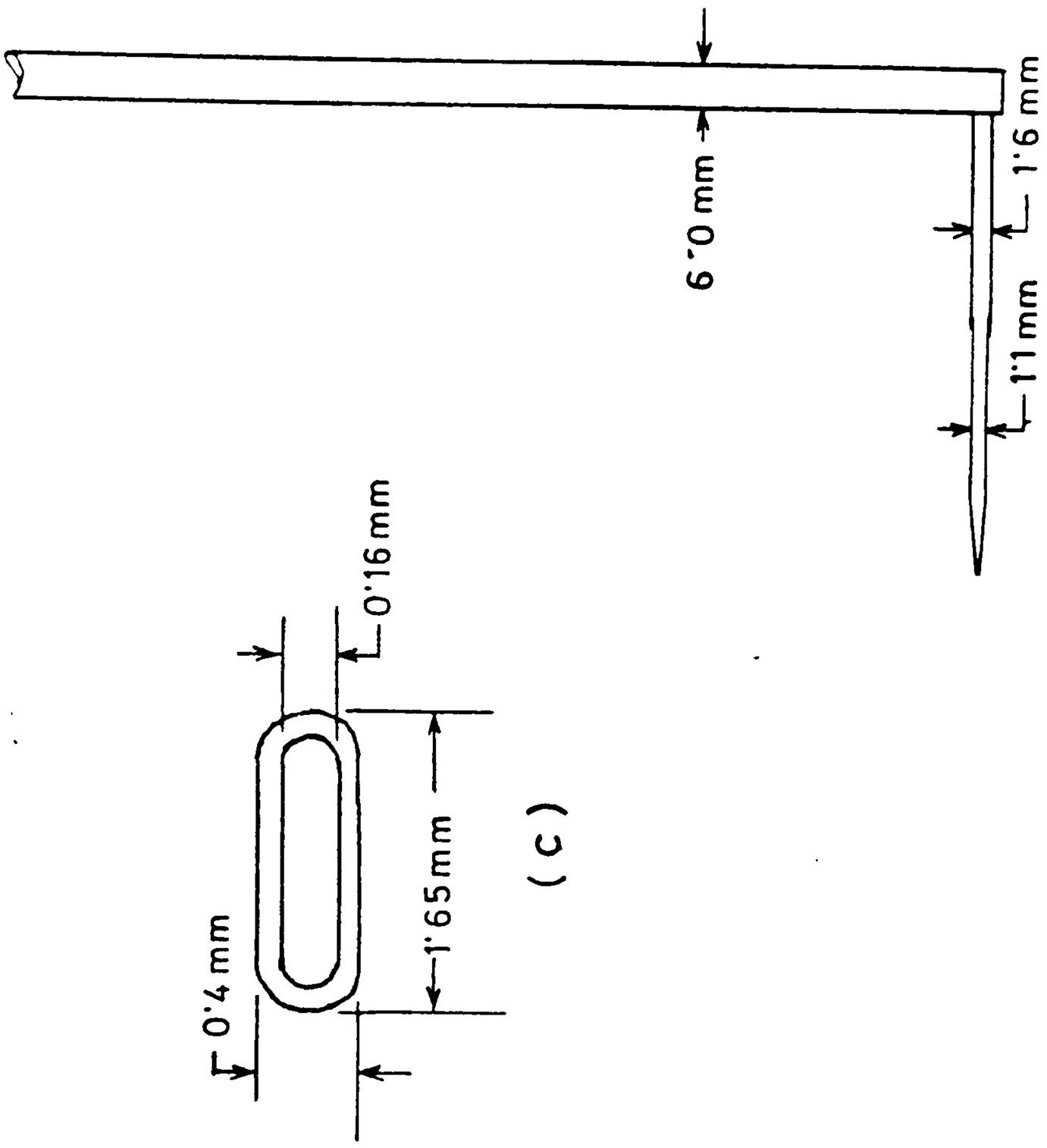

Fig. 3'3 (a) Sectional view of static pressure hole. (b) pitot tube, (c) pitot tube mouth.

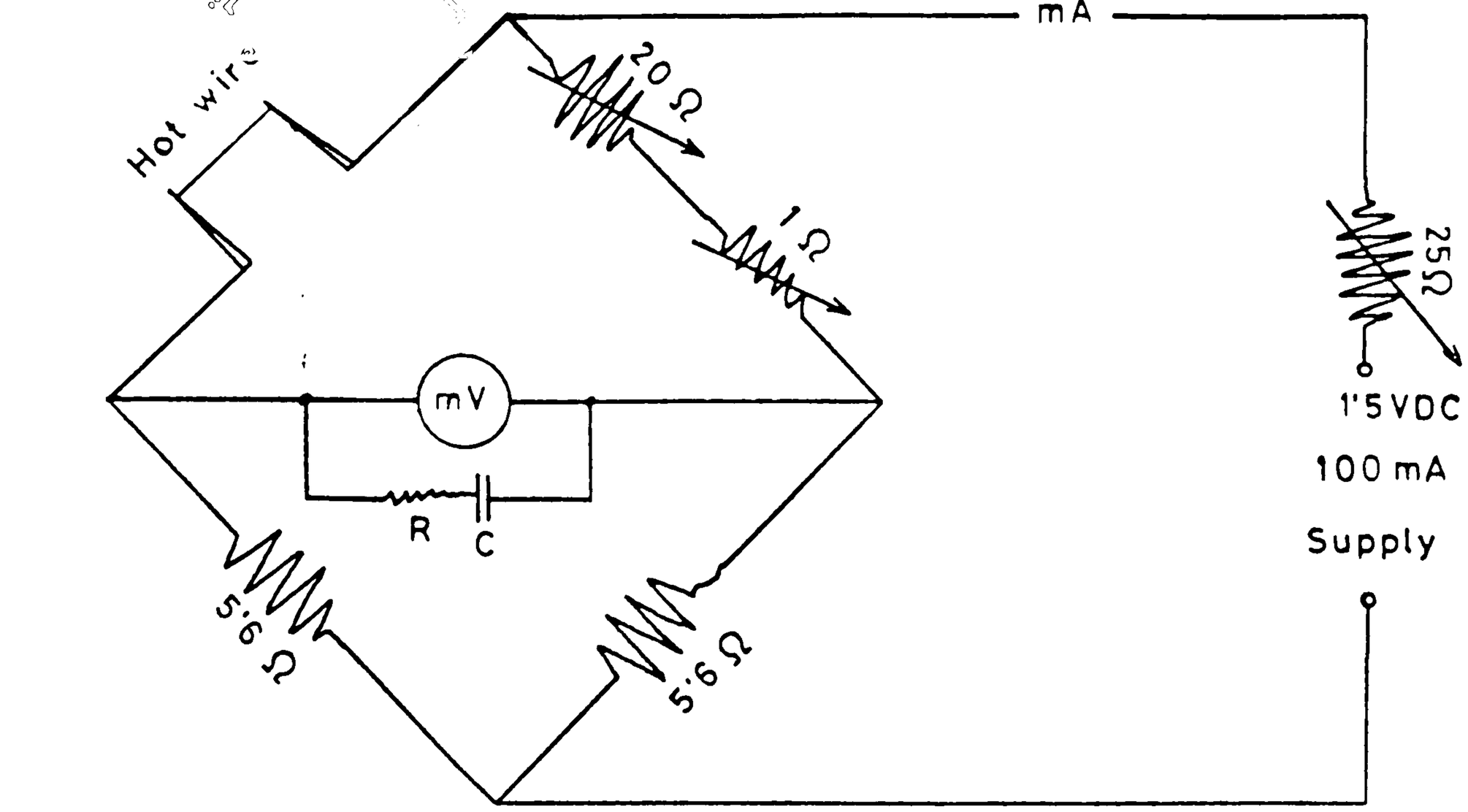

(a)

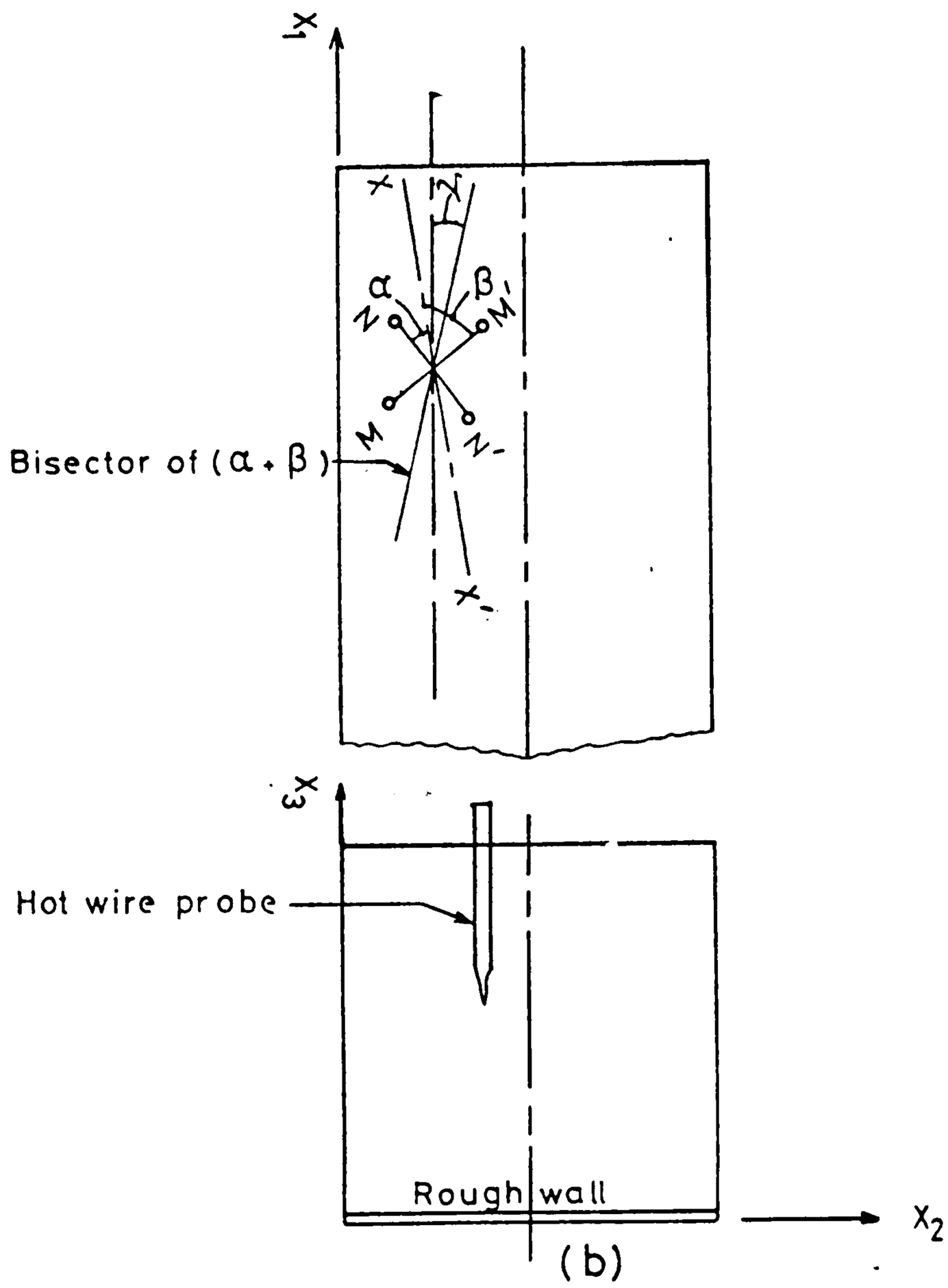

Fig. 3·4 (a) The Wheatston bridge circuit

(b) The measurement of secondary flow angle with hot wire.

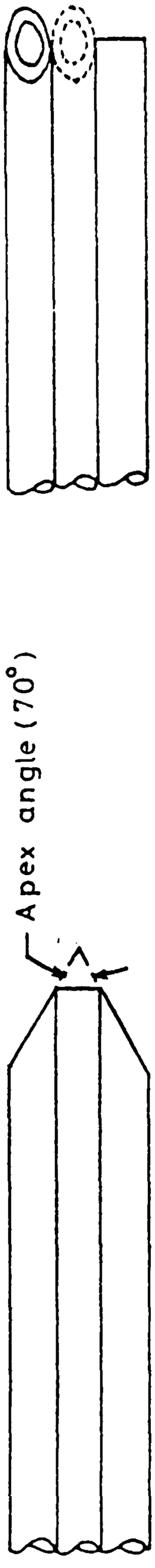

Fig. 3·5 Yawmeters used for measuring secondary flow angles (a) γ_2 and (b) γ_3

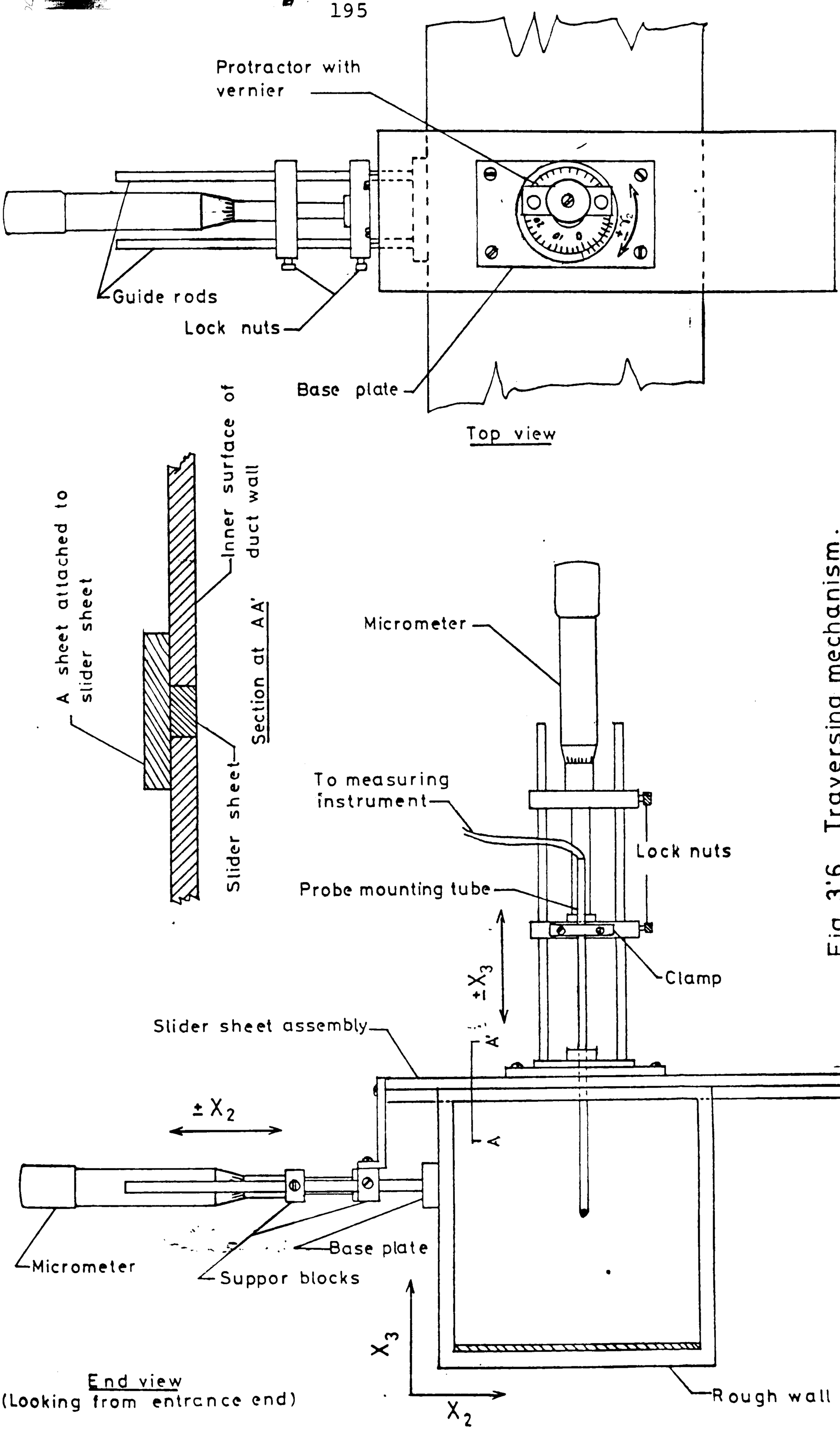

Fig. 3'6 Traversing mechanism.

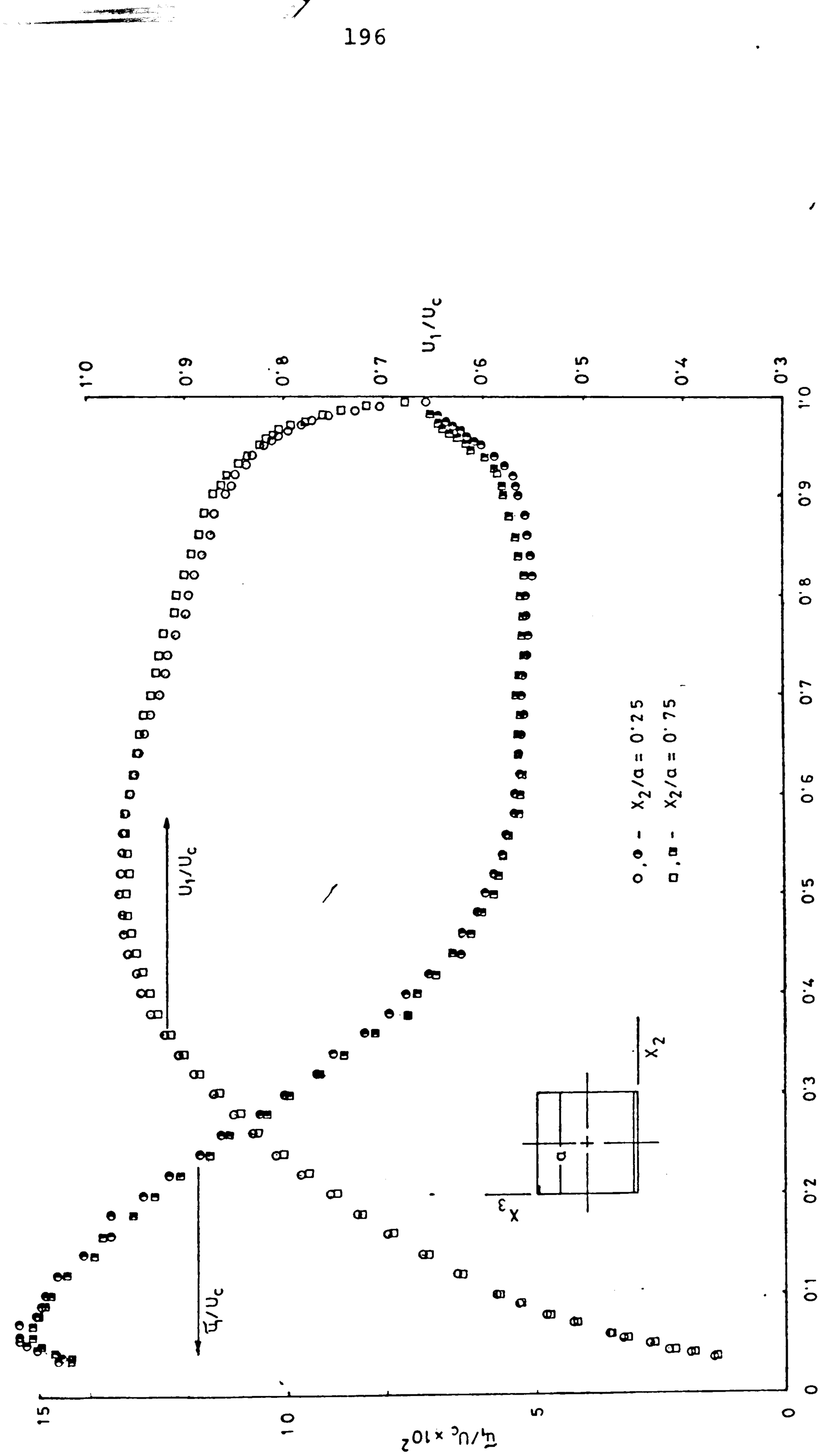

Fig. 3·7 Symmetry check of U_1/U_c & $\bar{u}_1/U_c$ for the duct with one rough wall.

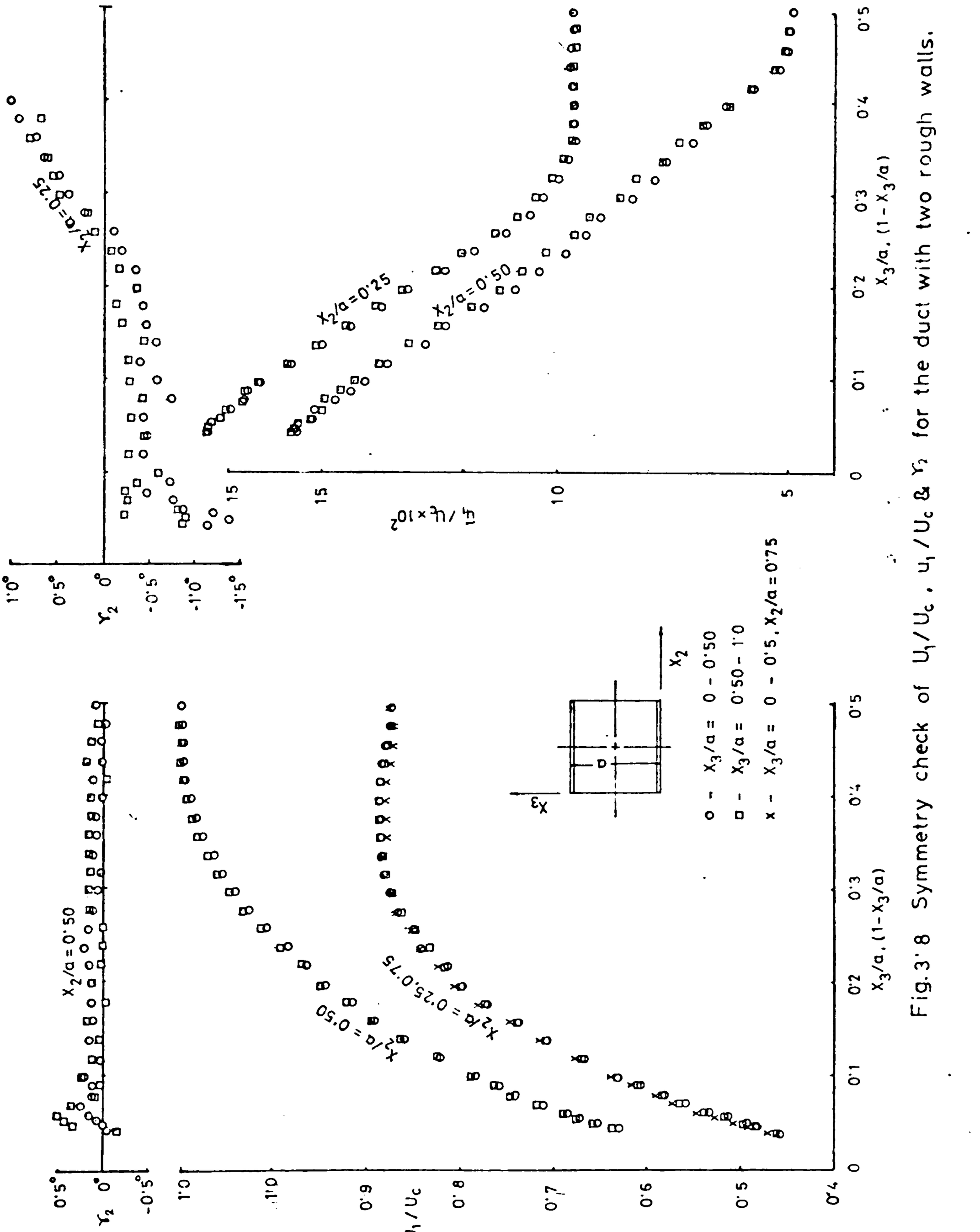

Fig.3·8 Symmetry check of U_1/U_c.

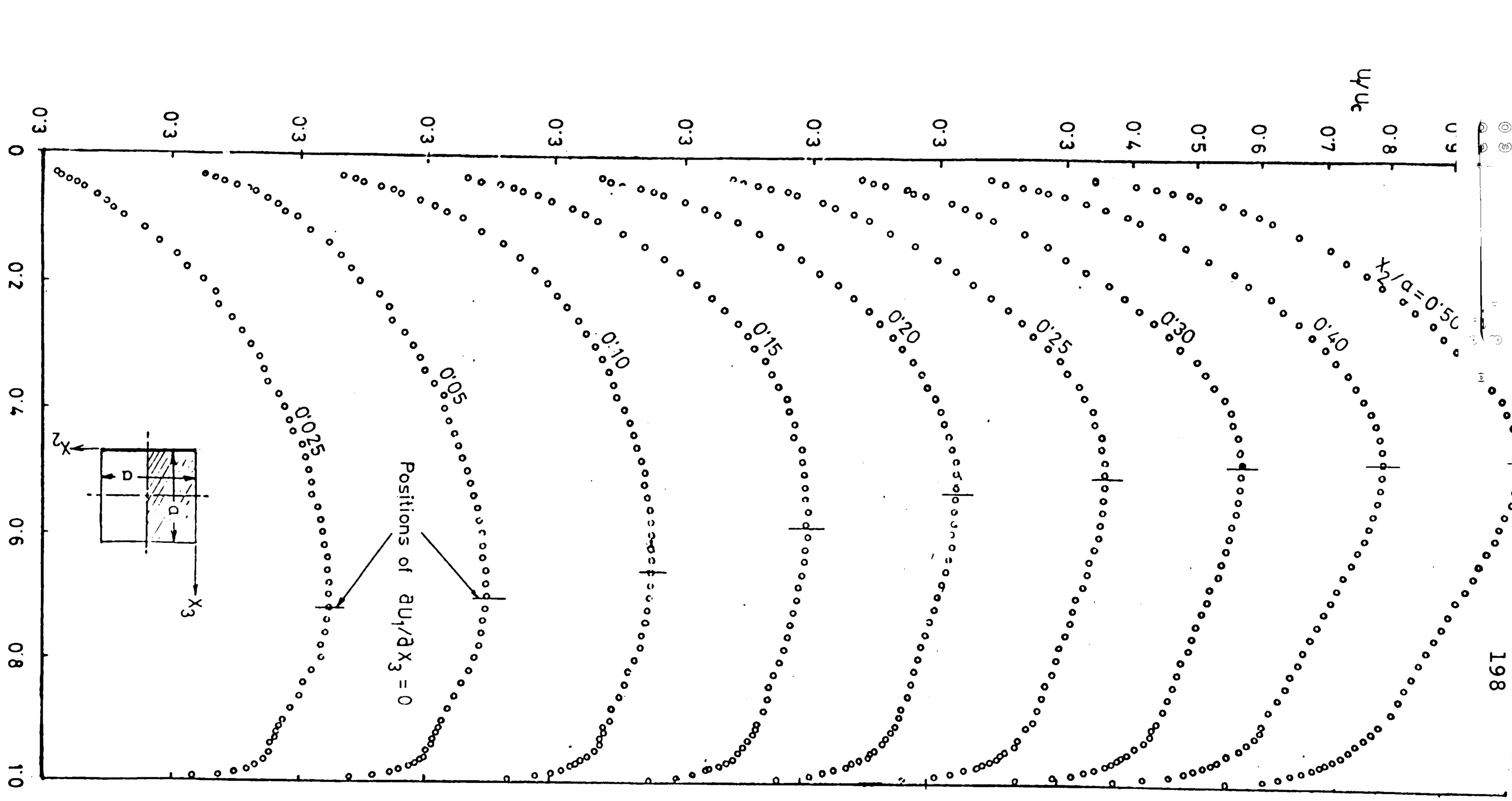

Fig. 4·1 Mean velocity profiles across the rough wall.

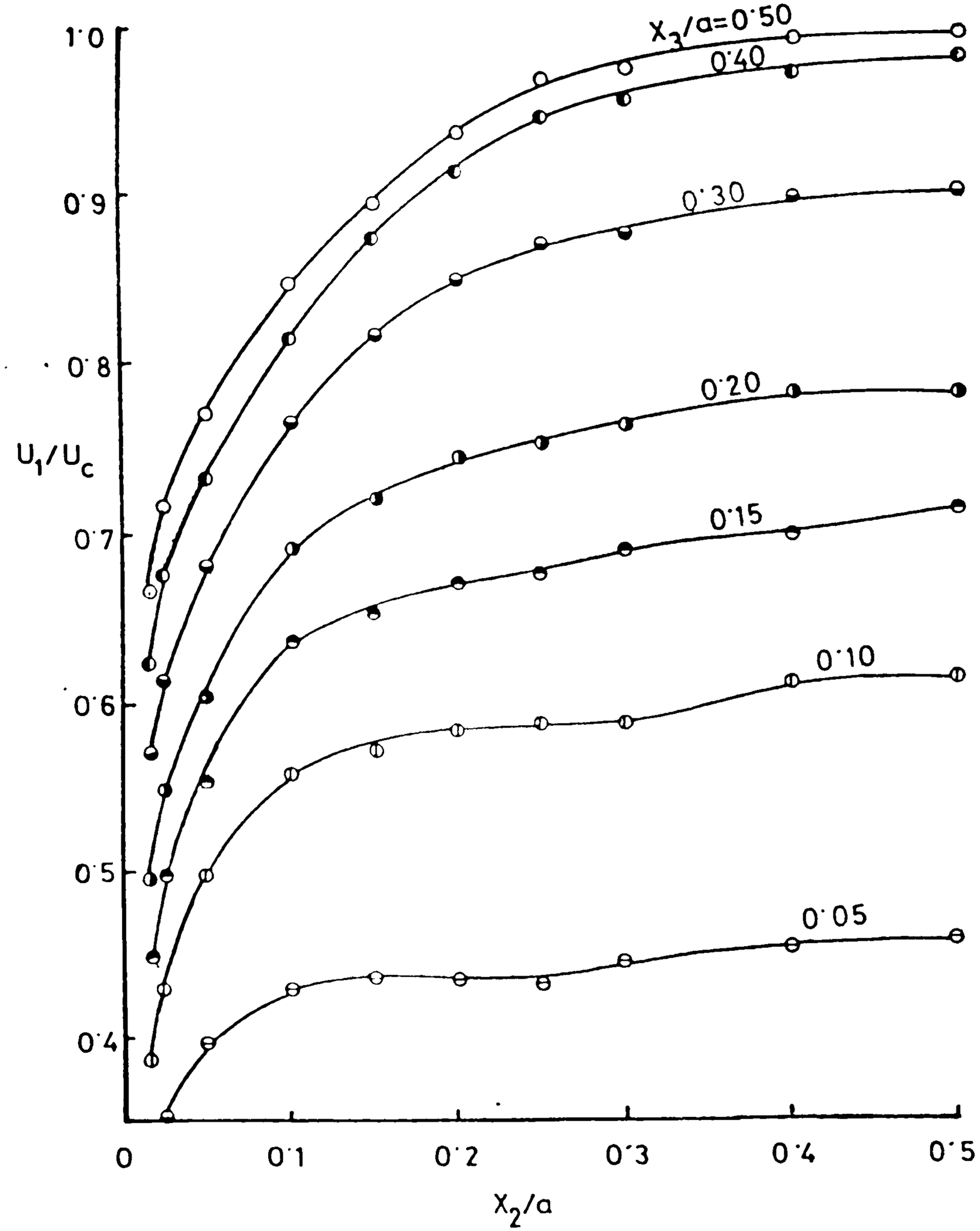

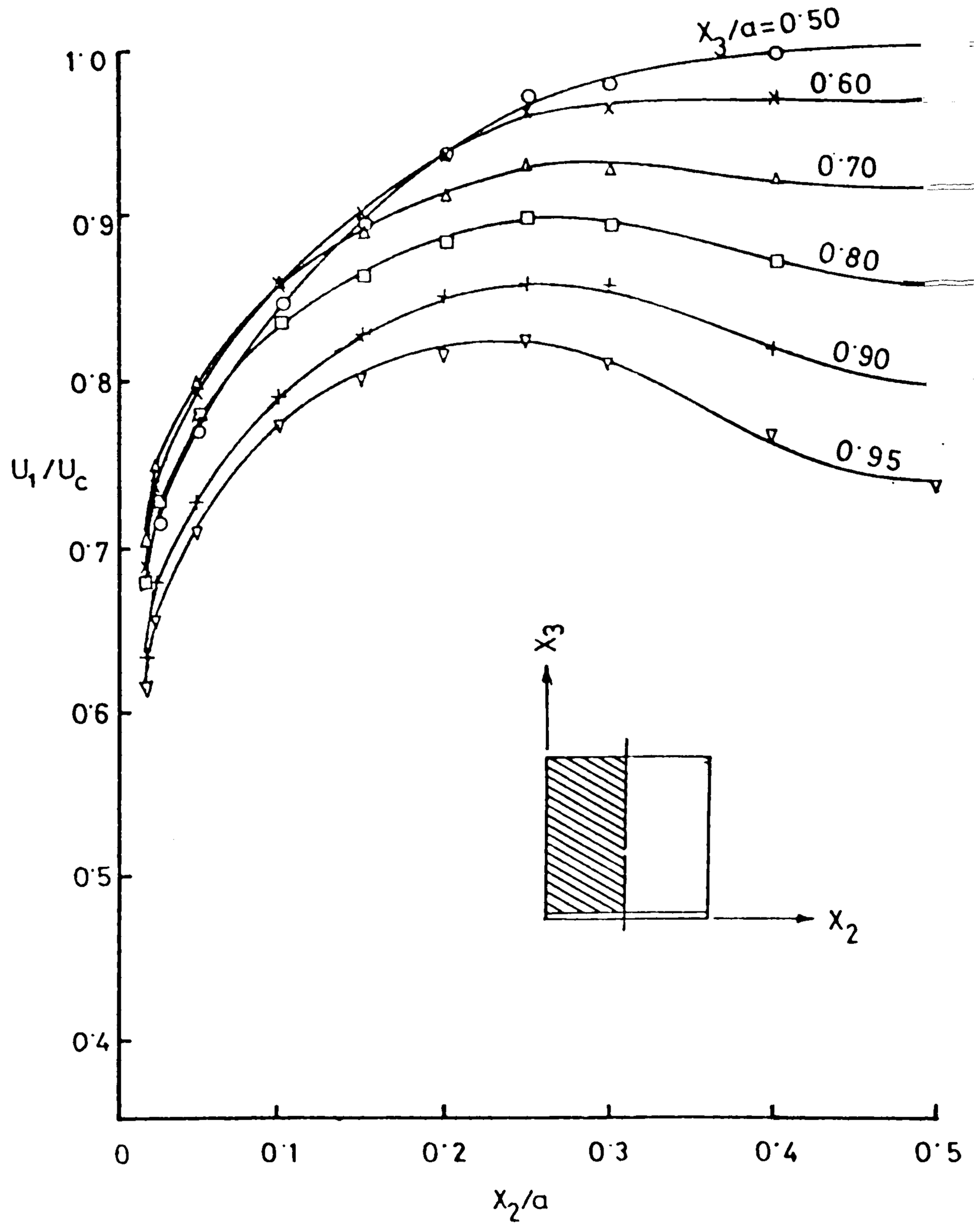

Fig. 4·2 Mean velocity profiles parallel to the rough wall (X_2 – axis).

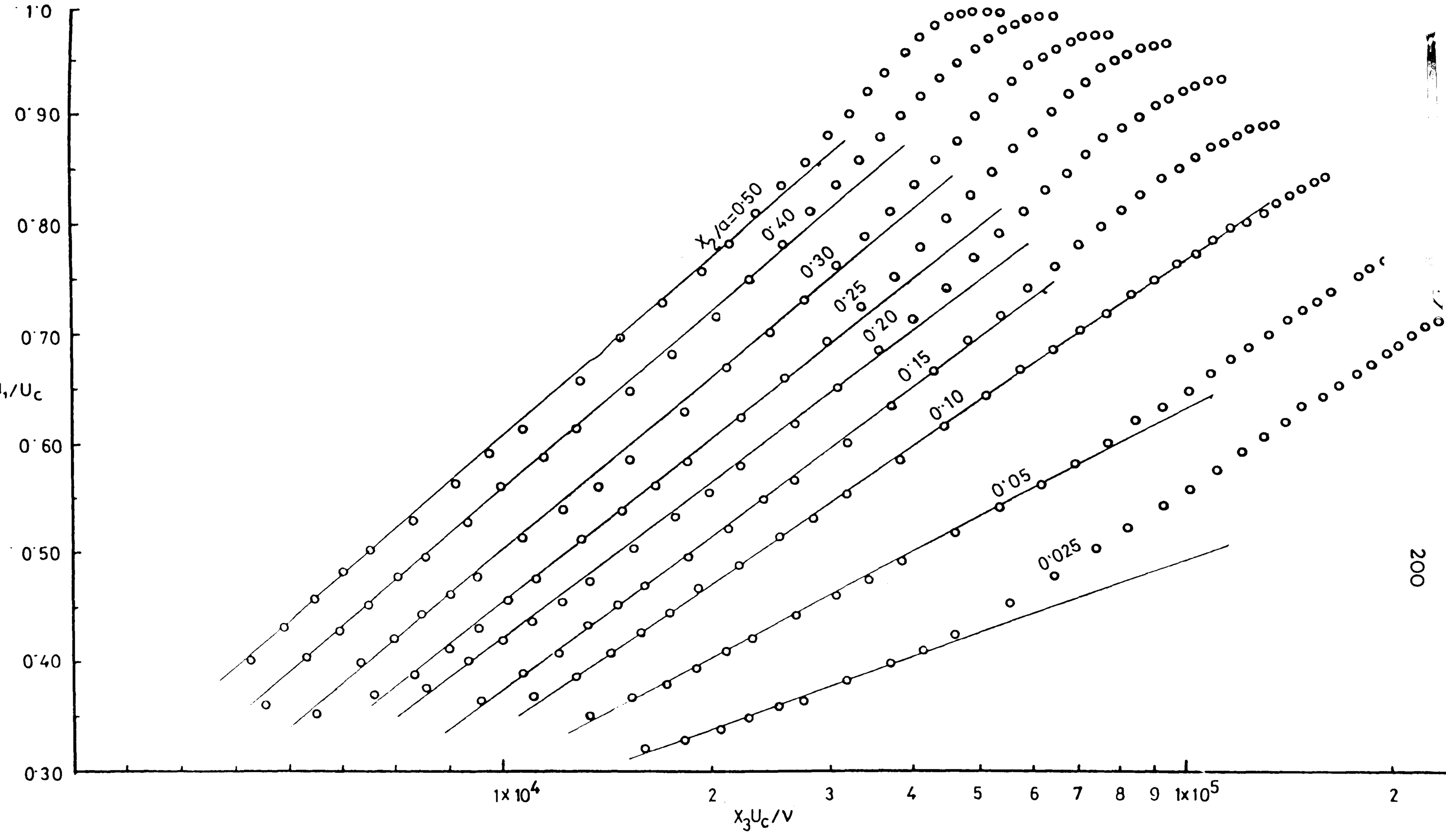

Fig.4·3 Clauser chart plot for the rough wall ($X_3 = 0$).

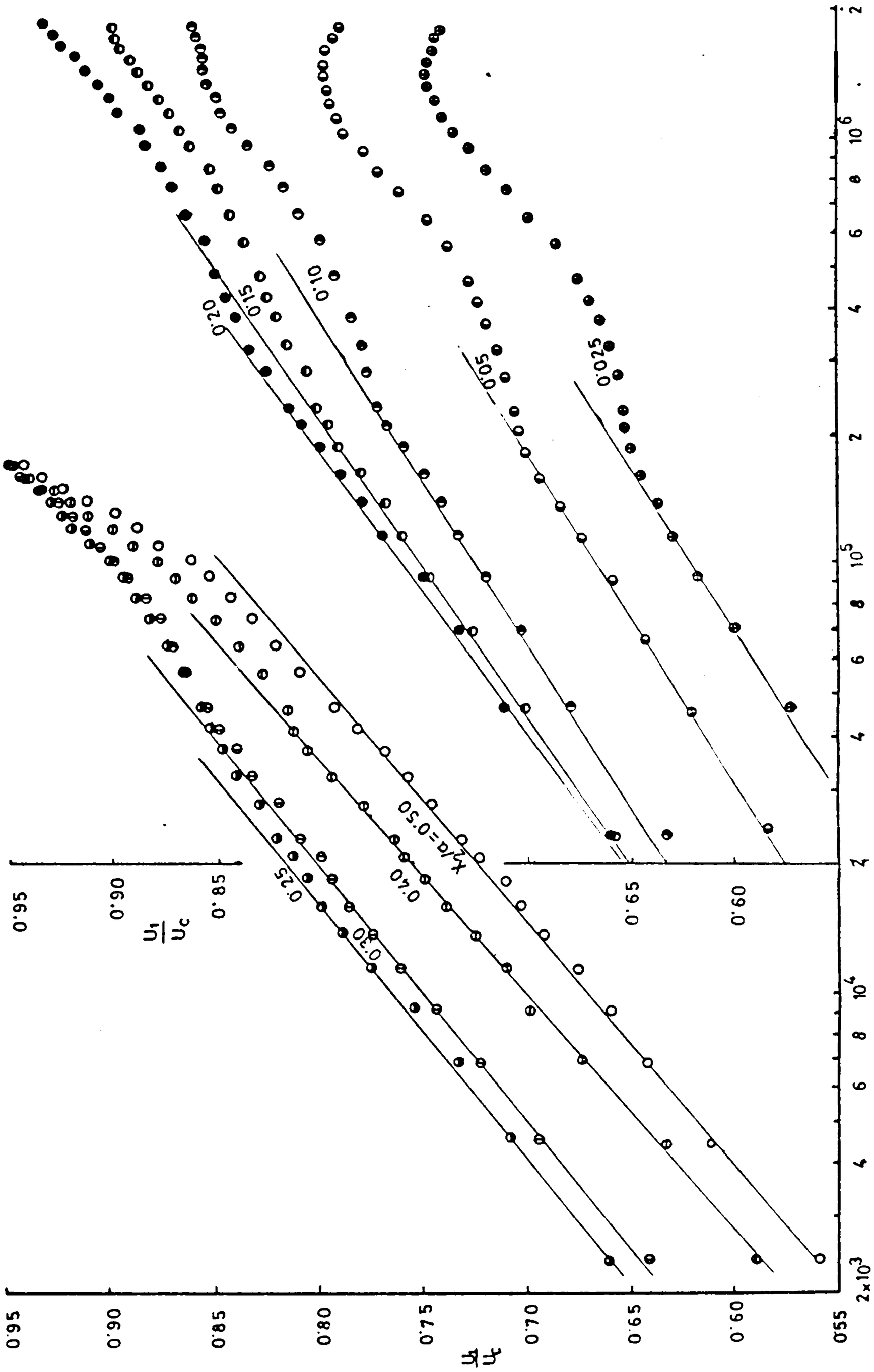

Fig. 4·4 Clauser chart plot for the smooth wall ($X_3 = a$)

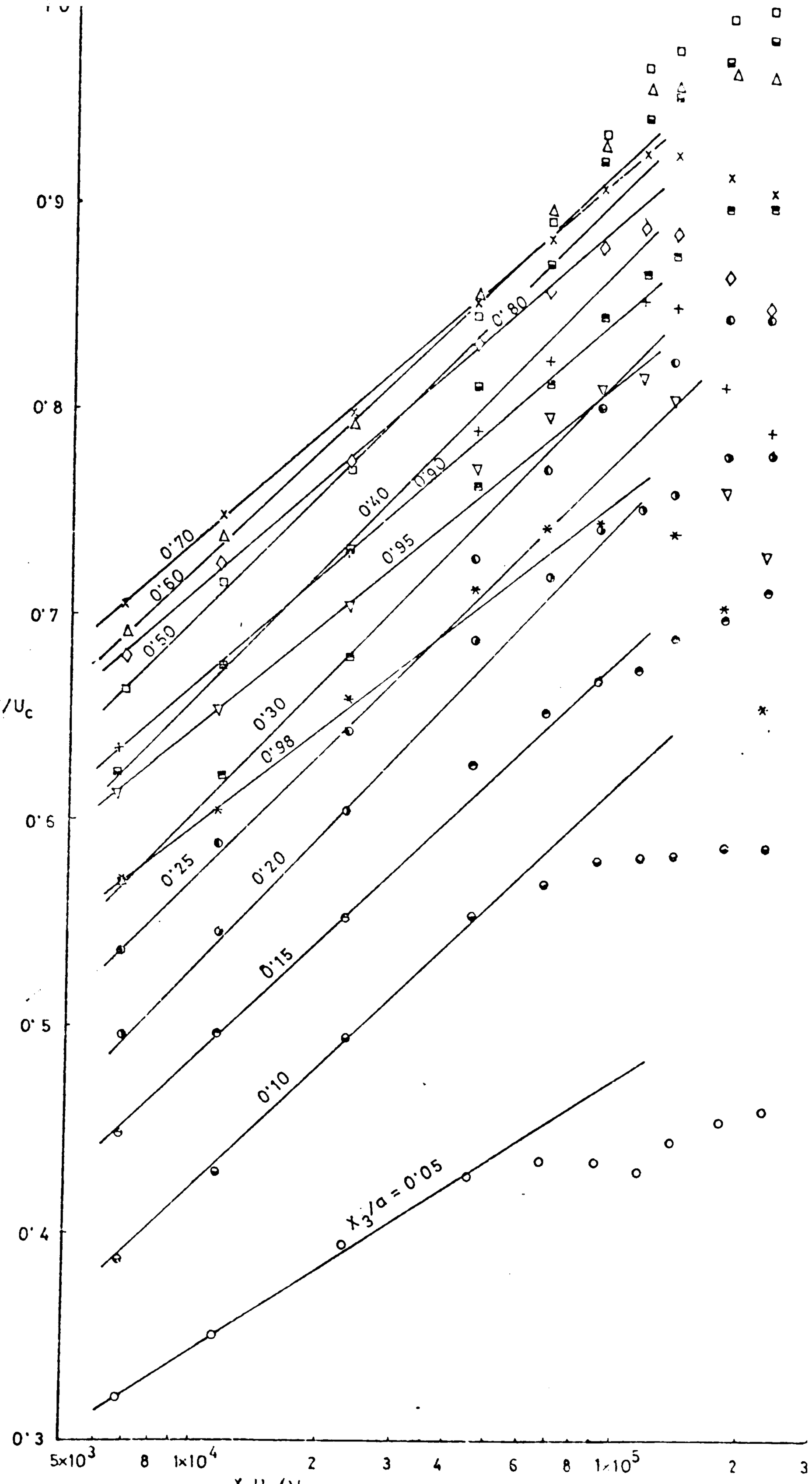

Fig. 4·5 Clauser chart plot for the side wall ($X_2 = 0$).

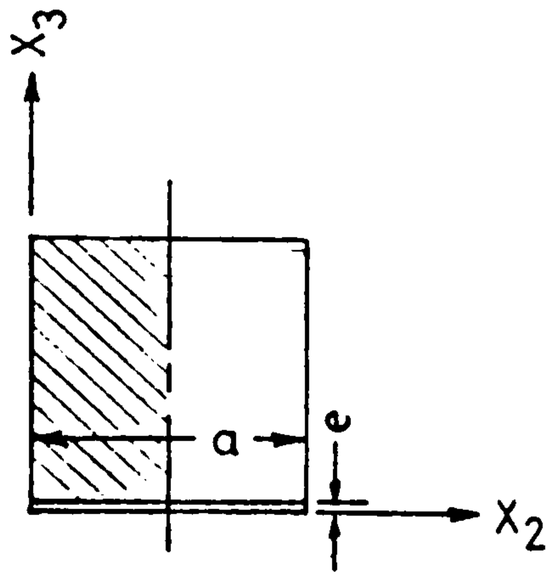

$U^+ = (1/0{\cdot}385)\ln(X_3/e) + 2{\cdot}85$

o – $X_2/a = 0{\cdot}50$
x – $X_2/a = 0{\cdot}40$
▲ – $X_2/a = 0{\cdot}30$
▽ – $X_2/a = 0{\cdot}25$
□ – $X_2/a = 0{\cdot}20$
△ – $X_2/a = 0{\cdot}15$
◐ – $X_2/a = 0{\cdot}10$
● – $X_2/a = 0{\cdot}05$

U^+

X_3/e

Fig.4·6 Logarithmic plot of mean velocity near the rough wall.

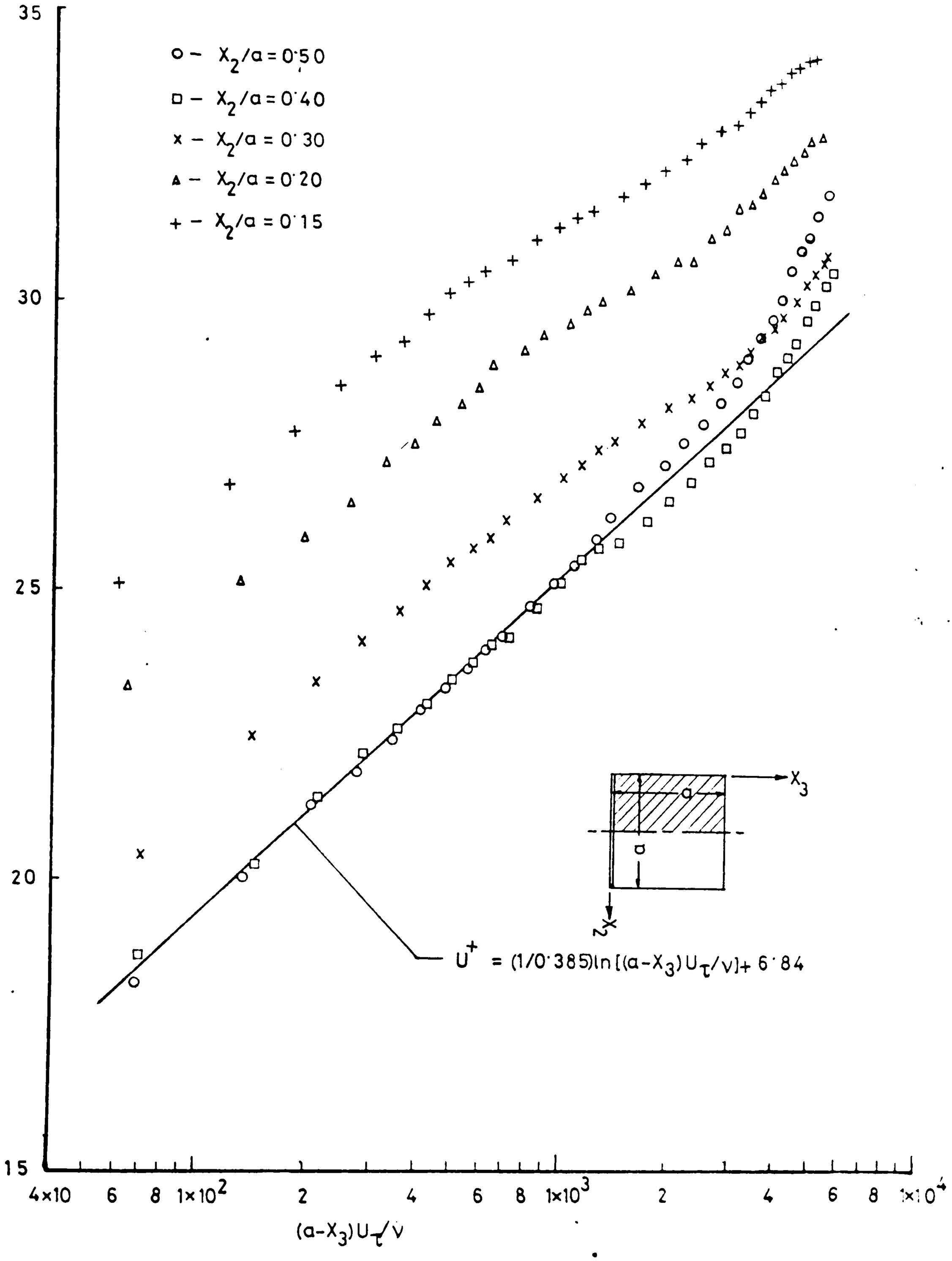

Fig.4·7 Logarithmic plot of mean velocity near the smooth wall.

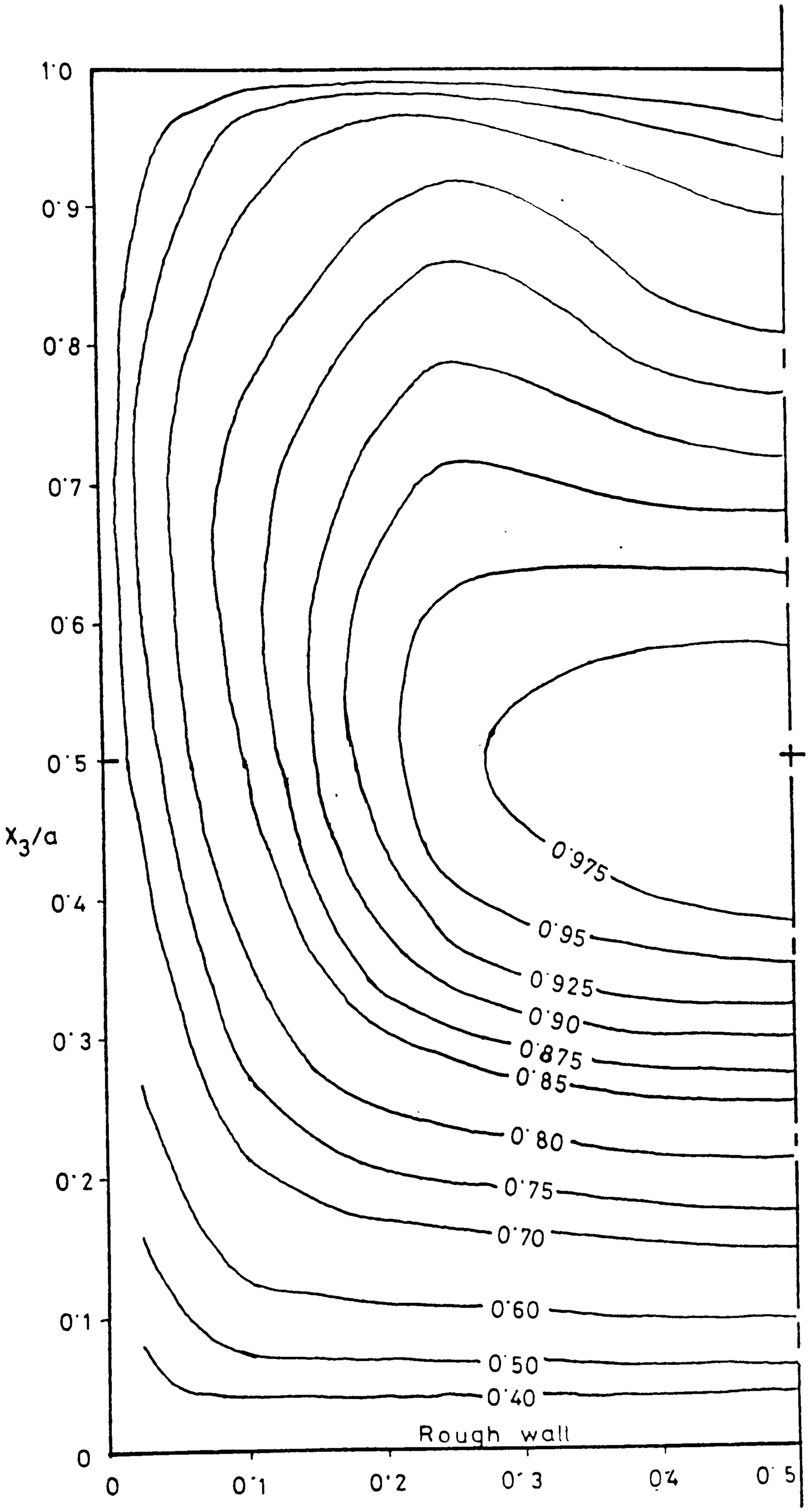

Fig.4·8 Contours of mean velocity, U_1/U_c.

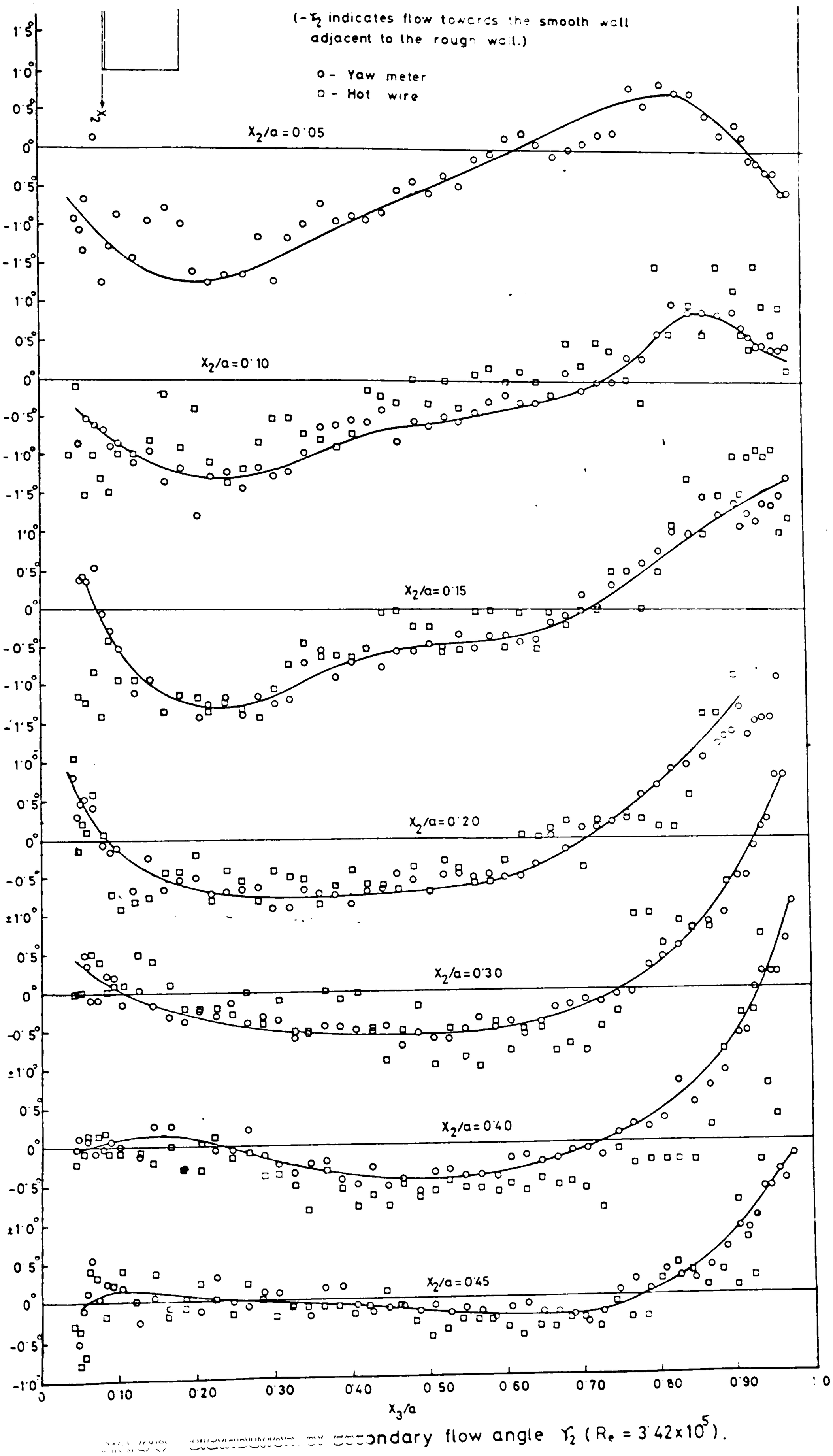

Secondary flow angle Υ_2 ($R_e = 3.42 \times 10^5$).

($-\gamma_3$ indicate flow towards the rough wall.)

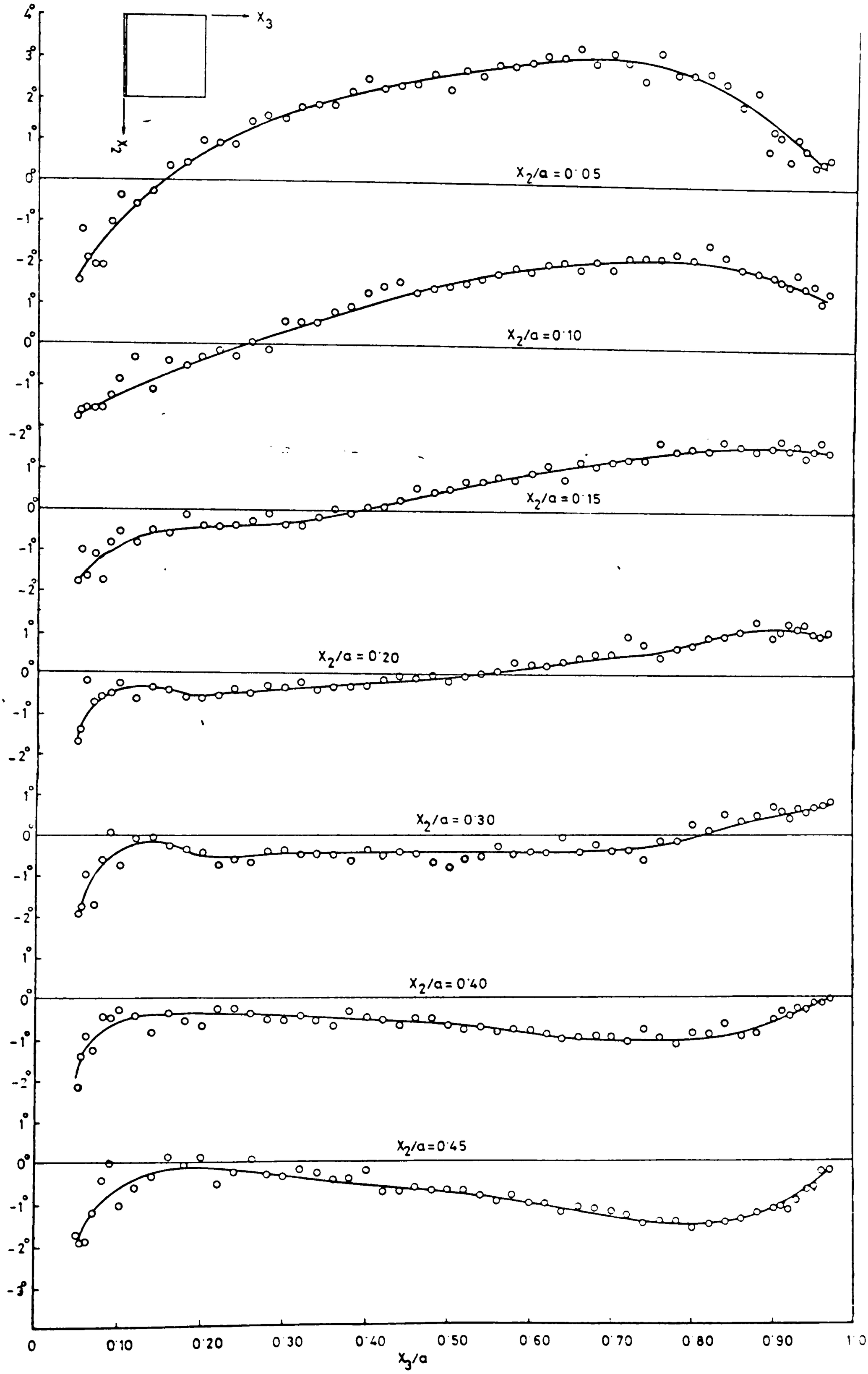

Fig. 4.10 Distribution of secondary flow angle γ_3 ($R_e = 3.42 \times 10^5$).

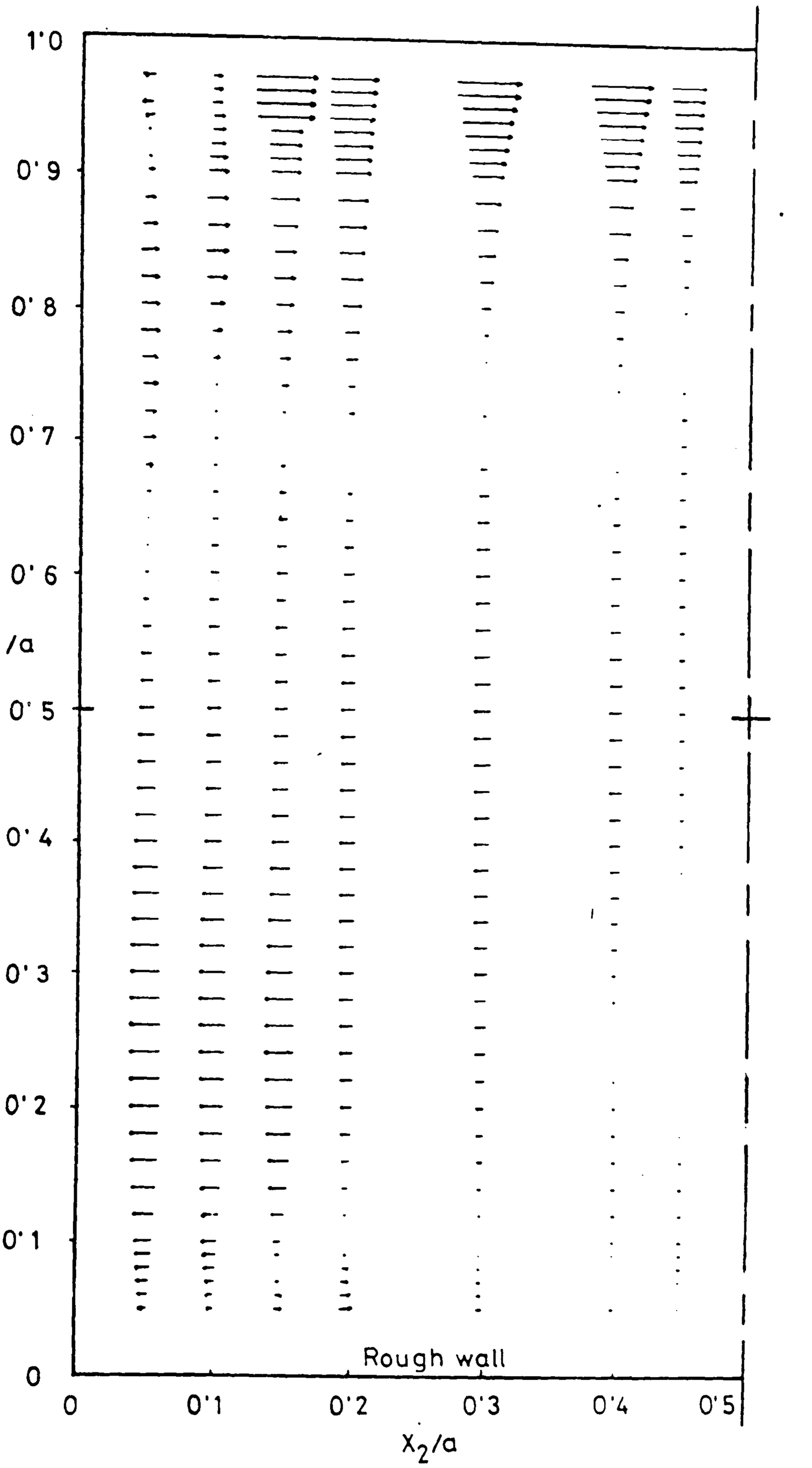

Fig. 4·11 Distribution of U_2/U_c vectors.

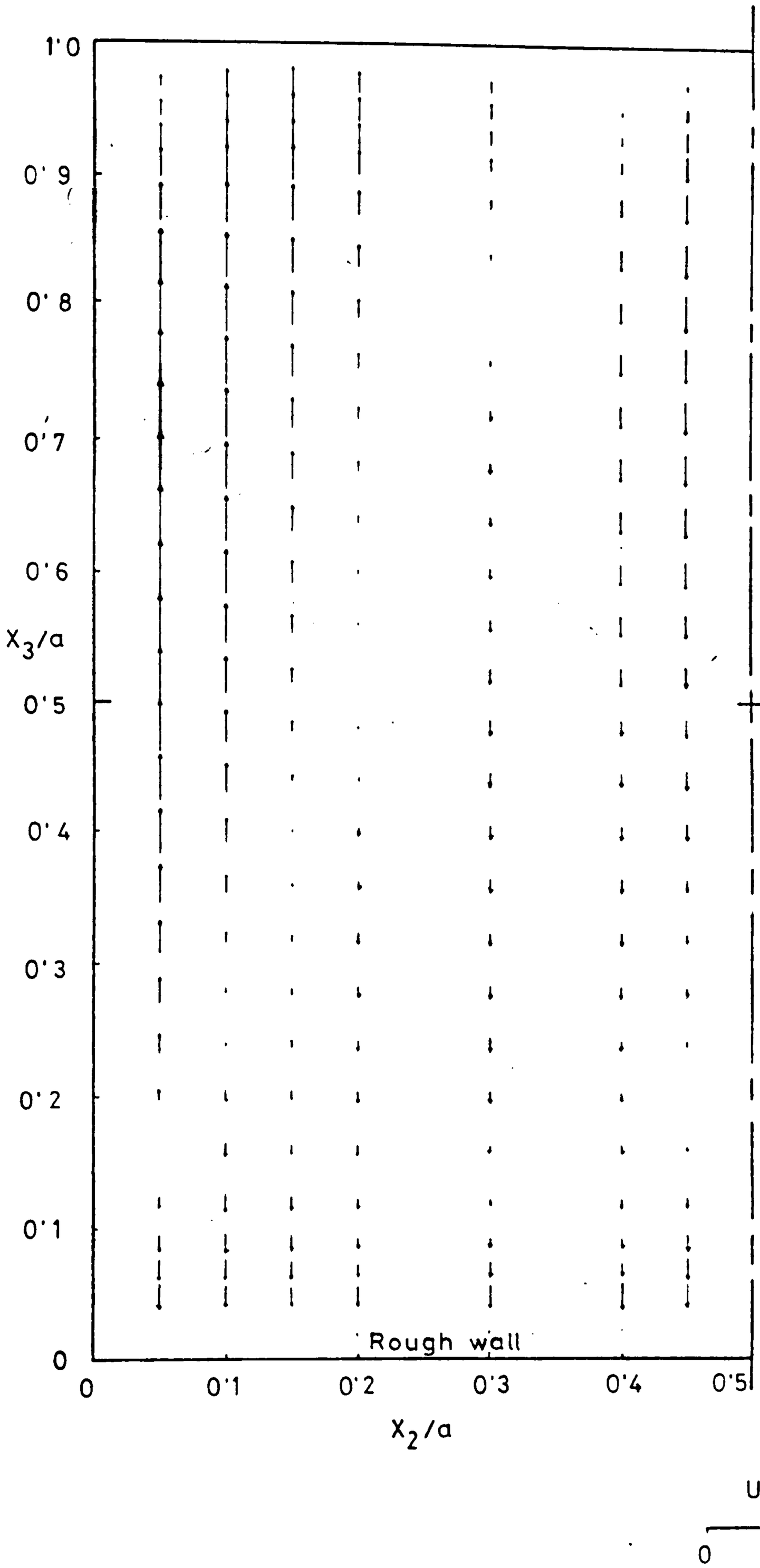

Fig. 4·12 Distribution of U_3/U_c vectors.

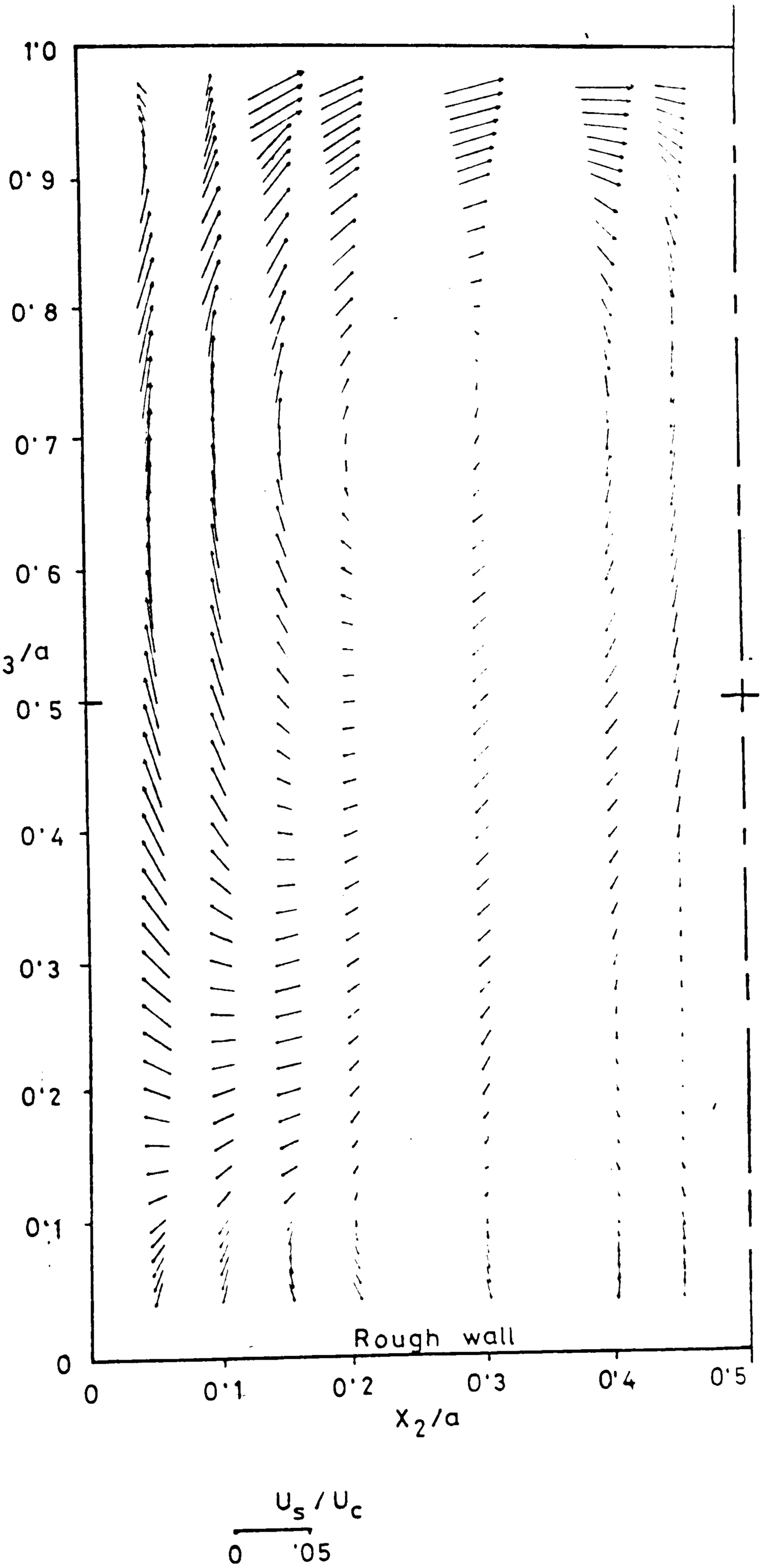

Fig. 4·13 Distribution of secondary velocity vectors, U_S/U_C.

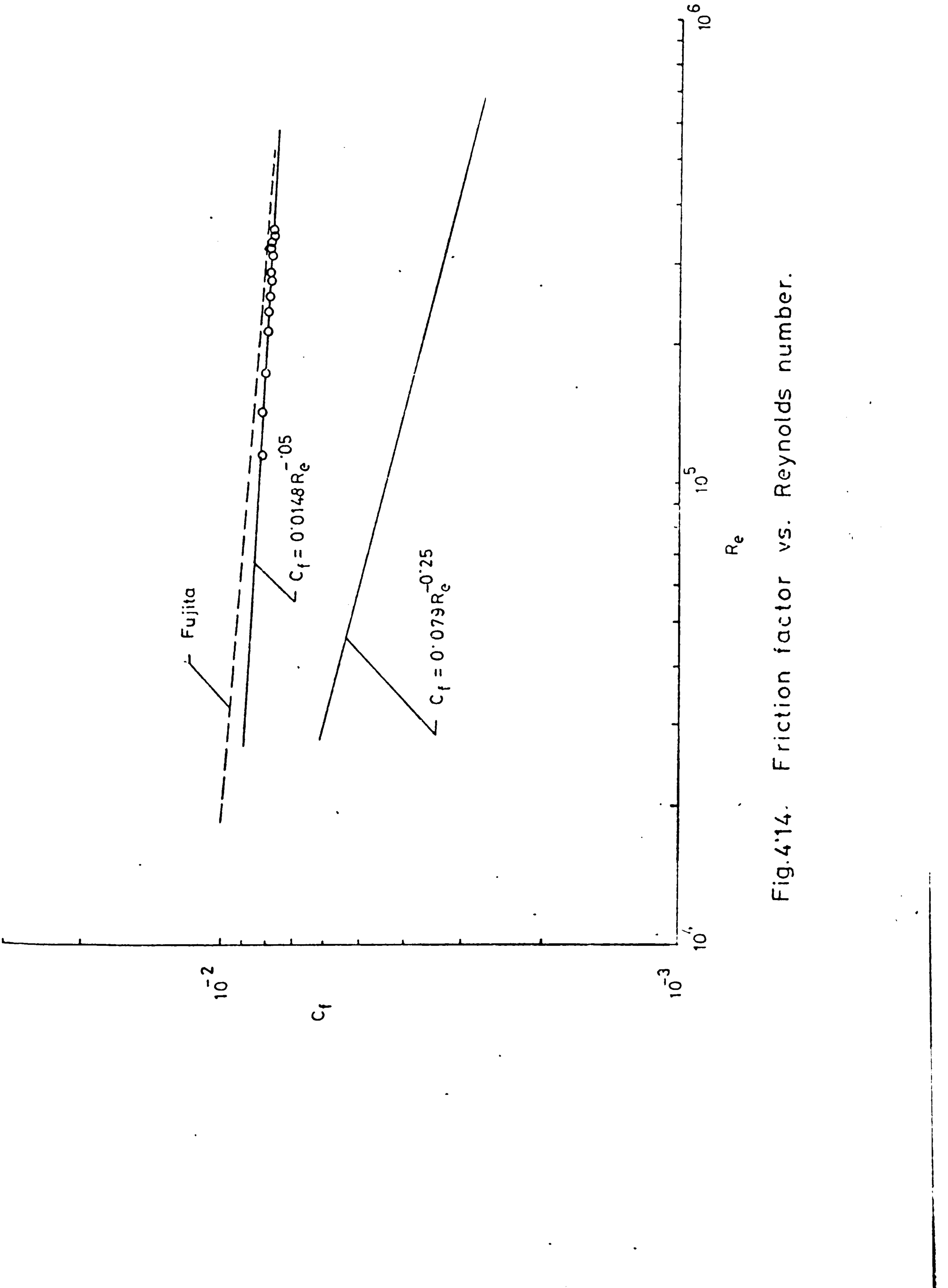

Fig.4.14. Friction factor vs. Reynolds number.

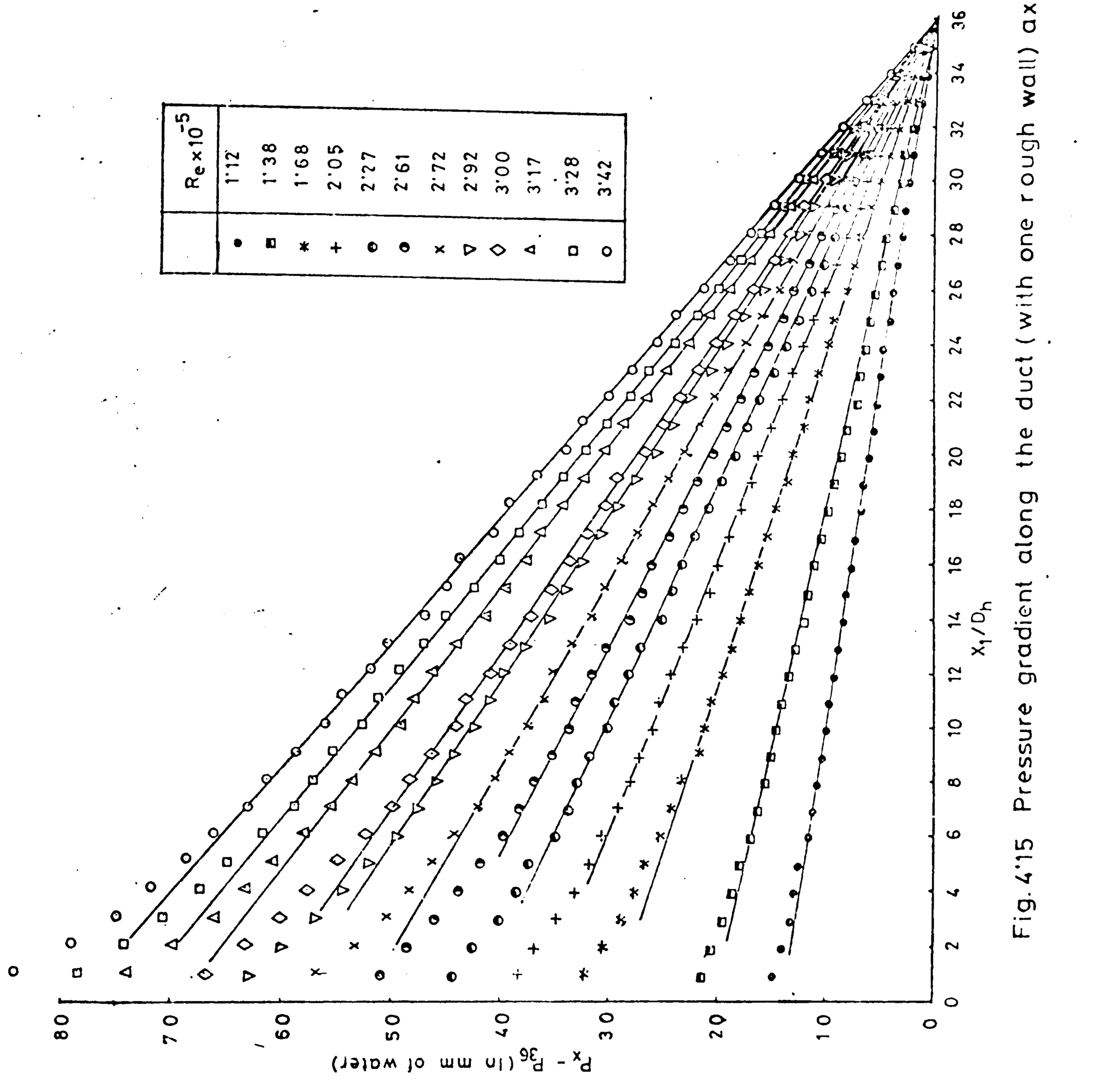

Fig. 4'15 Pressure gradient along the duct (with one rough wall)

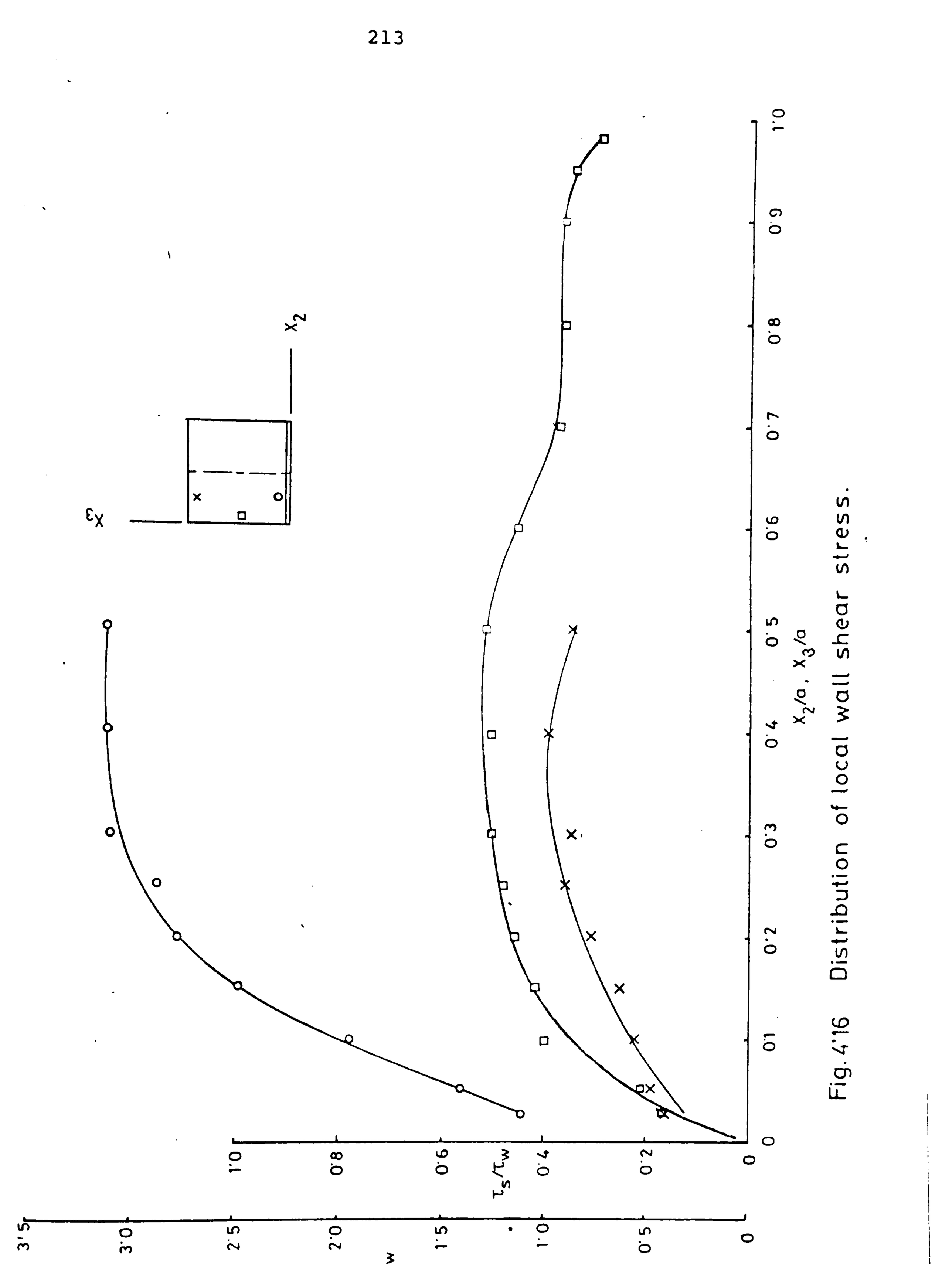

Fig. 4·16 Distribution of local wall shear stress.

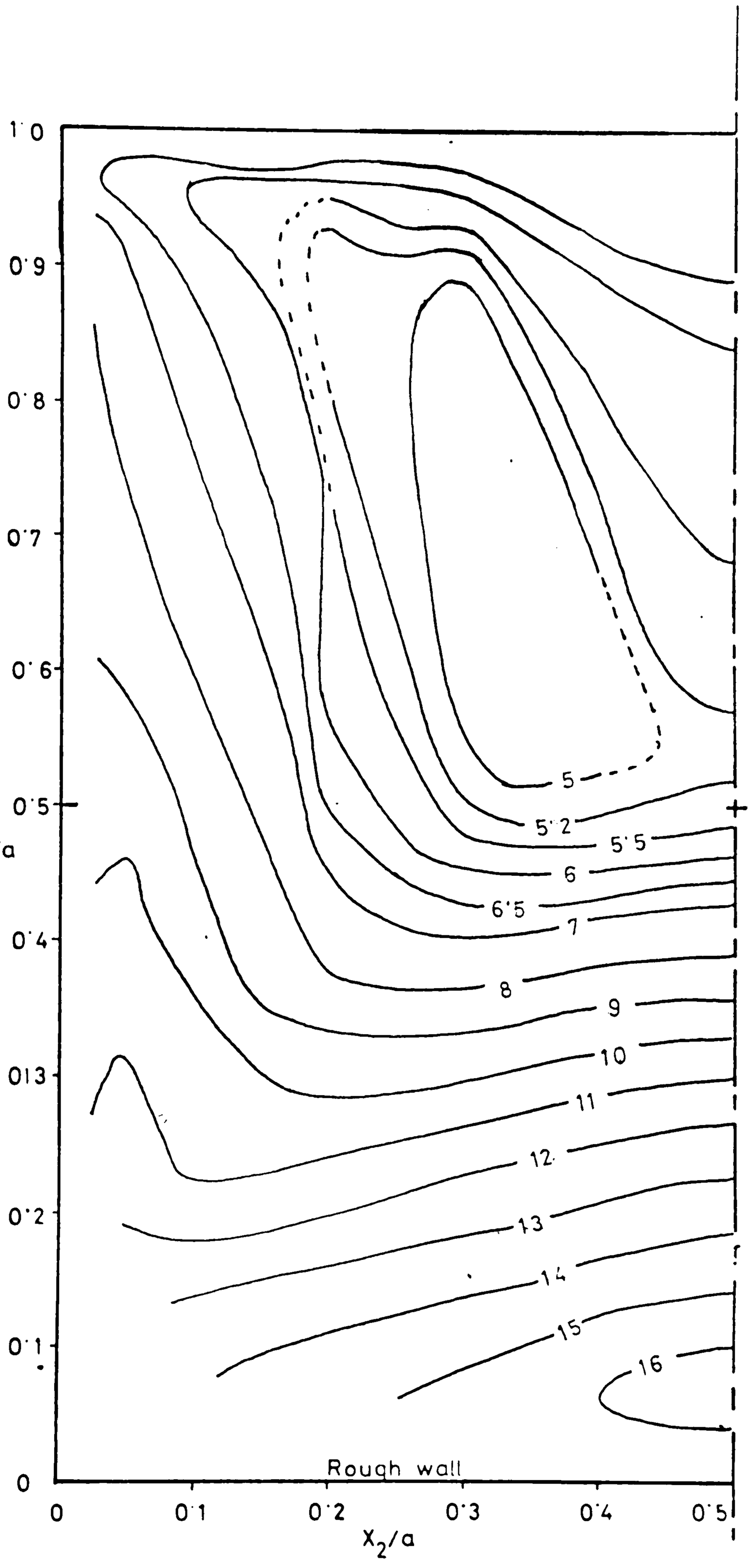

Fig. 4·17 Contours of $\overline{u_1}/U_c \times 10^2$.

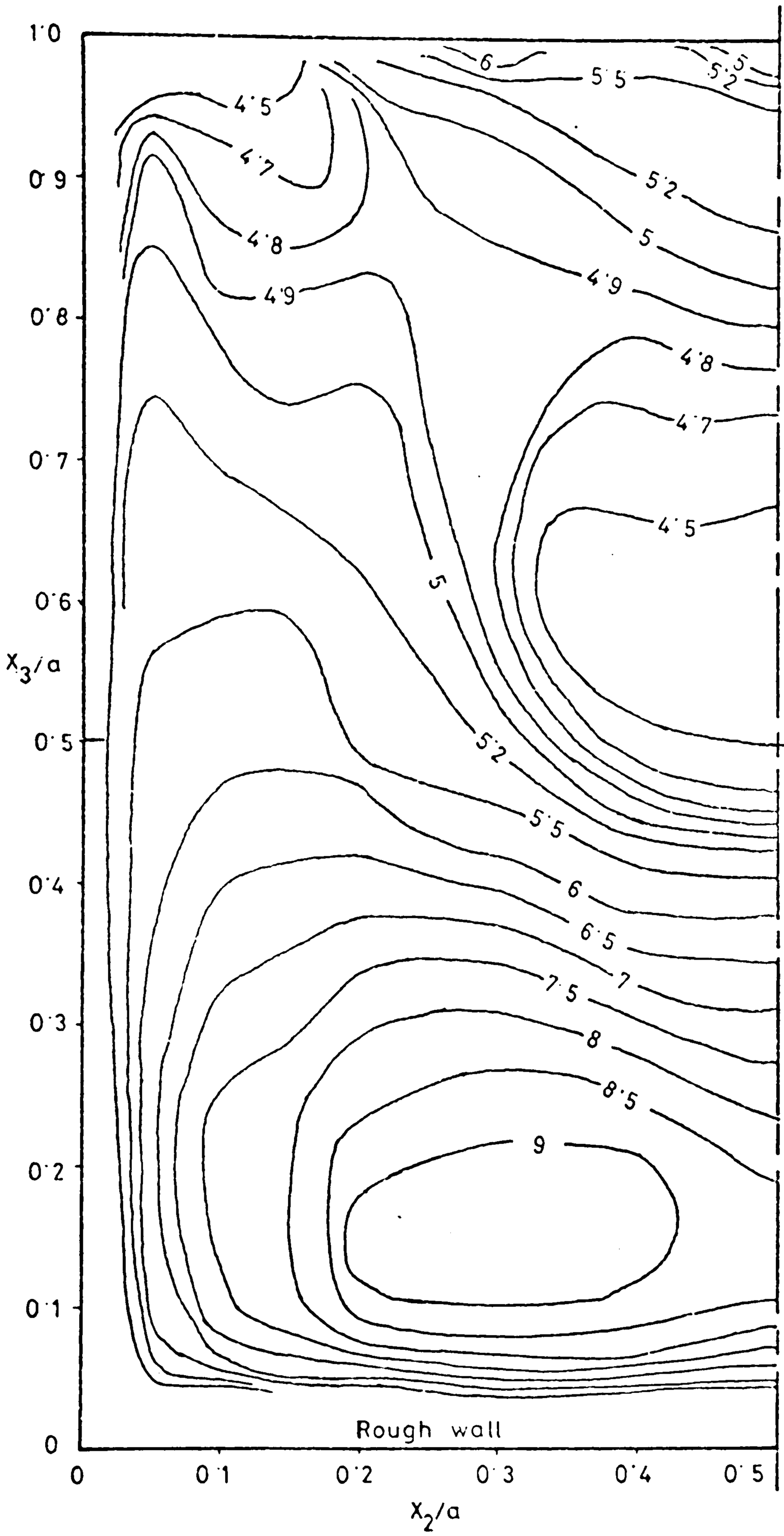

Fig. 4·18 Contours of $\tilde{u}_2/U_c \times 10^2$.

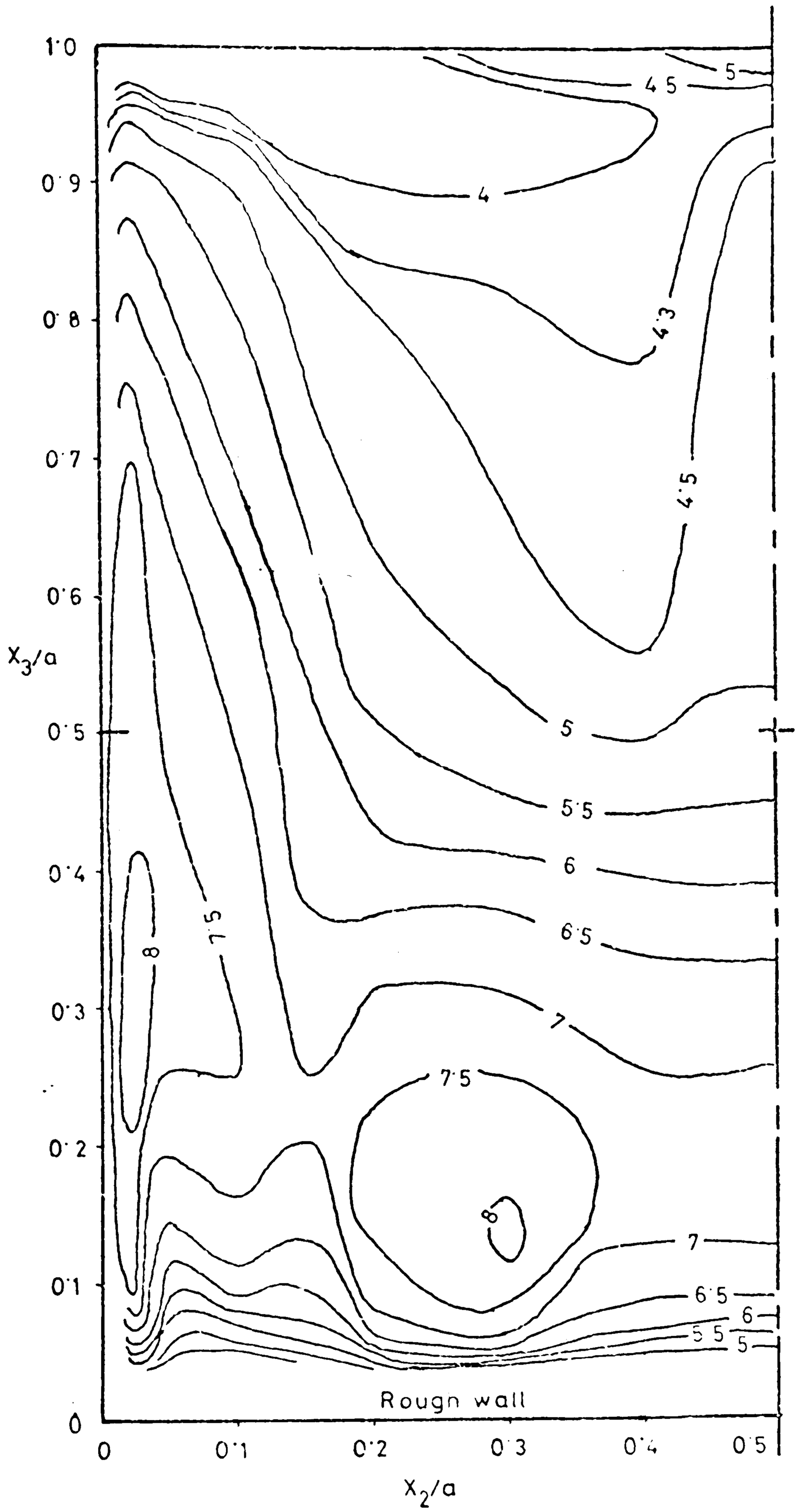

Fig. 4·19 Contours of $\bar{u}_3/U_c \times 10^2$.

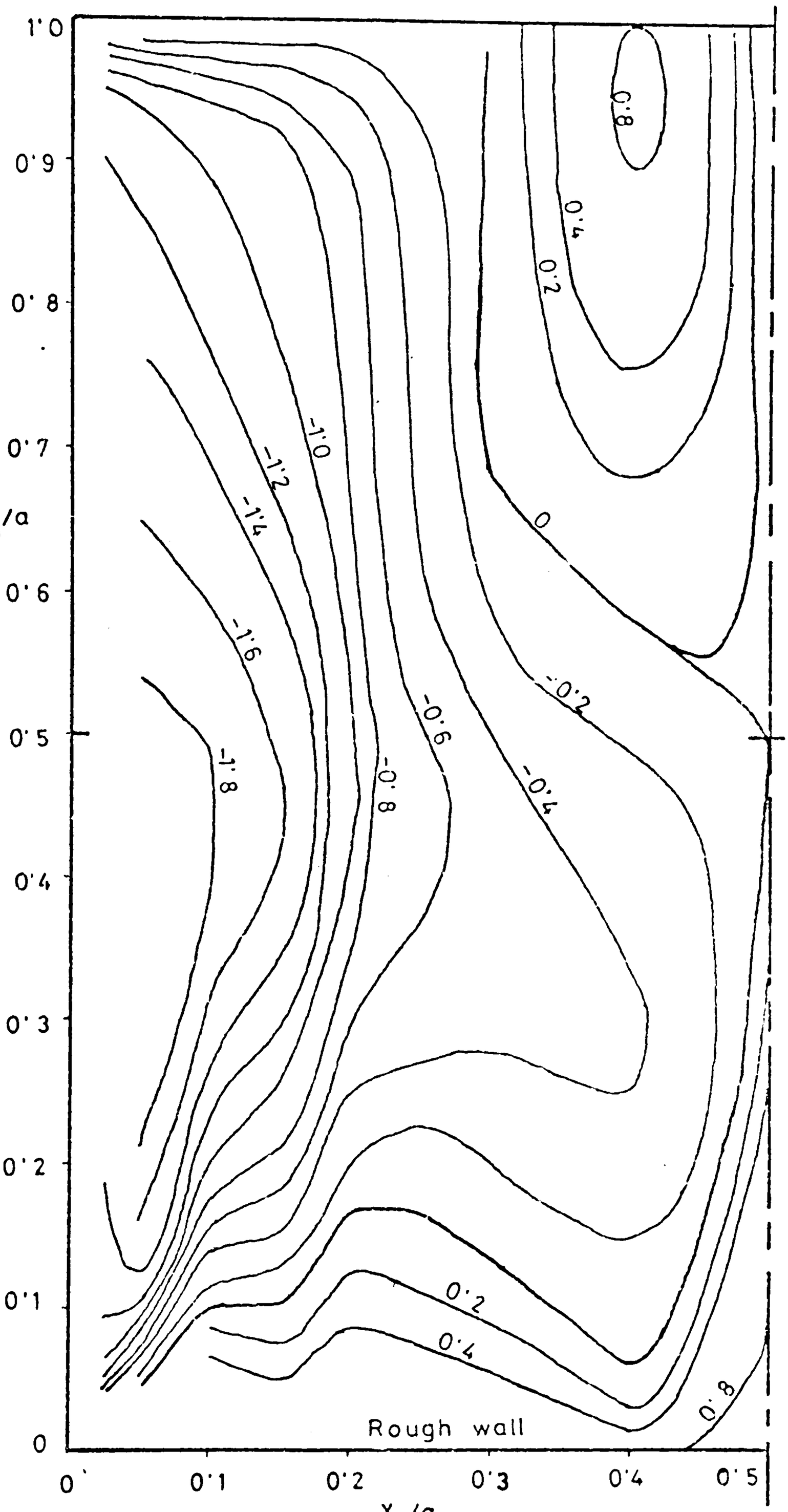

Fig. 4·20 Contours of $\overline{u_1 u_2}/U_c^2 \times 10^3$.

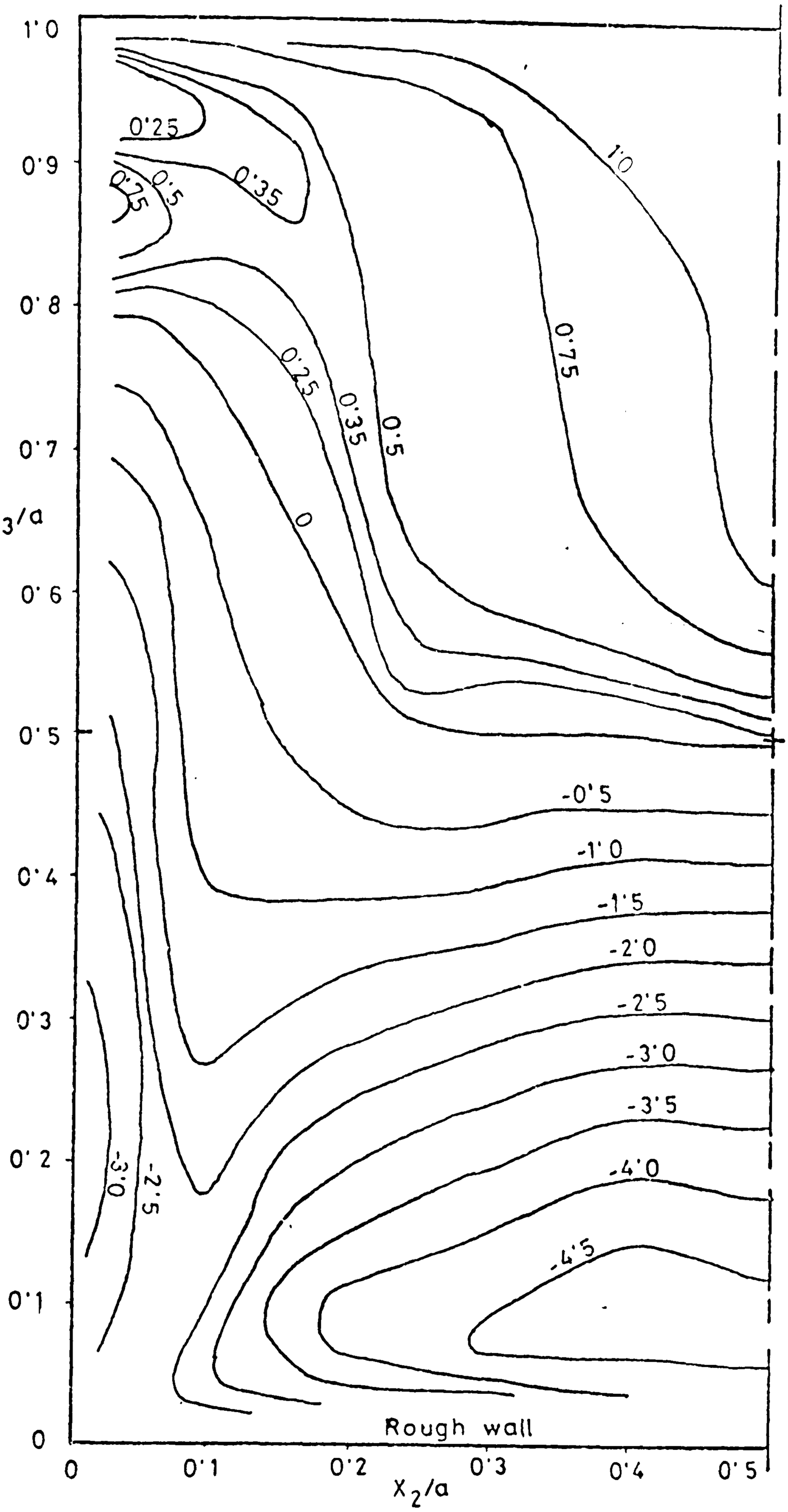

Fig.4·21 Contours of $\overline{u_1 u_3}/U_c^2 \times 10^3$.

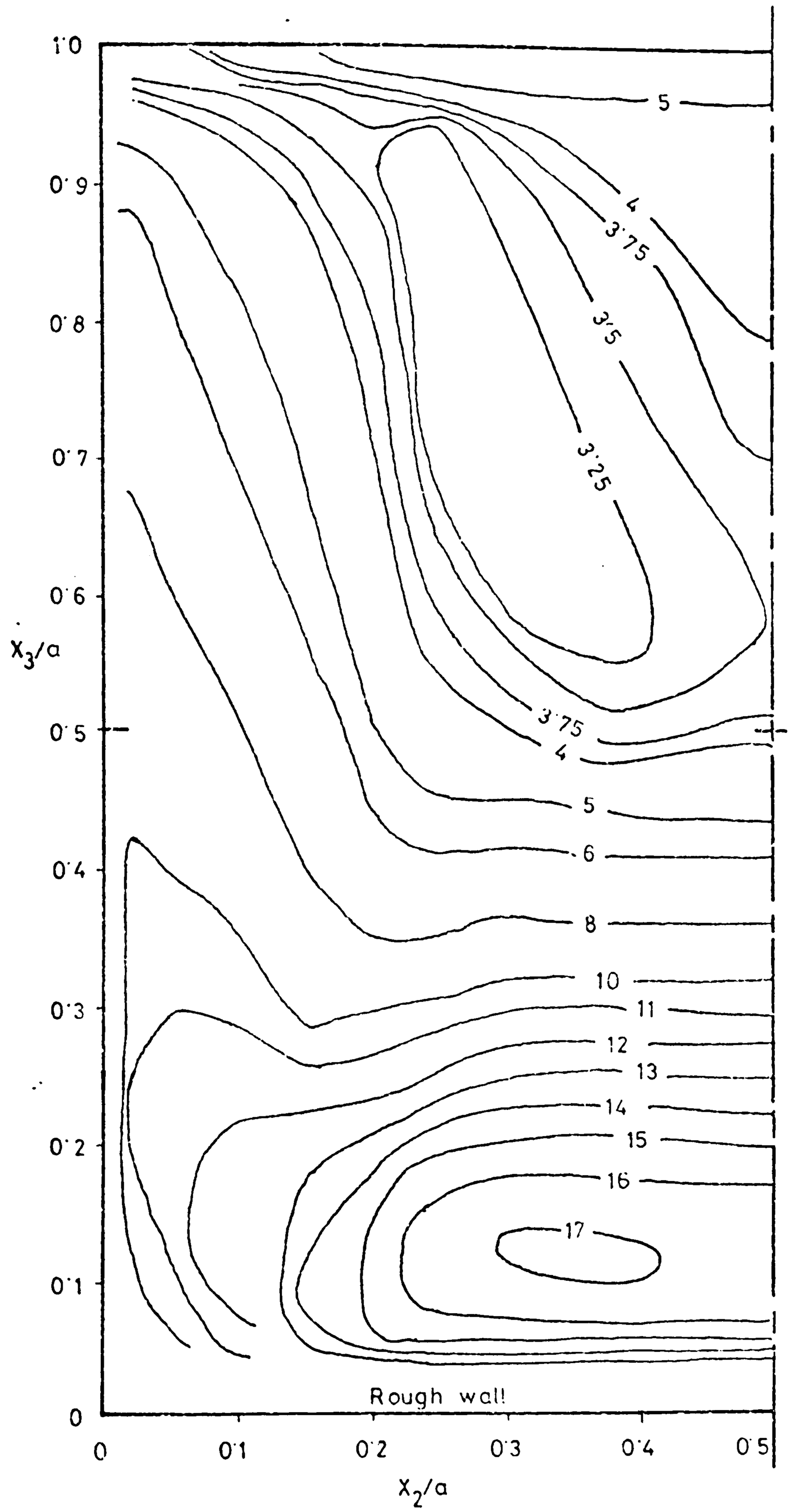

Fig. 4·22 Contours of $k/U_c^2 \times 10^3$

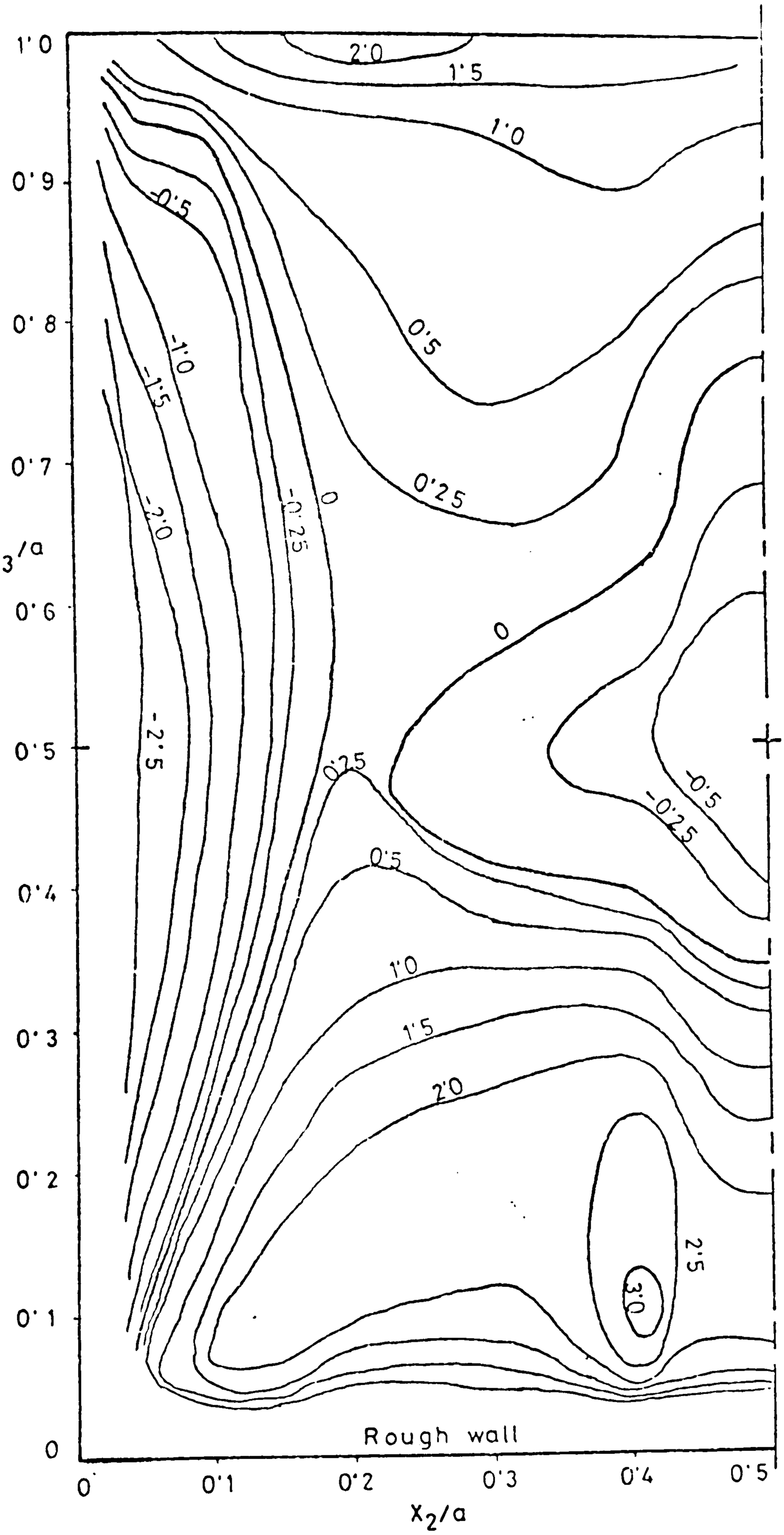

Fig. 4·23 Contours of $(\overline{u_2^2}-\overline{u_3^2})/U_c^2 \times 10^3$.

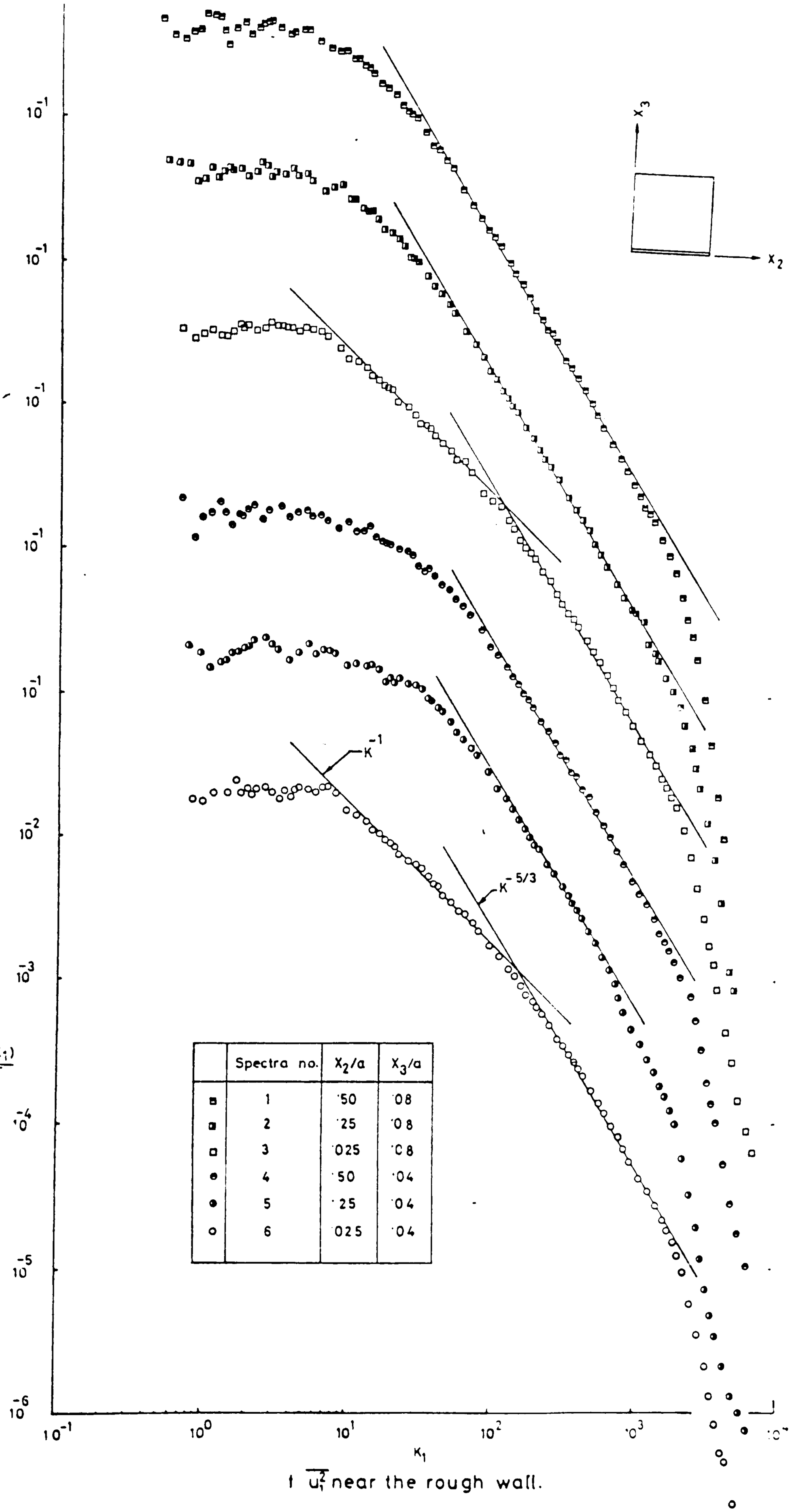

	Spectra no.	X_2/a	X_3/a
▫	1	·50	·08
◪	2	·25	·08
□	3	·025	·08
●	4	·50	·04
◉	5	·25	·04
○	6	·025	·04

Fig. 1 $\overline{u_1^2}$ near the rough wall.

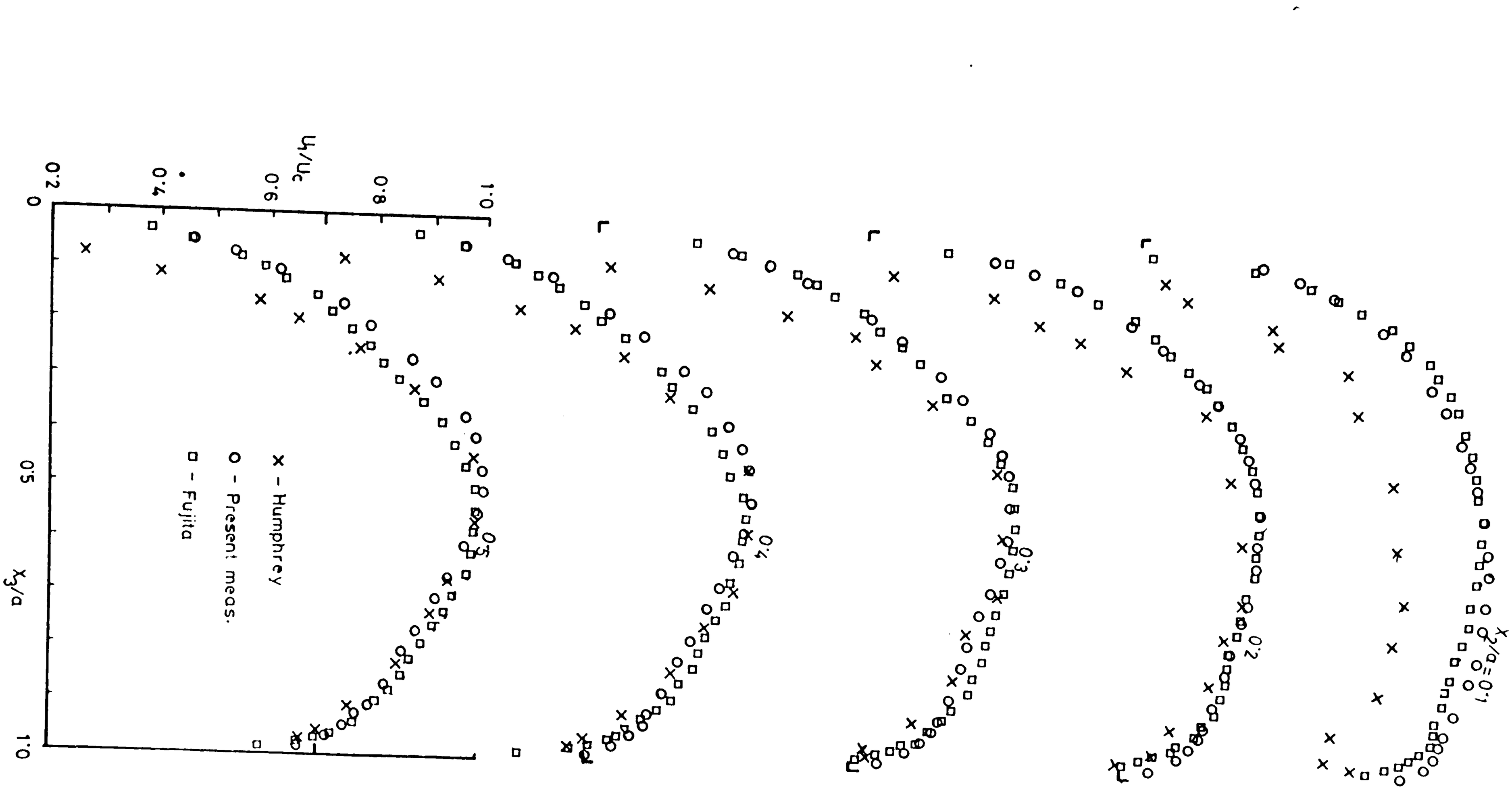

Fig. 4'25 Comparison of mean velocity profiles.

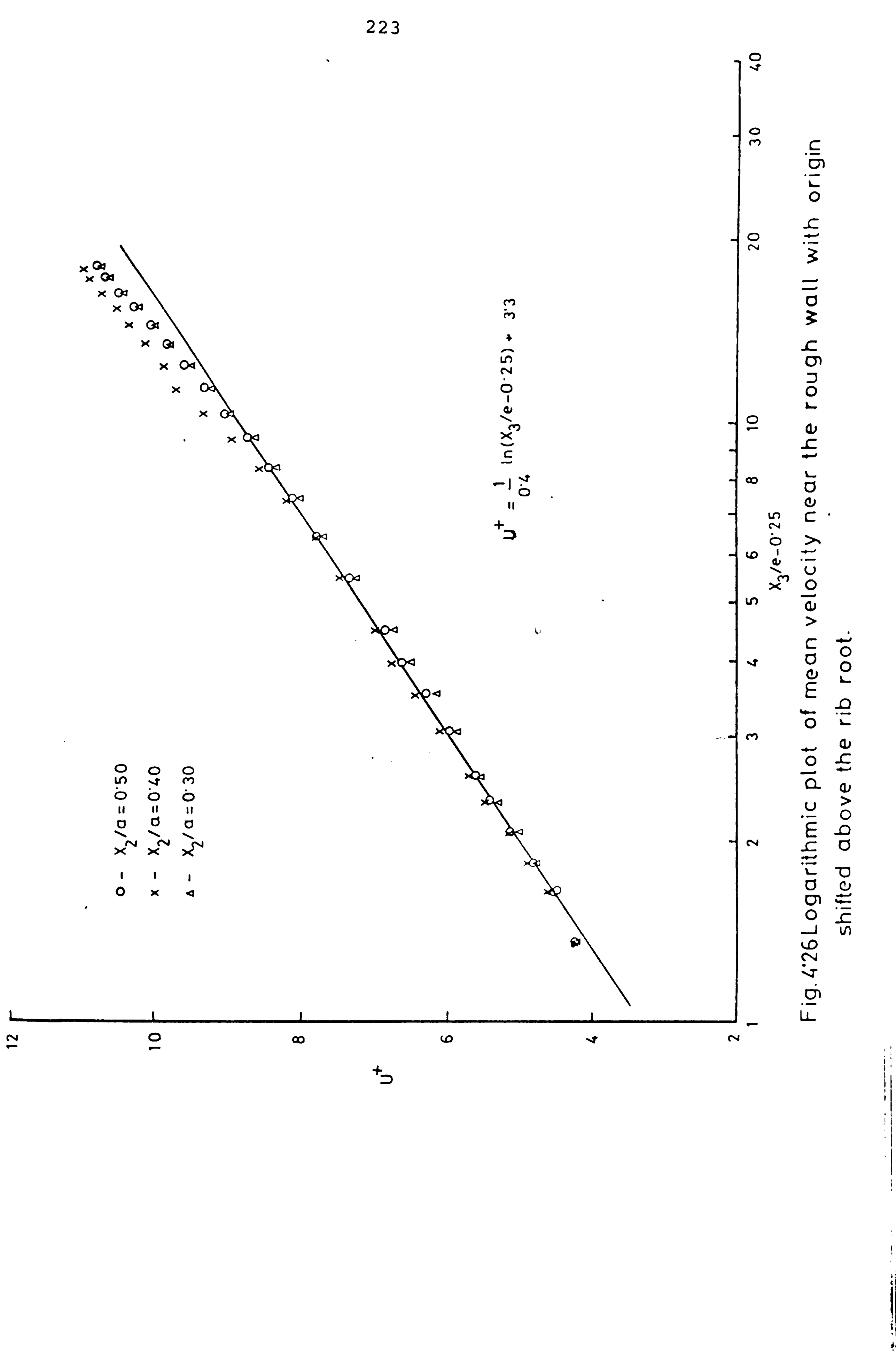

Fig.4.26 Logarithmic plot of mean velocity near the rough wall with origin shifted above the rib root.

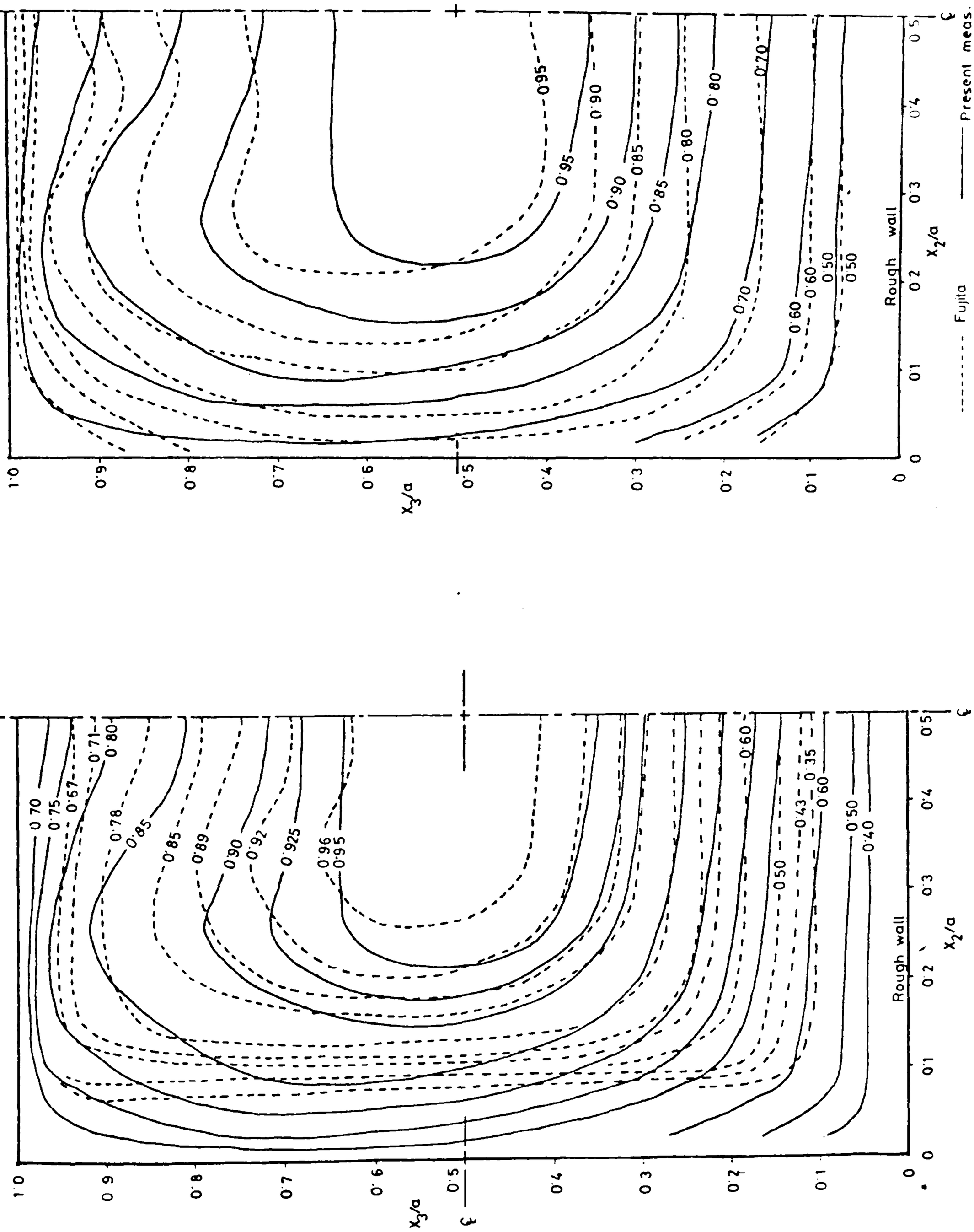

Fig.4·27b Comparison of U_1/U_c contours.
(Fujita – $R_e = 6·4 \times 10^4$, $e/d_h = 0·02$
Present meas. – $R_e = 3·42 \times 10^5$, $e/d_h = 0·0212$)

Fig.4·27a Comparison of U_1/U_c contours.
(Humphrey – $R_e = 3·64 \times 10^4$, $e/d_h = 0·098$
Present meas. – $R_e = 3·42 \times 10^5$, $e/d = 0·02$)

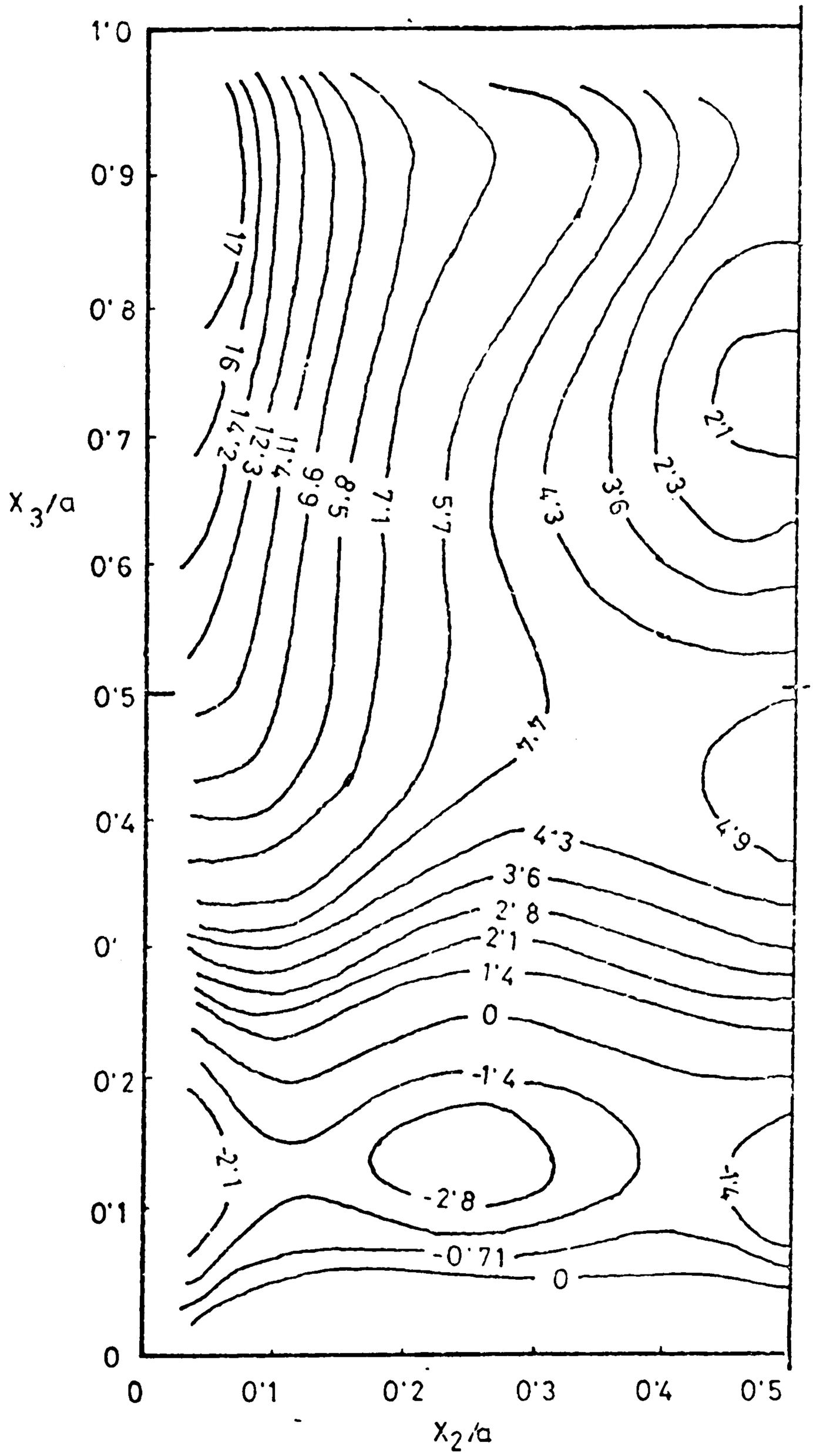

Fig. 4'28 Contours of $U_3 / U_c \times 10^2$ of Humphrey.

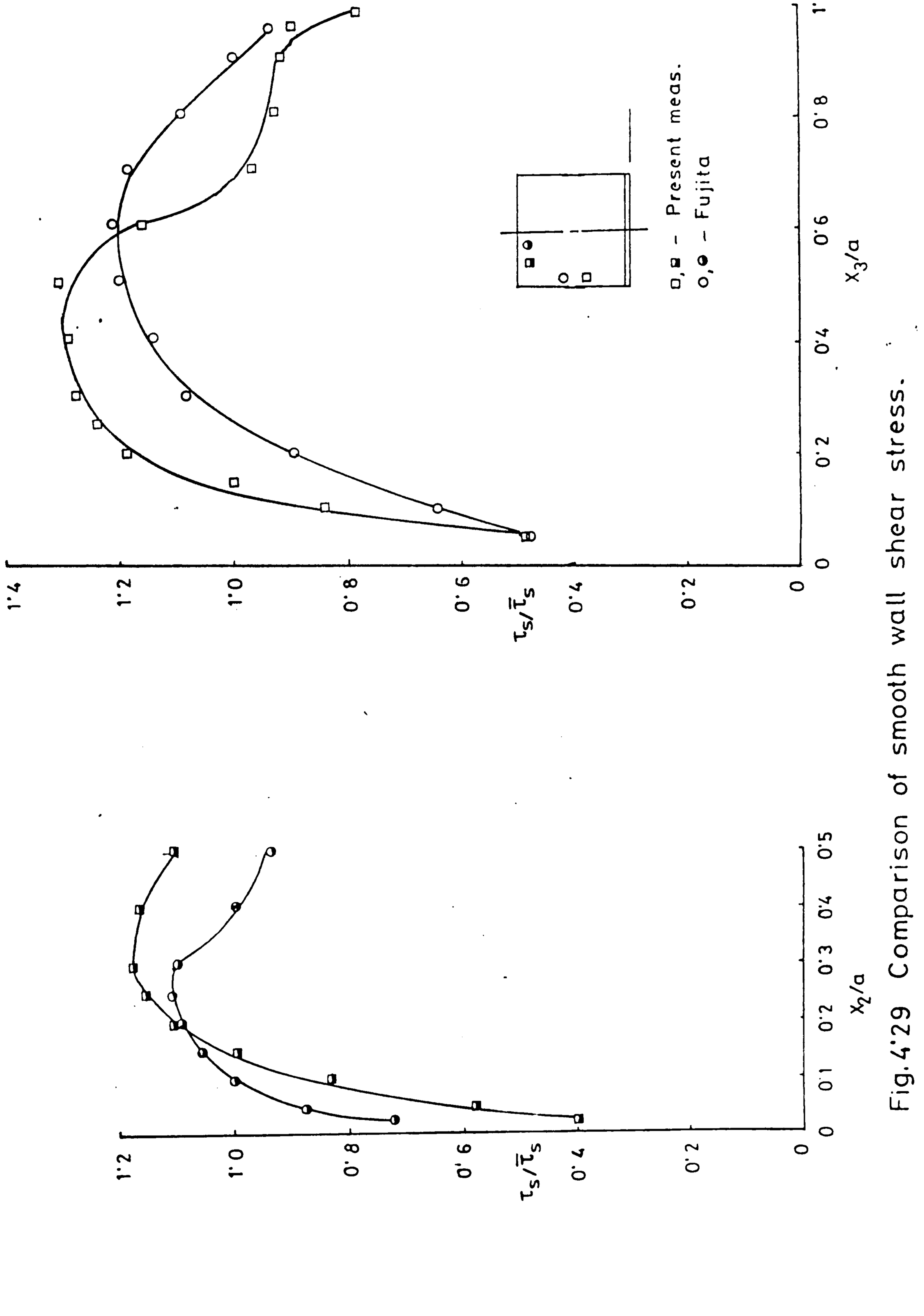

Fig. 4·29 Comparison of smooth wall shear stress.

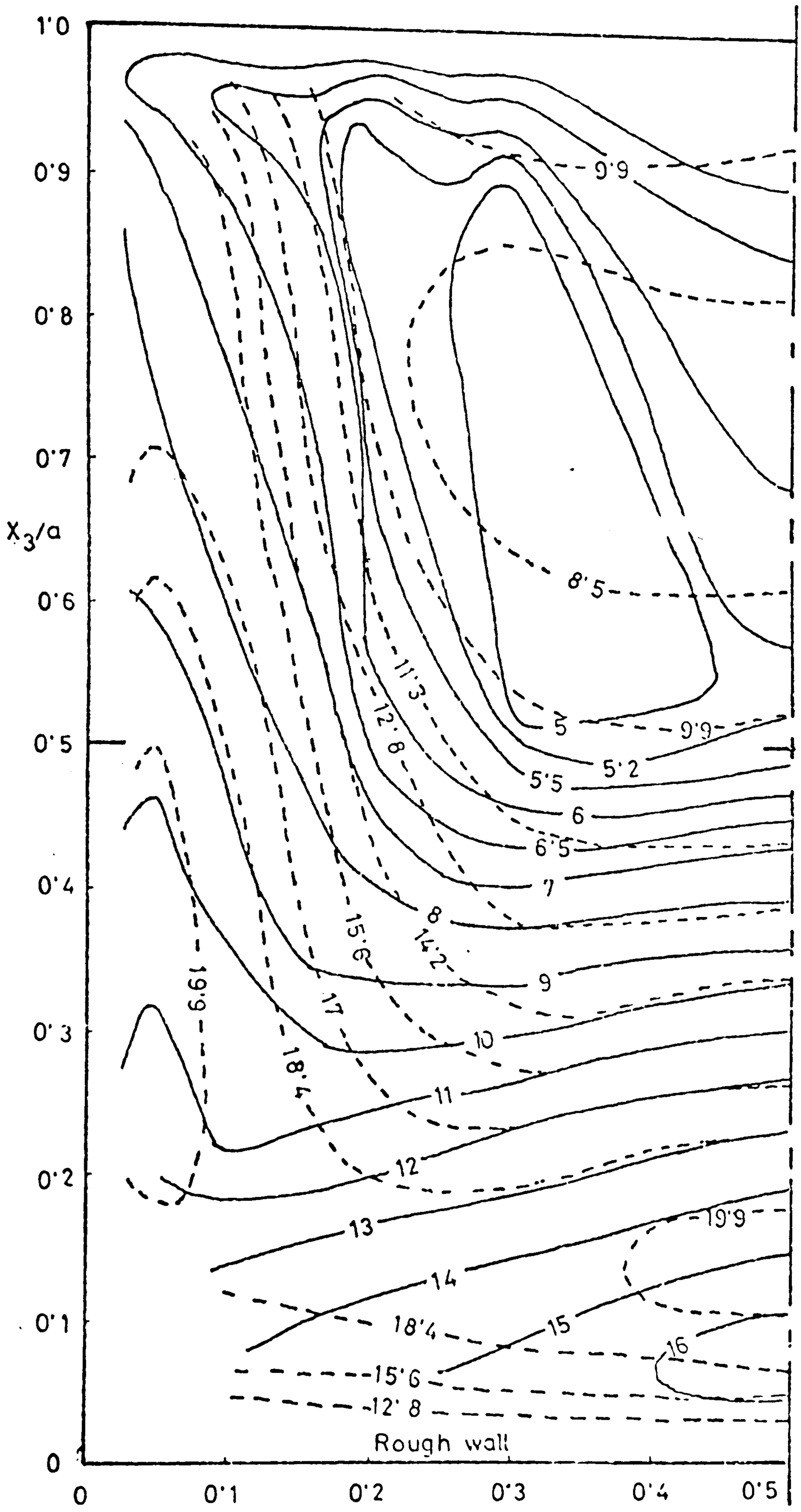

Fig. 4·30 Comparison of $\overline{u_1}/U_c \times 10^2$ contours.

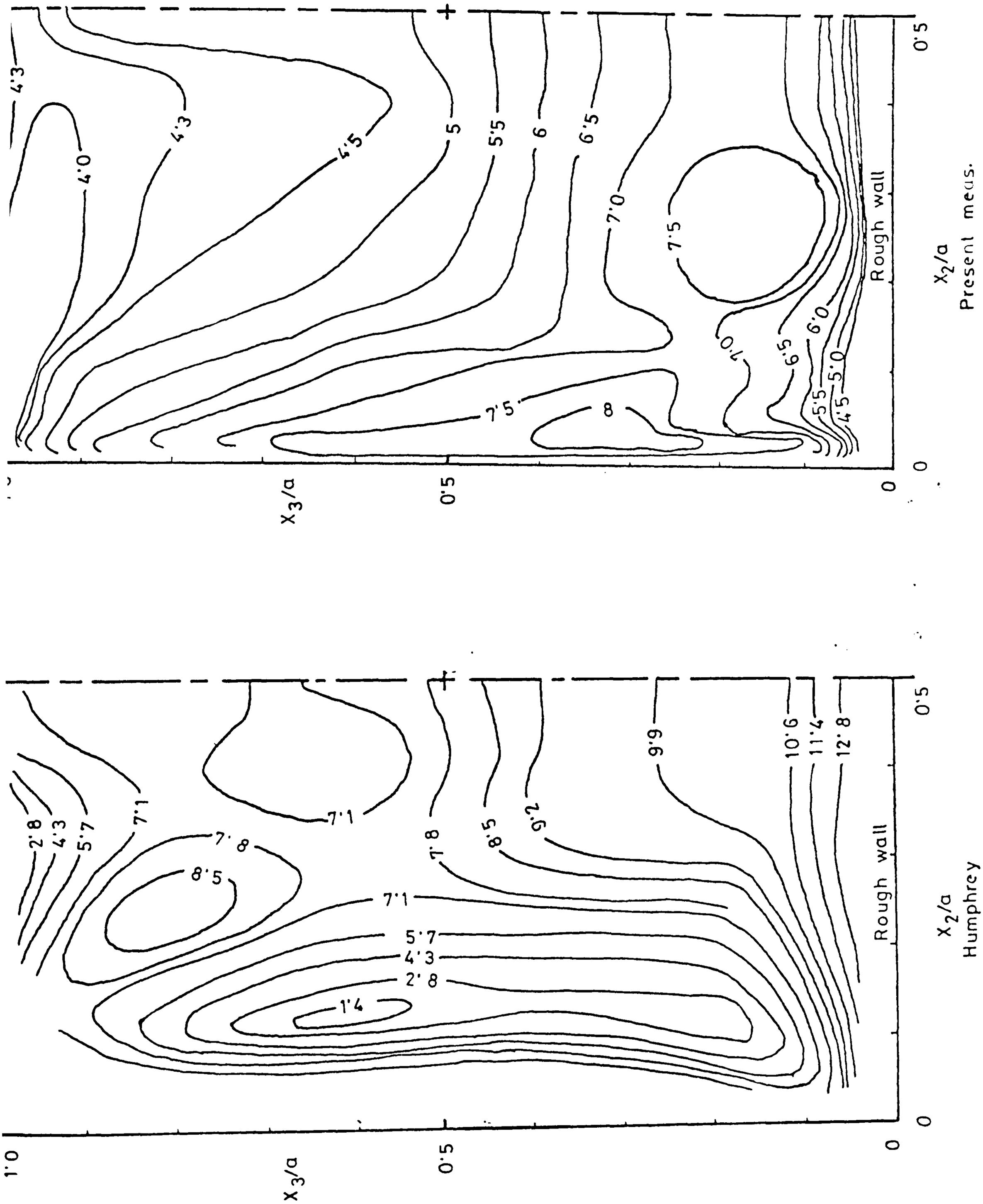

Fig. 4'31 Comparison of $\overline{u}_3 / U_c \times 10^2$ contours.

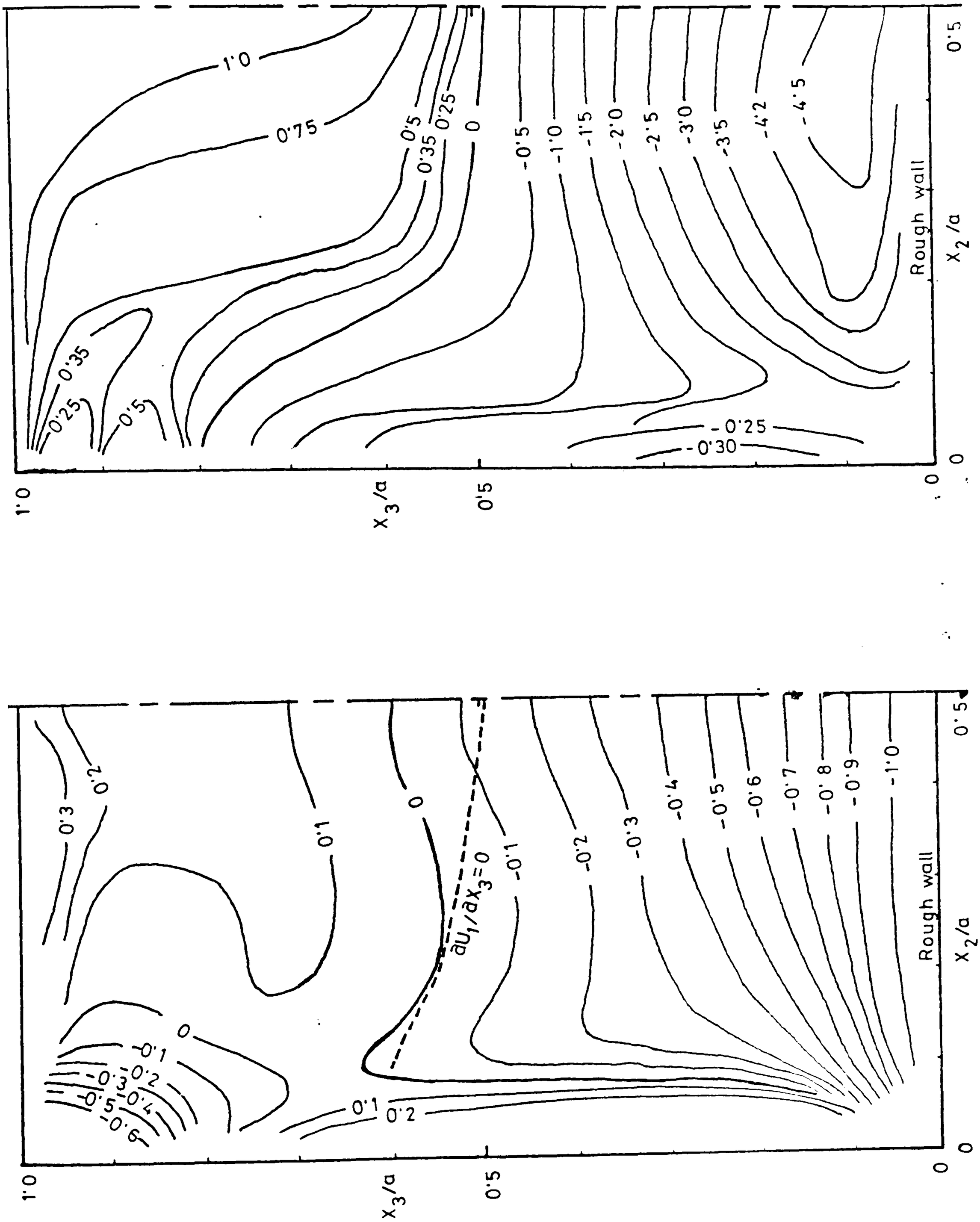

Fig.4·32 Comparison of $\overline{u_1 u_3}/U_c^2 \times 10^3$ contours.

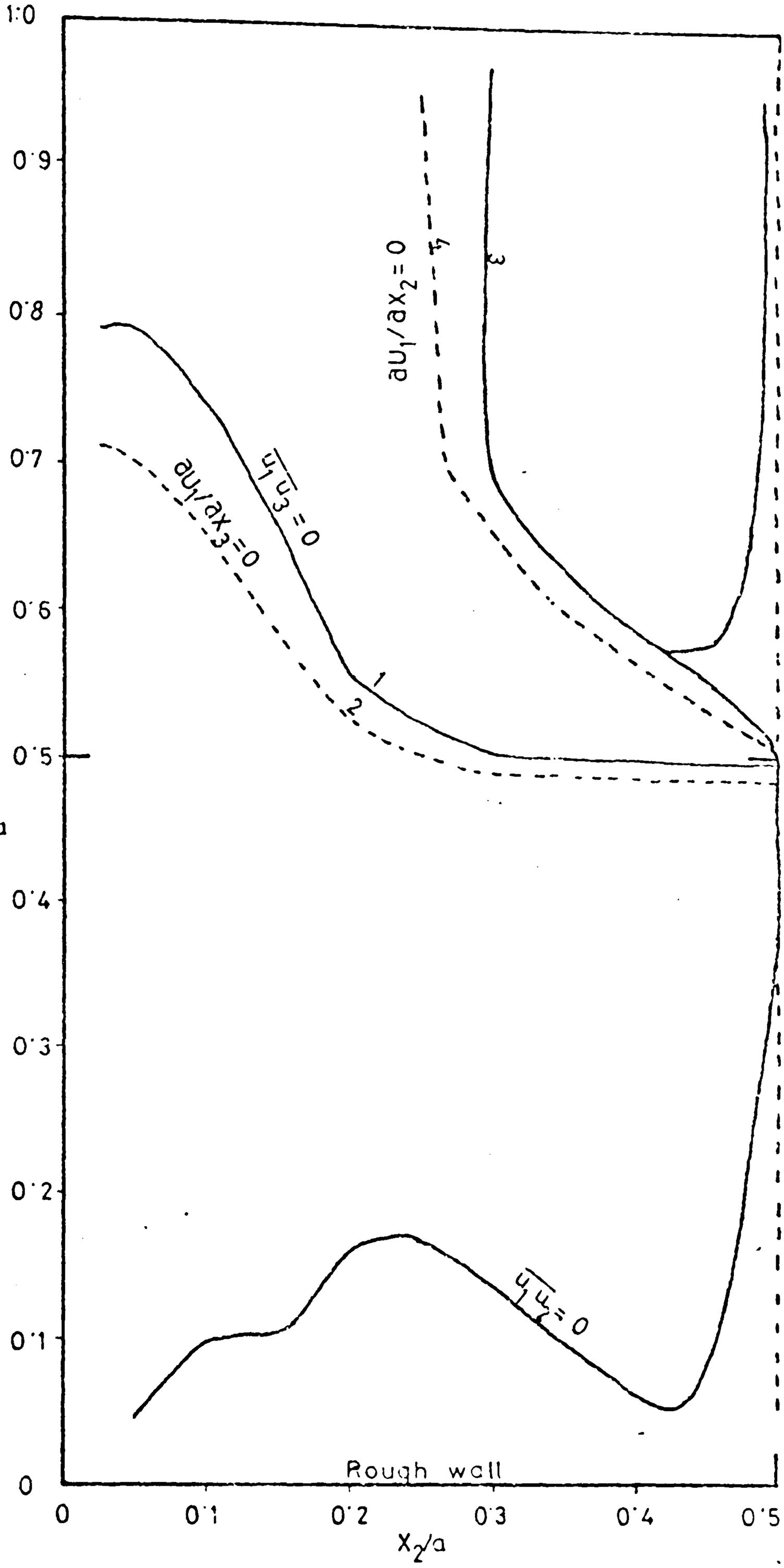

Fig. 4·33 Contours of zero shear stress and zero velocity gradient.

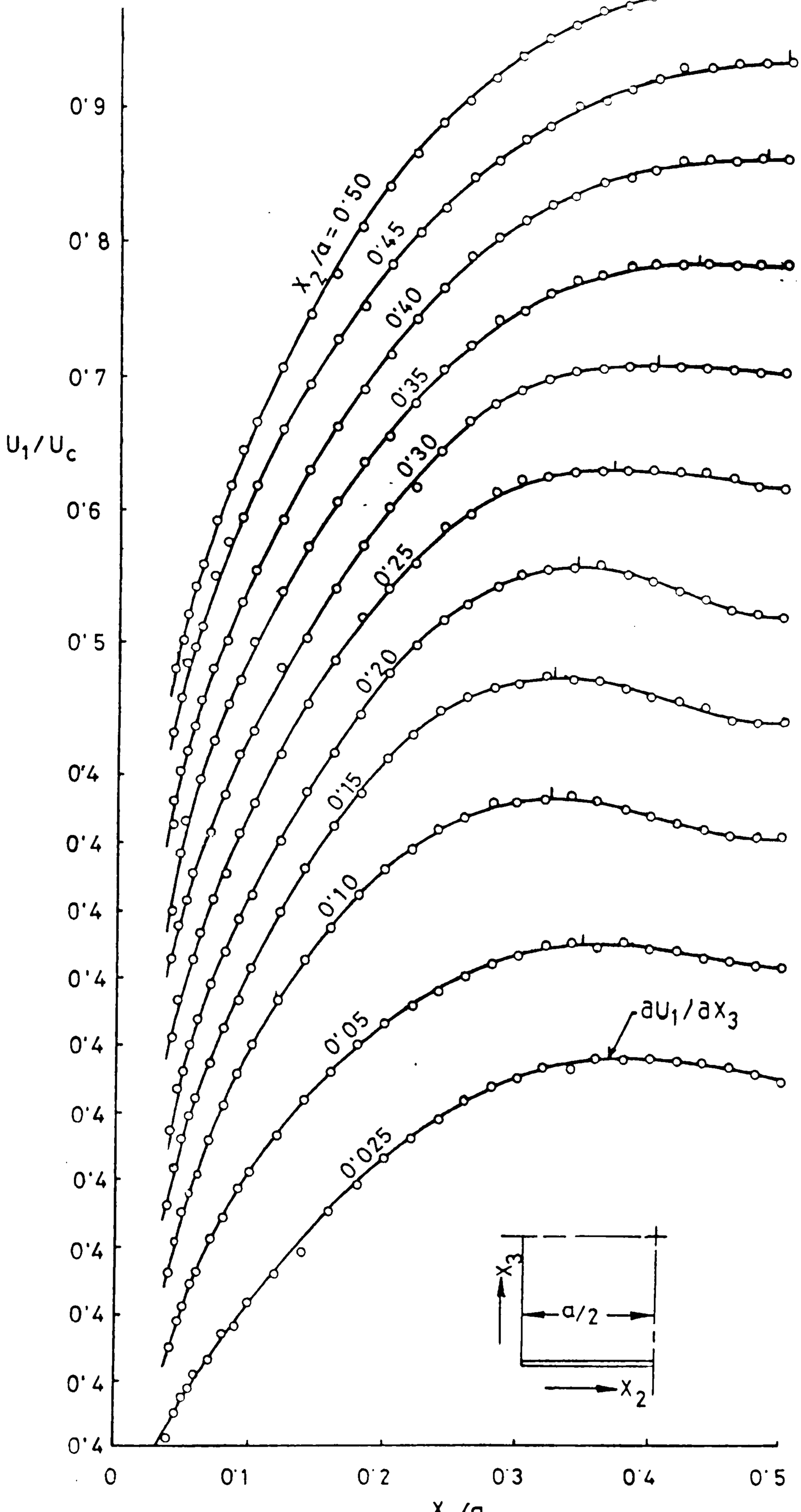

Fig. 5·1 Mean velocity profiles across the rough wall.

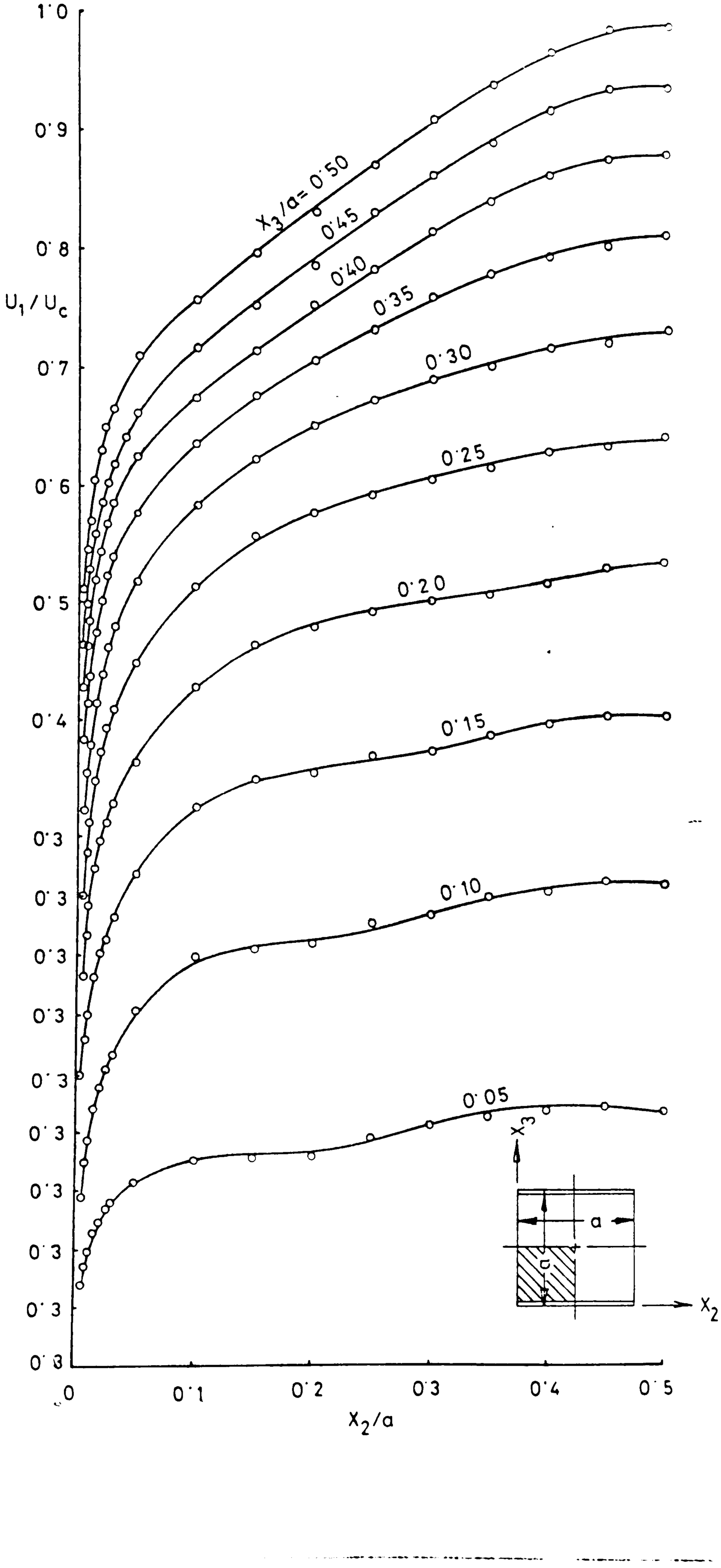

Mean velocity profiles parallel to the rough wall.

Fig. 5·2

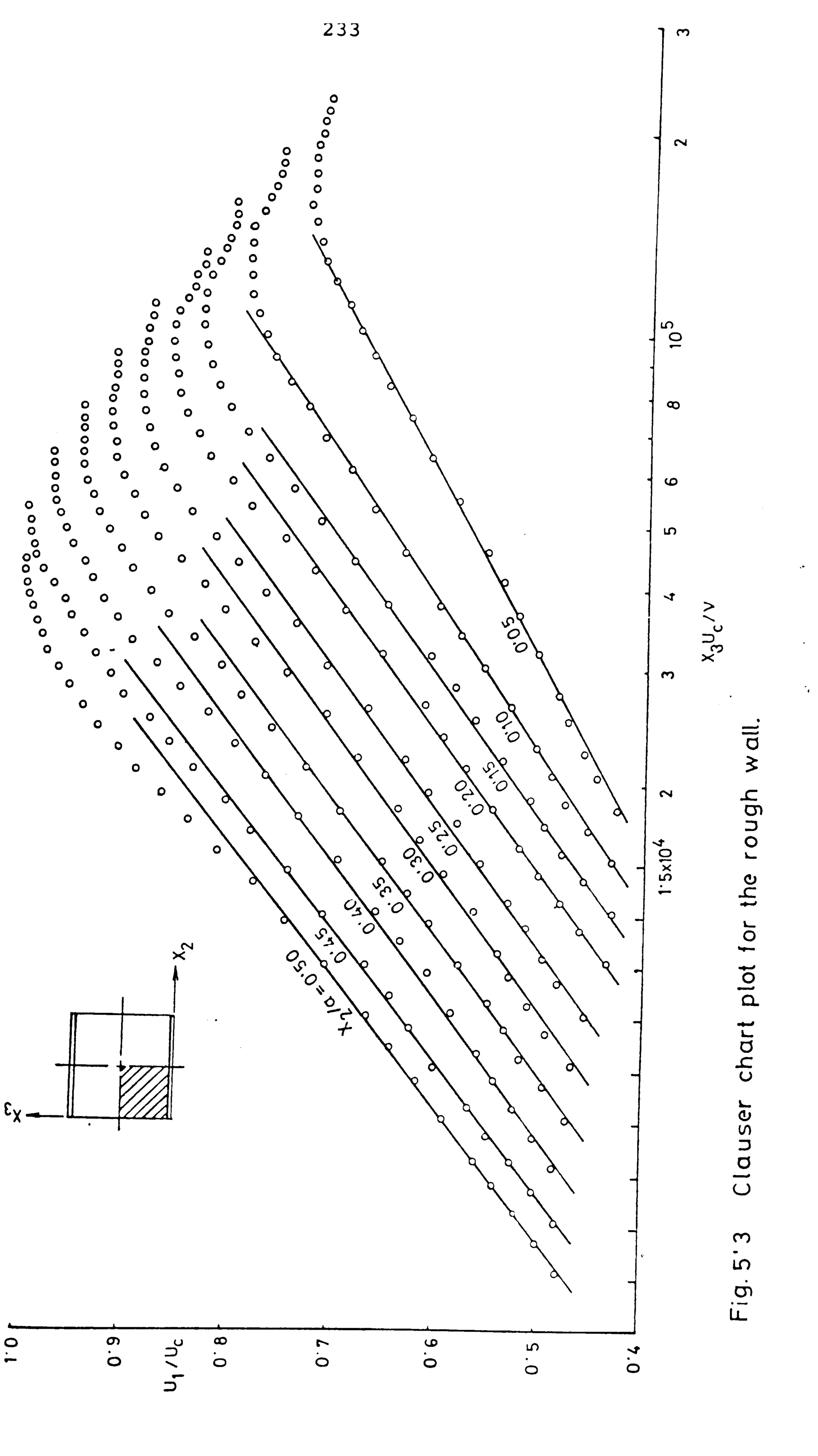

Fig. 5'3 Clauser chart plot for the rough wall.

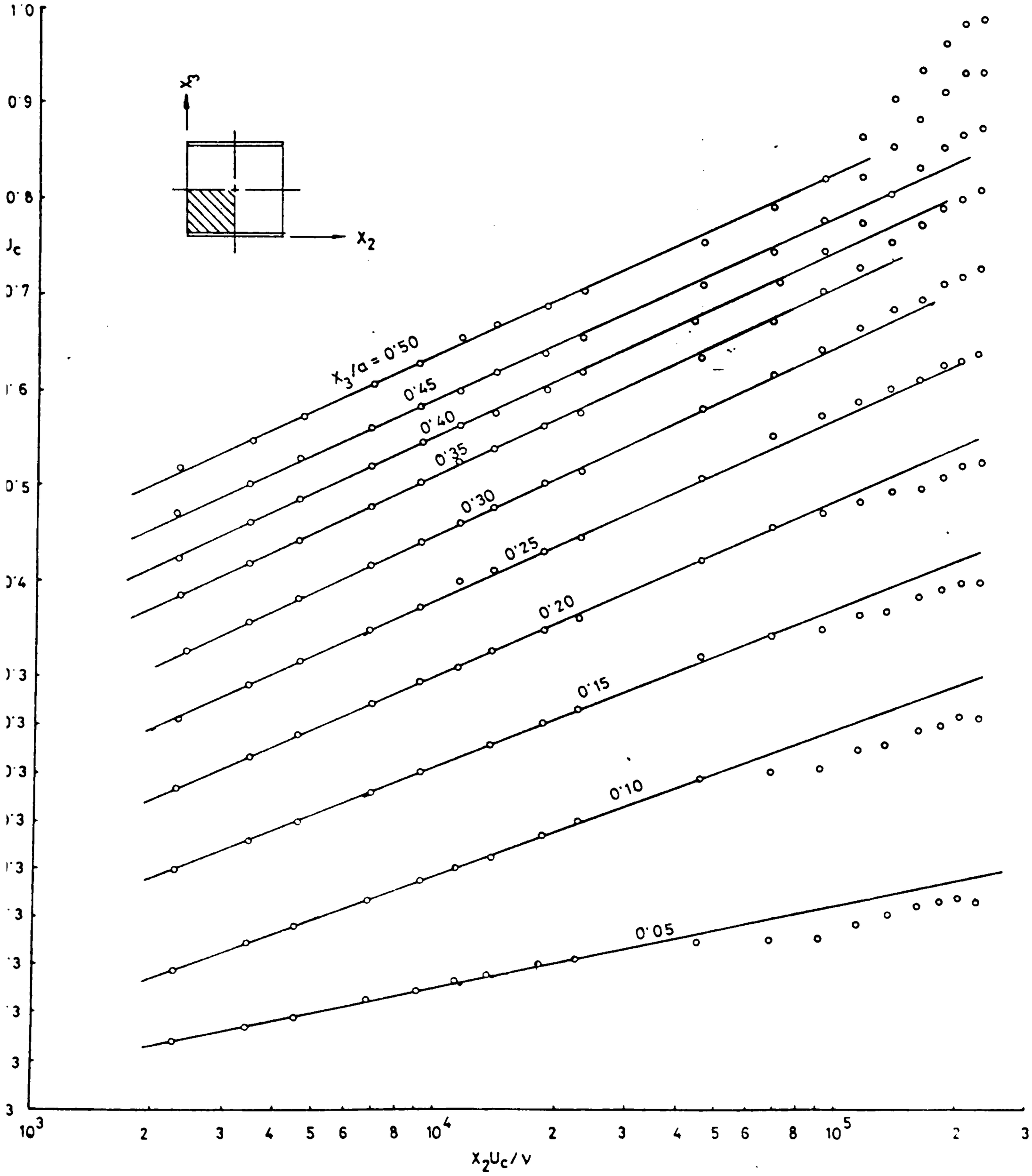

Fig. 5.4 Clauser chart plot for the smooth wall.

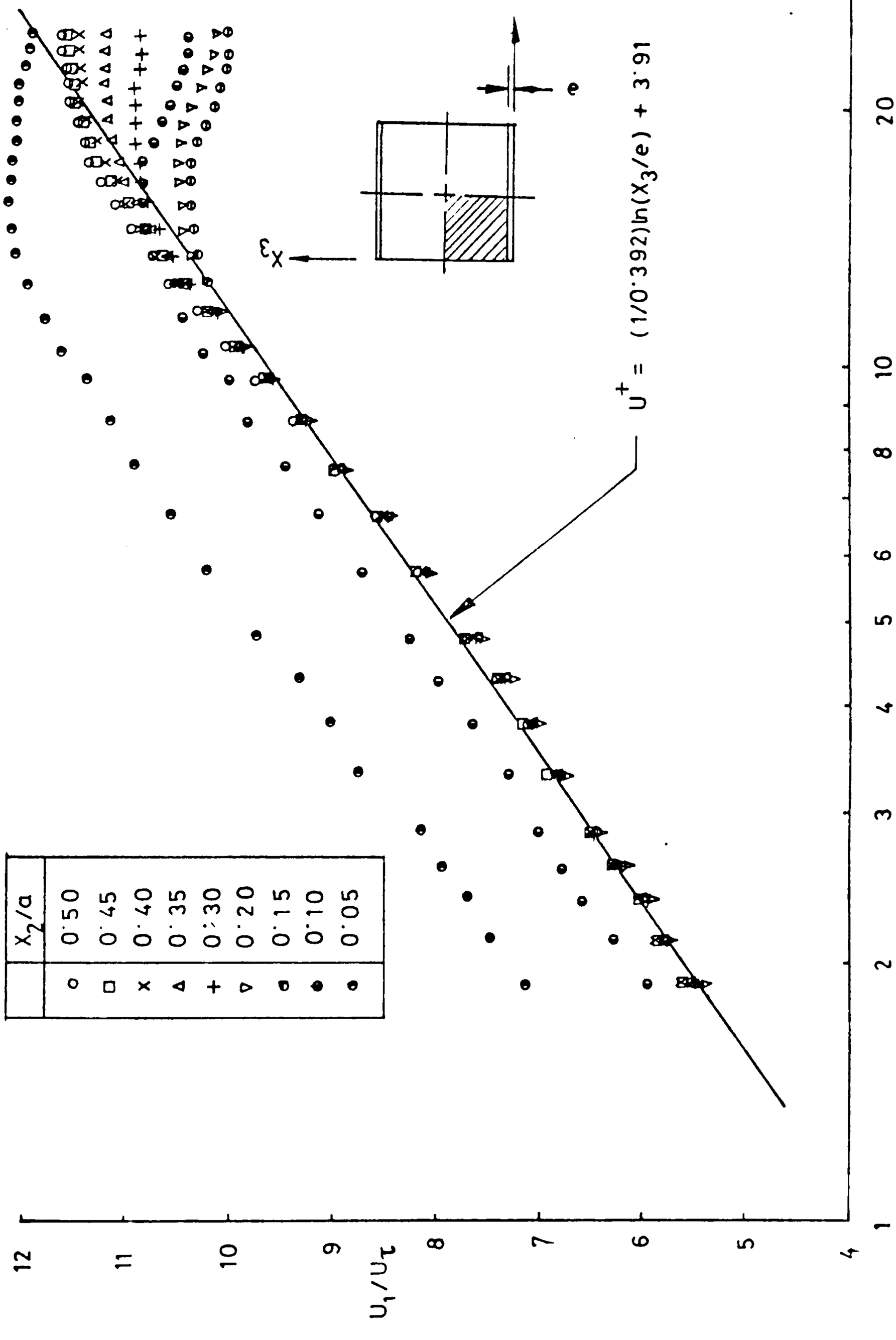

Fig.5.5 Logarithmic plot of mean velocity near the rough wall.

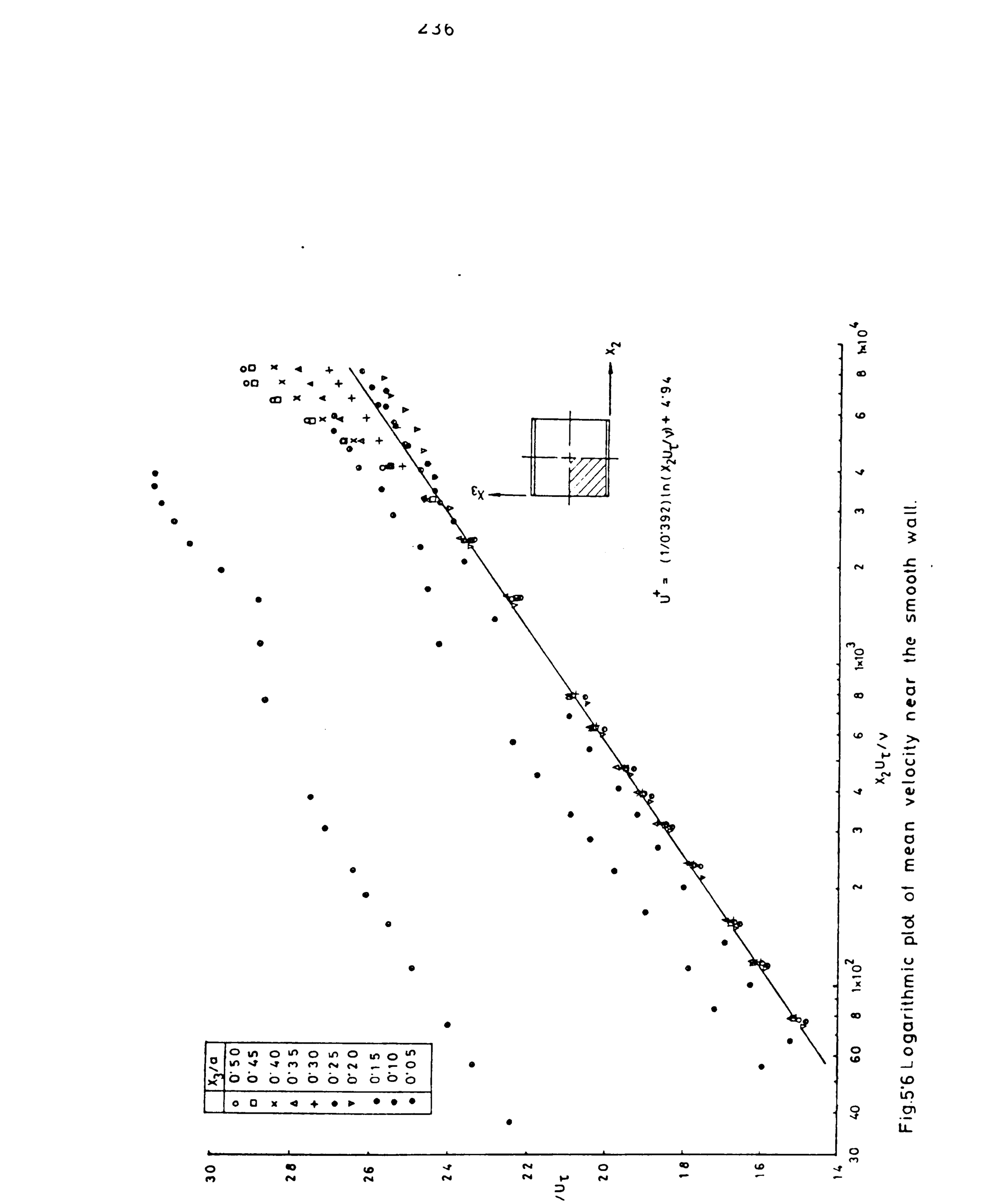

Fig.5·6 Logarithmic plot of mean velocity near the smooth wall.

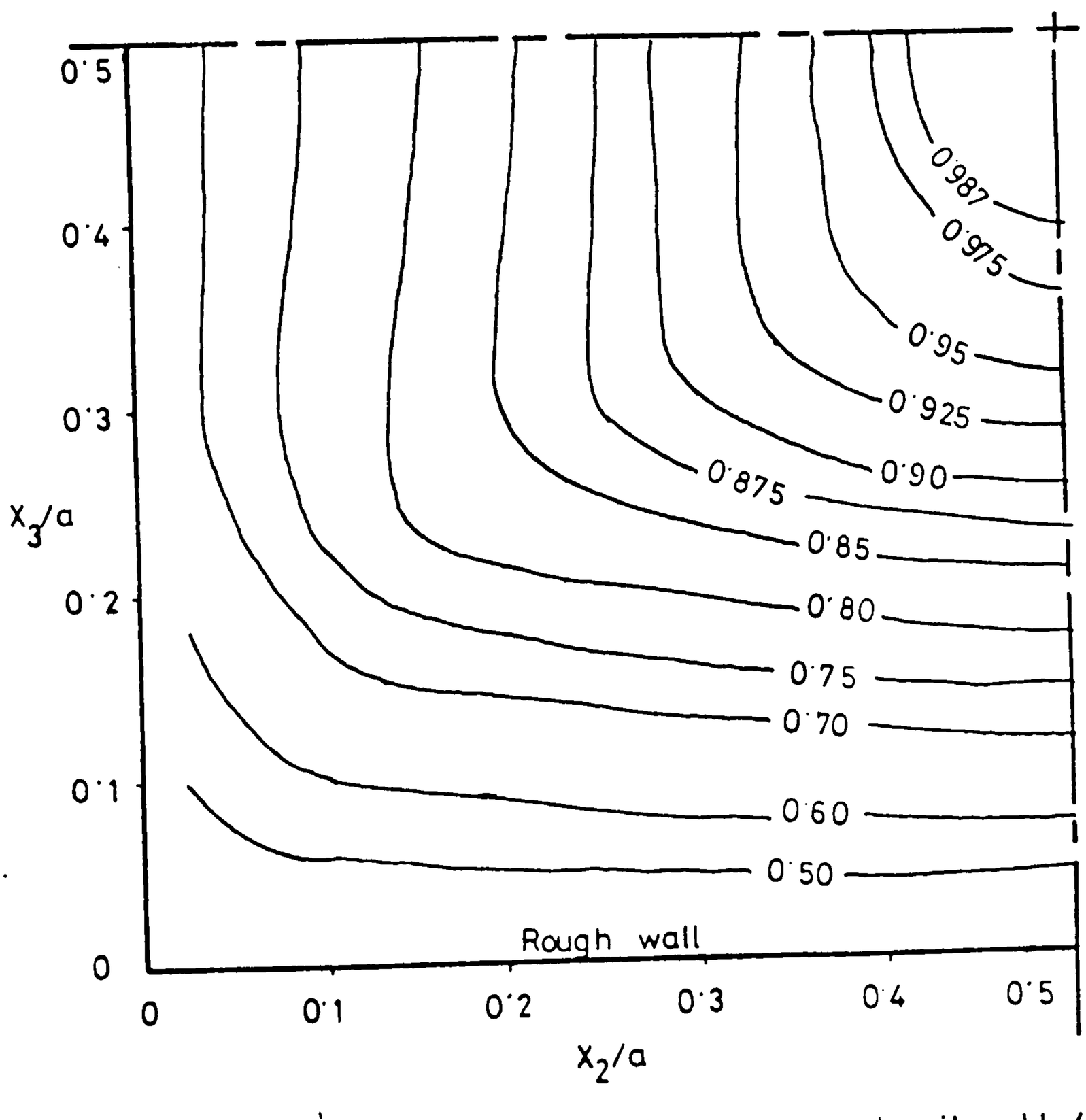

Fig. 5·7 Contours of mean velocity, U_1/U_c.

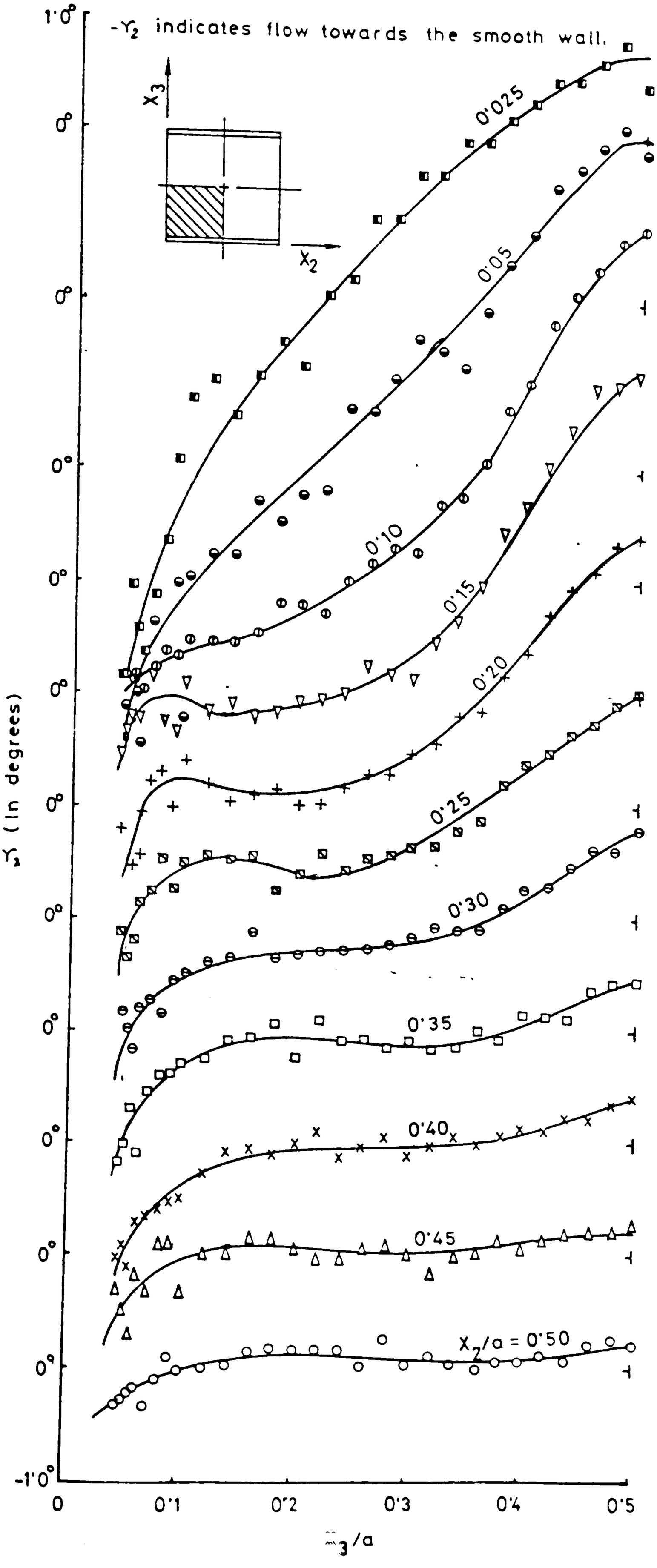

Fig.5·8 Distribution of secondary flow angle, γ_2.

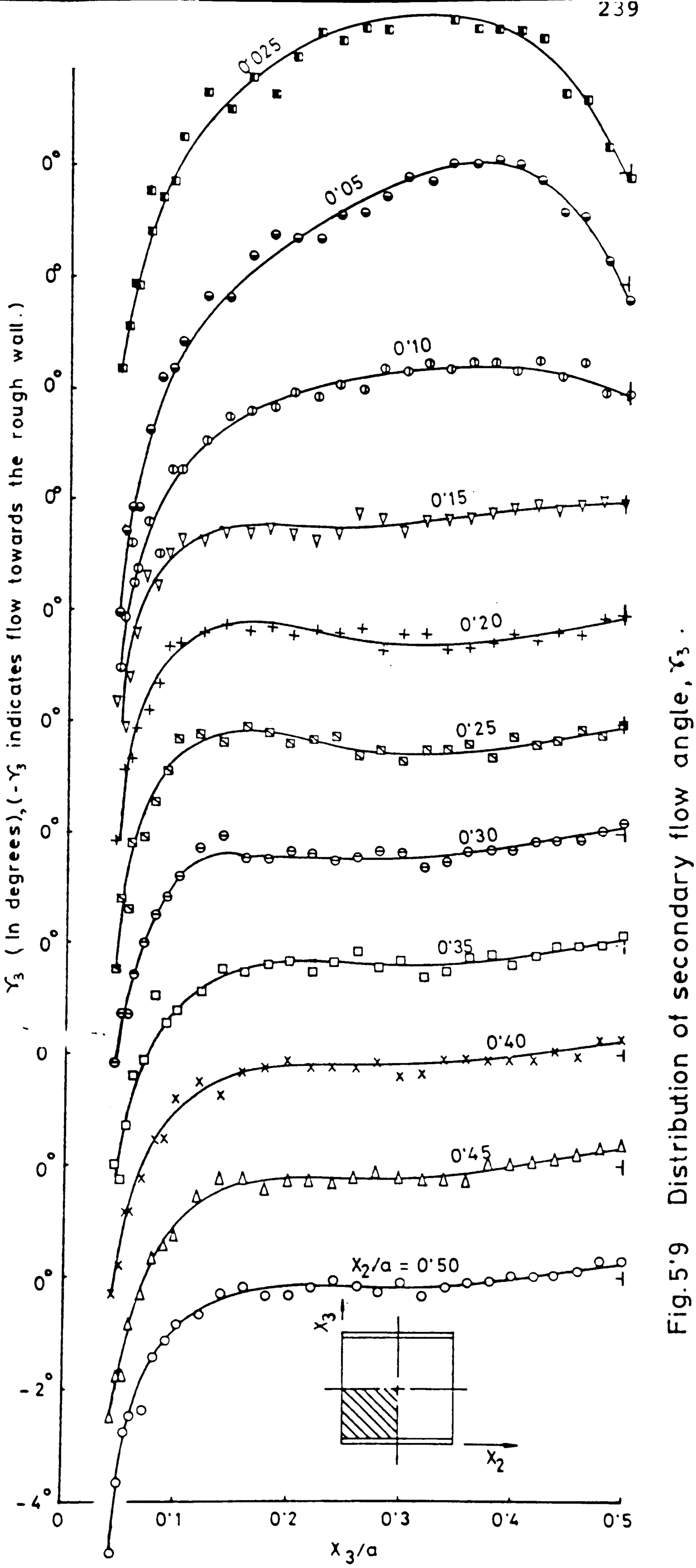
0·025
0·05
0·10
0·15
0·20
0·25
0·30
0·35
0·40
0·45
X2/a = 0·50
X3
X2
0°
-2°
-4°
0
0·1
0·2
0·3
0·4
0·5
X3/a
Y3 (In degrees), (-Y3 indicates flow towards the rough wall.)
Distribution of secondary flow angle, Y3.

Fig. 5·9

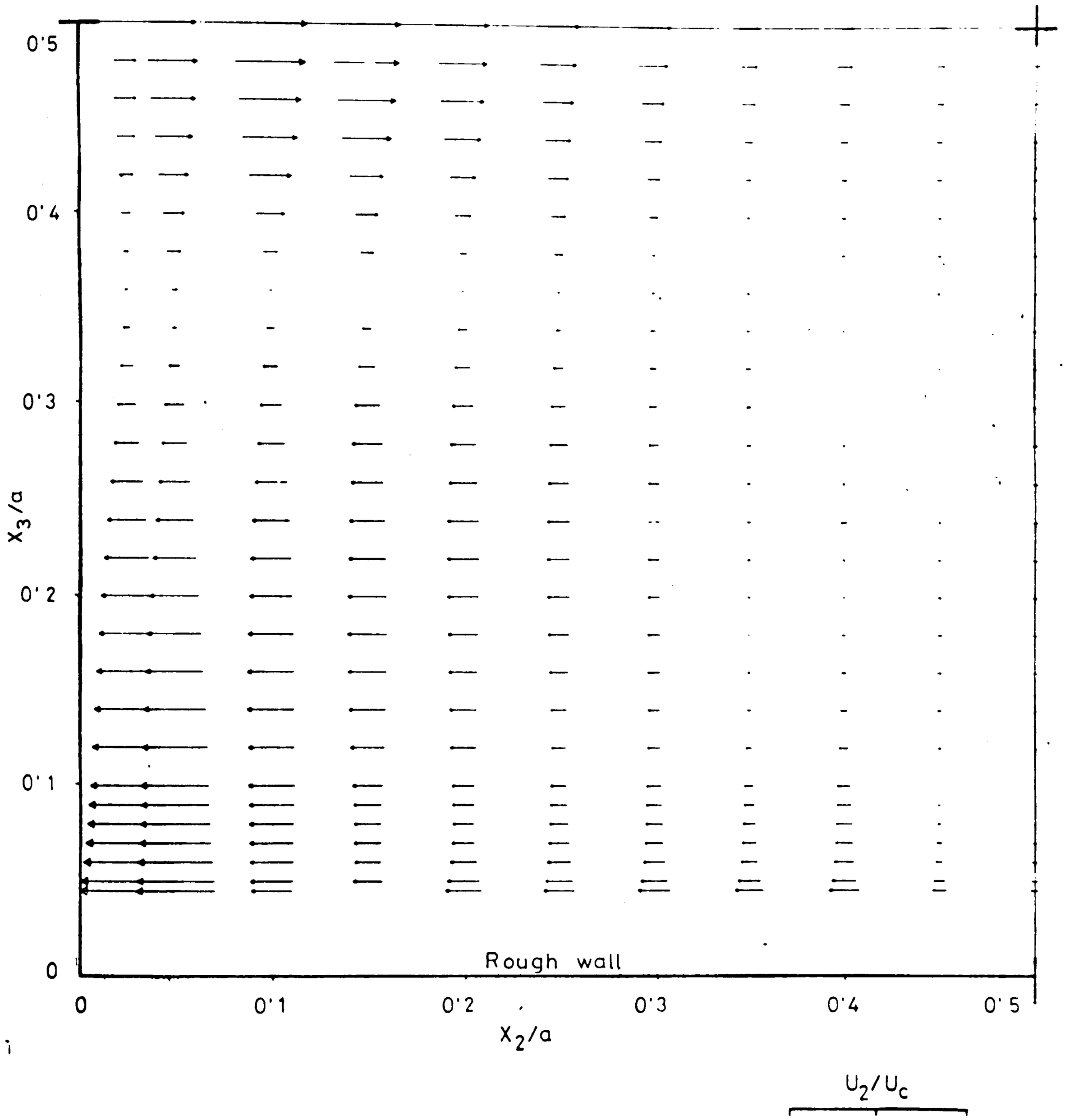

Fig. 5'10 Distribution of U_2/U_c vectors.

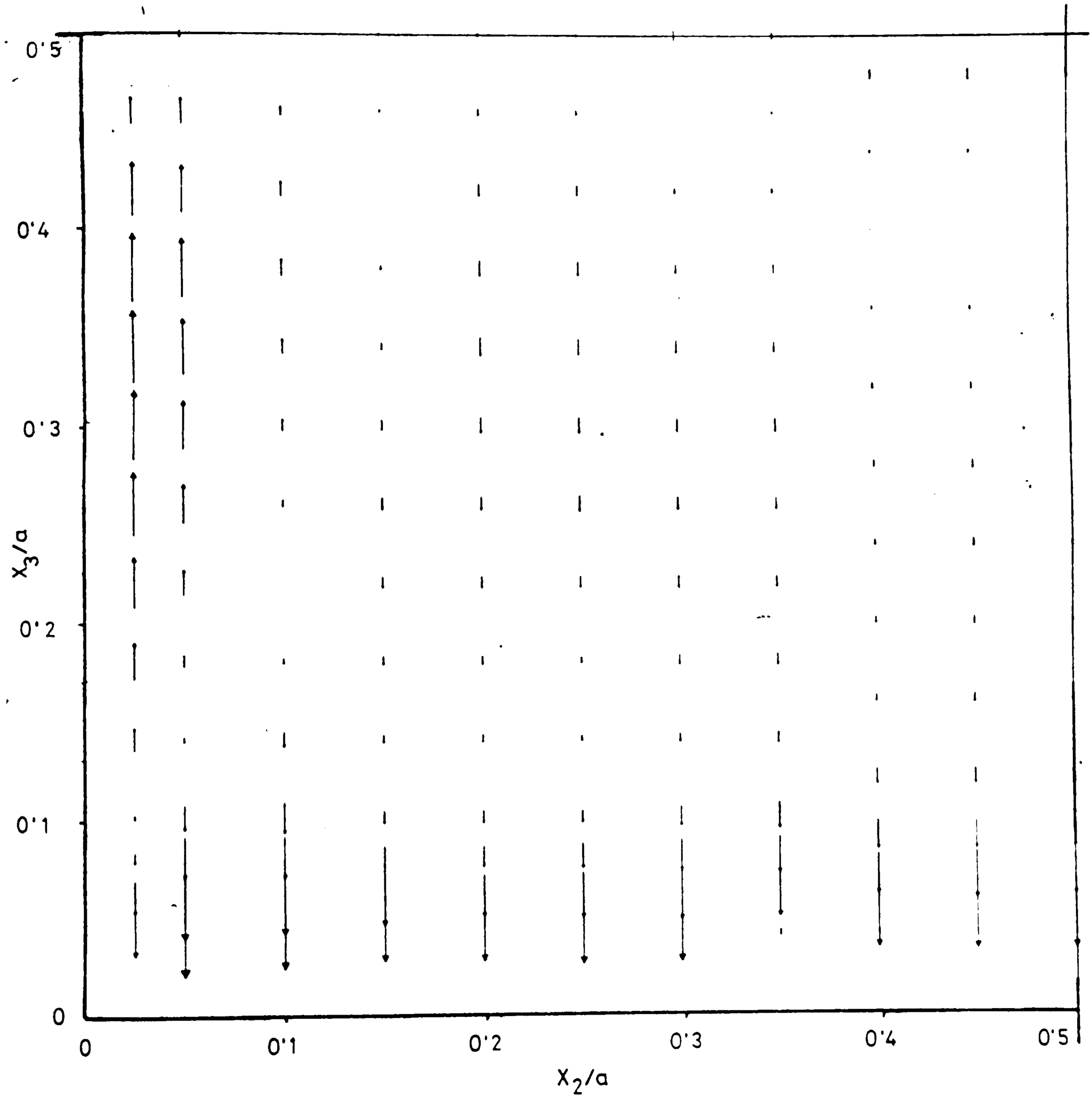

Fig. 5·11 Distribution of U_3/U_c vectors.

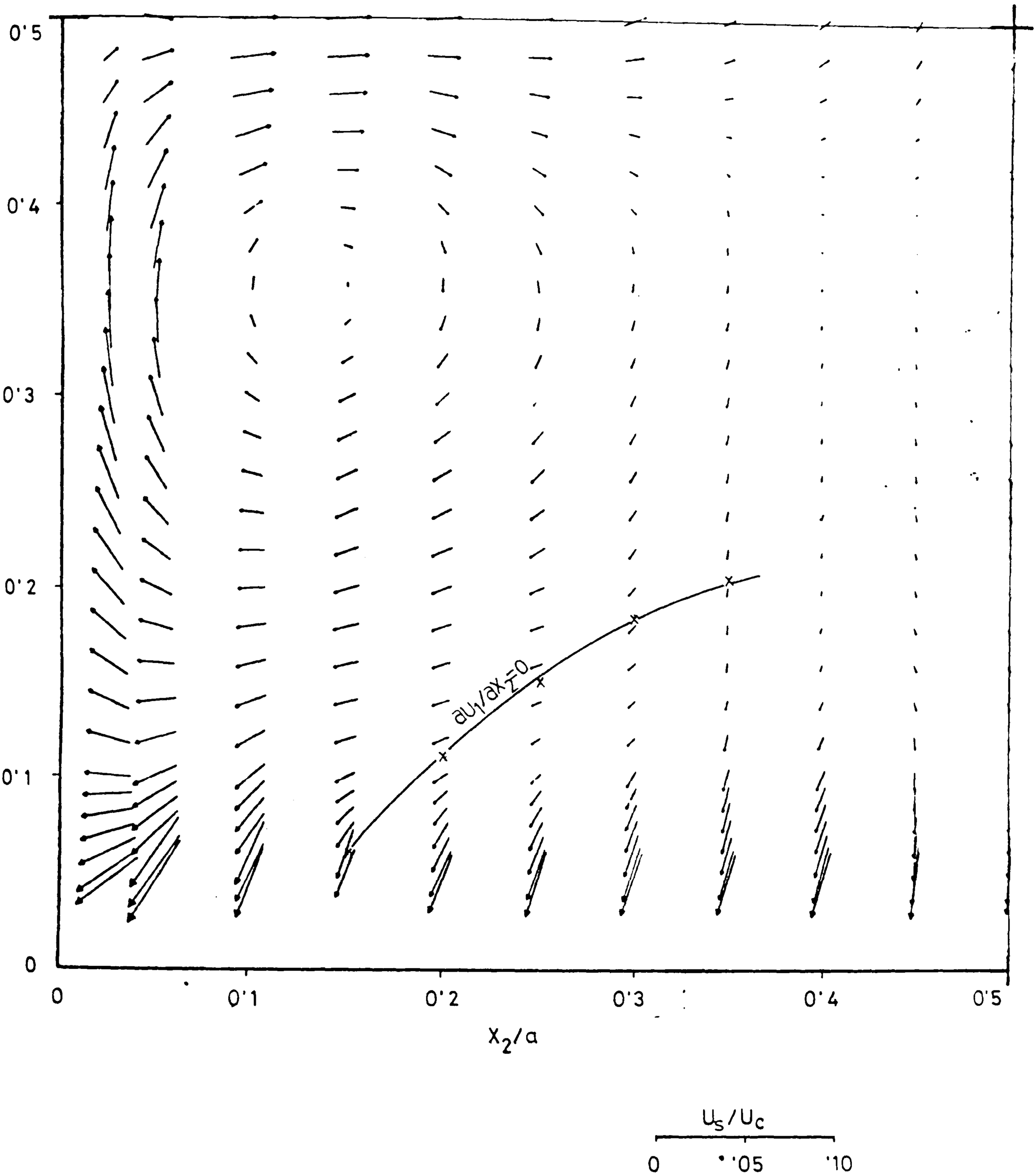

Fig. 5'12 Distribution of U_s/U_c vectors.

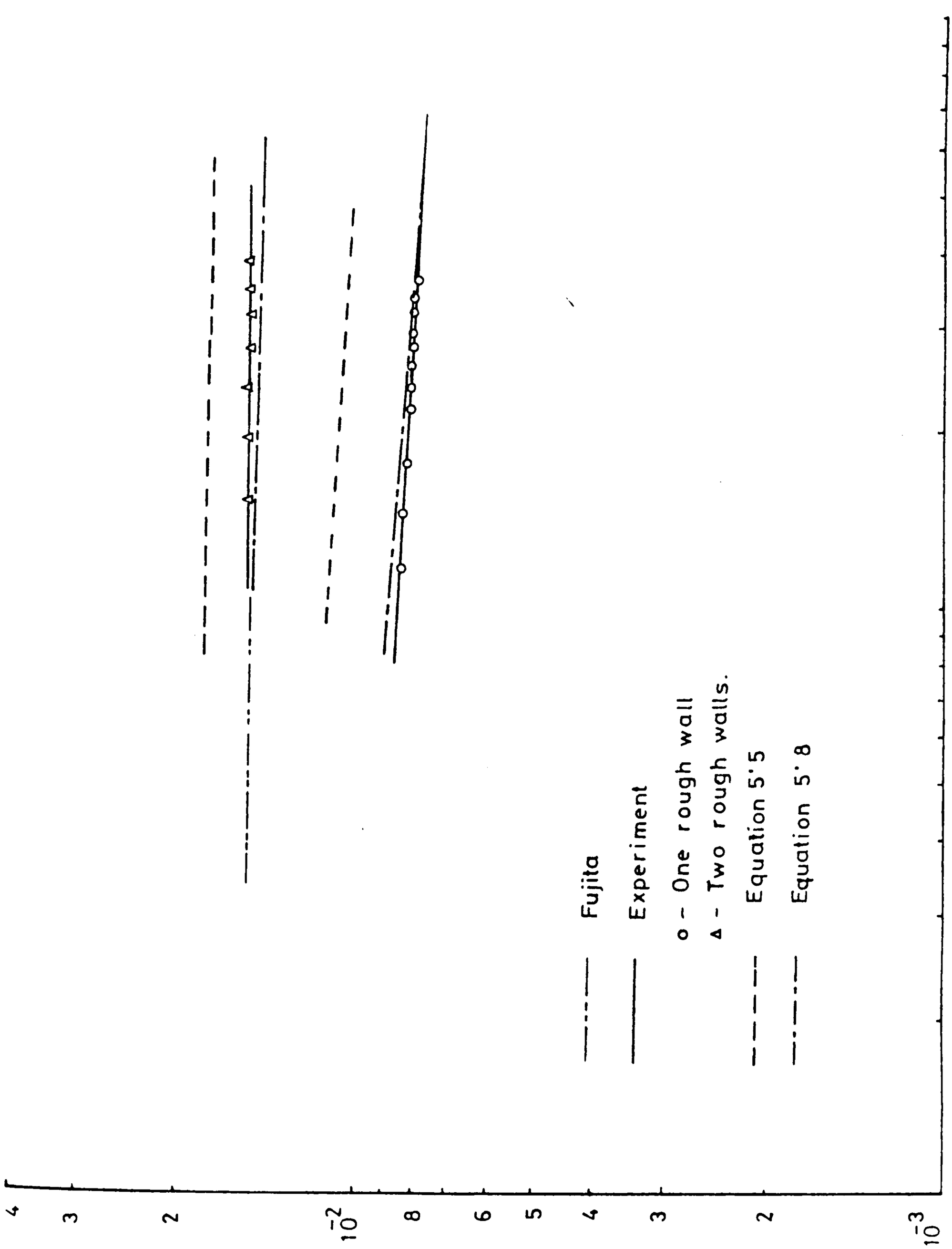

Fig.5'13 Variation of friction factor with R_e.

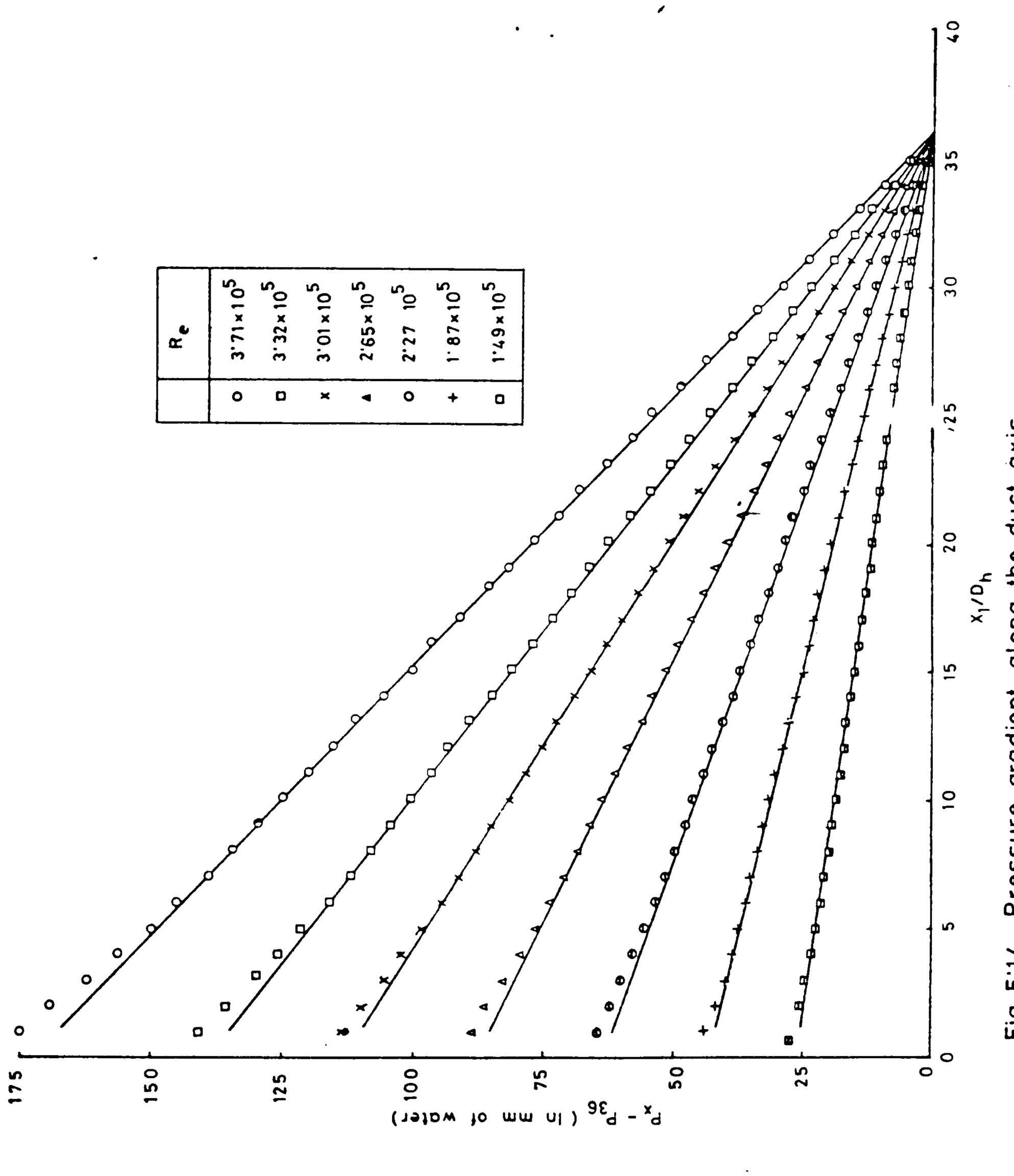

Fig. 5'14 Pressure gradient along the duct axis.

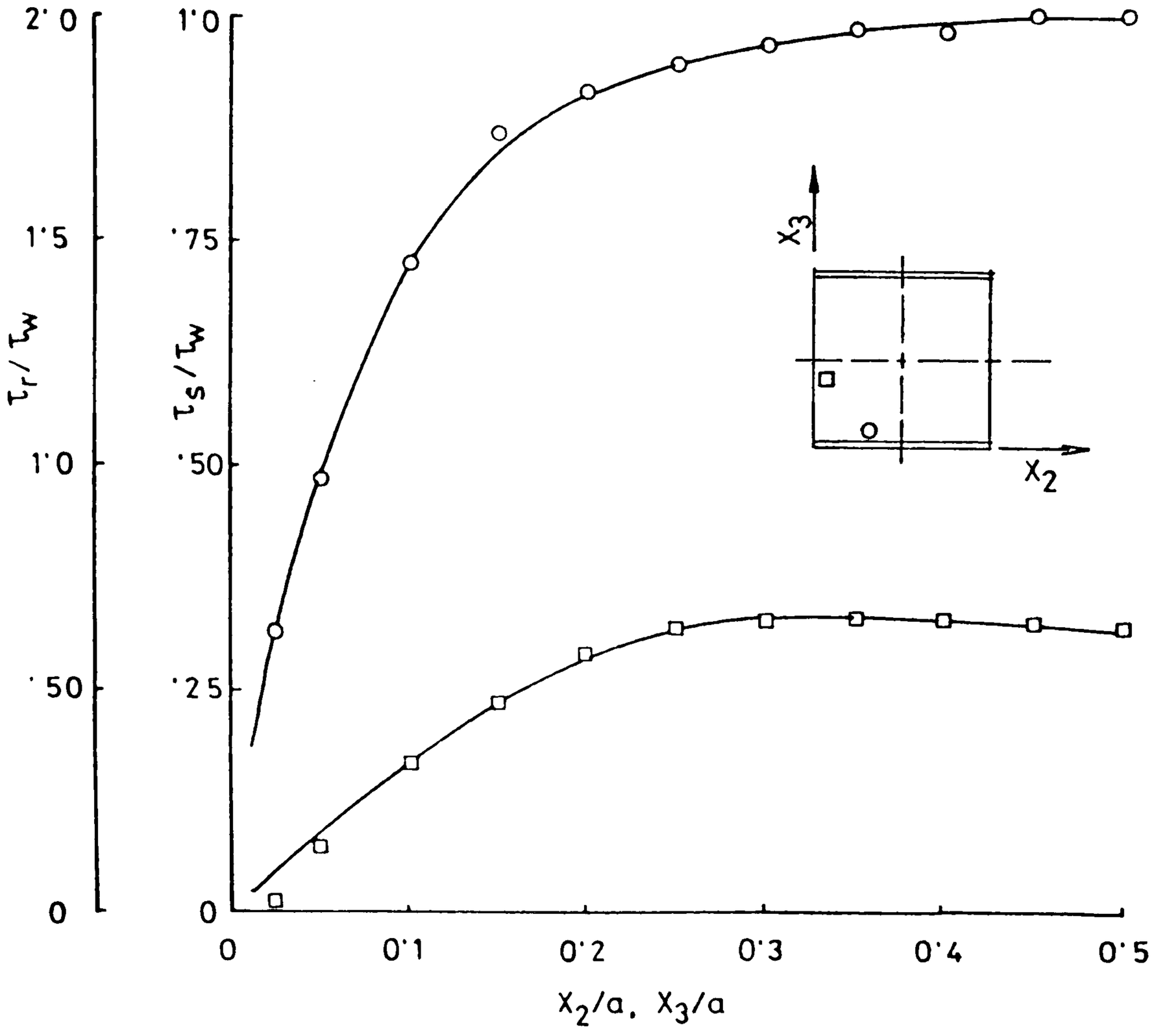

Fig.5'15 Distribution of local wall shear stress.

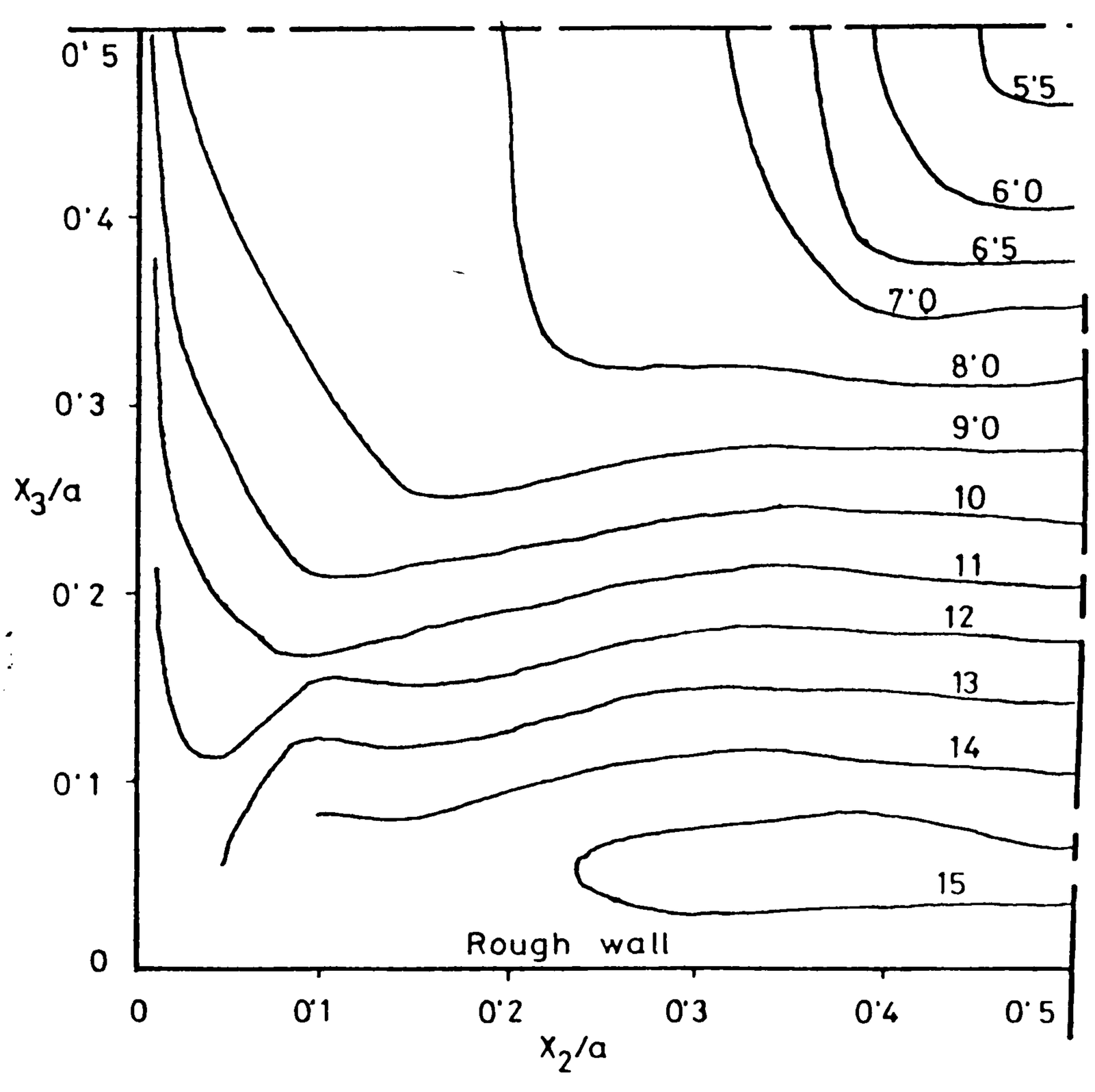

Fig. 5'16 Contours of $\bar{u}_1/U_c \times 10^2$.

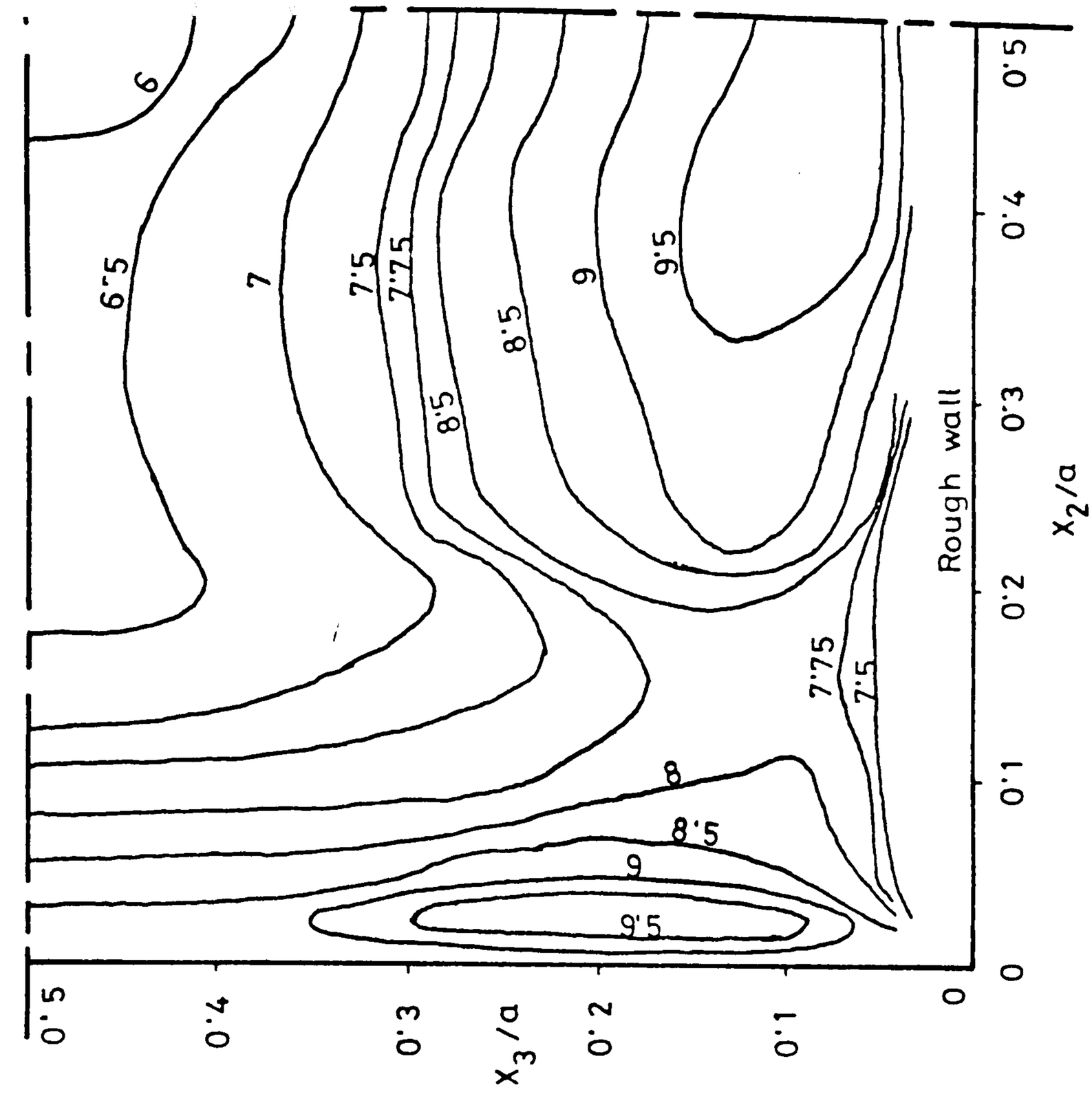

Fig.5·18 Contours of $\tilde{u}_3/U_c \times 10^2$

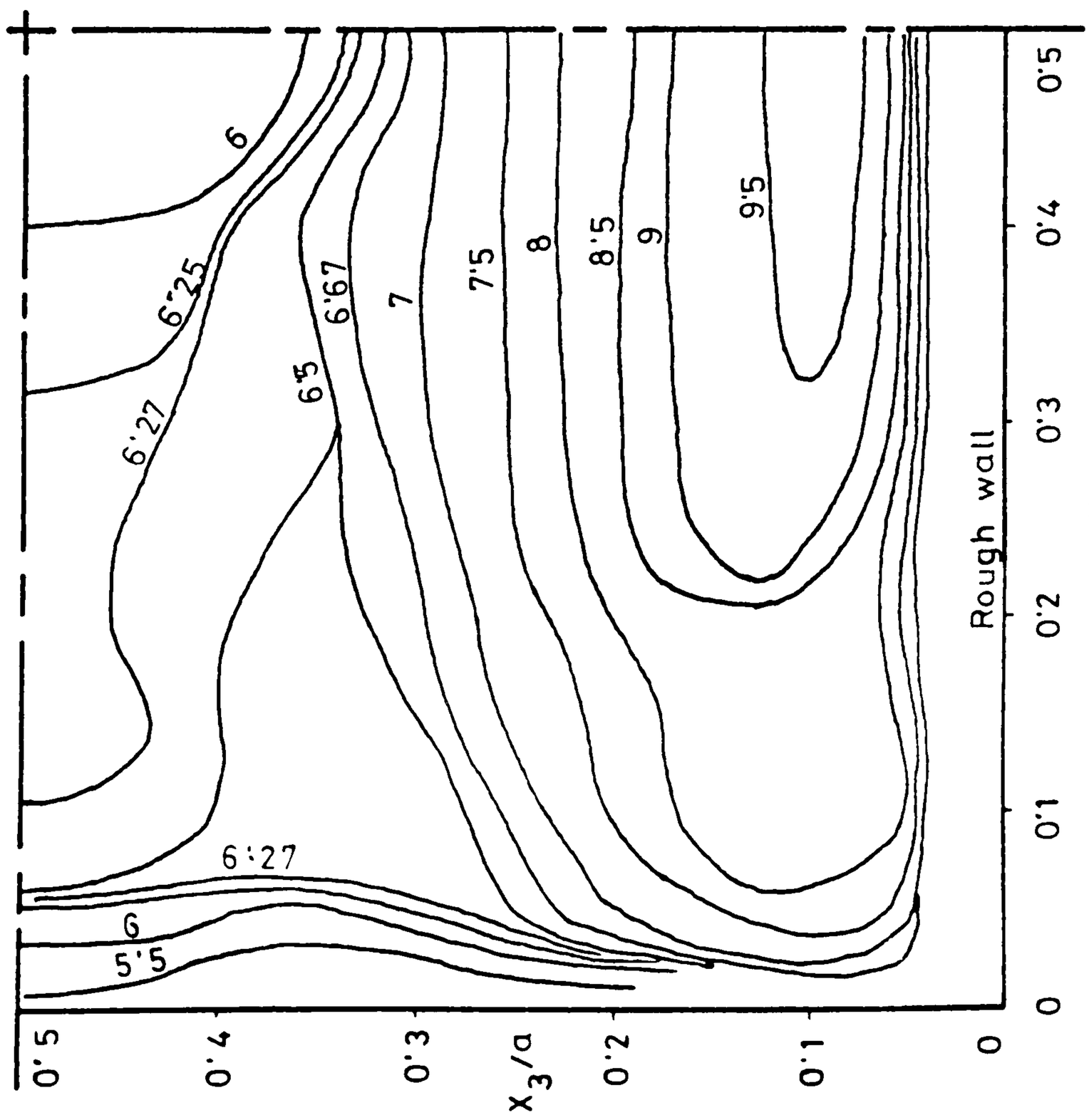

Fig.5·17 Contours of $\tilde{u}_2/U_c \times 10^2$

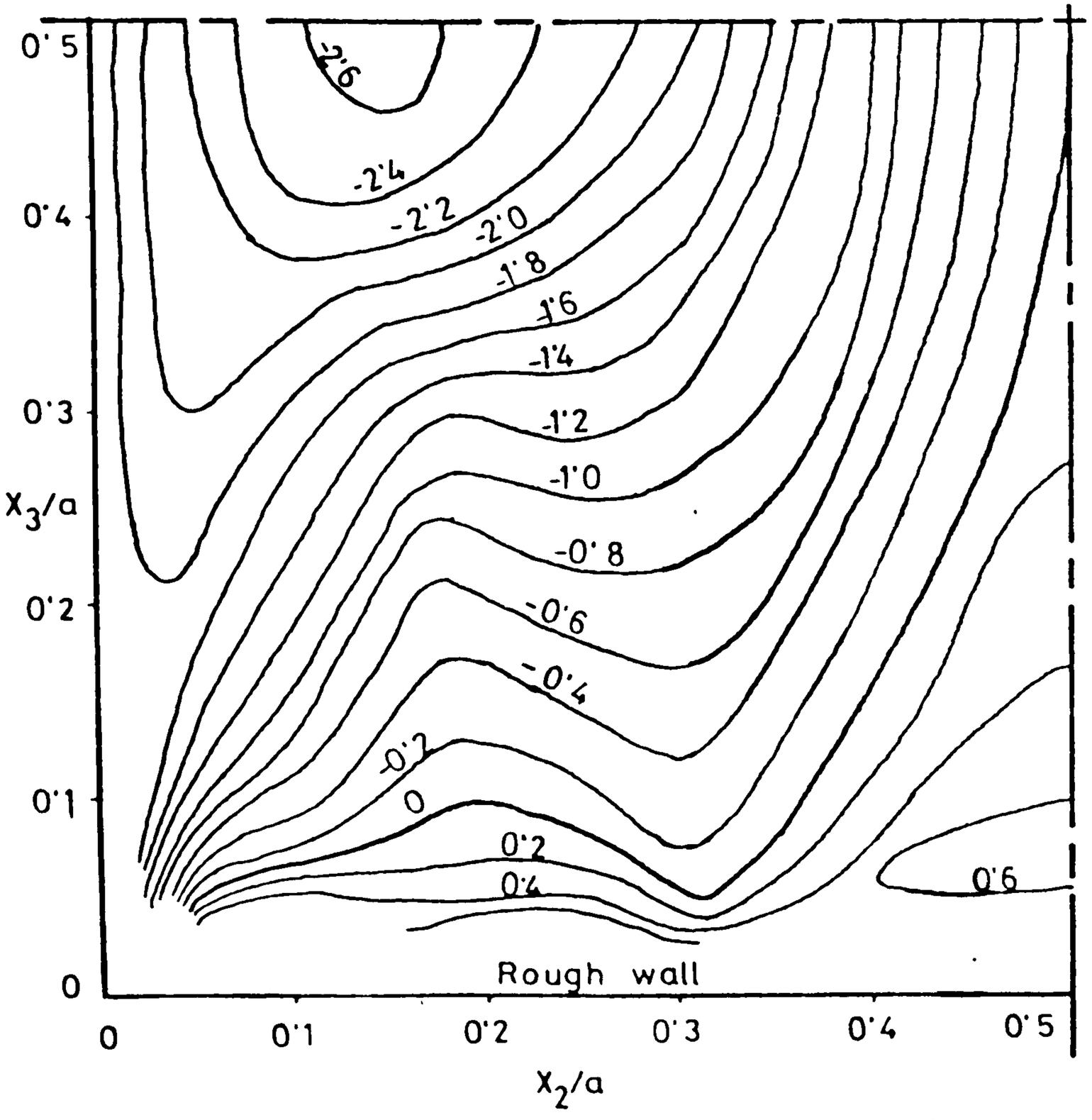

Fig. 5·19 Contours of $\overline{u_1 u_2}/U_c^2 \times 10^3$

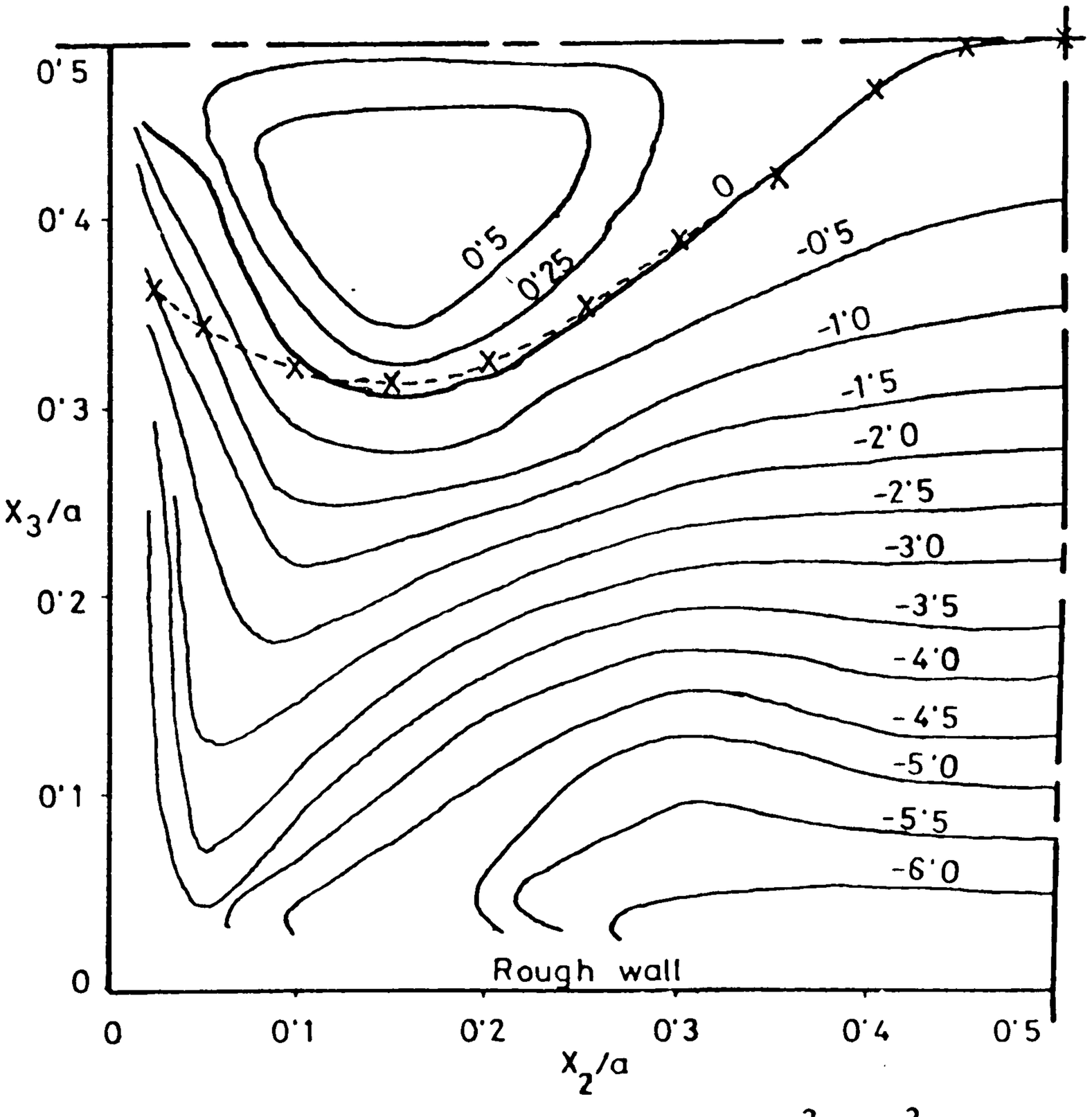

Fig. 5·20 Contours of $\overline{u_1 u_3}/U_c^2 \times 10^3$

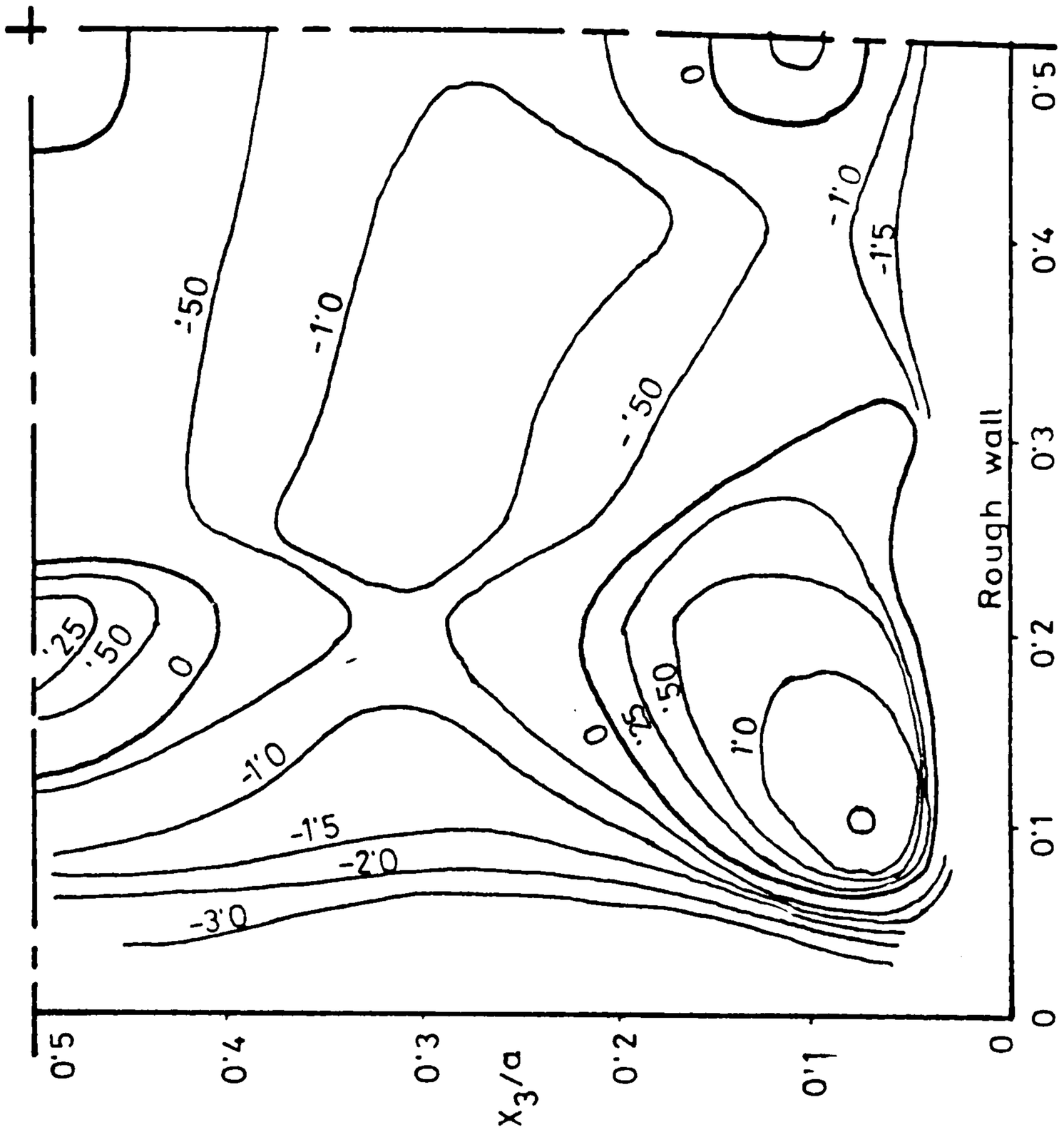

Fig. 5·22 Contours of $(\overline{u_2^2} - \overline{u_3^2}) / U_c^2 \times 10^3$

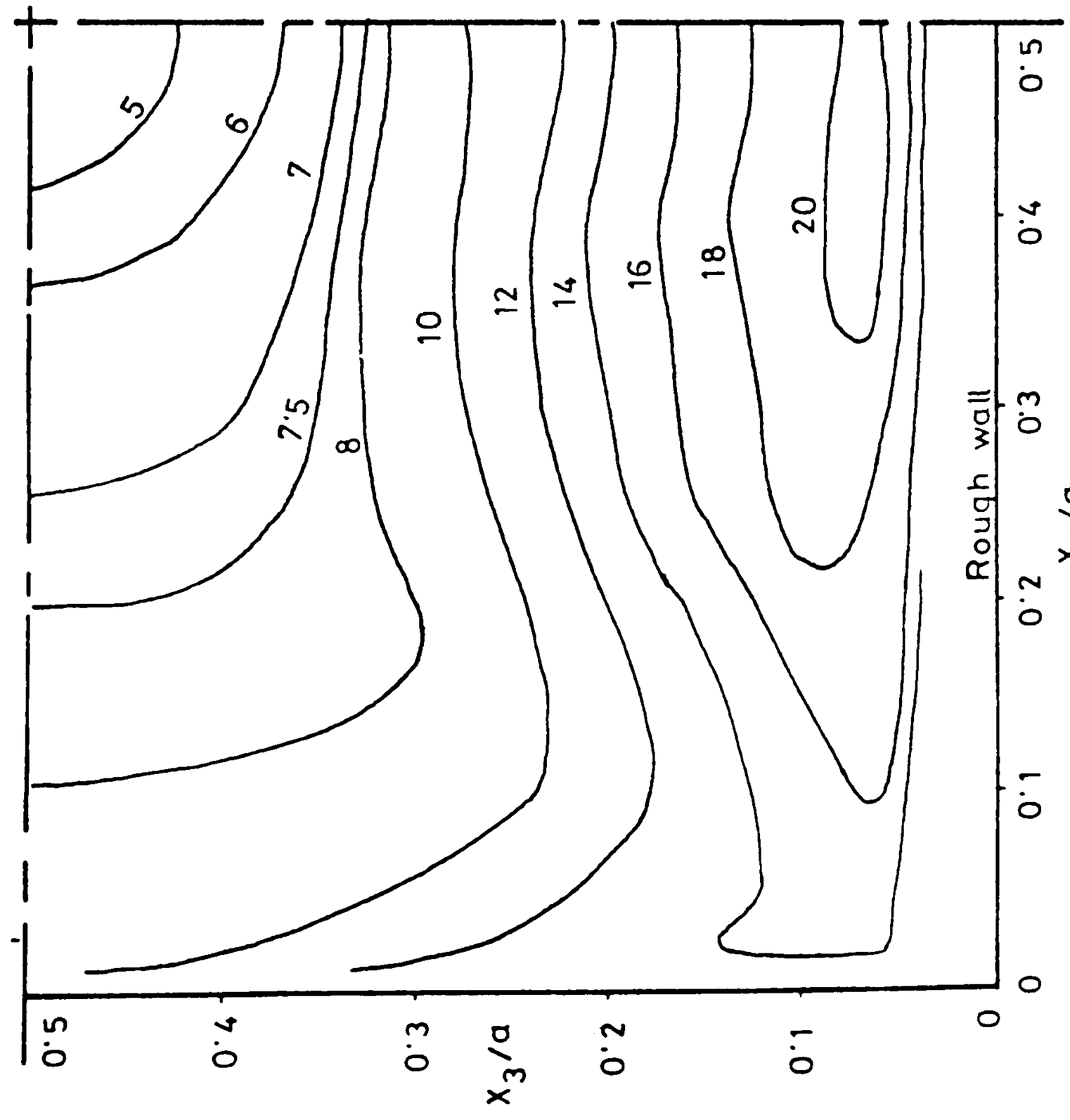

Fig. 5·21 Contours of $k / U_c^2 \times 10^3$

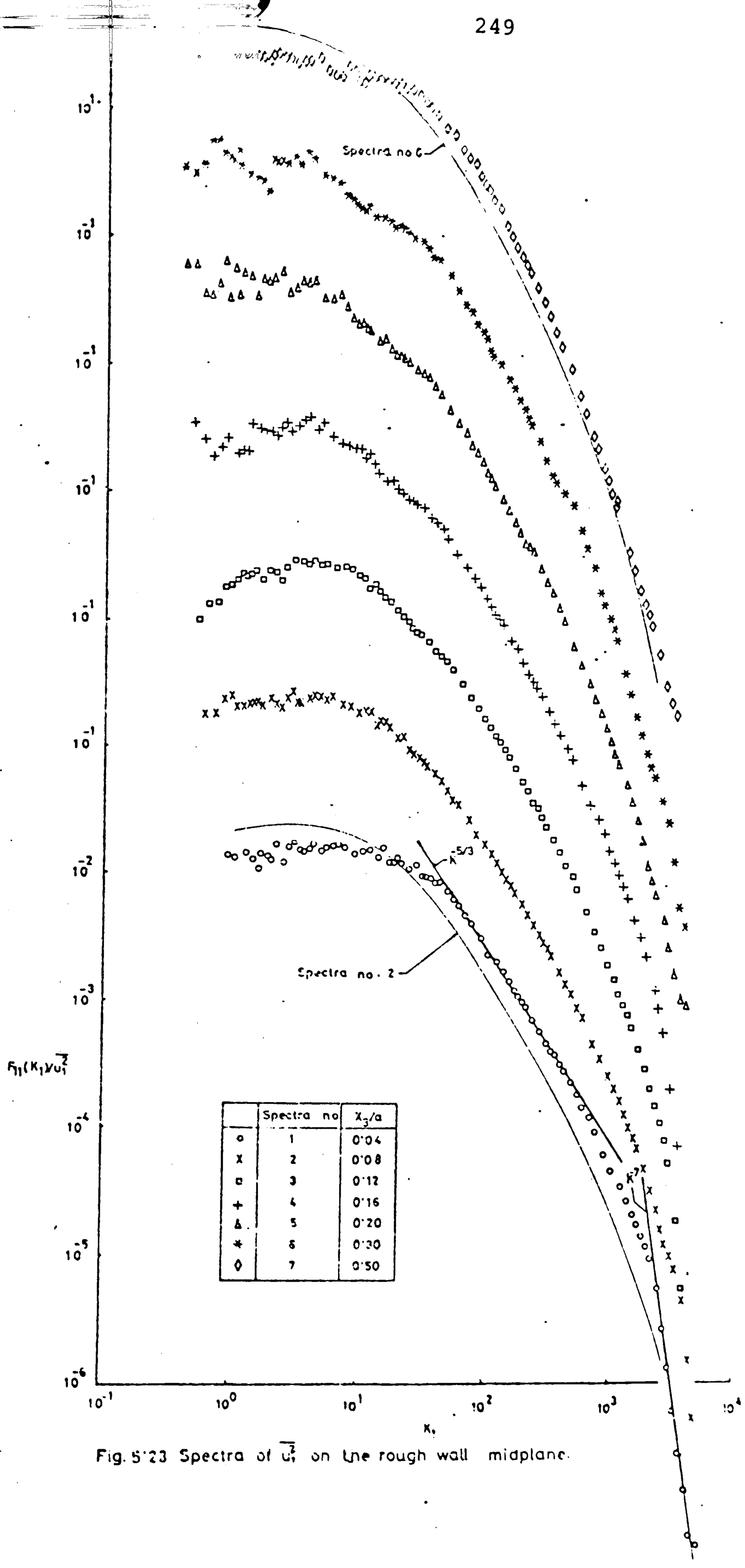

	Spectra no	x_3/a
o	1	0·04
x	2	0·08
□	3	0·12
+	4	0·16
Δ	5	0·20
*	6	0·30
◇	7	0·50

Fig. 5·23 Spectra of $\overline{u_1^2}$ on the rough wall midplane.

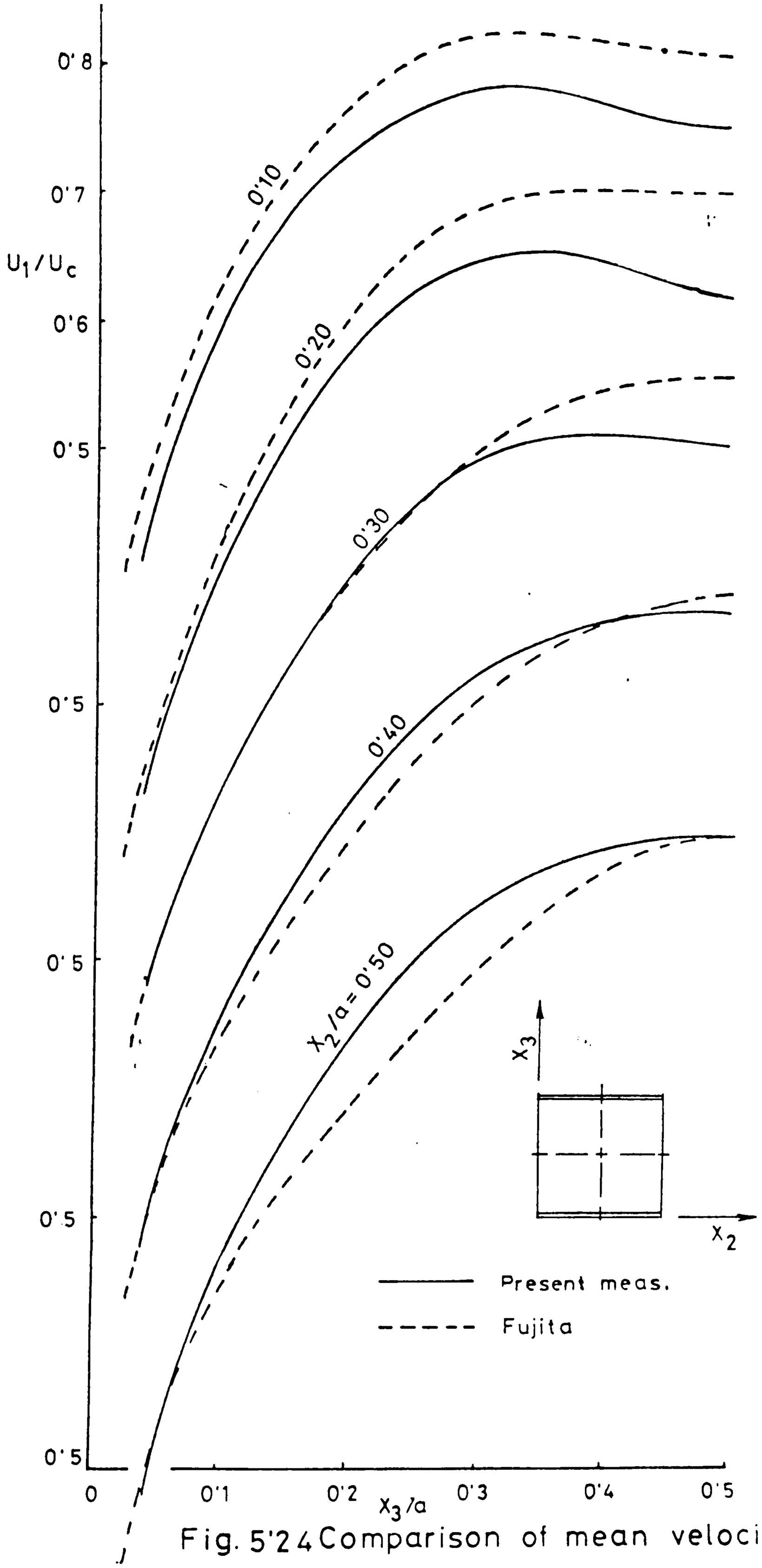

Fig. 5'24 Comparison of mean velocity profiles.

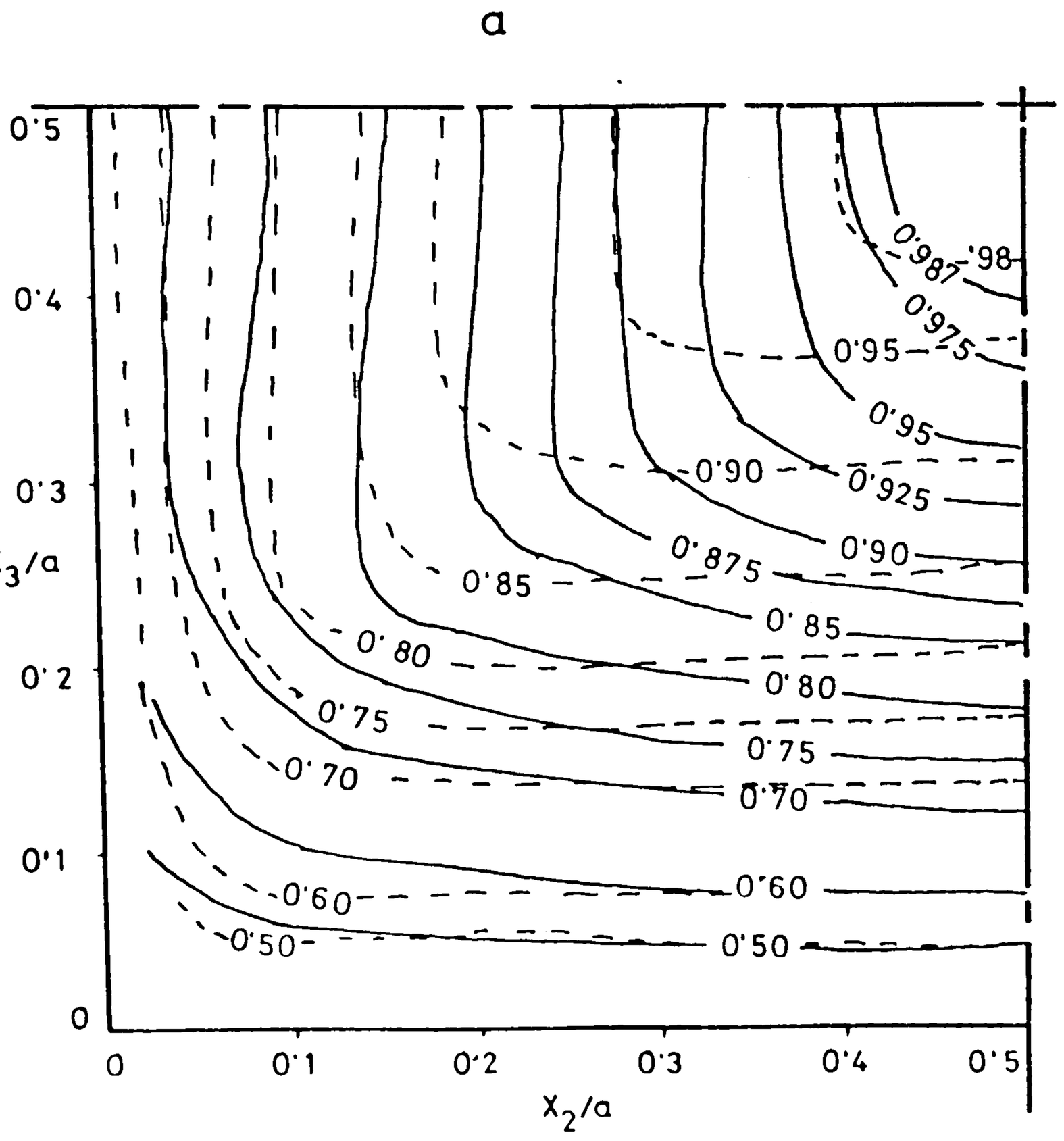

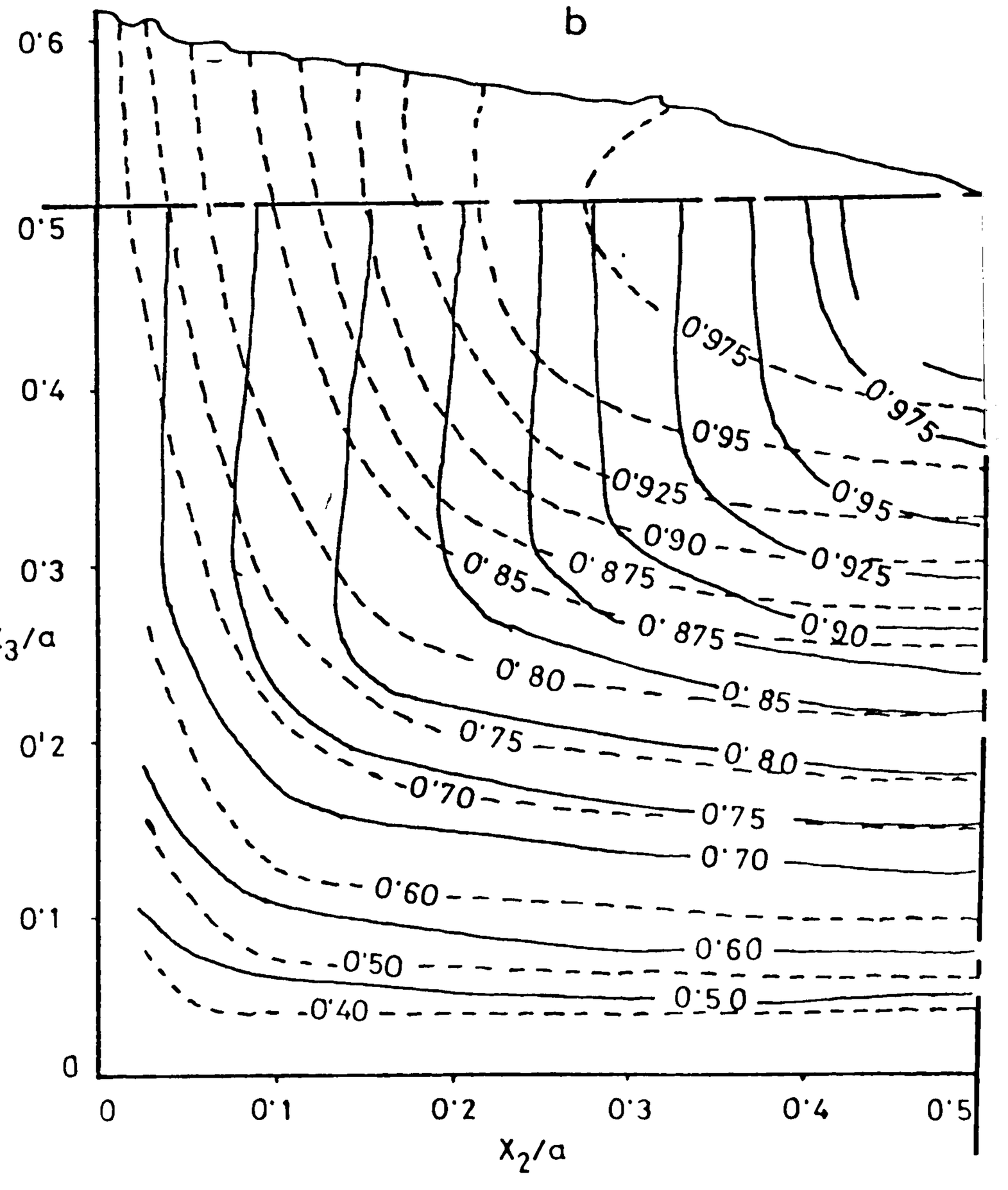

Fig.5·25 Comparison of U_1/U_c contours.

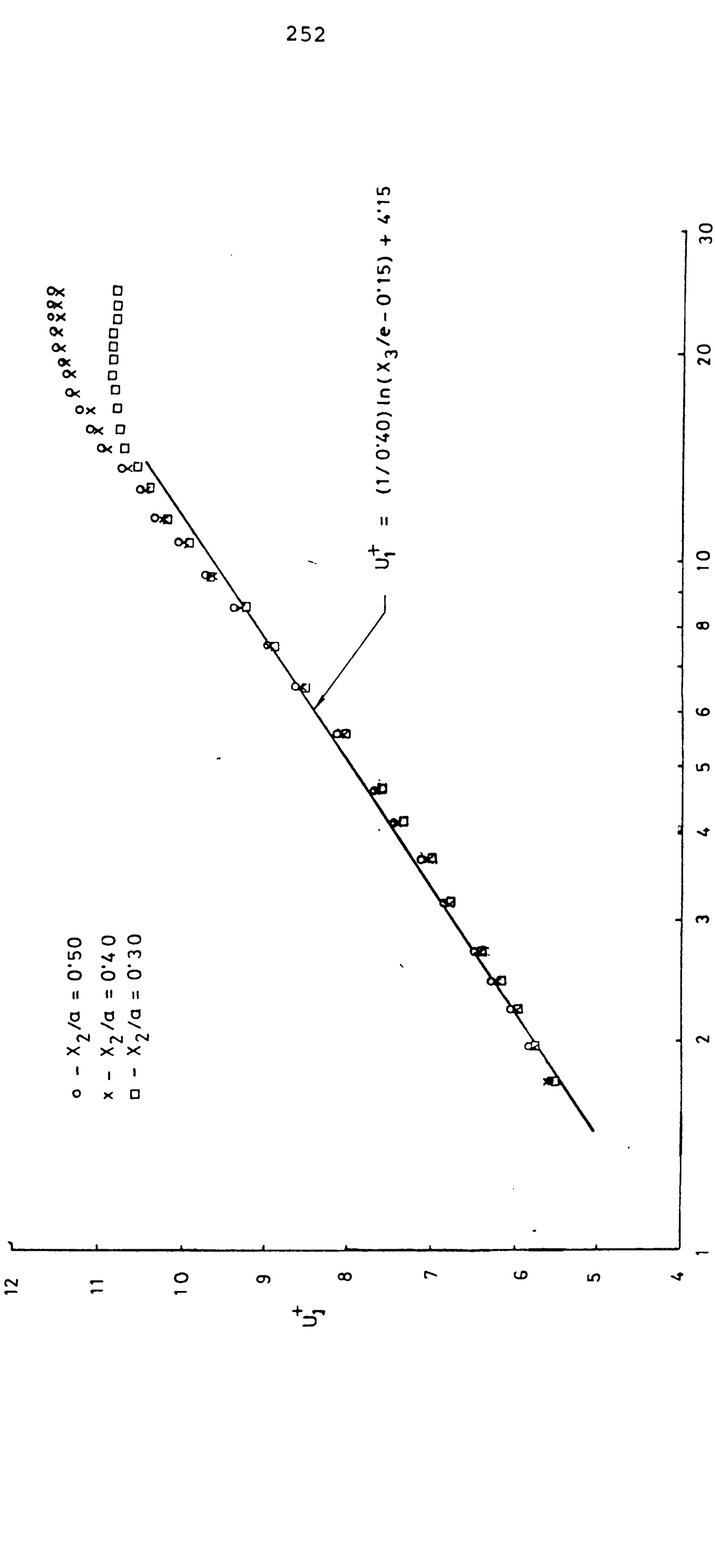

Fig. 5.26 Logarithmic plot of mean velocity near the rough wall with origin shifted above the rib root.

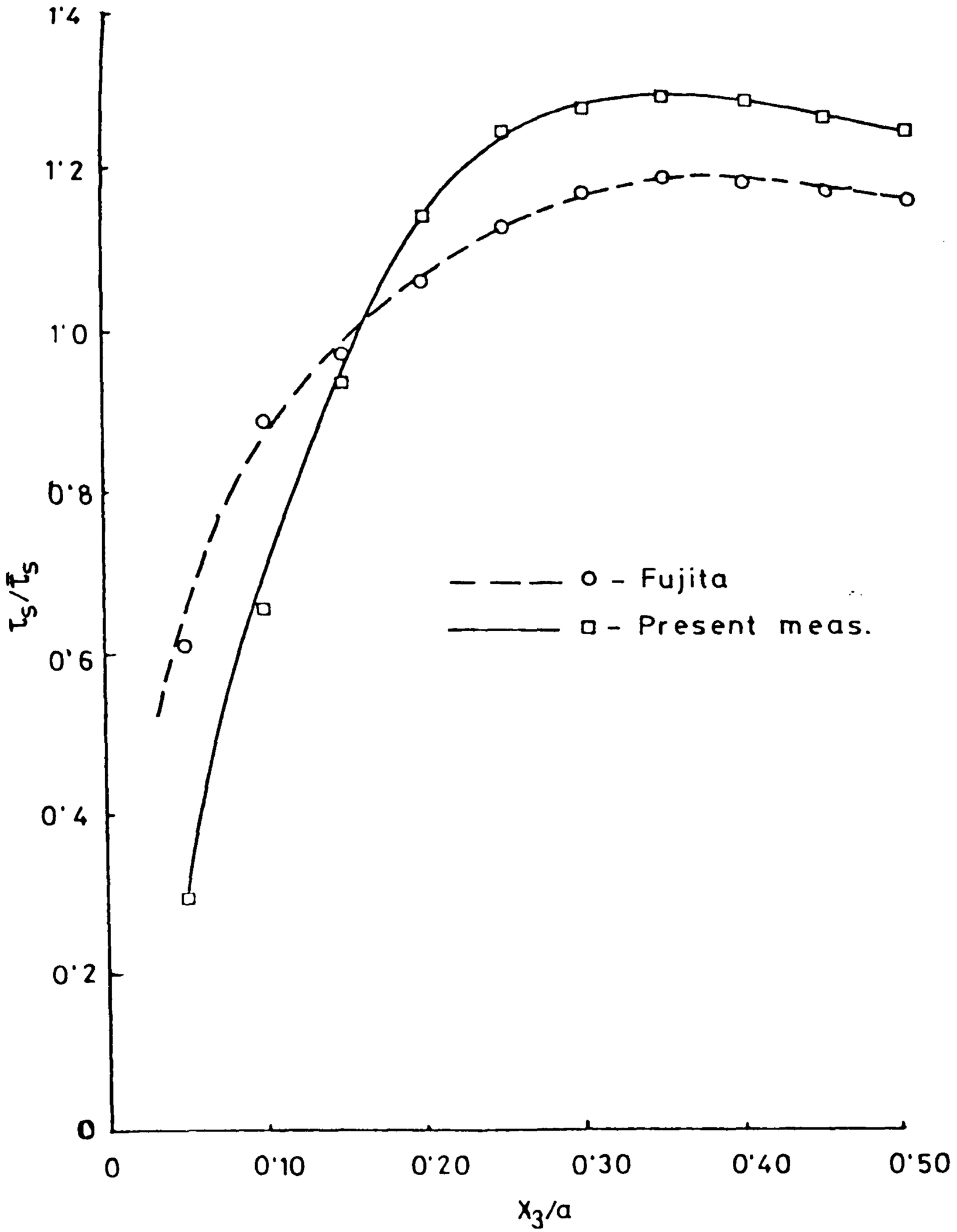

Fig. 5·27 Comparison of smooth wall shear stress.

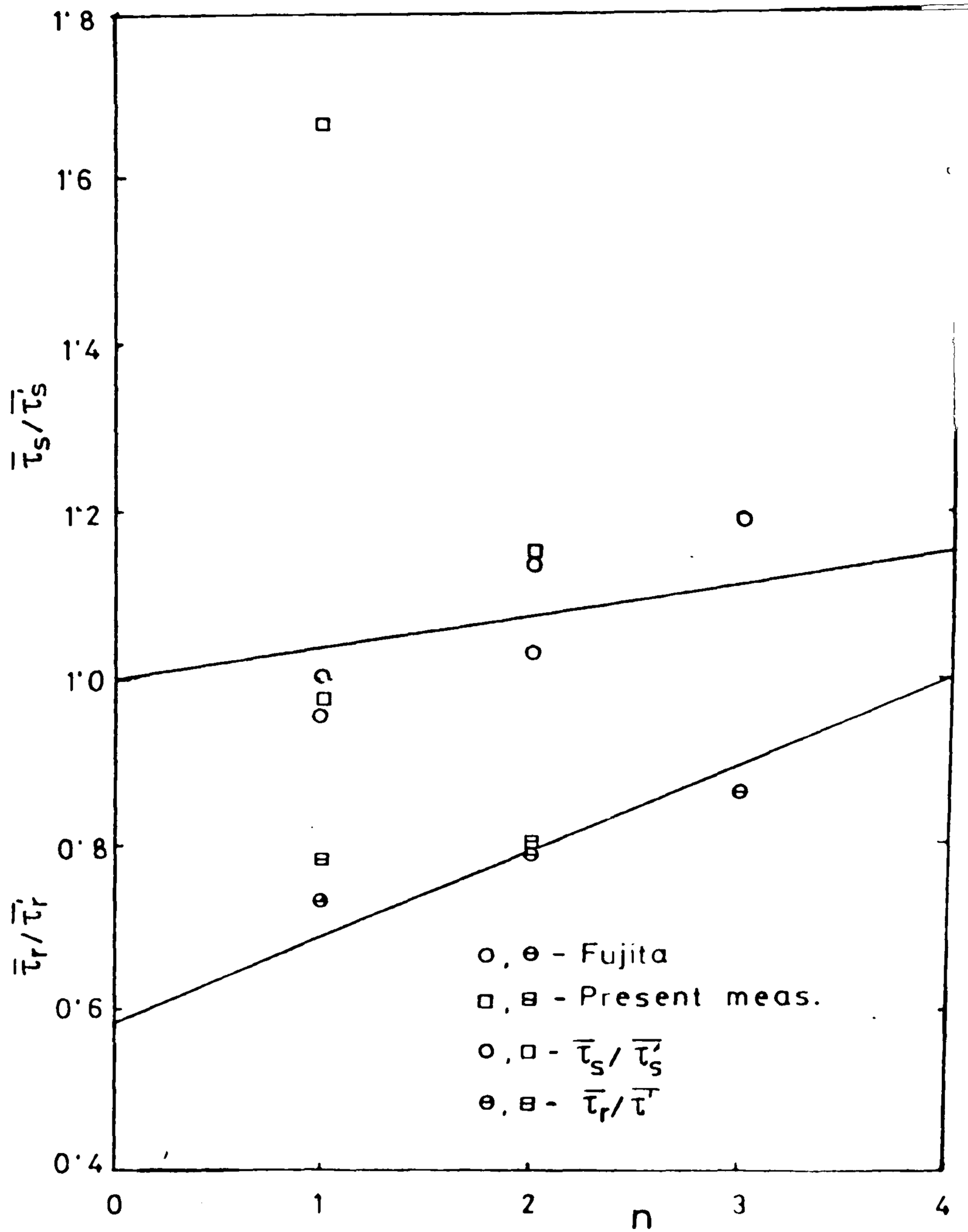

Fig. 5·28 Relation between the ratios of $\bar{\tau}_s/\bar{\tau}_s'$ and $\bar{\tau}_r/\bar{\tau}_r'$ and number of rough planes of duct, n.

a

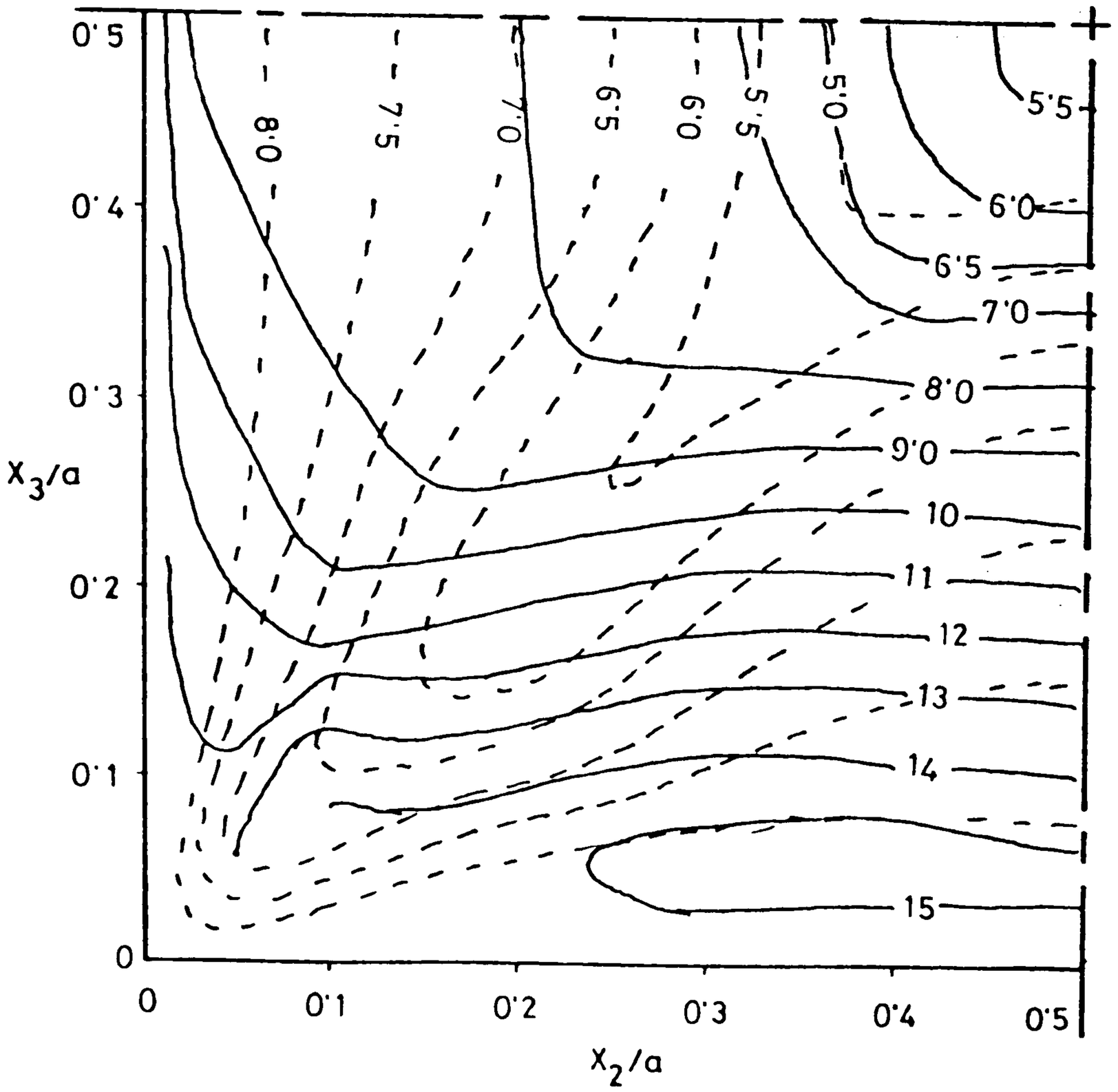

b

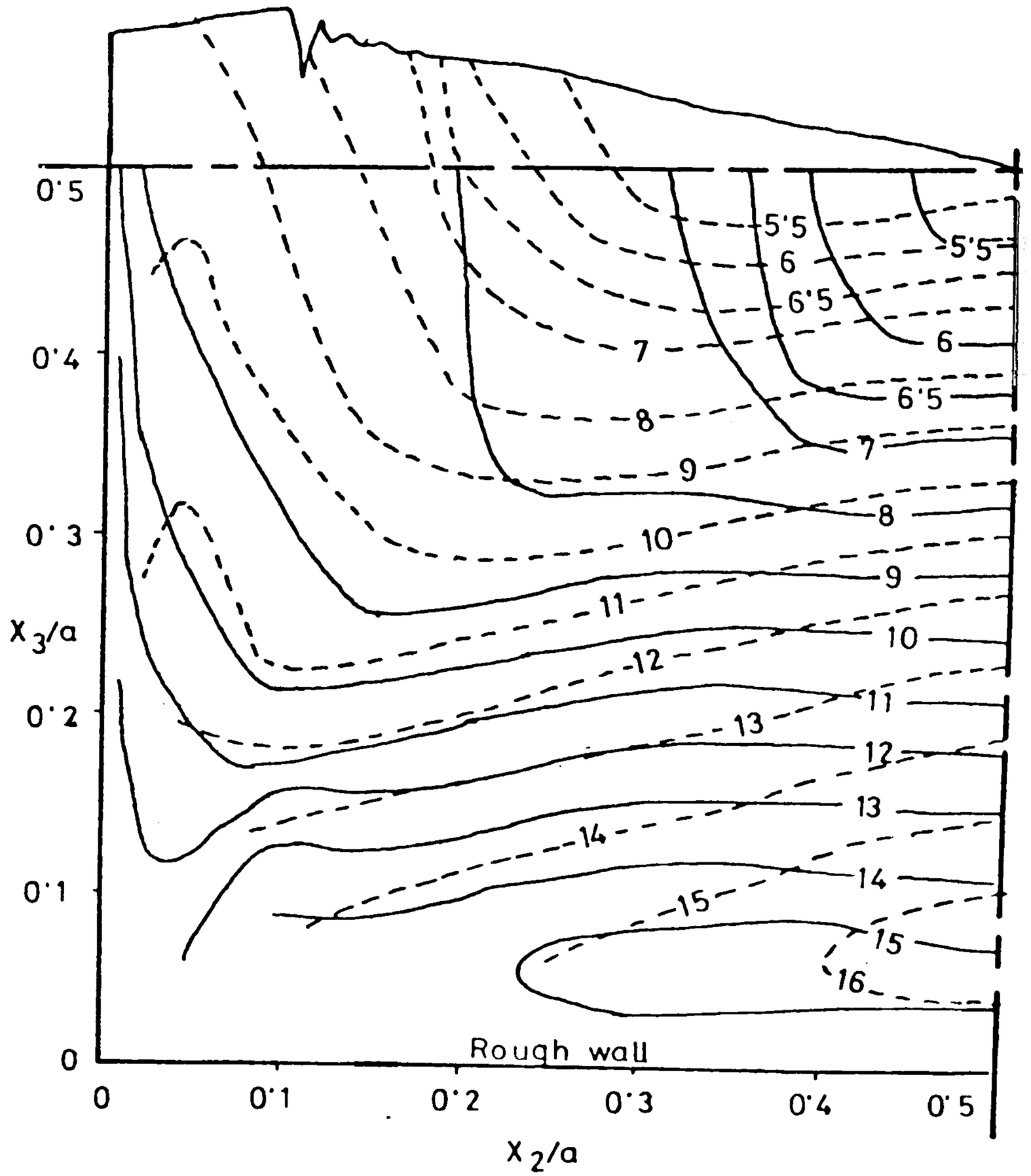

----- Melling ——— Present meas.

----- One rough wall ——— Two rough walls

Fig.5·29 Comparison of $\tilde{u}_1 / U_c \times 10^2$ contours.

---- One rough wall

——— Two rough walls.

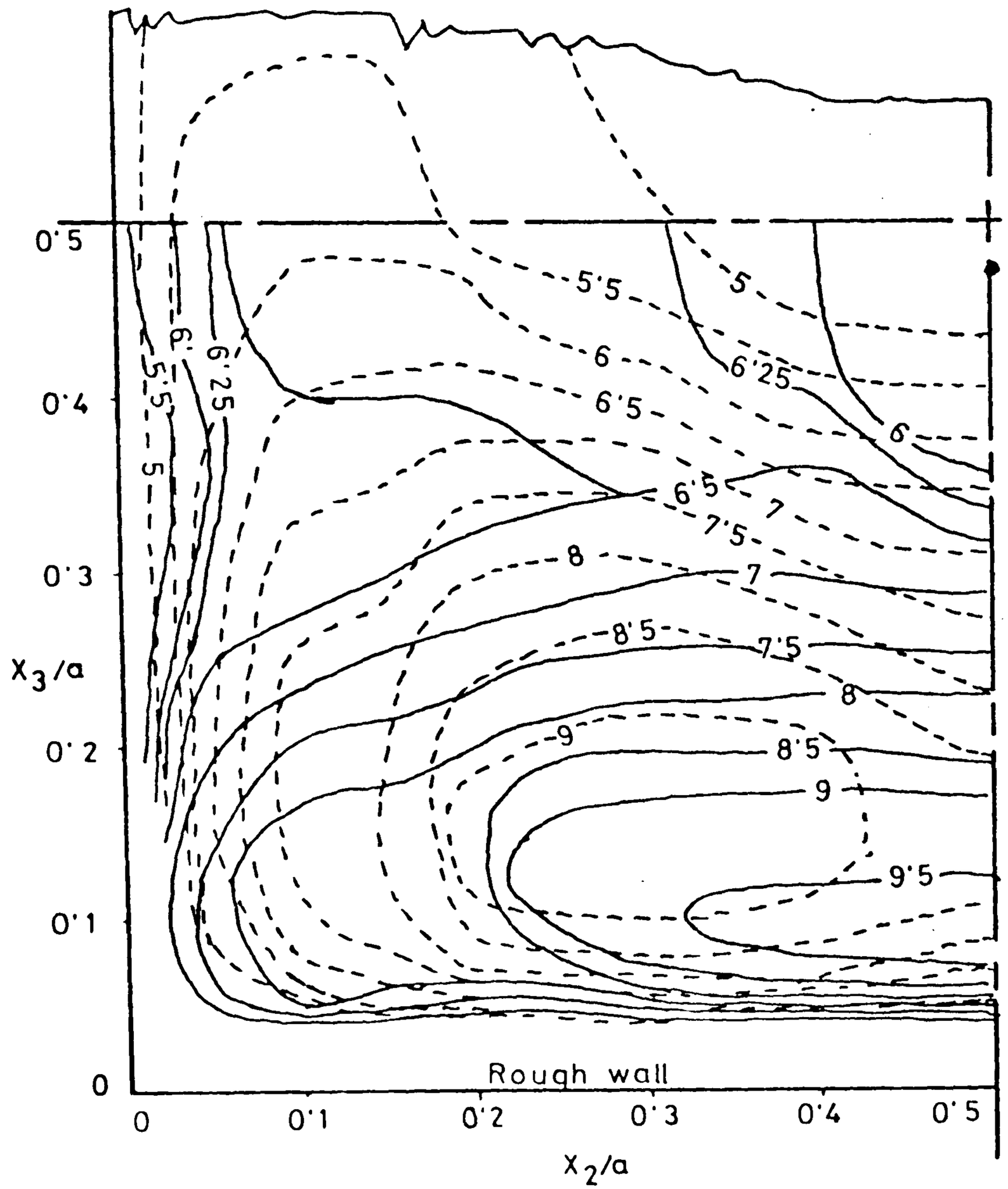

Fig. 5·30 Comparison of $\bar{u}_2/U_c \times 10^2$ contours.

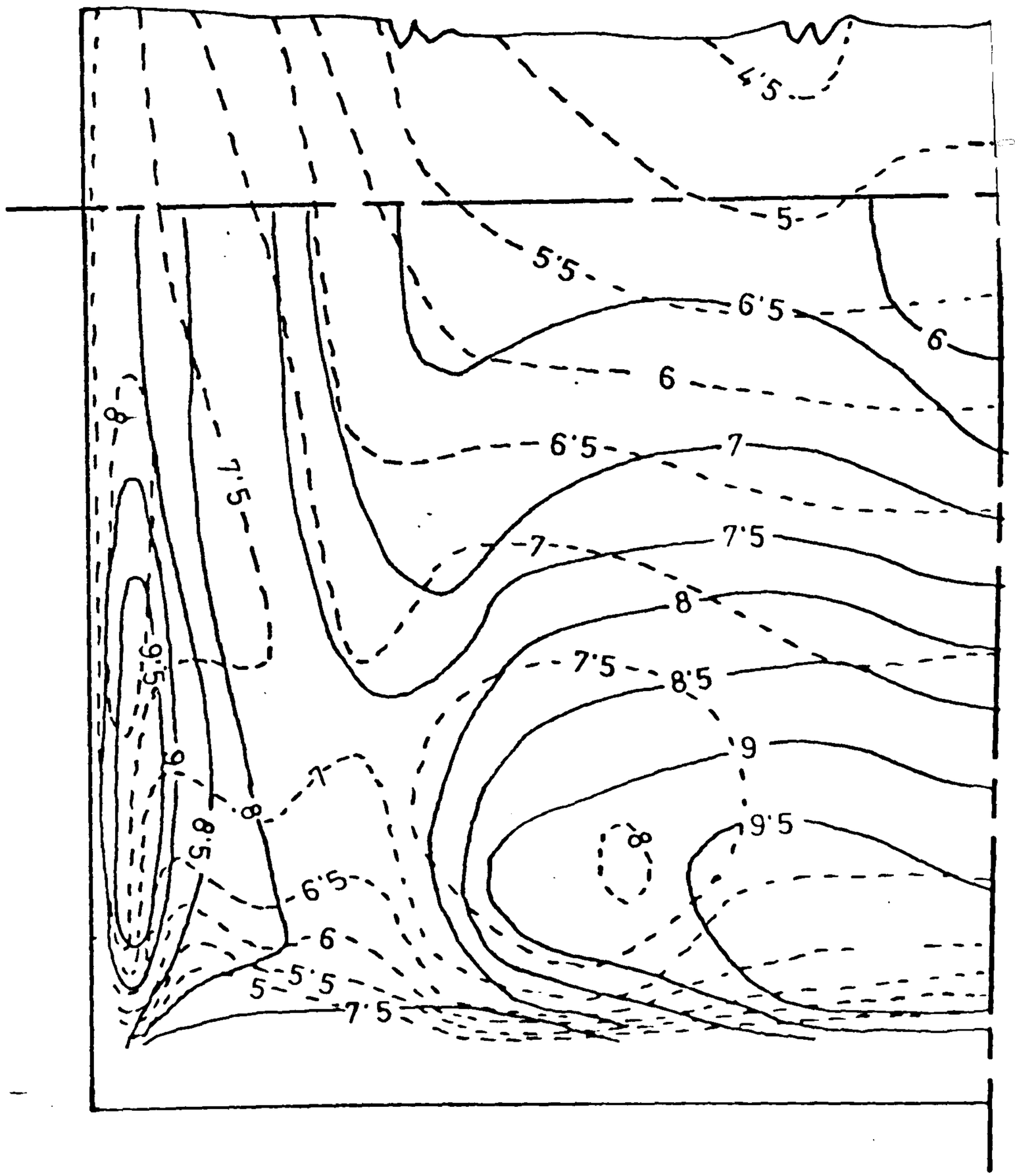

Fig. 5·31 Comparison of $\bar{u}_3/U_c \times 10^2$ contou

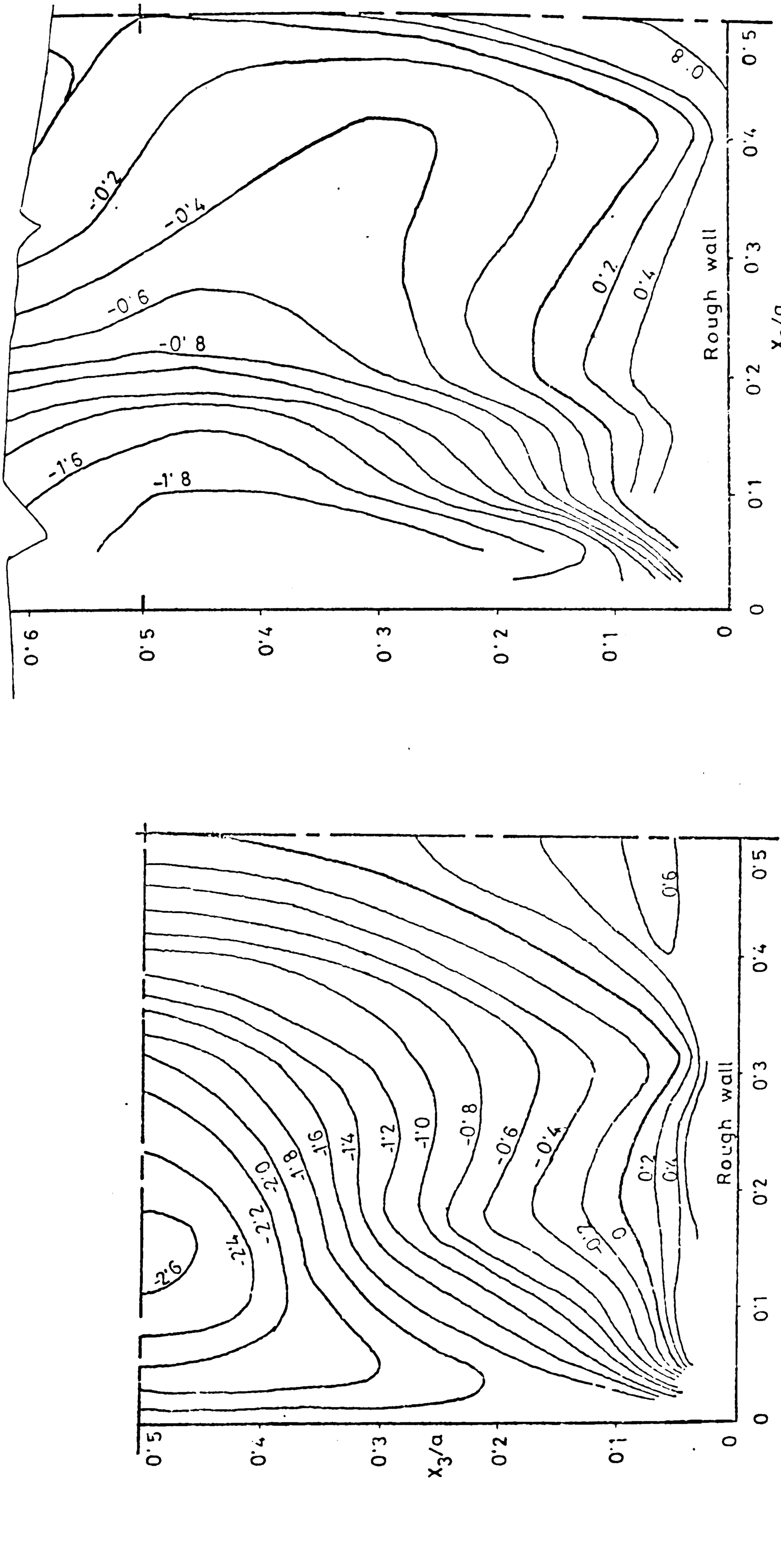

Fig. 5·32 Comparison of $\overline{u_1u_2}/U_c^2 \times 10^3$ contours.

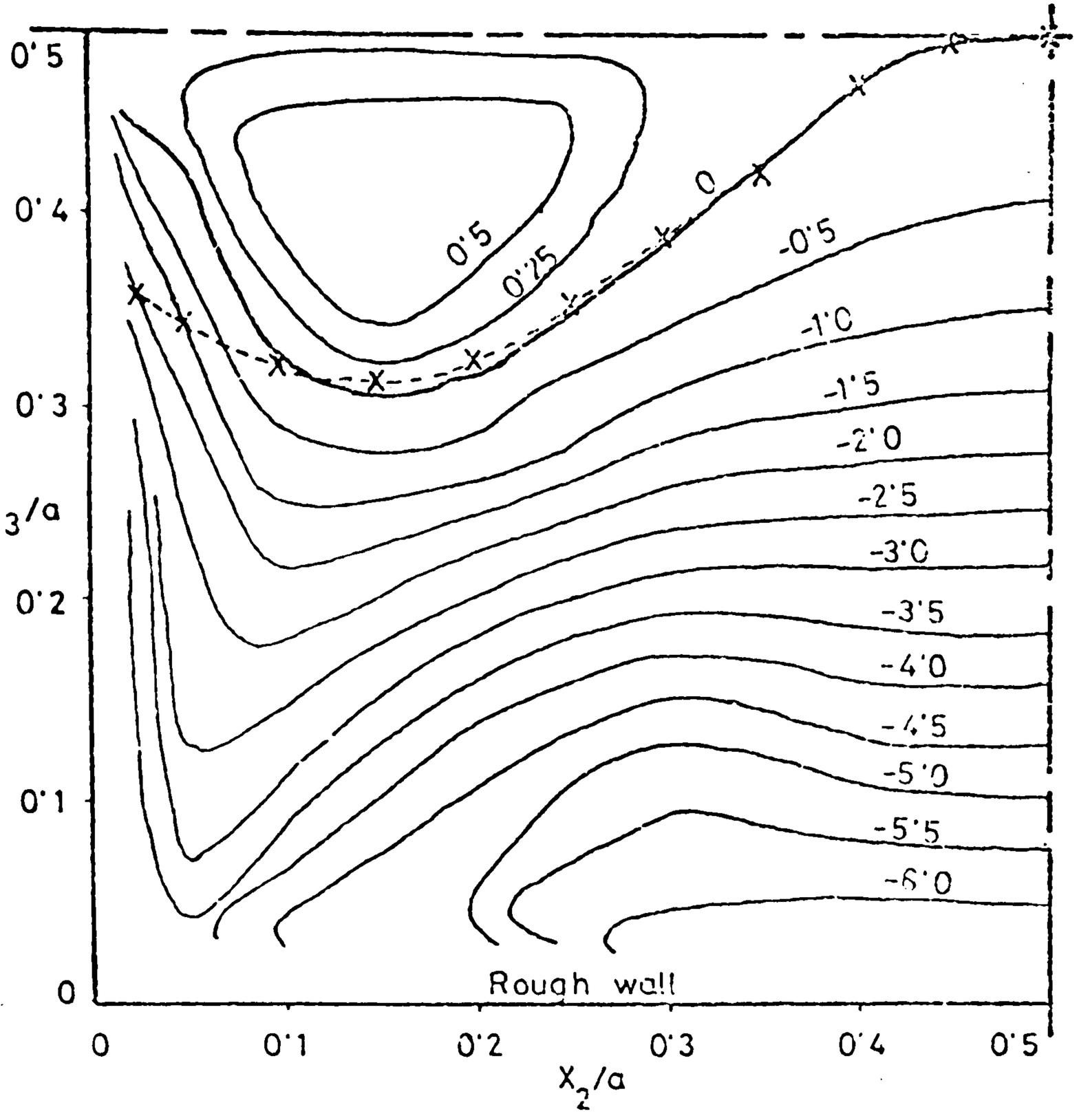

Two rough walls

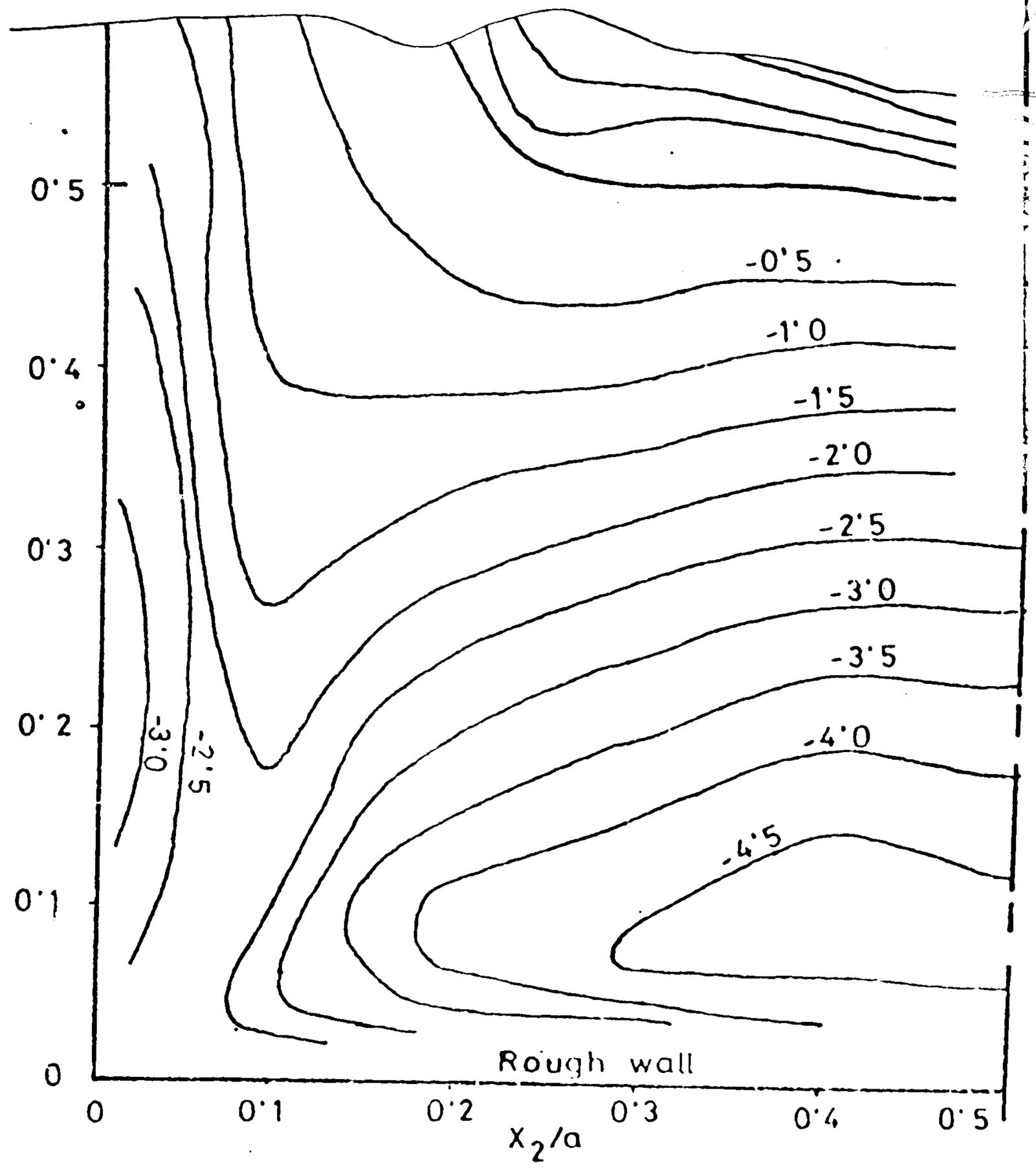

One rough wall

Fig. 5·33 Comparison of $\overline{u_1 u_3}/U_c^2 \times 10^3$ contours

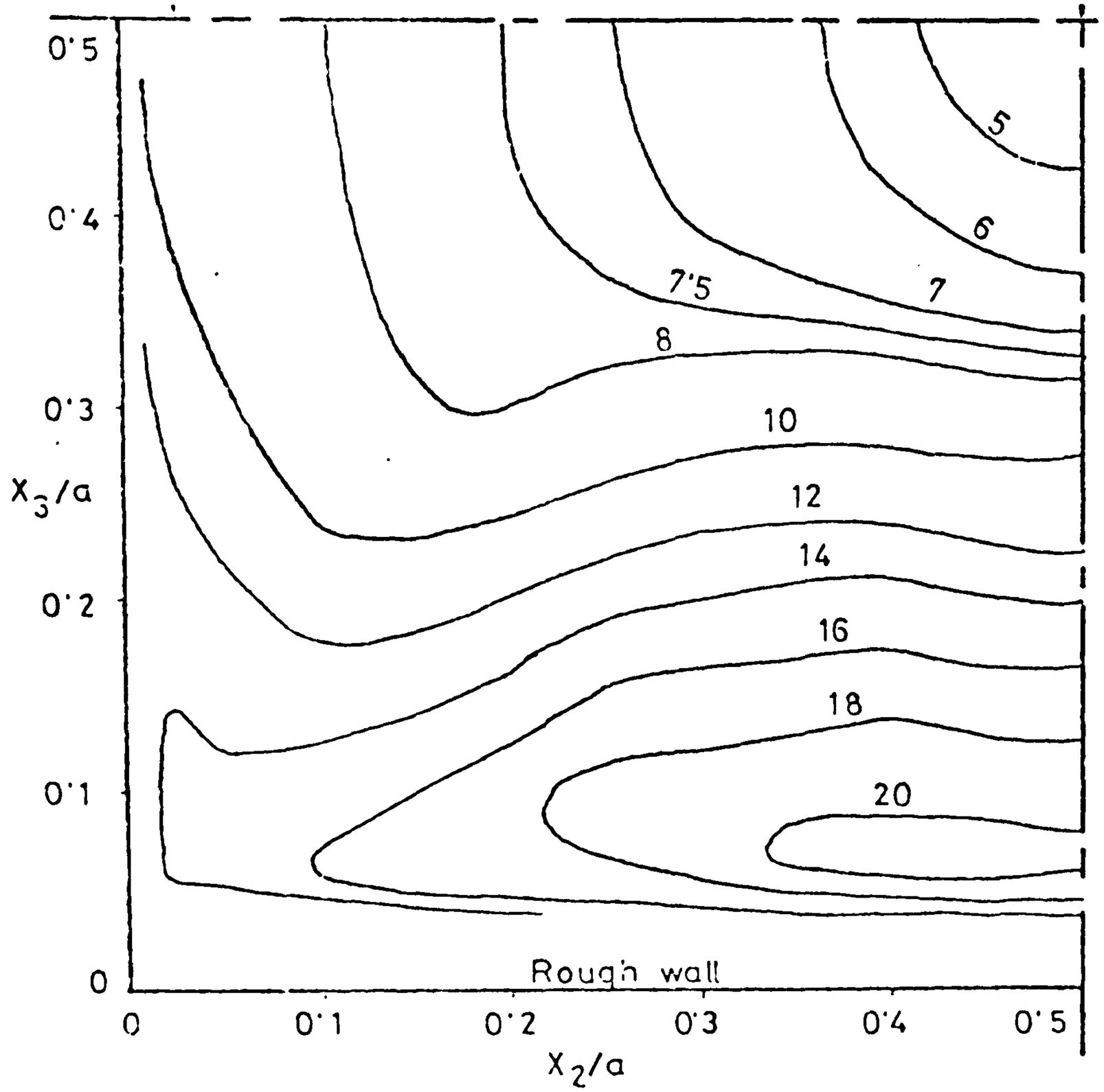

Two rough walls

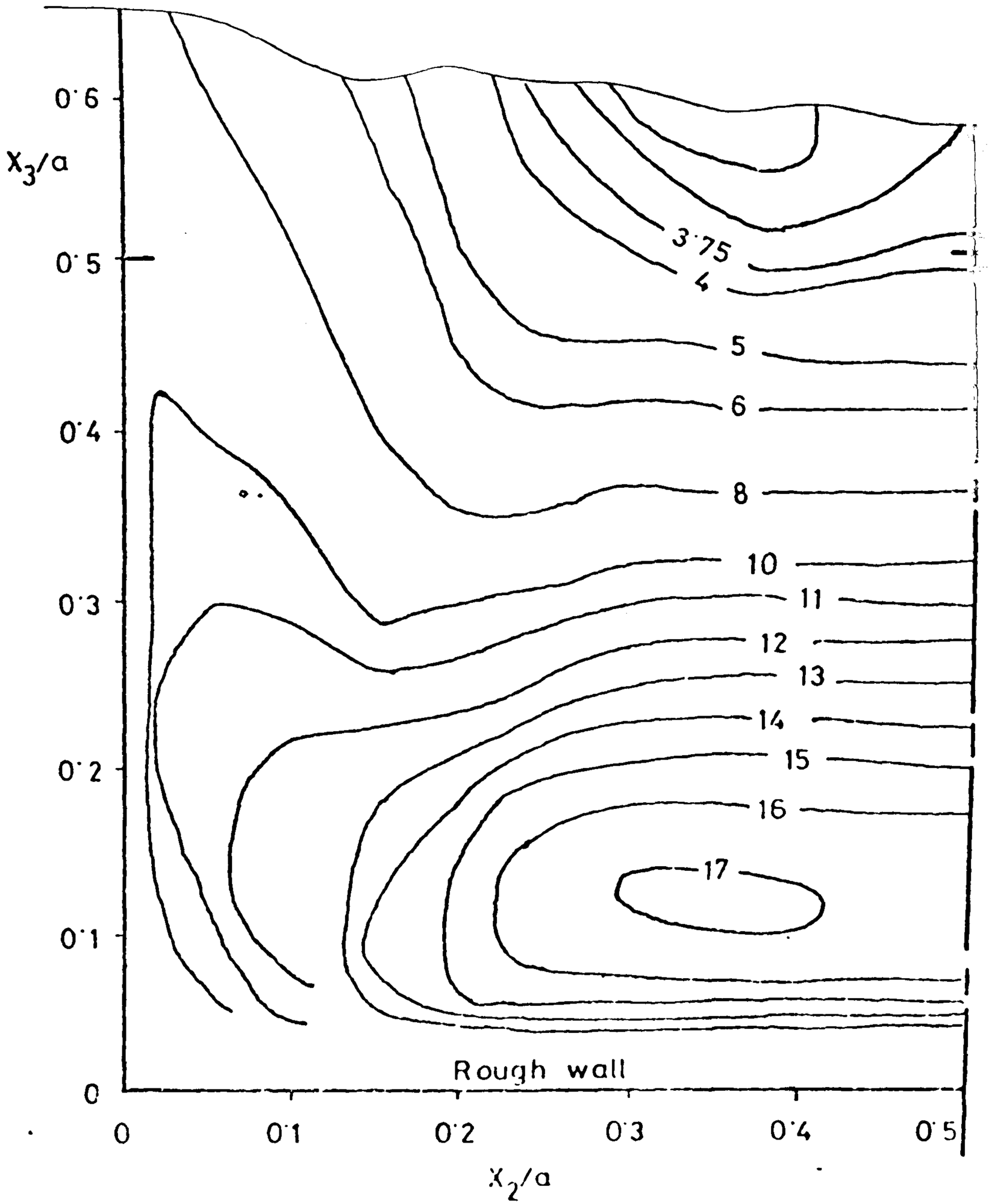

One rough wall

Fig. 5·34 Comparison of $k/U_c^2 \times 10^3$ contours.

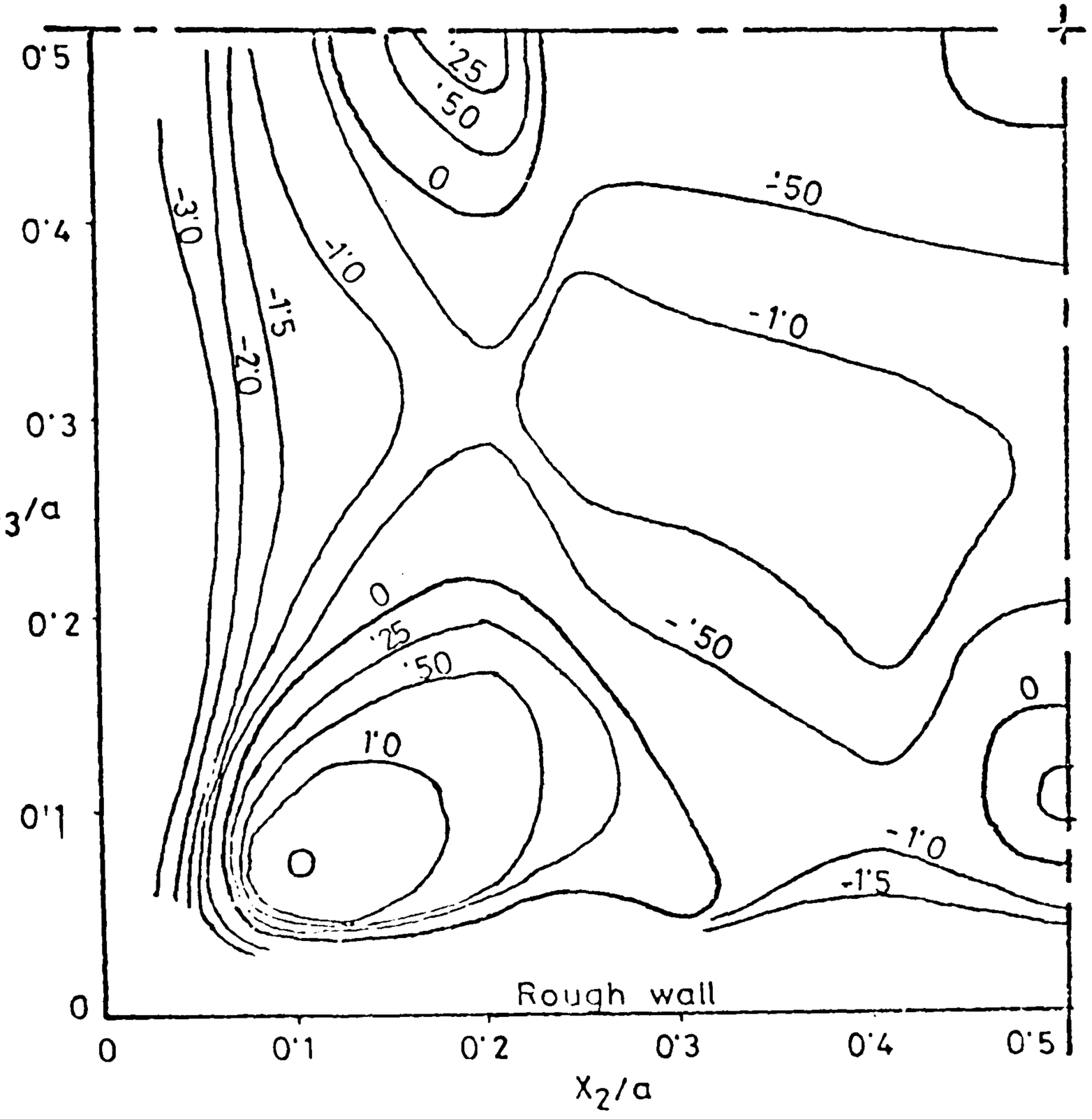

Two rough walls

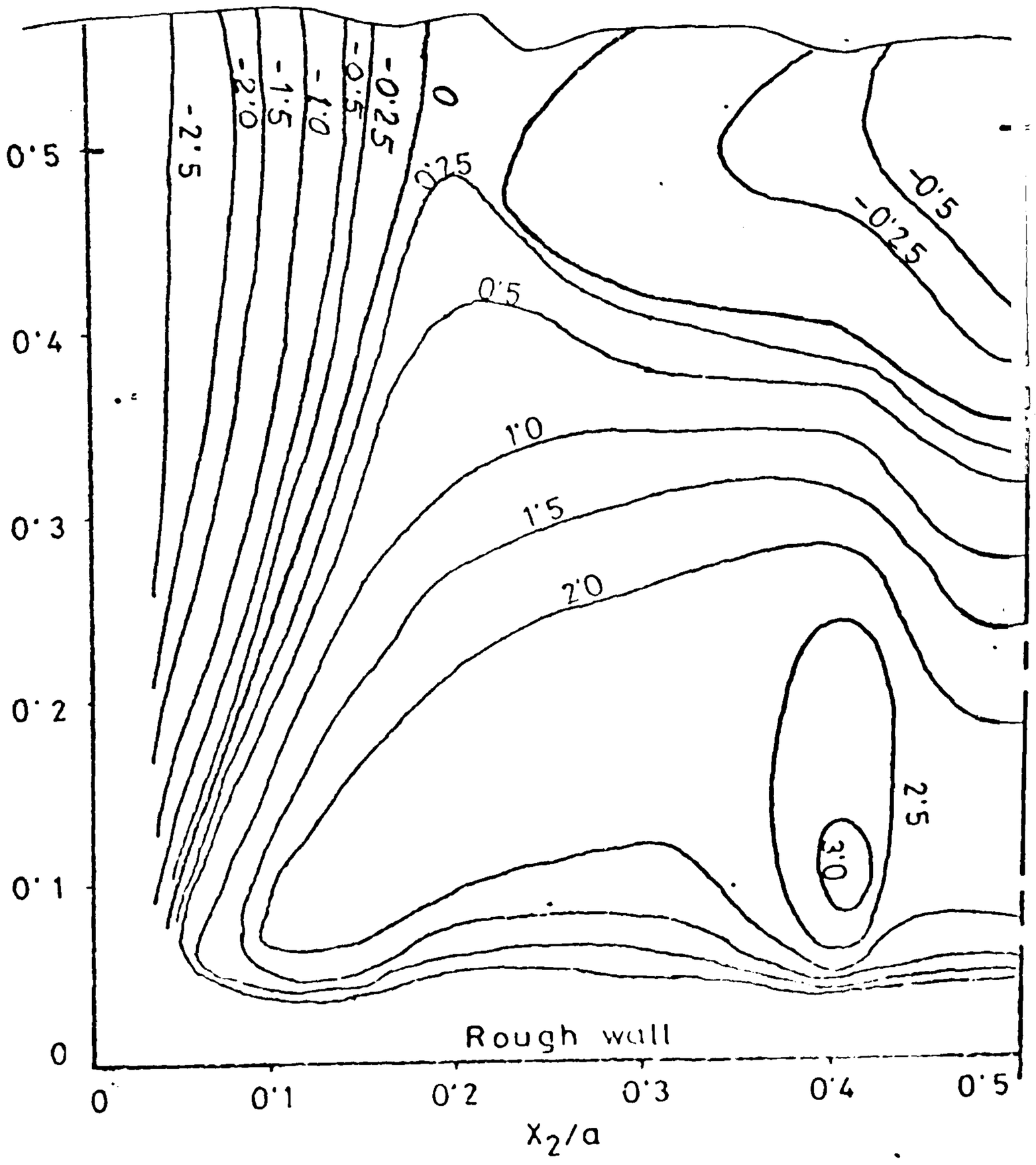

One rough wall

Fig. 5·35 Comparison of $(\overline{u_2^2} - \overline{u_3^2})/U_c^2 \times 10^3$ contours

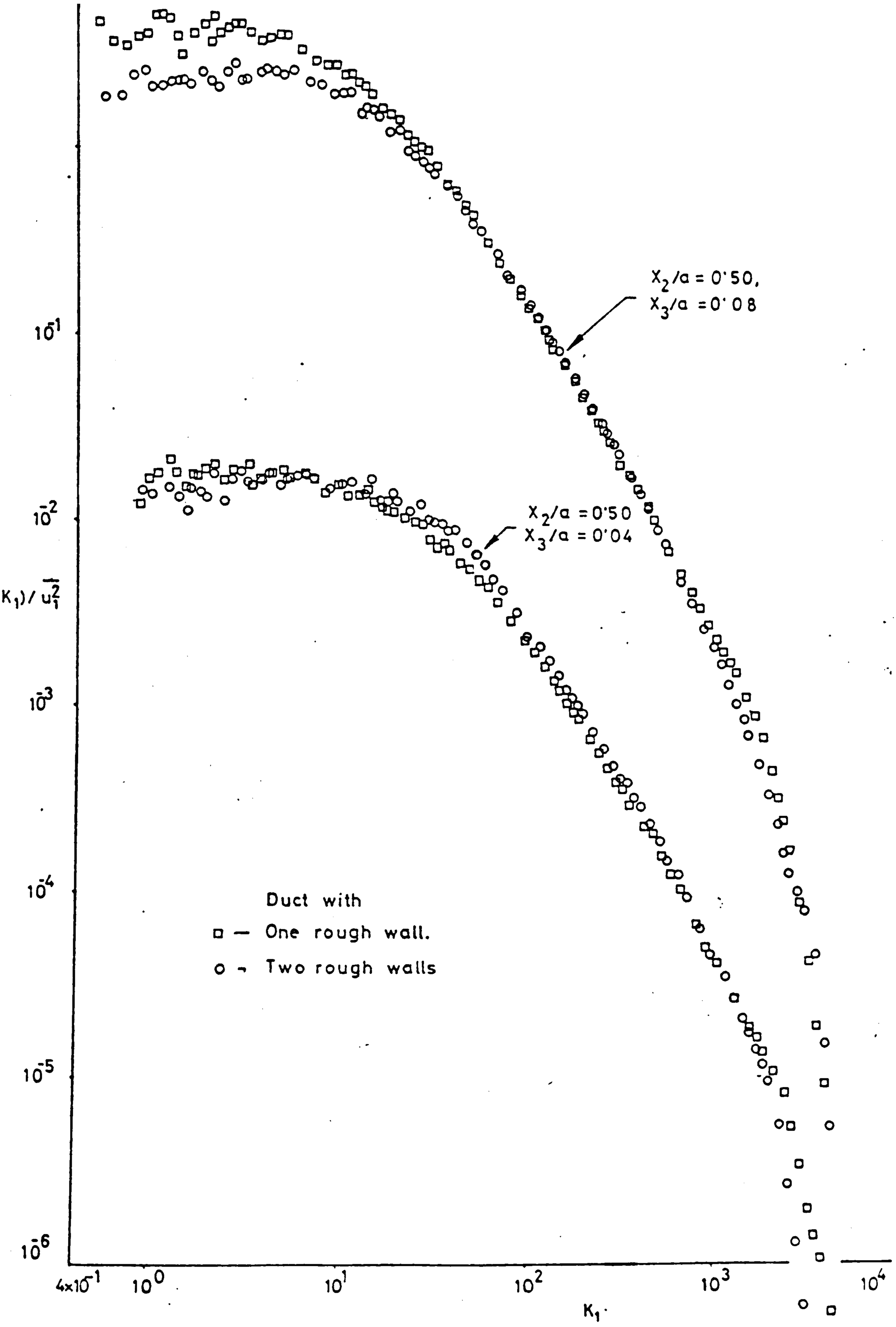

Fig. 5'36 Comparison of $\overline{u_1^2}$ spectra near the rough wall.

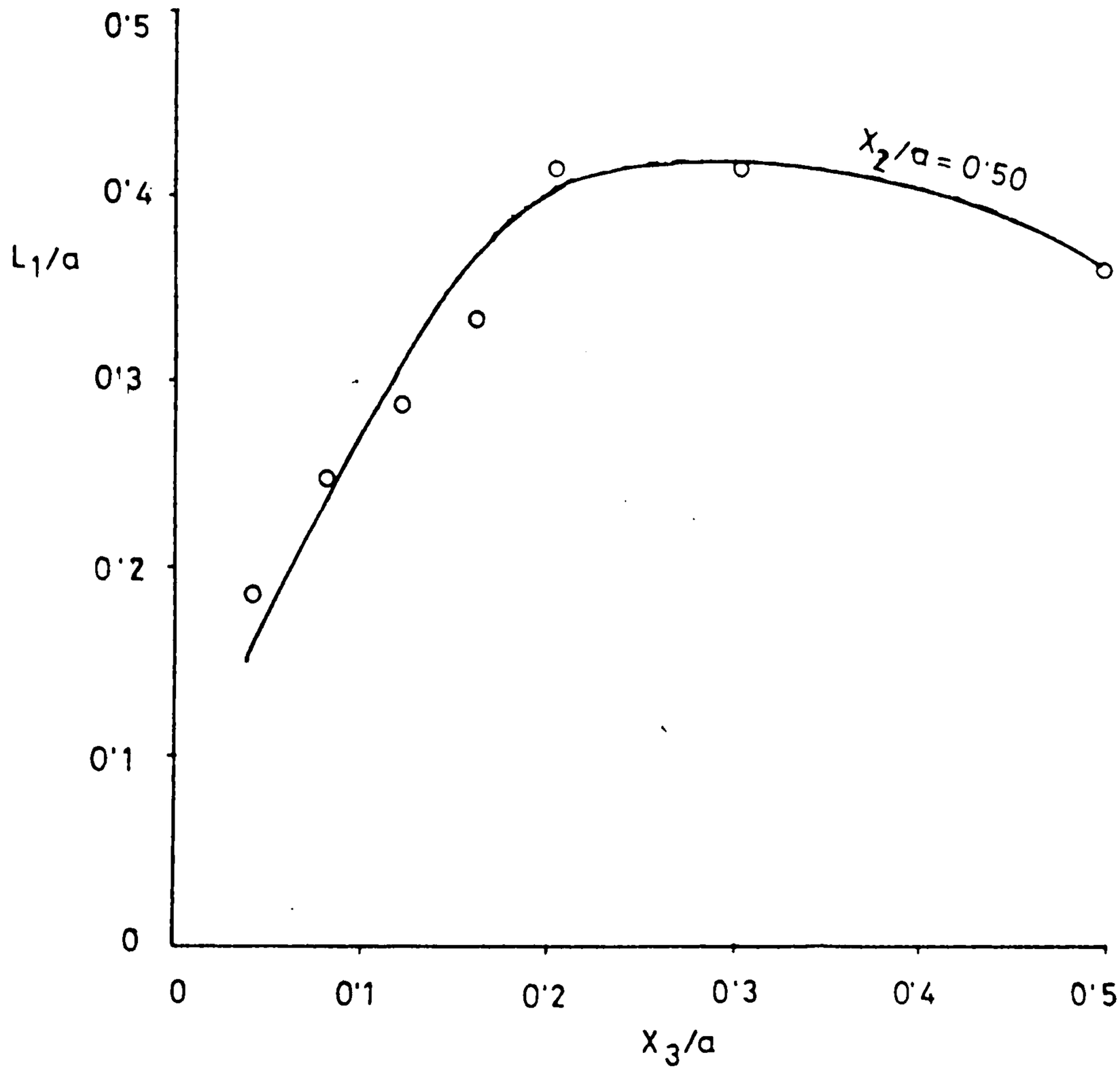

Fig. 5·37 Profile of longitudinal integral scales.

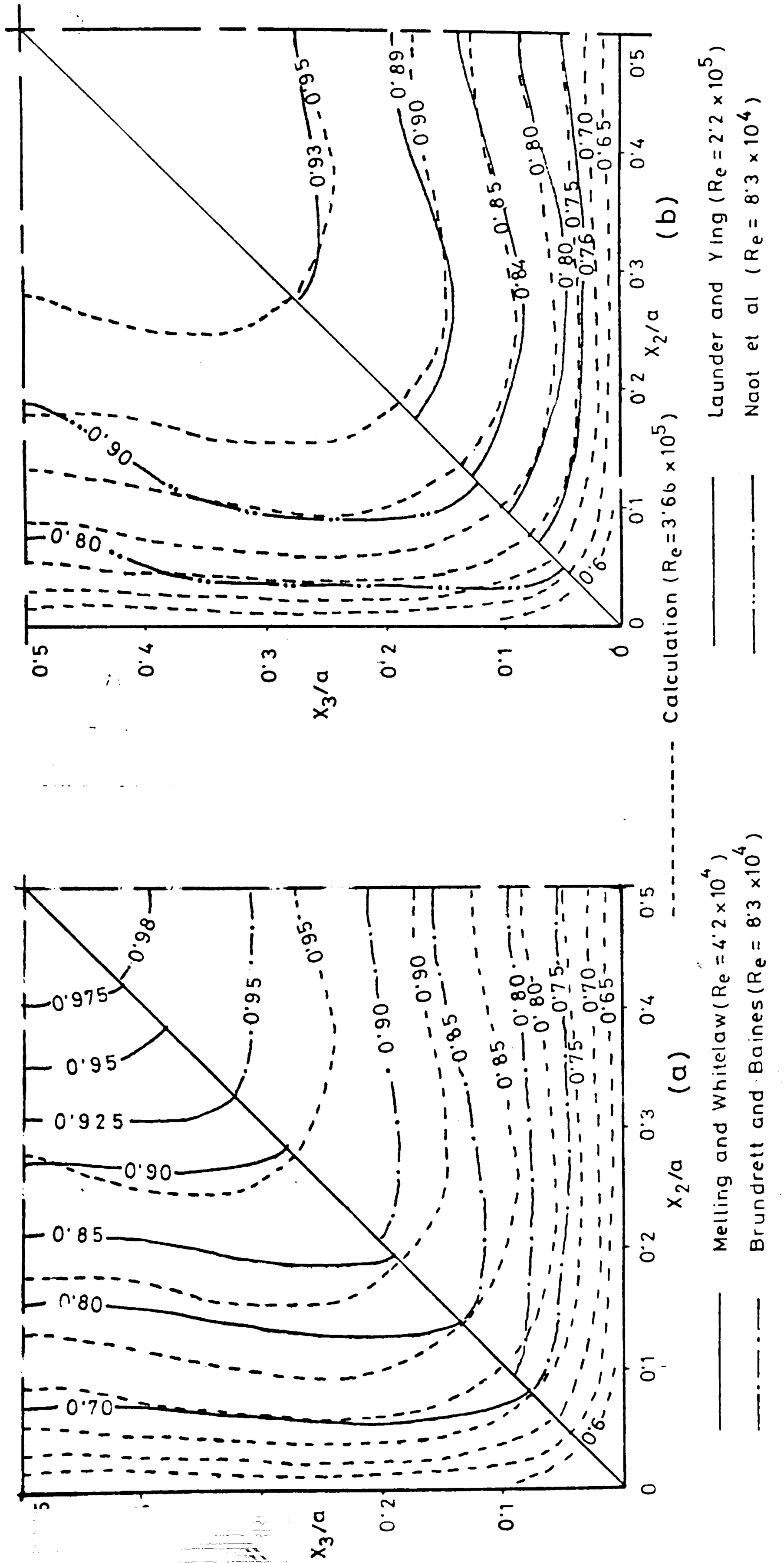

Comparison of U_1 / U_c contours in smooth ducts.

Fig. 6·1

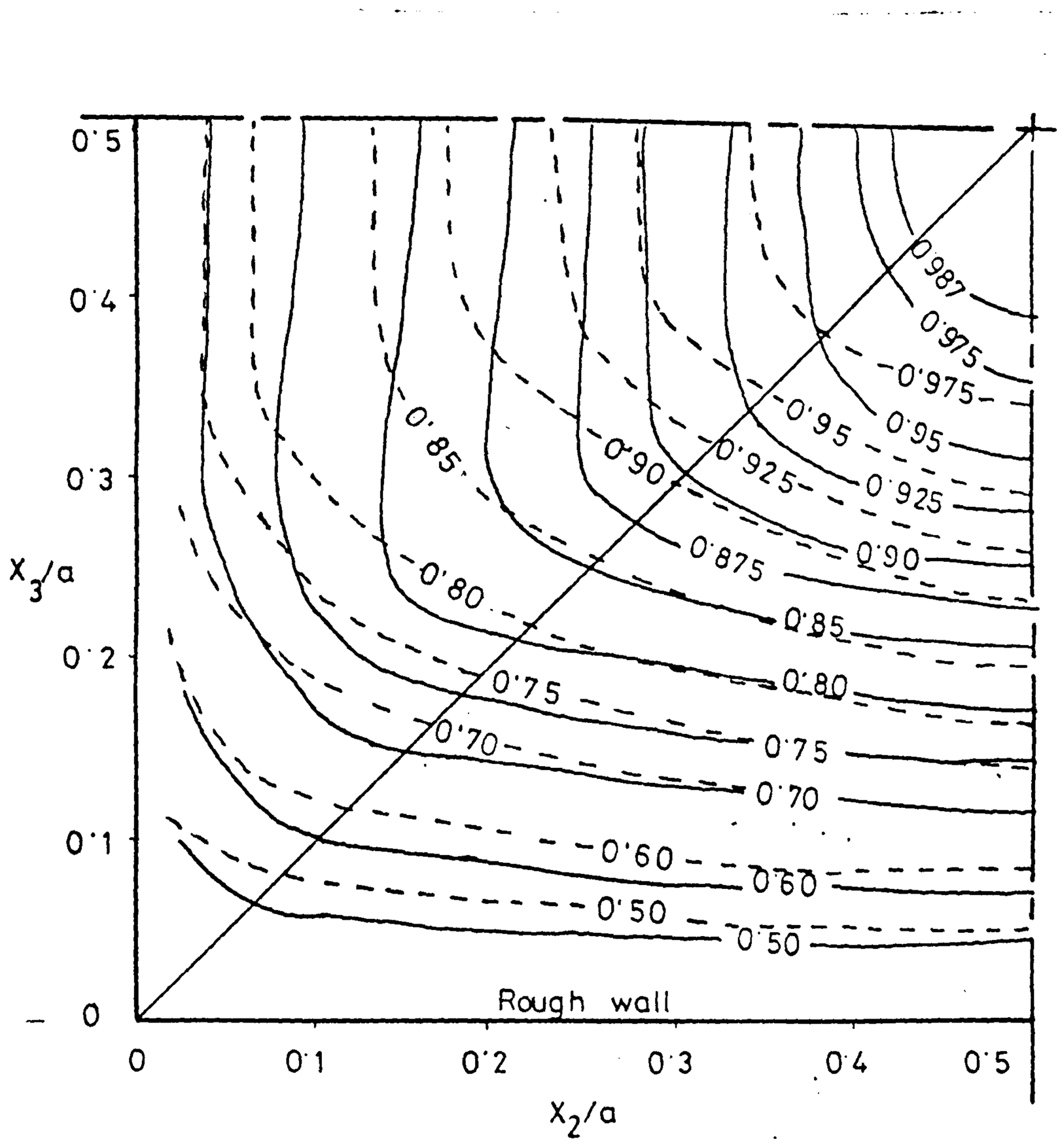

Fig. 6'2 Comparison of U_1/U_c contours in a duct with two rough walls.

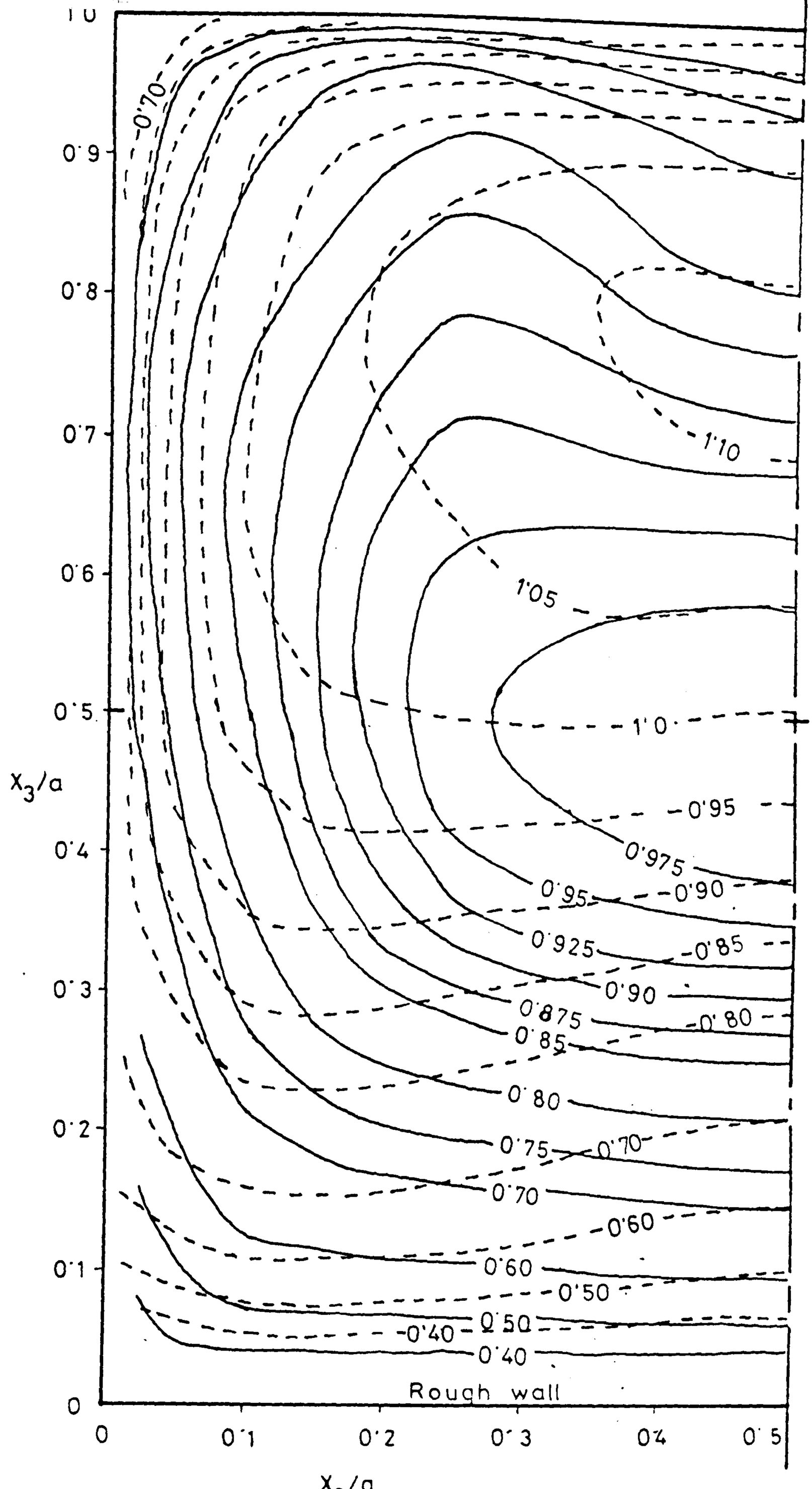

Fig. 6·3 Comparison of U_1/U_c contours in a duct with one rough wall.

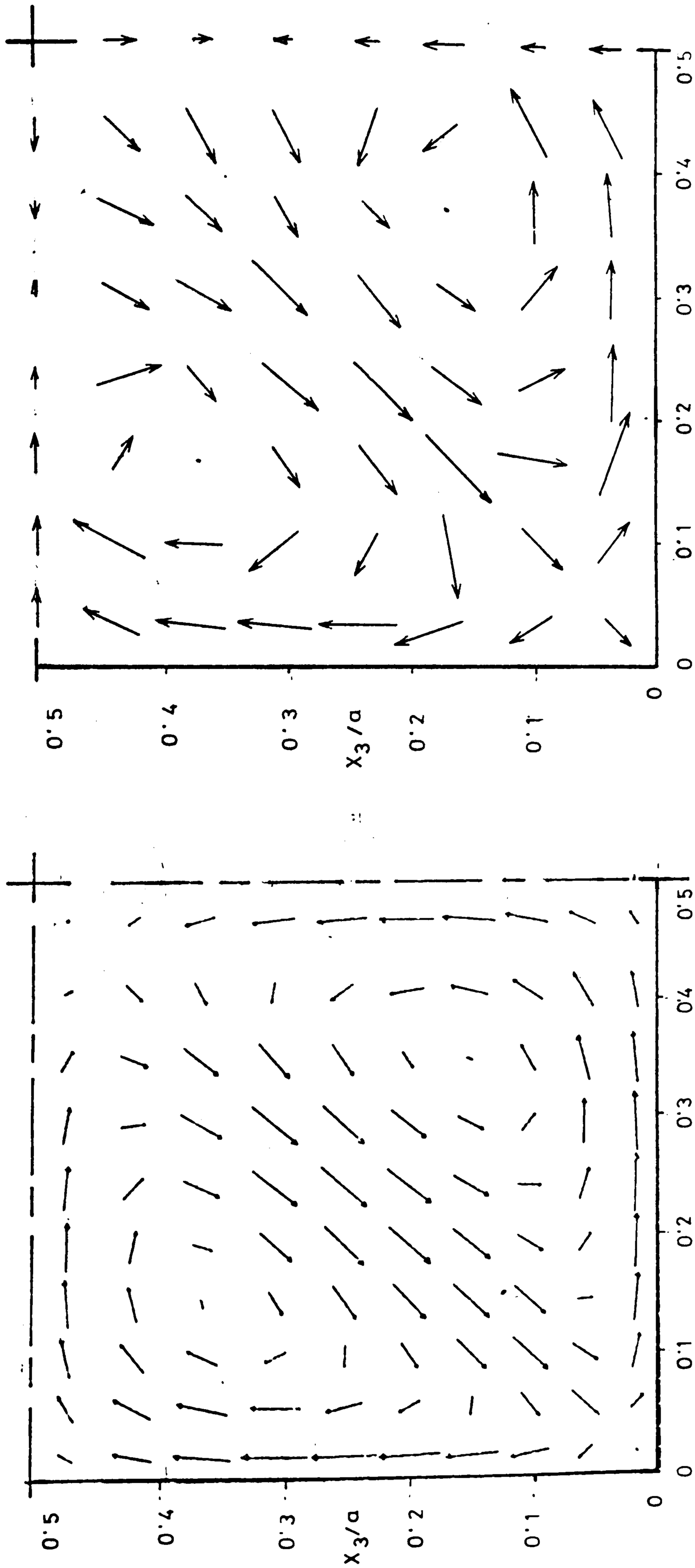

Fig. 6·4 Comparison of secondary velocity vector in a smooth duct.

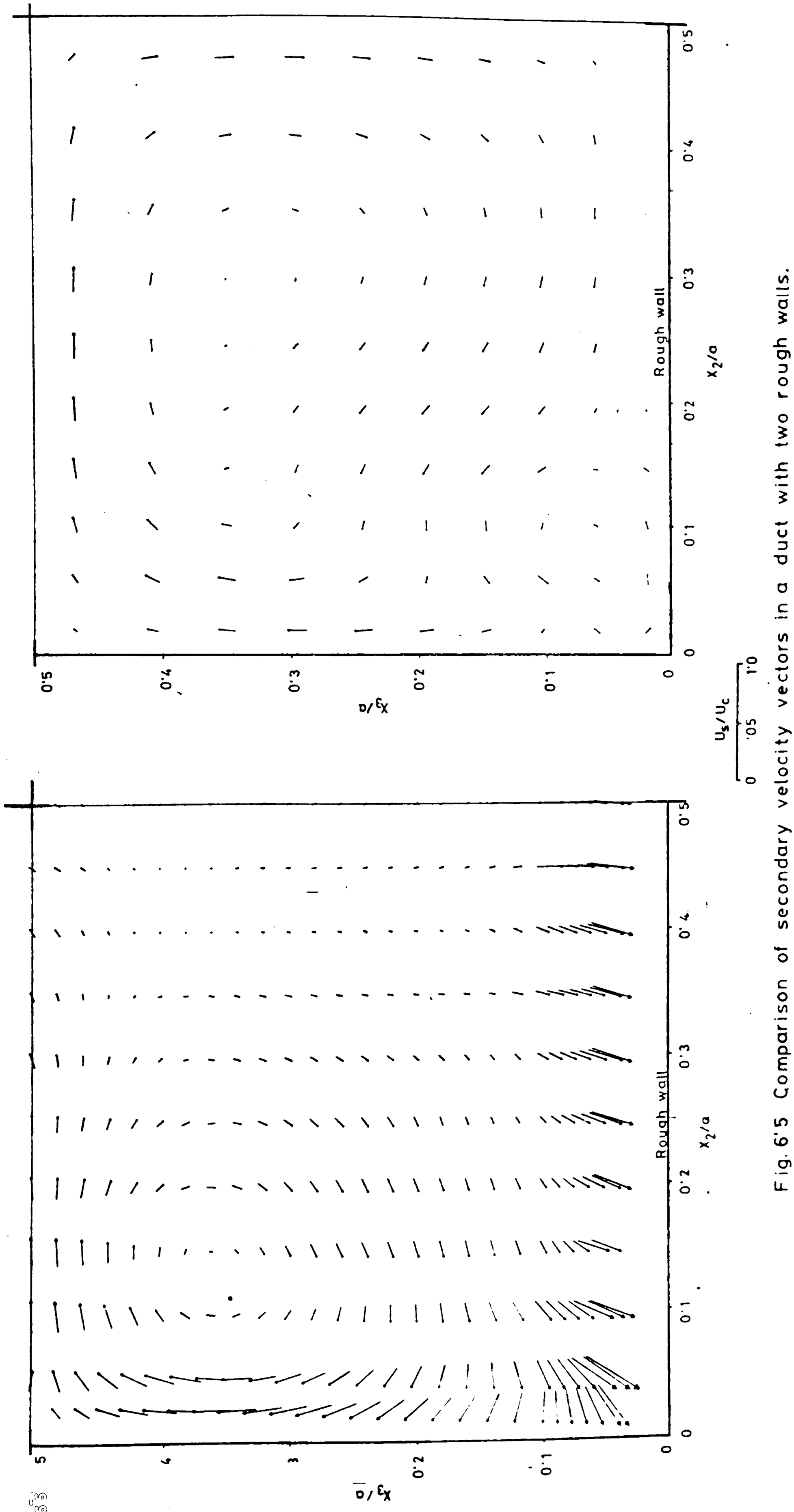

Fig. 6·5 Comparison of secondary velocity vectors in a duct with two rough walls.

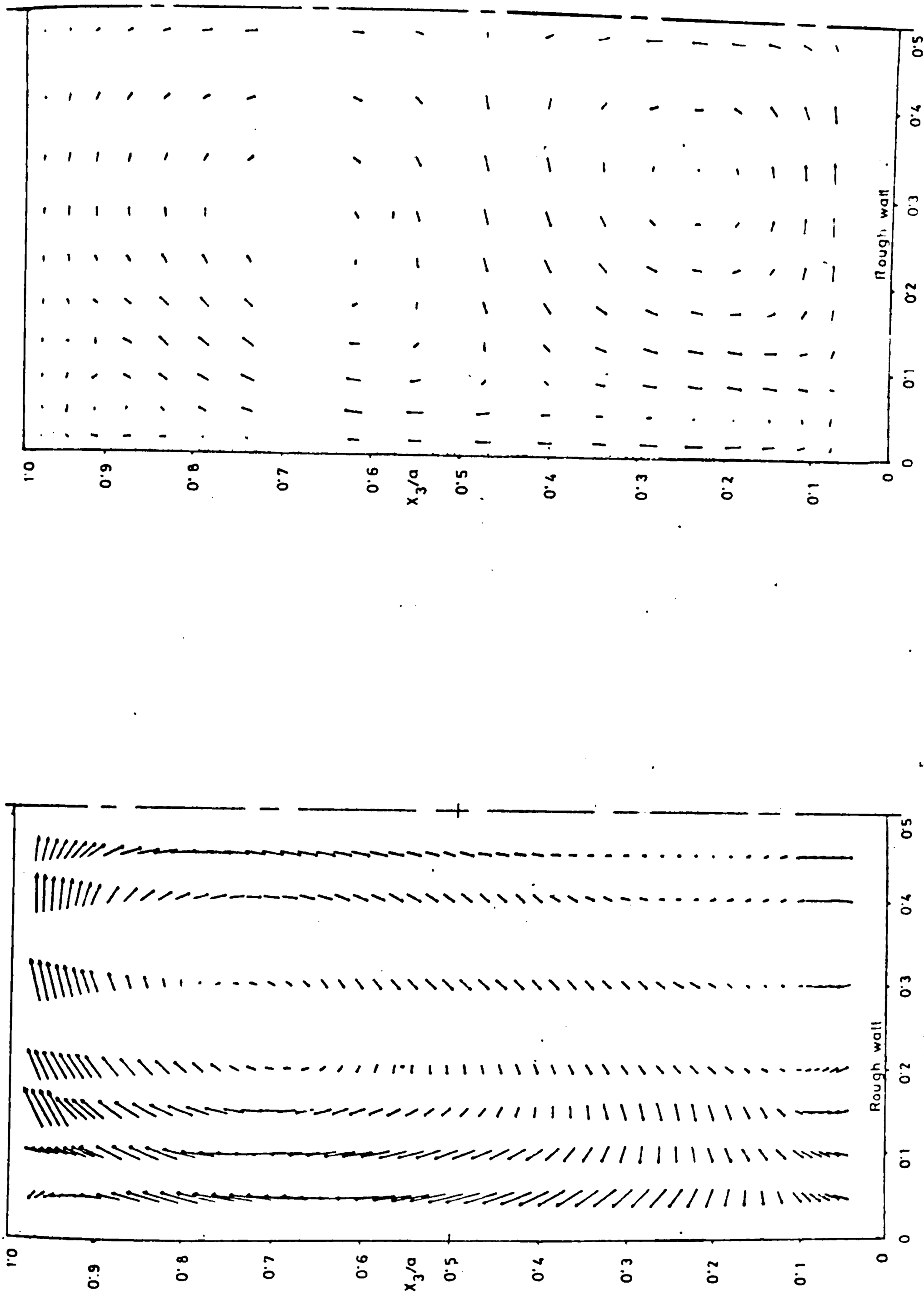

Fig. 6·6 Comparison of secondary velocity vectors in a duct with one rough wall.

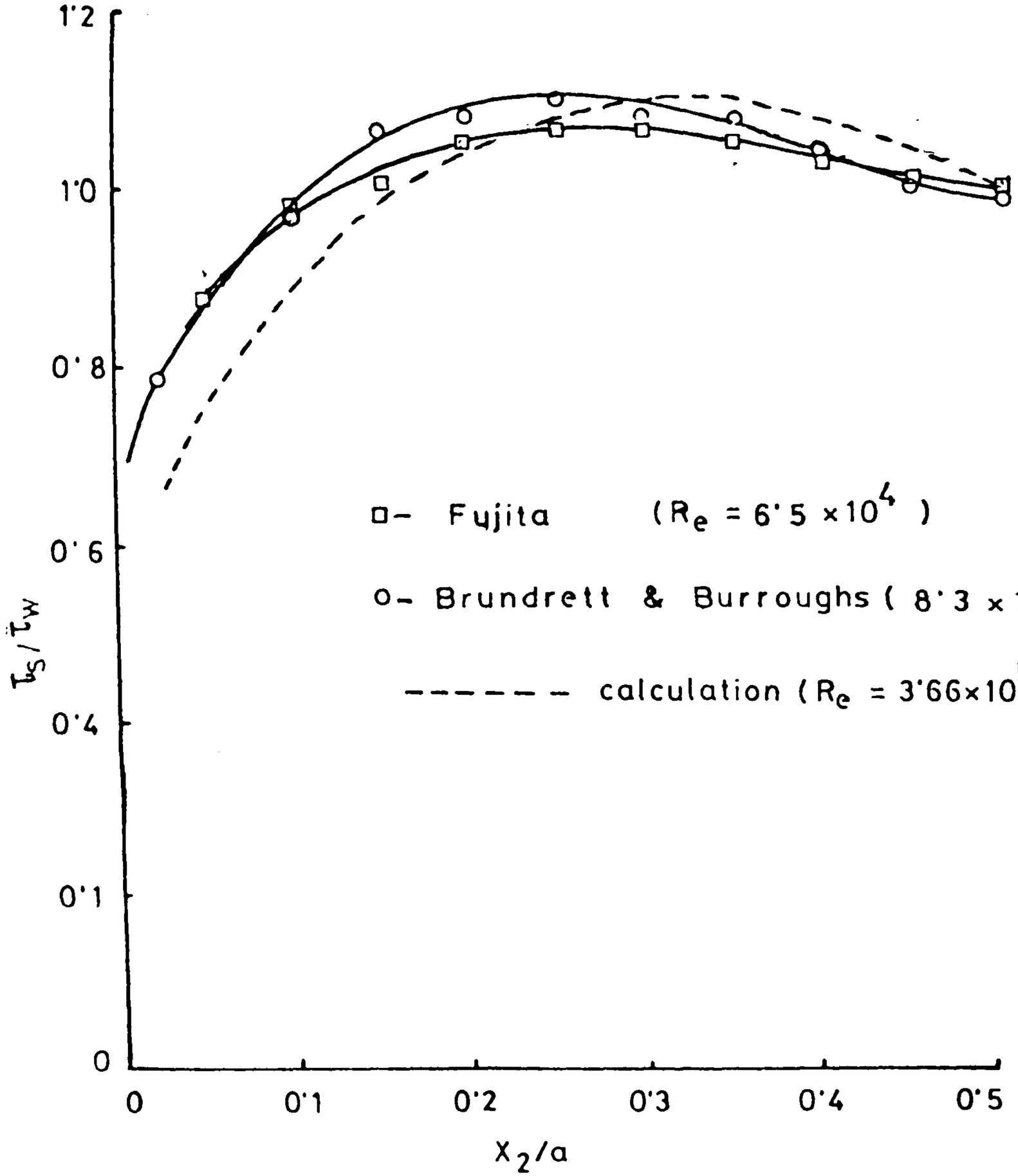

Fig. 6·7 Comparison of wall shear stress distribution of smooth ducts.

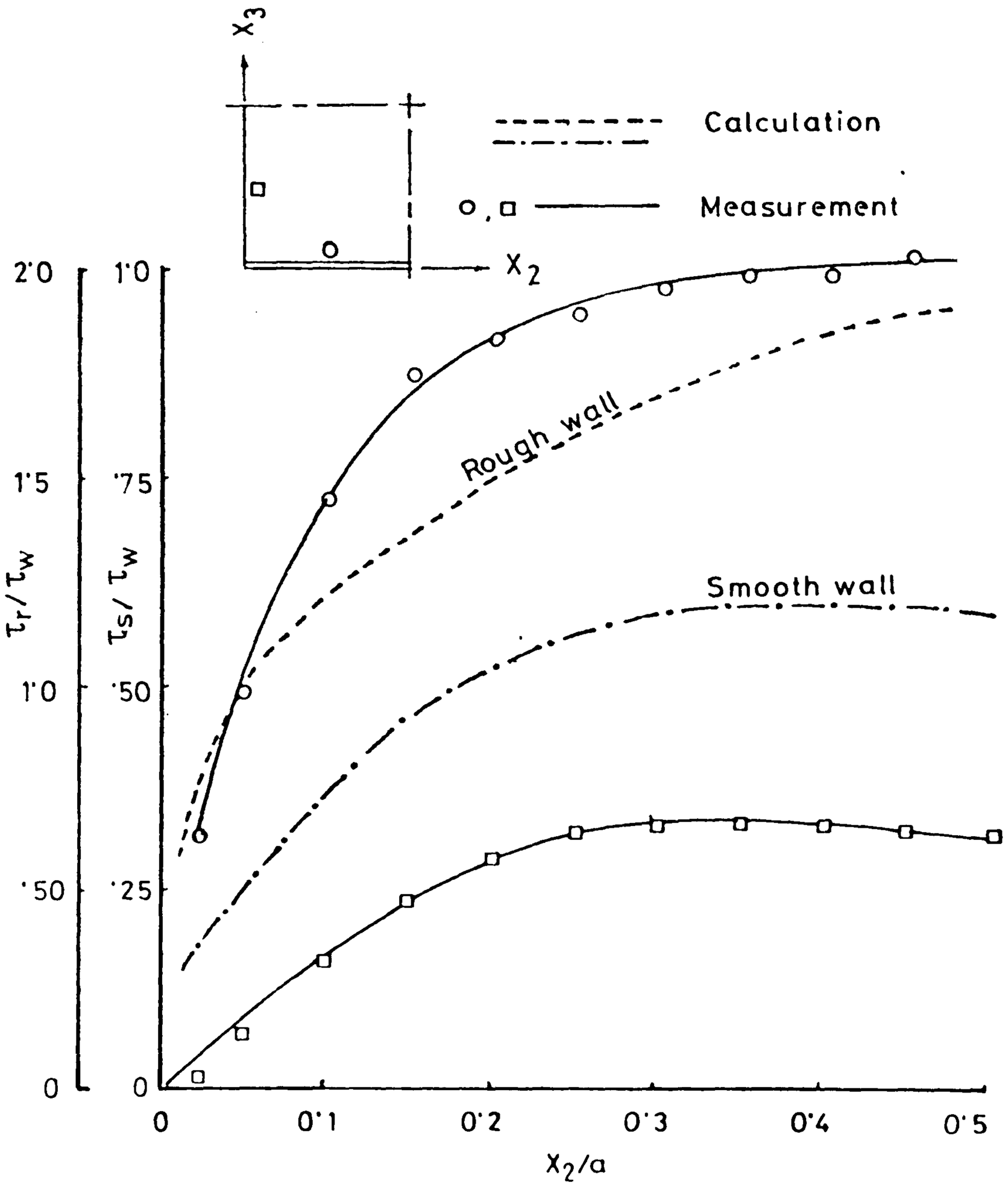

Fig. 6·8 Comparison of wall shear stress distribution of a duct with two rough walls.

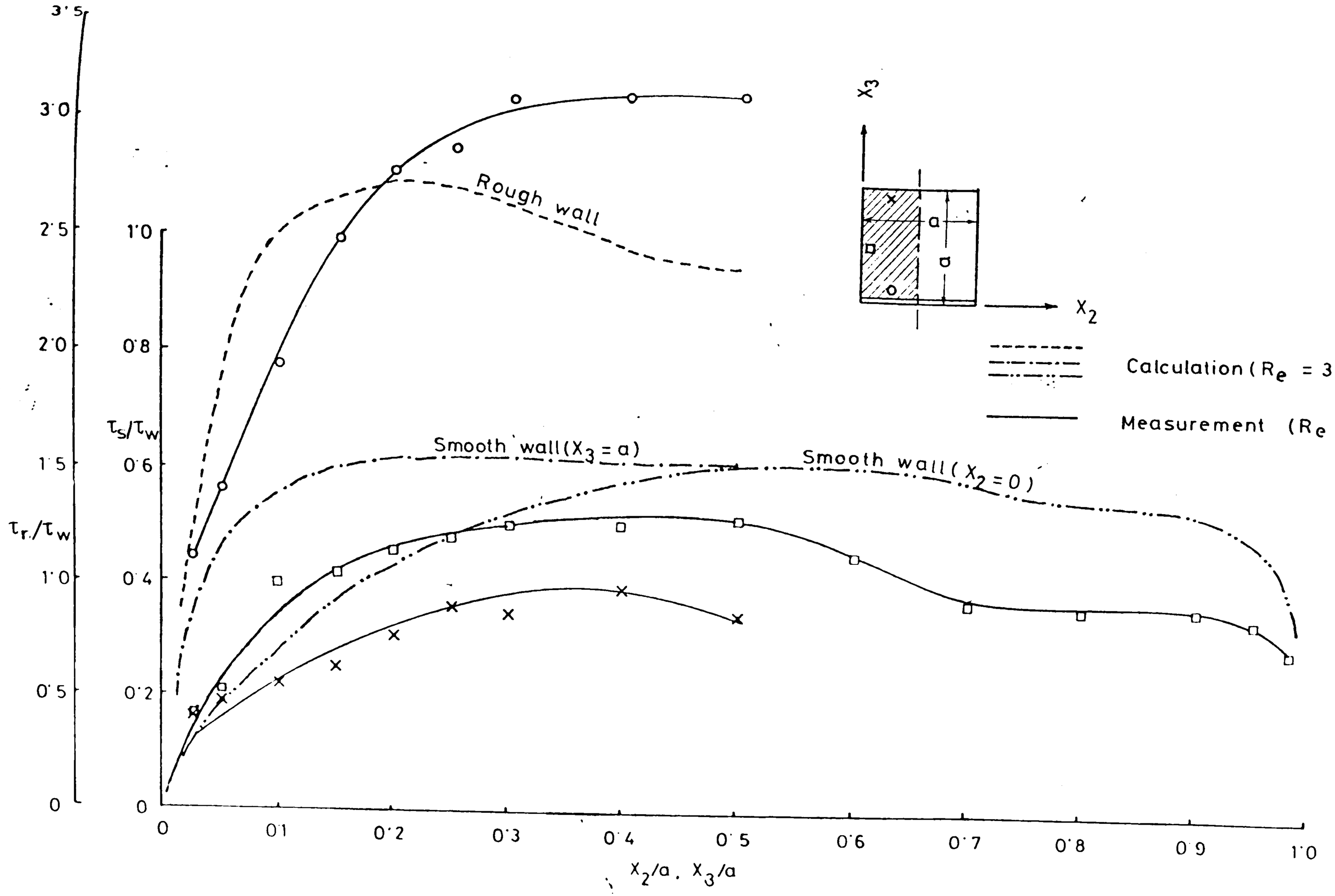

Fig. 6·9 Comparison of wall shear stress distribution of a duct with one rough wall.

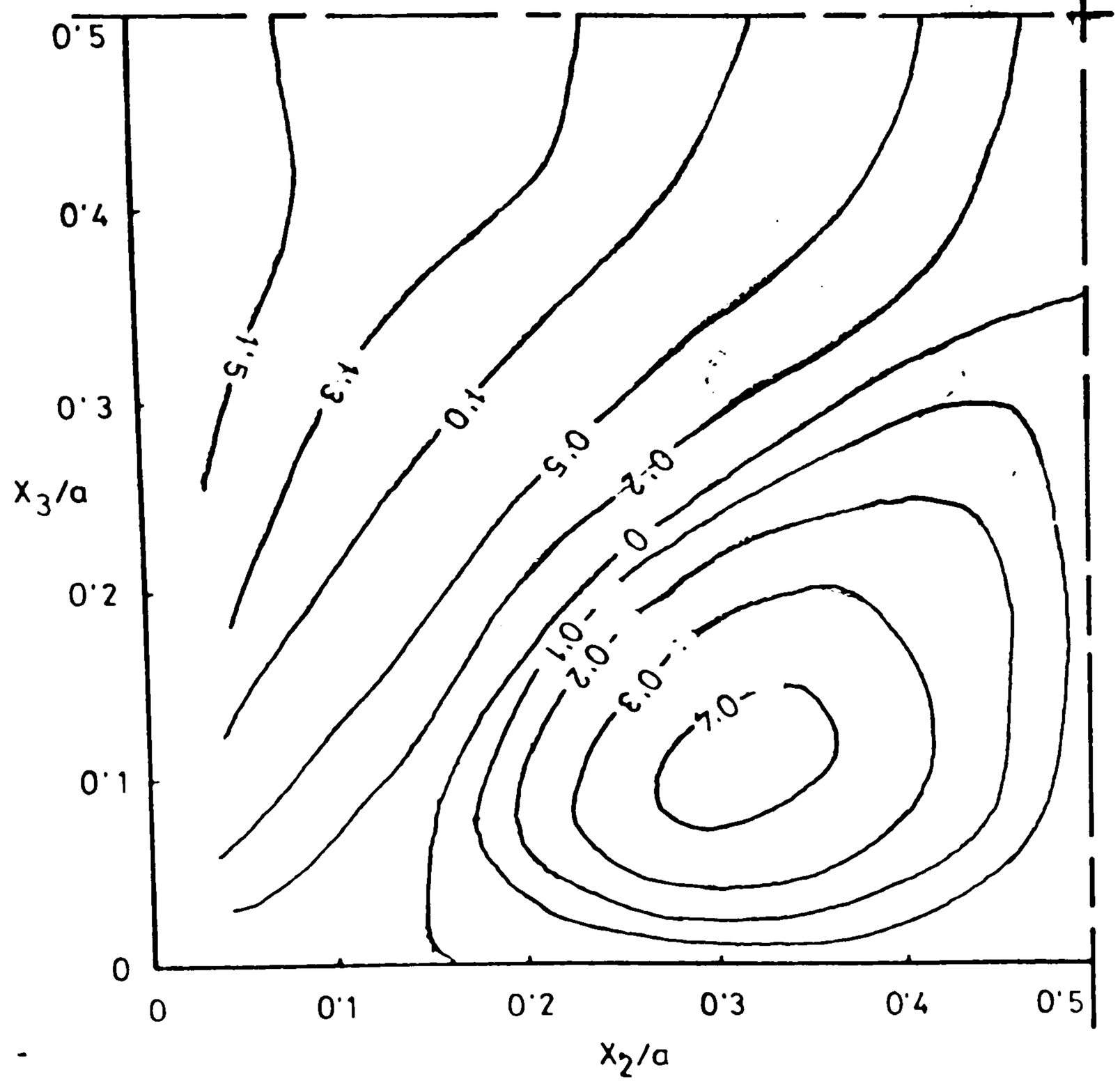

Melling and Whitelaw ($R_e = 4{\cdot}2 \times 10^4$)

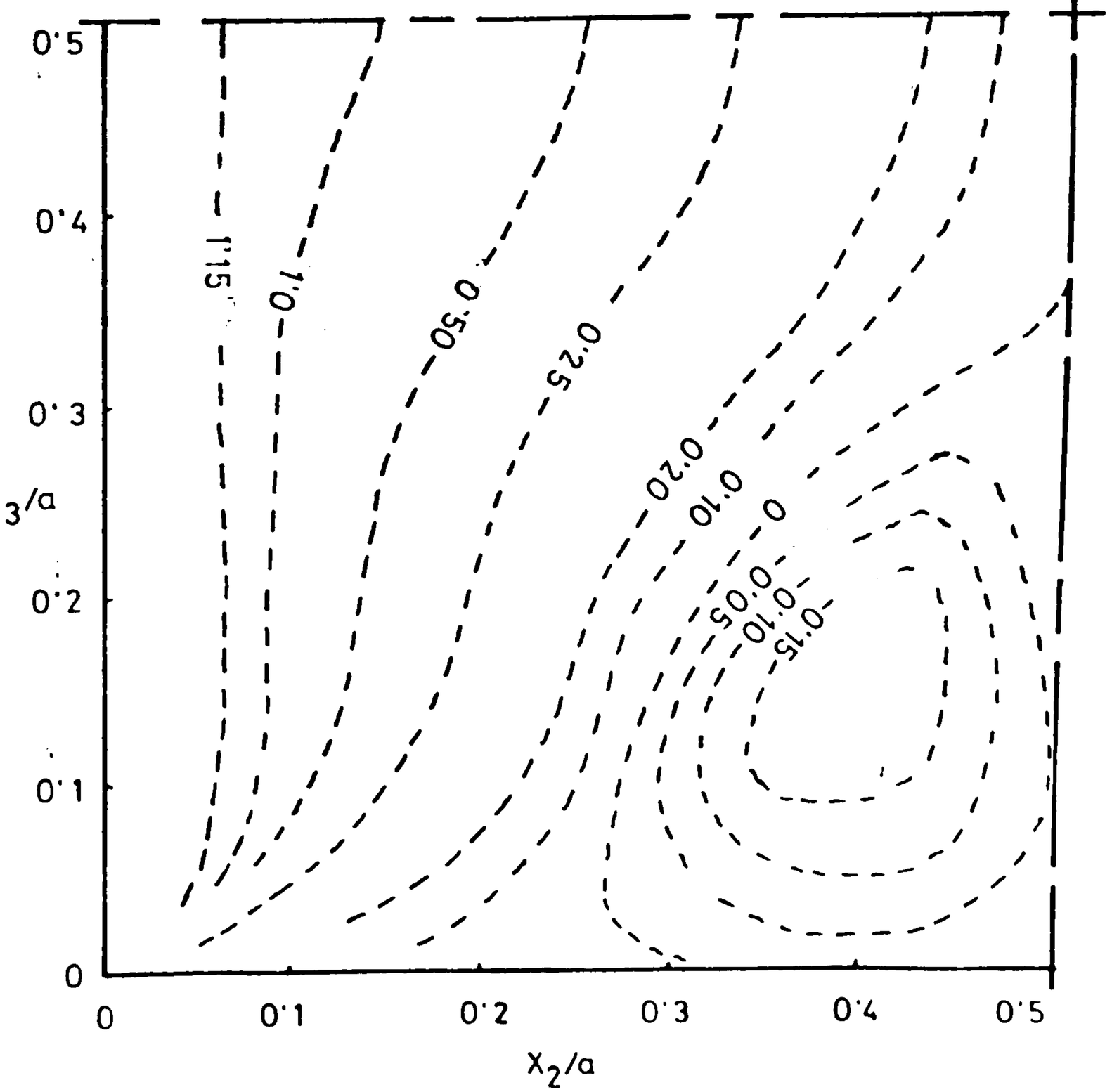

calculation ($R_e = 3{\cdot}66 \times 10^5$)

Fig. 6·10 Comparison of $u_1 u_2 / U_c^2 \times 10^3$ contours in a smooth duct.

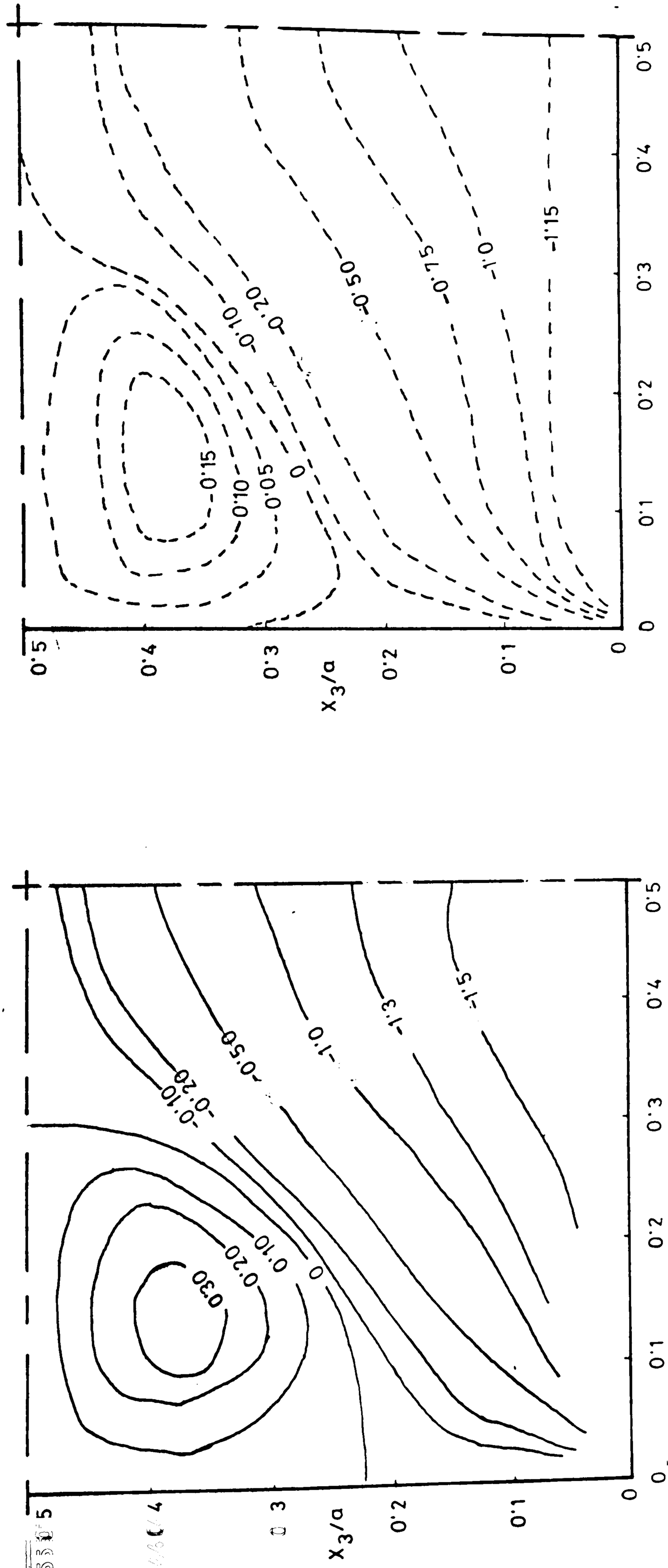

Fig. 6·11 Comparison of $\overline{u_i u_3} / U_c^2 \times 10^3$ contours (smooth duct calculation ($R_e = 3{\cdot}66 \times 10^5$)
Melling and Whitelaw ($R_e = 4{\cdot}2 \times 10^4$)

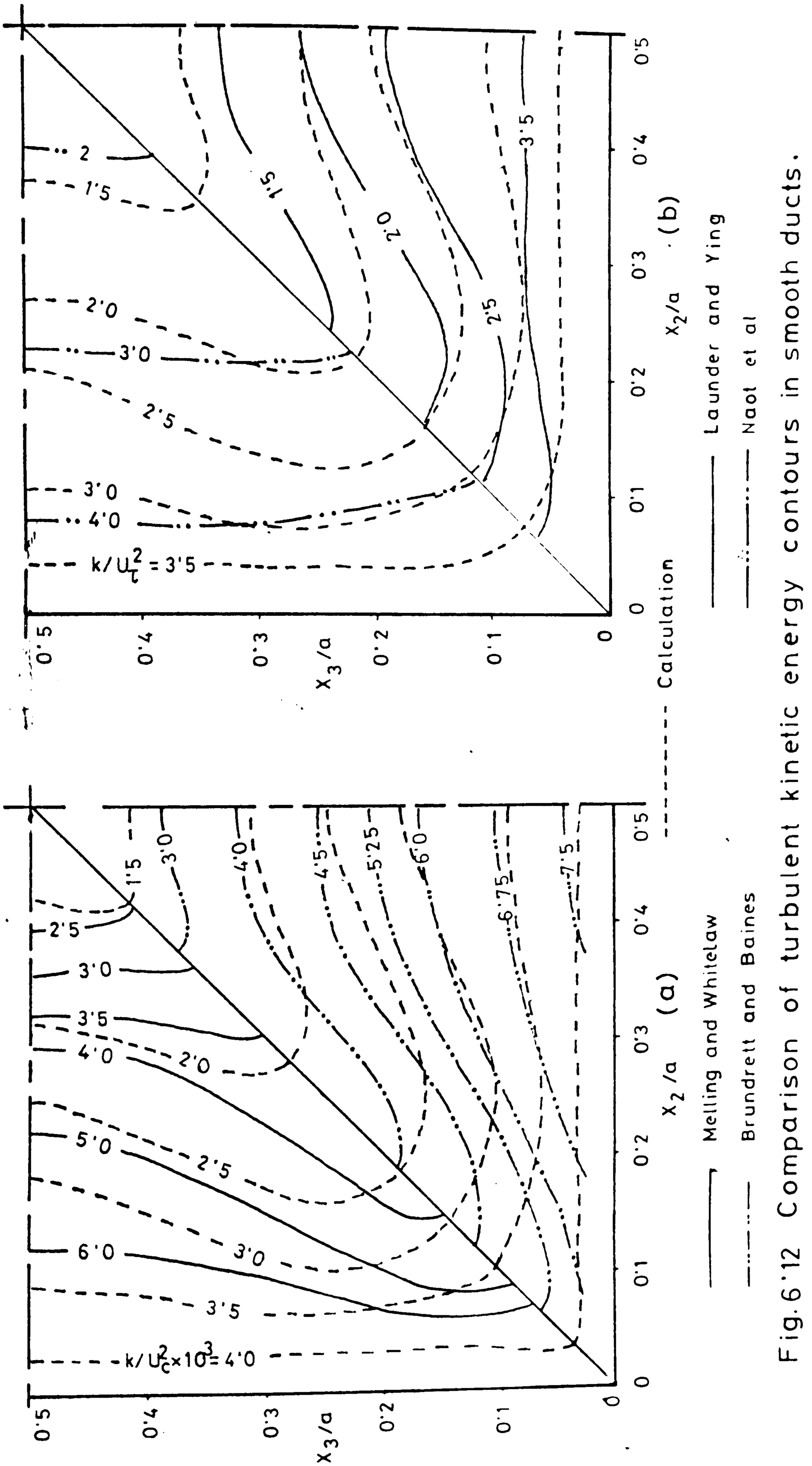

Fig. 6·12 Comparison of turbulent kinetic energy contours in smooth ducts.

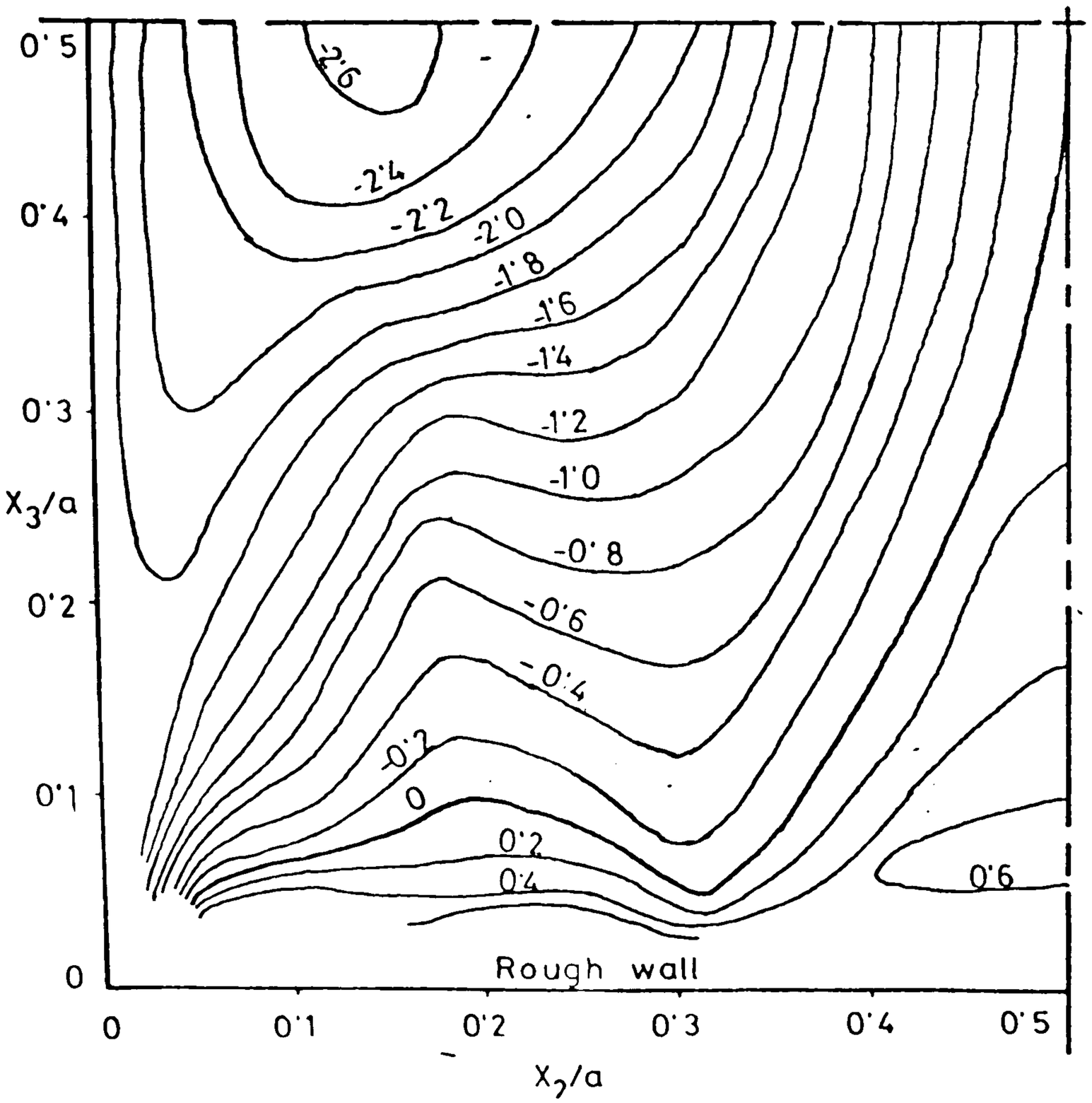

Measurement

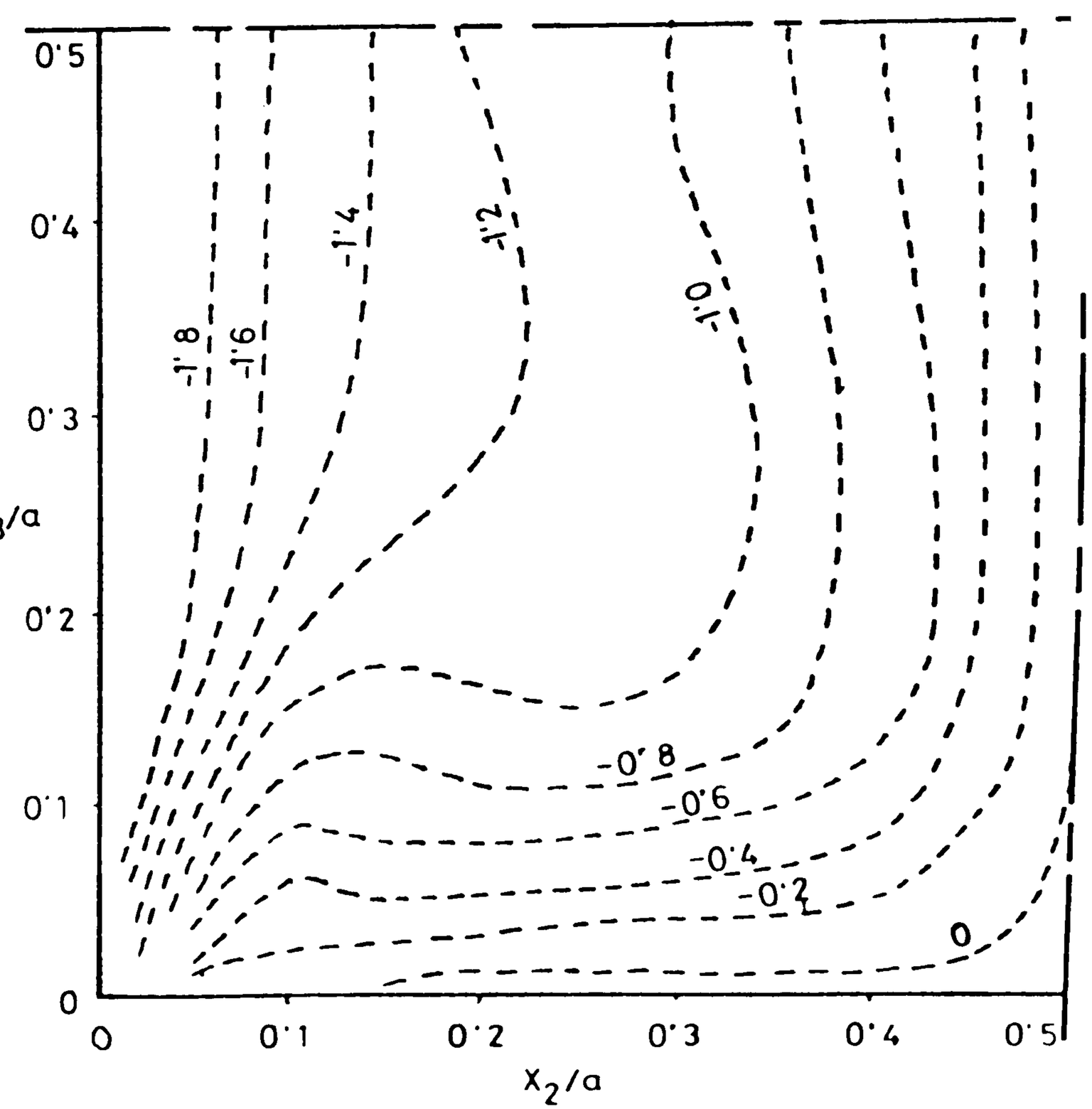

Calculation

Fig. 6·13 Comparison of $\overline{u_1 u_2}/U_c^2 \times 10^3$ contours in a duct with two rough walls.

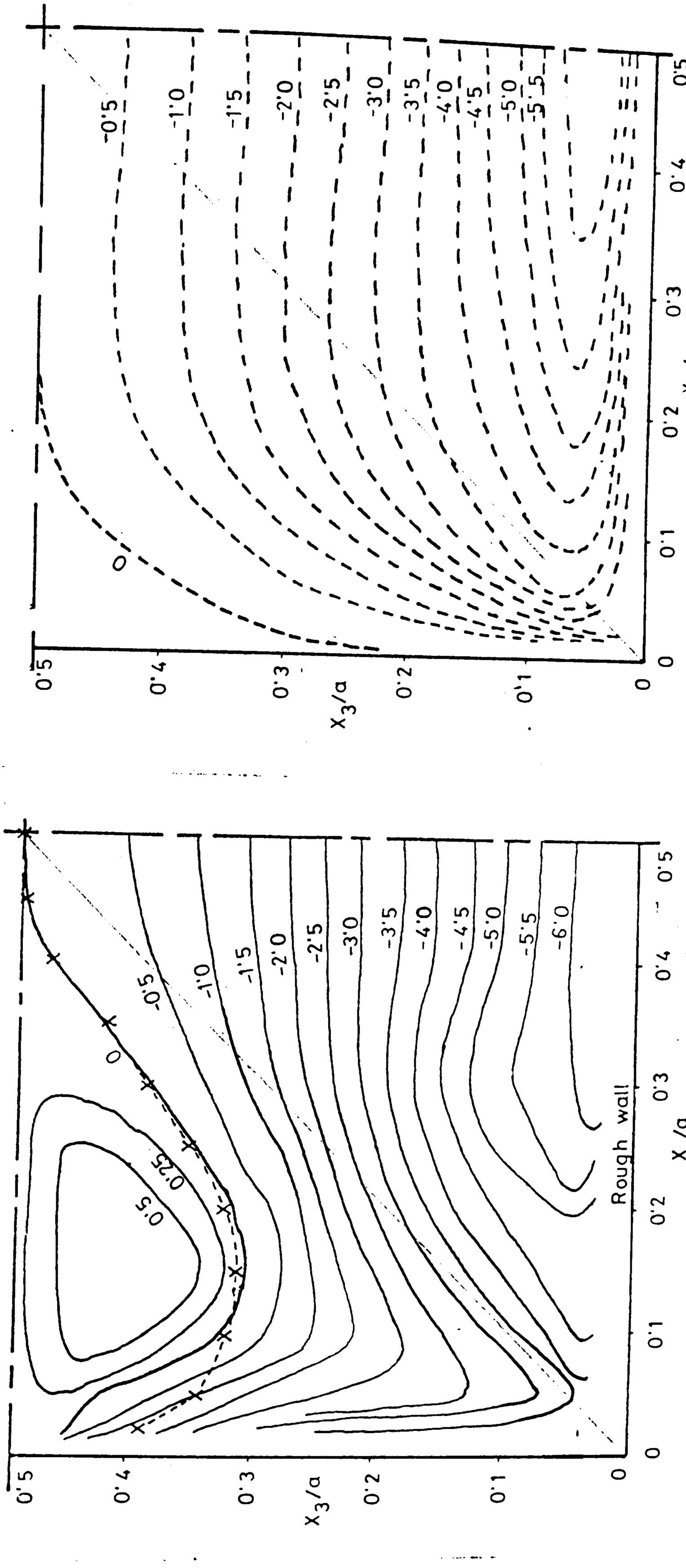

Fig. 6·14 Comparison of $\overline{u_1 u_3} / U_c^2 \times 10^3$. contours in a duct with two rough walls.

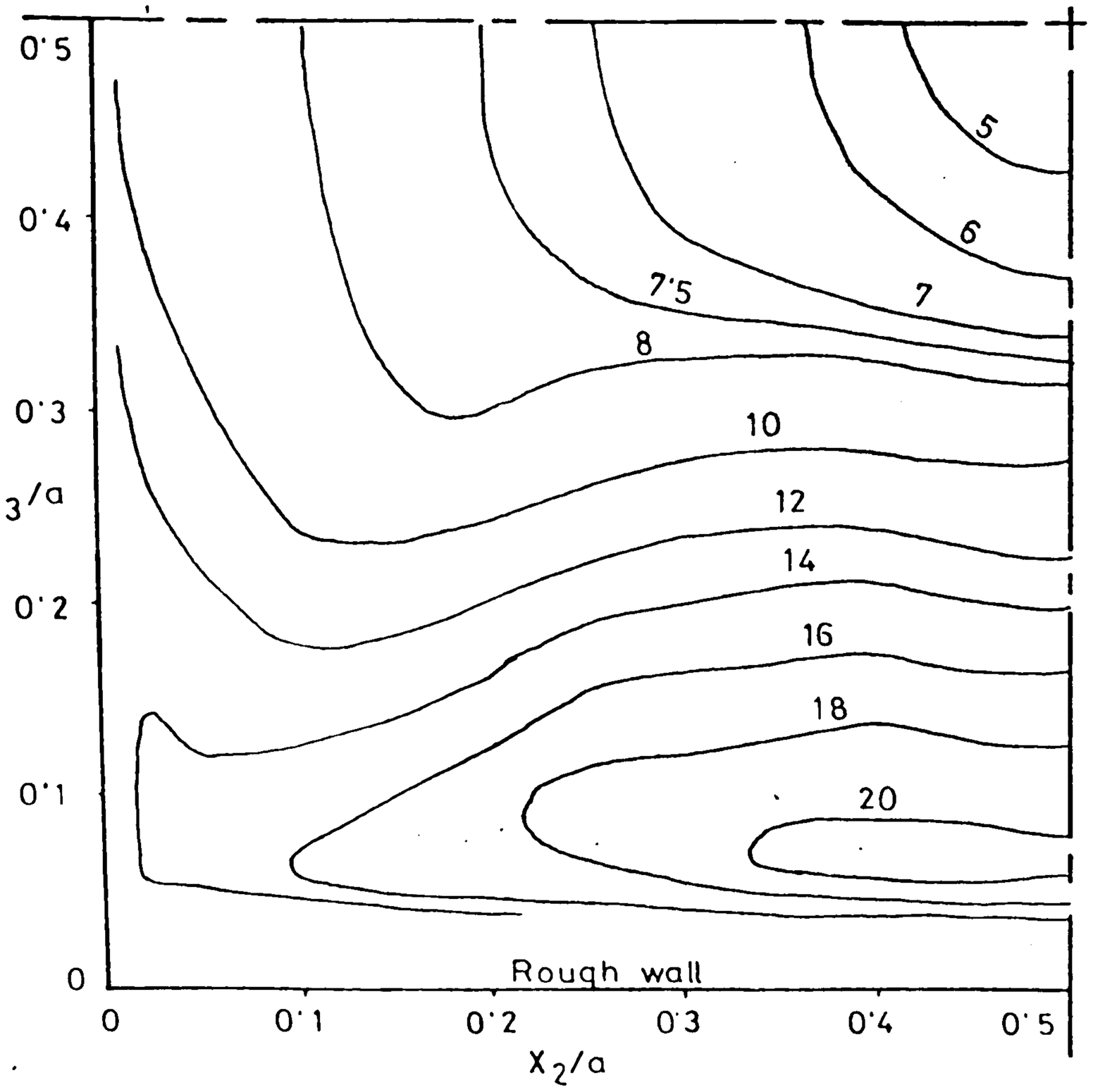

Measurement

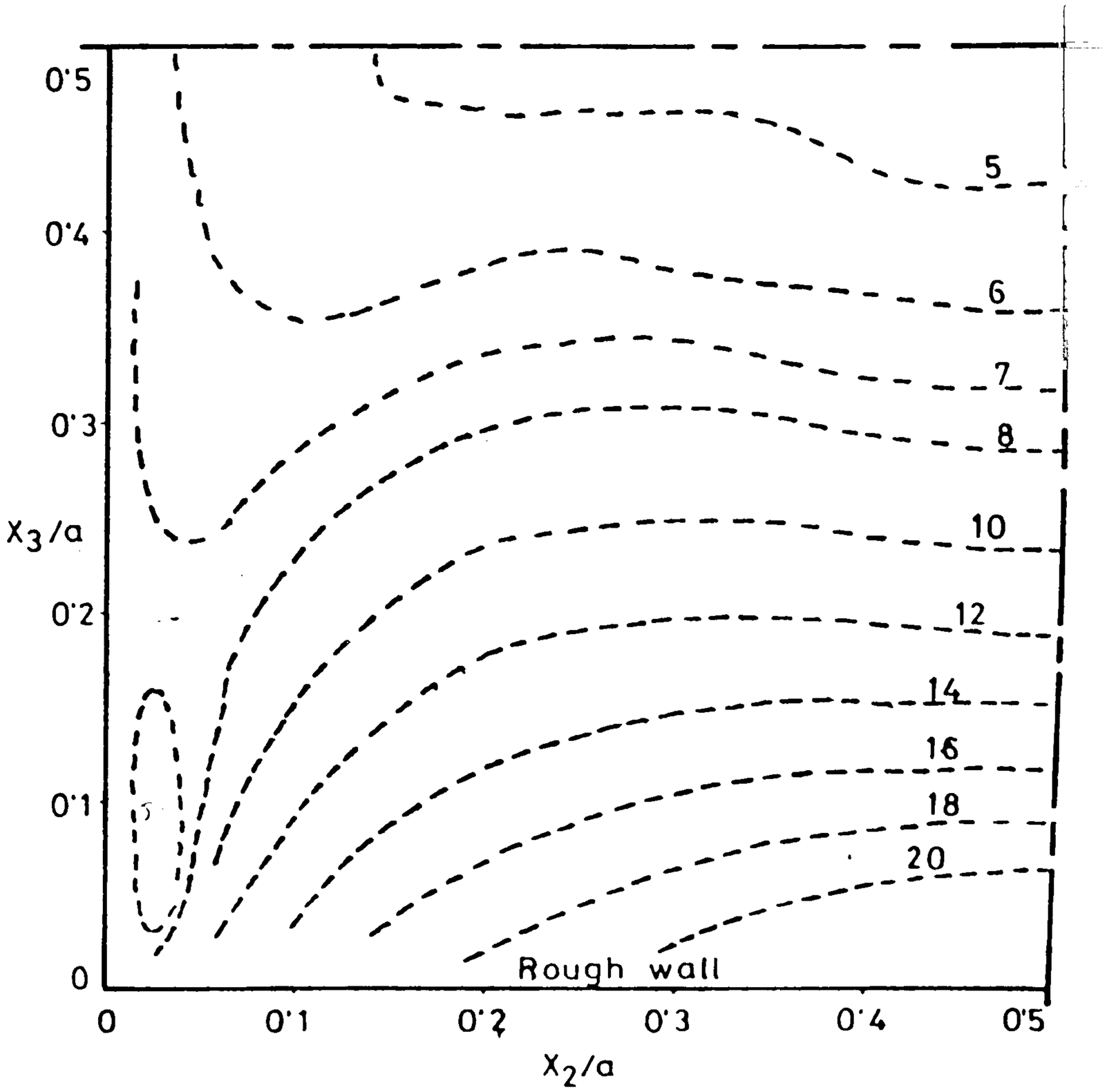

Calculation

Fig. 6·15 Comparison of $k/U_c^2 \times 10^3$ contours in a duct with two rough walls.

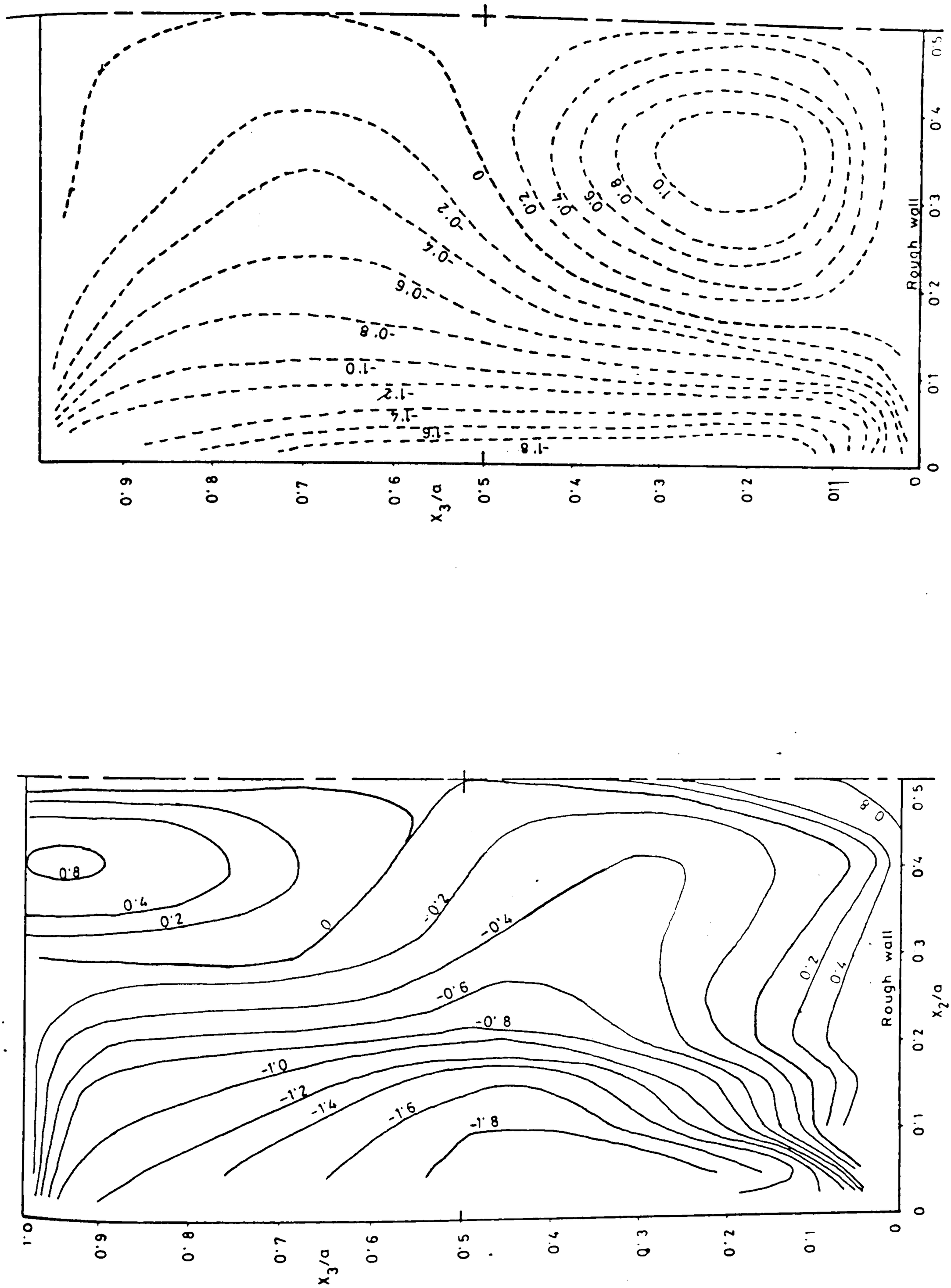

Fig 6'16 Comparison of $\overline{u_1 u_2}/U_c^2 \times 10^3$ contours in a duct with one rough wall.

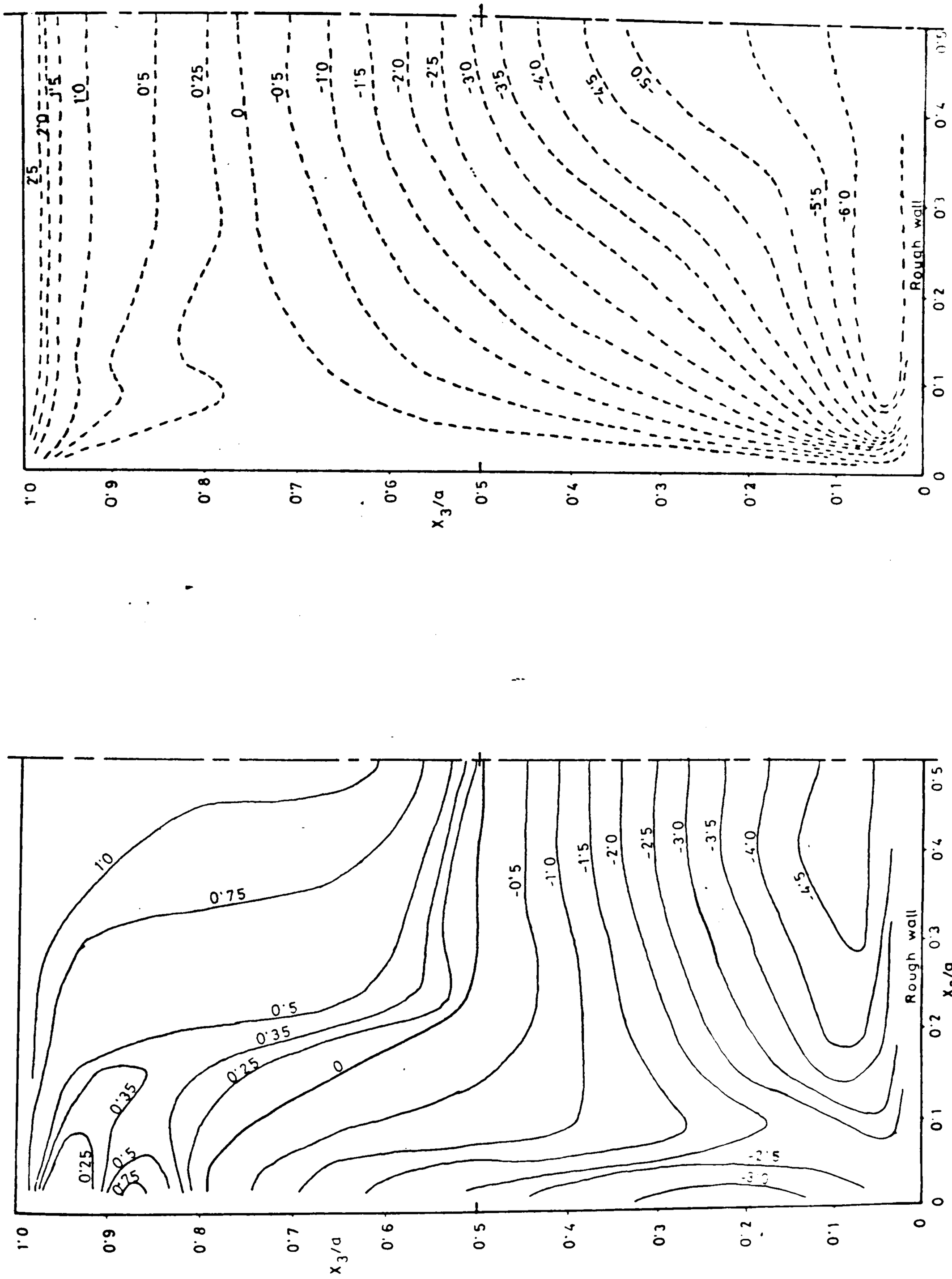

Fig. 6·17 Comparison of $\overline{u_1 u_3}/U_c^2 \times 10^3$ contours in a duct with one rough wall.

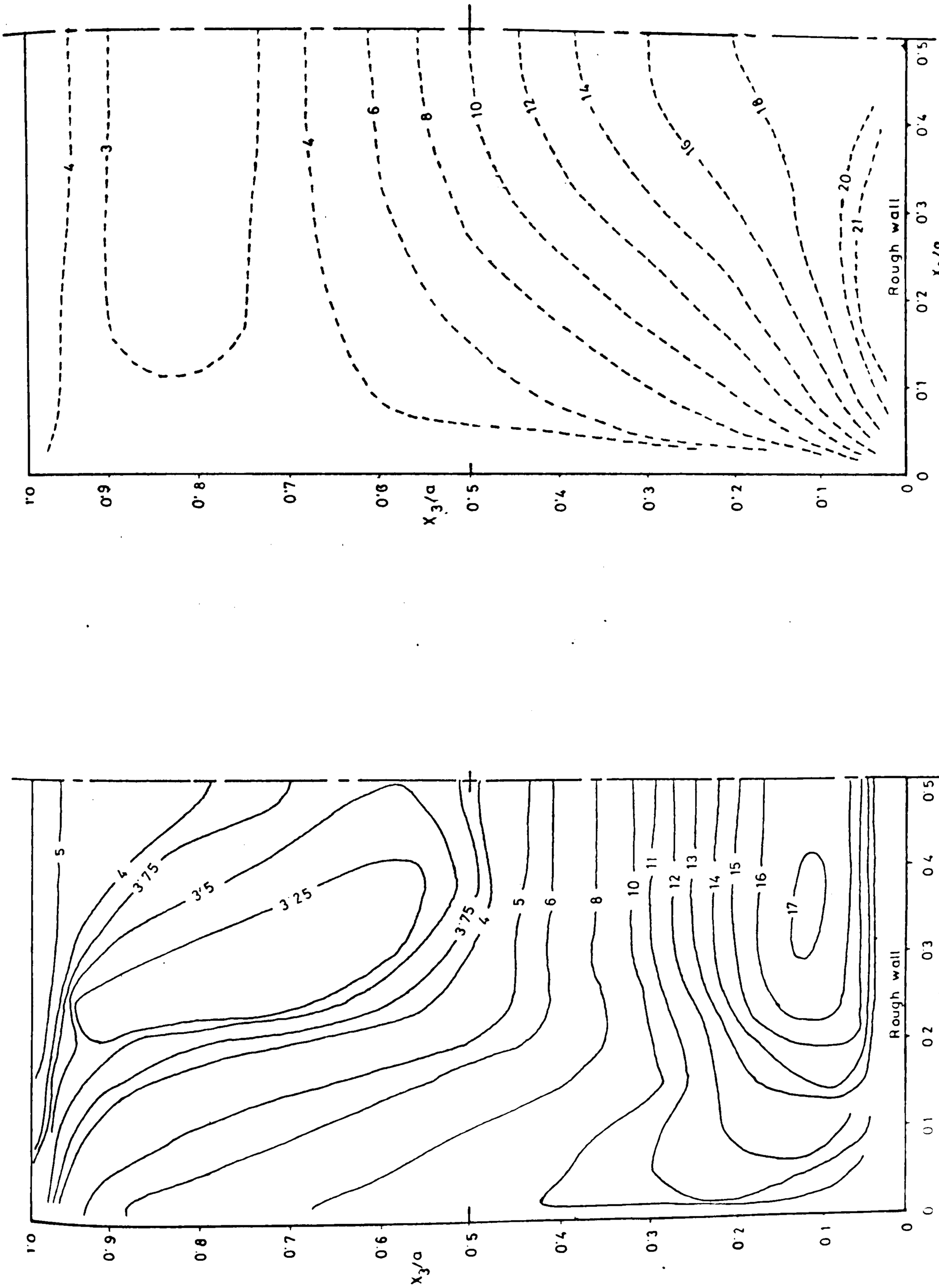

Fig. 6·18 Comparison of $k/U_c^2 \times 10^3$ contours in a duct with one rough wall..

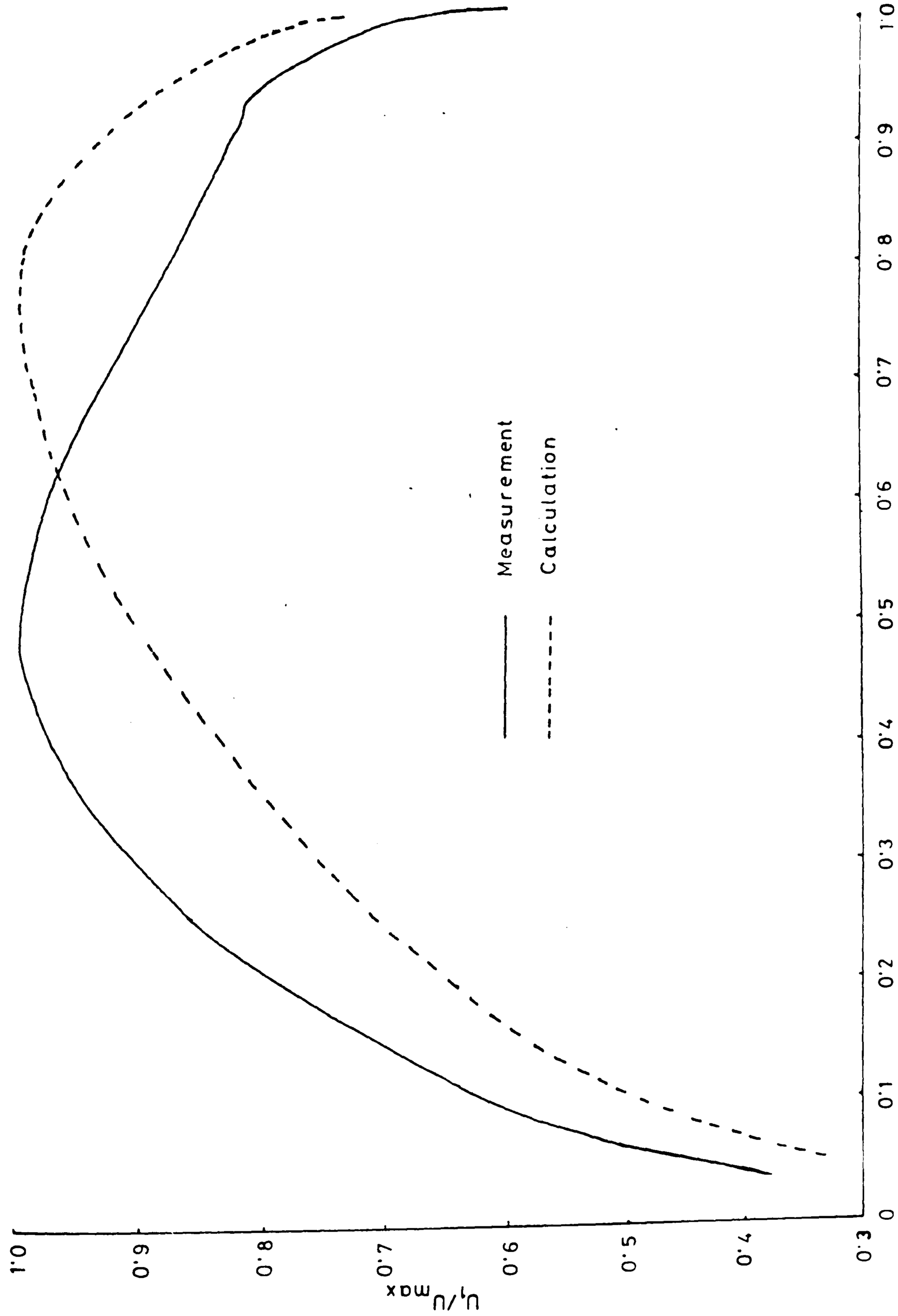

Fig.6.19 Comparison of mean velocity profile in a duct with one rough wall.

P/e	Flow pattern
∞	Flow a Flow reattachment
10	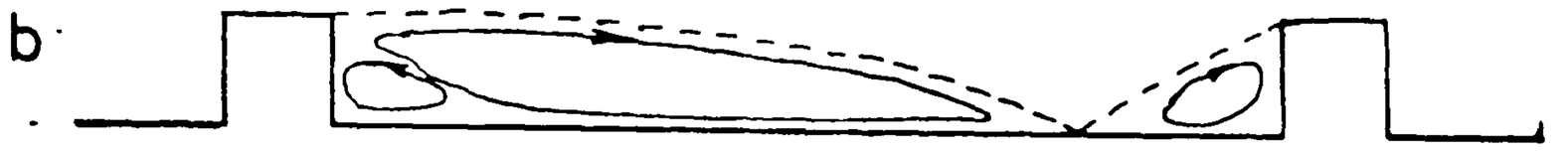 b Flow reattachment
5	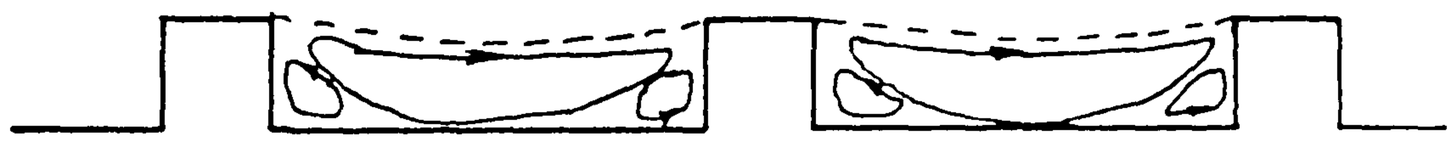 c Wake interference flow
1	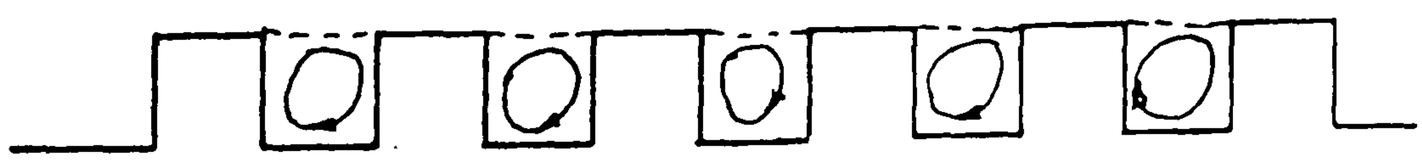 d Skimming flow

Fig. 7'1 Variation of flow pattern with P/e

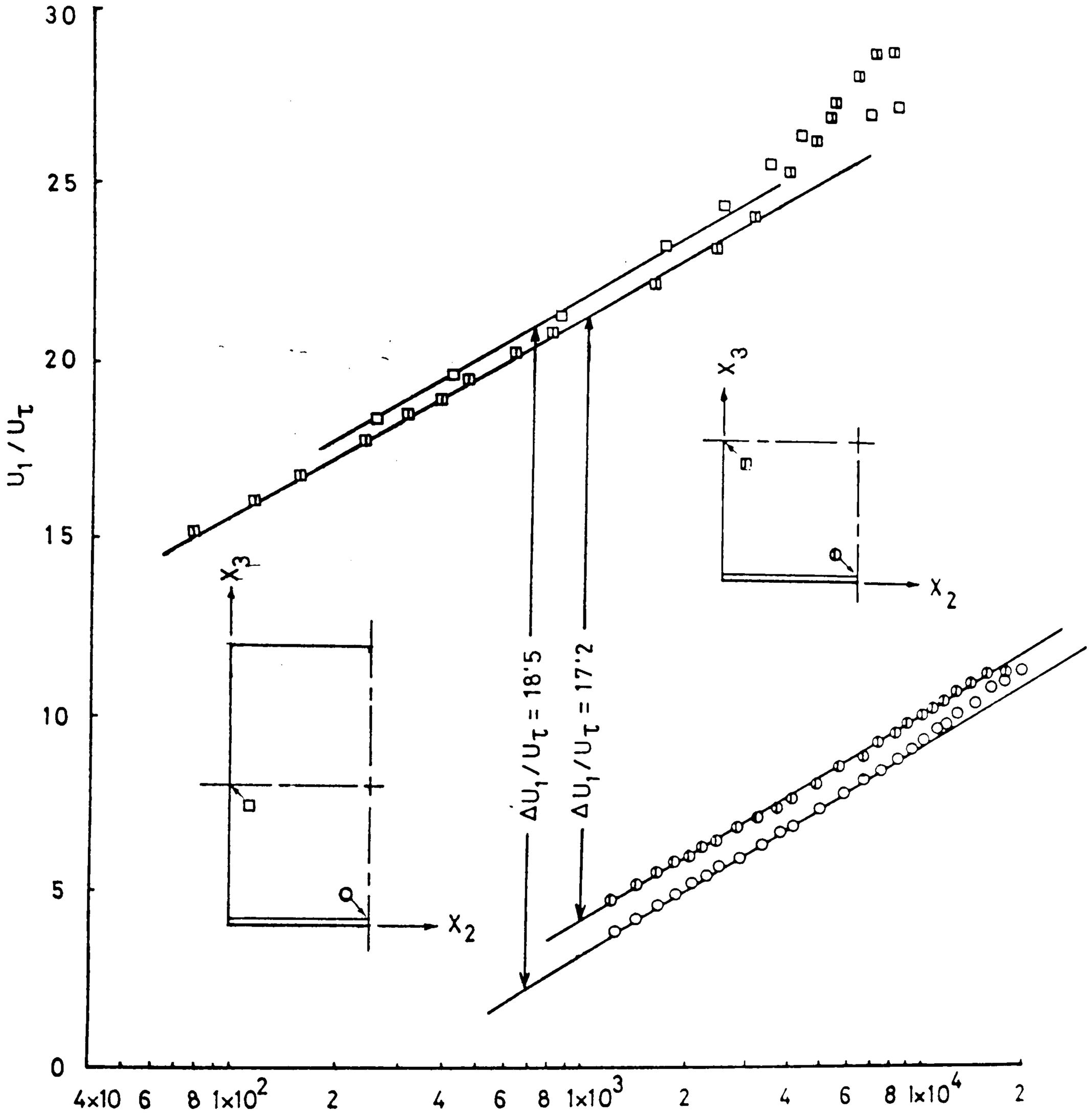

Fig. 7'2 Law of the wall for rough and smooth walls in rough-smooth ducts.

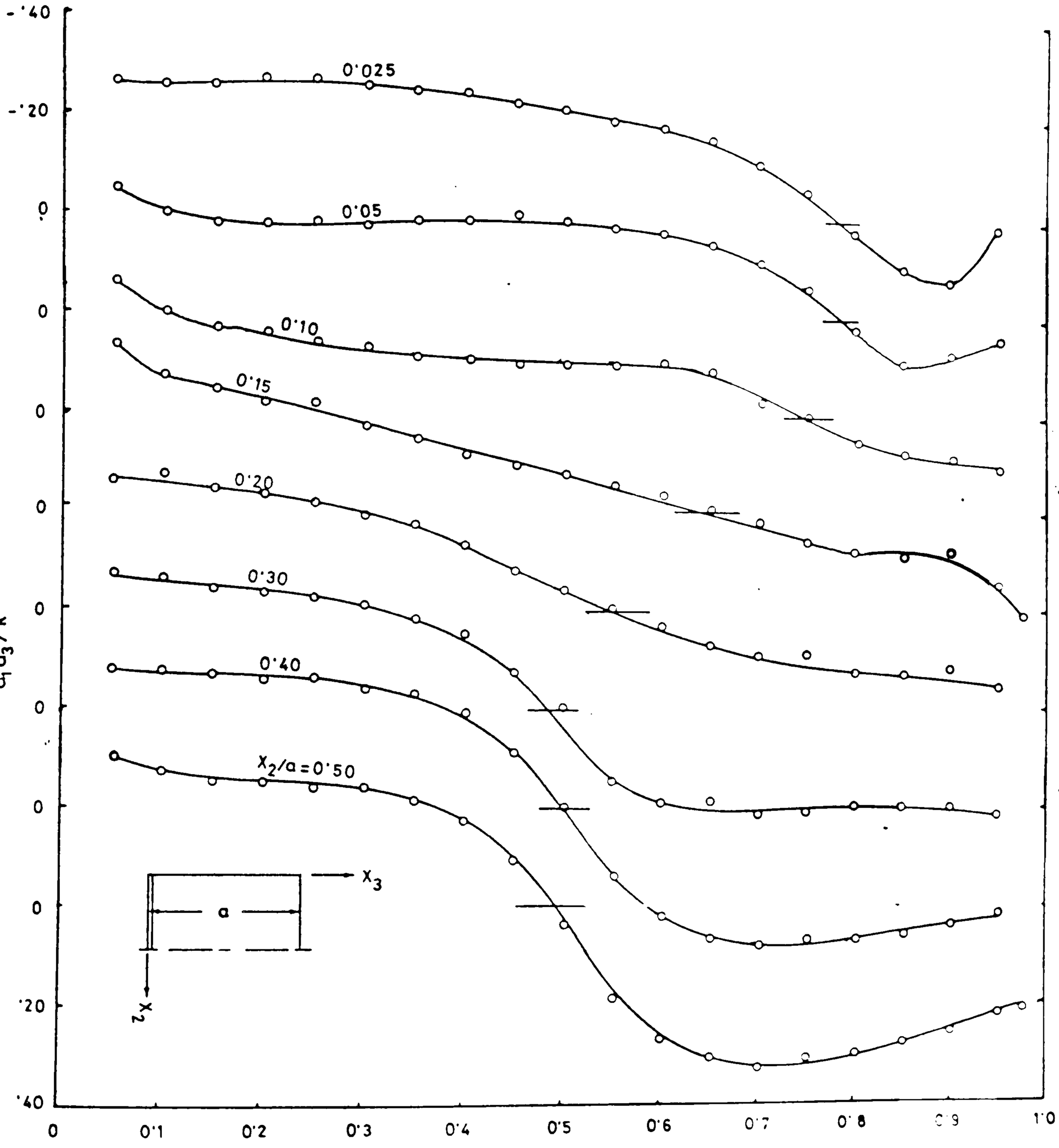

Fig. 7·3 Profiles of $\overline{u_1 u_3}/k^2$ in a duct with one rough wall.

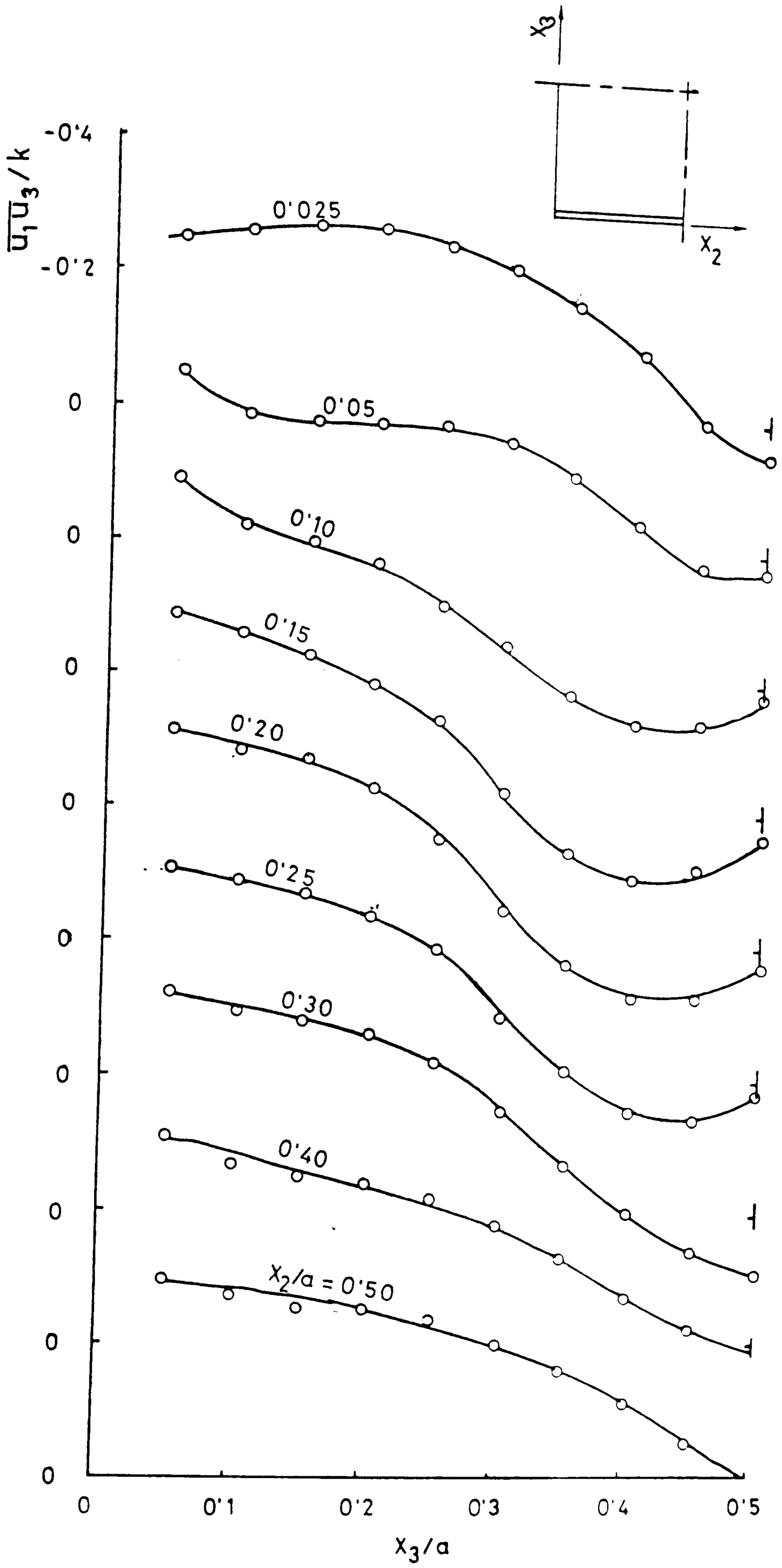

Fig. 7·4 Profiles of $\overline{u_1 u_3}/k$ in a duct with two rough walls.

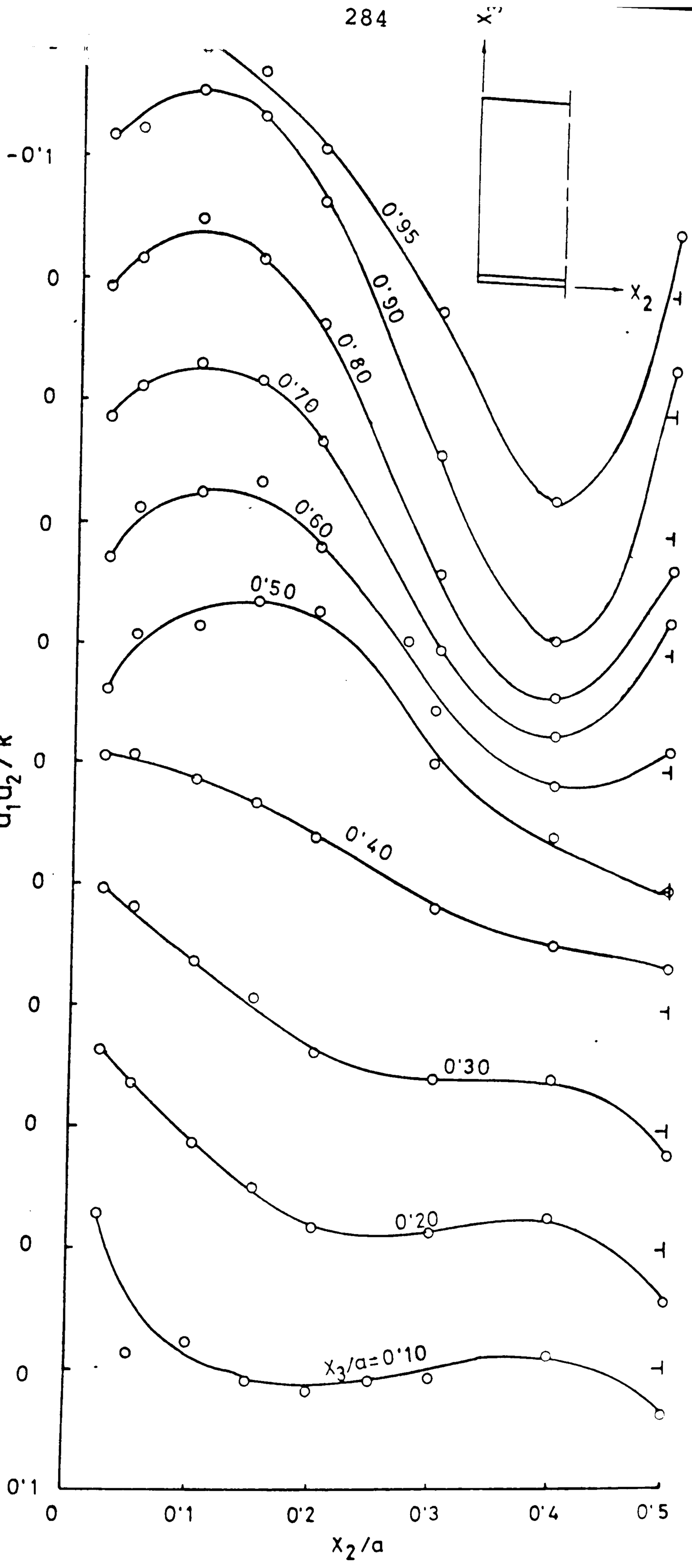

Fig. 7·5 Profiles of $\overline{u_1 u_2}/k$ in a duct with one rough wall.

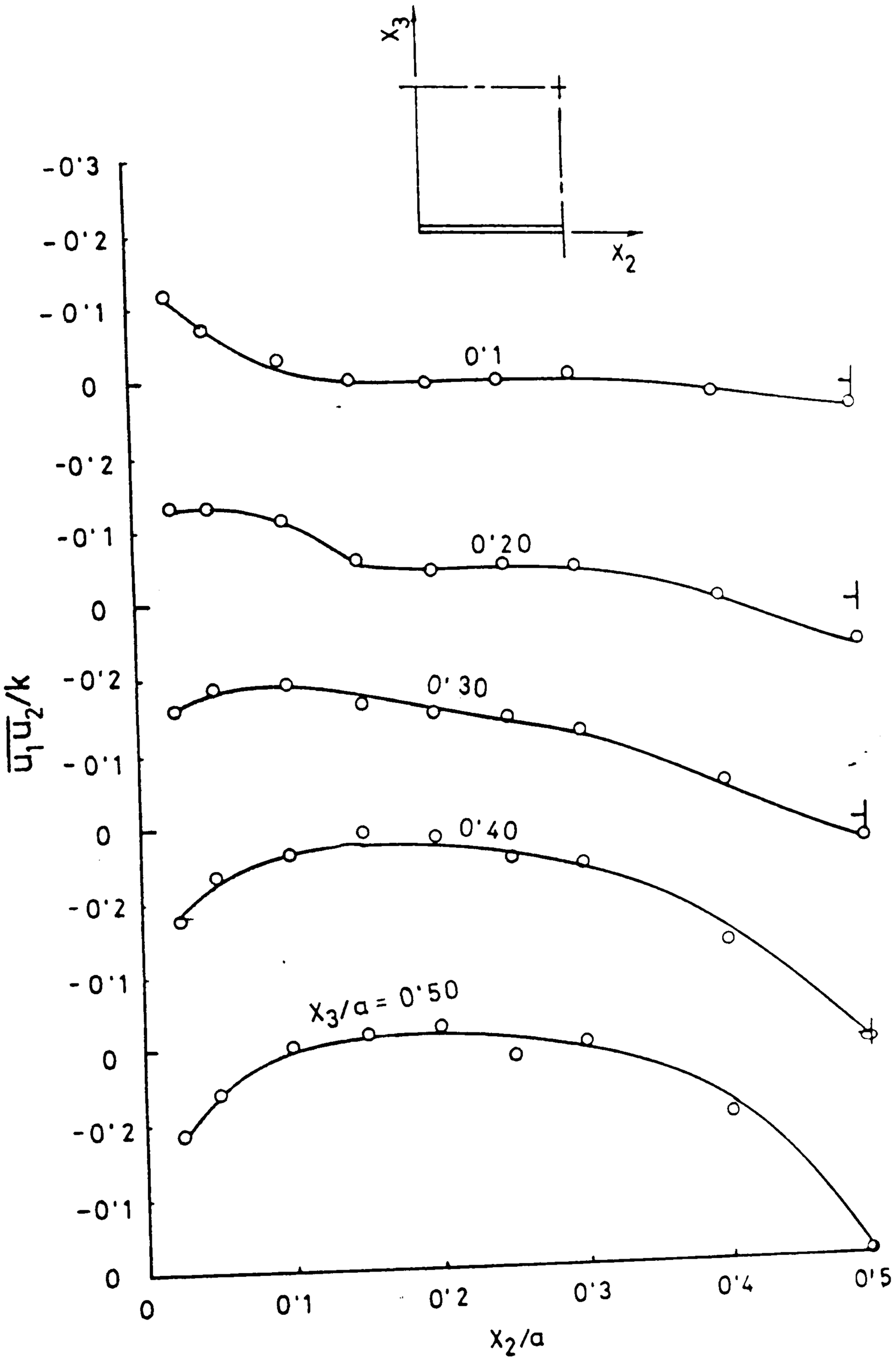

Fig. 7·6 Profiles of $\overline{u_1u_2}/k$ in a duct with two rough walls.

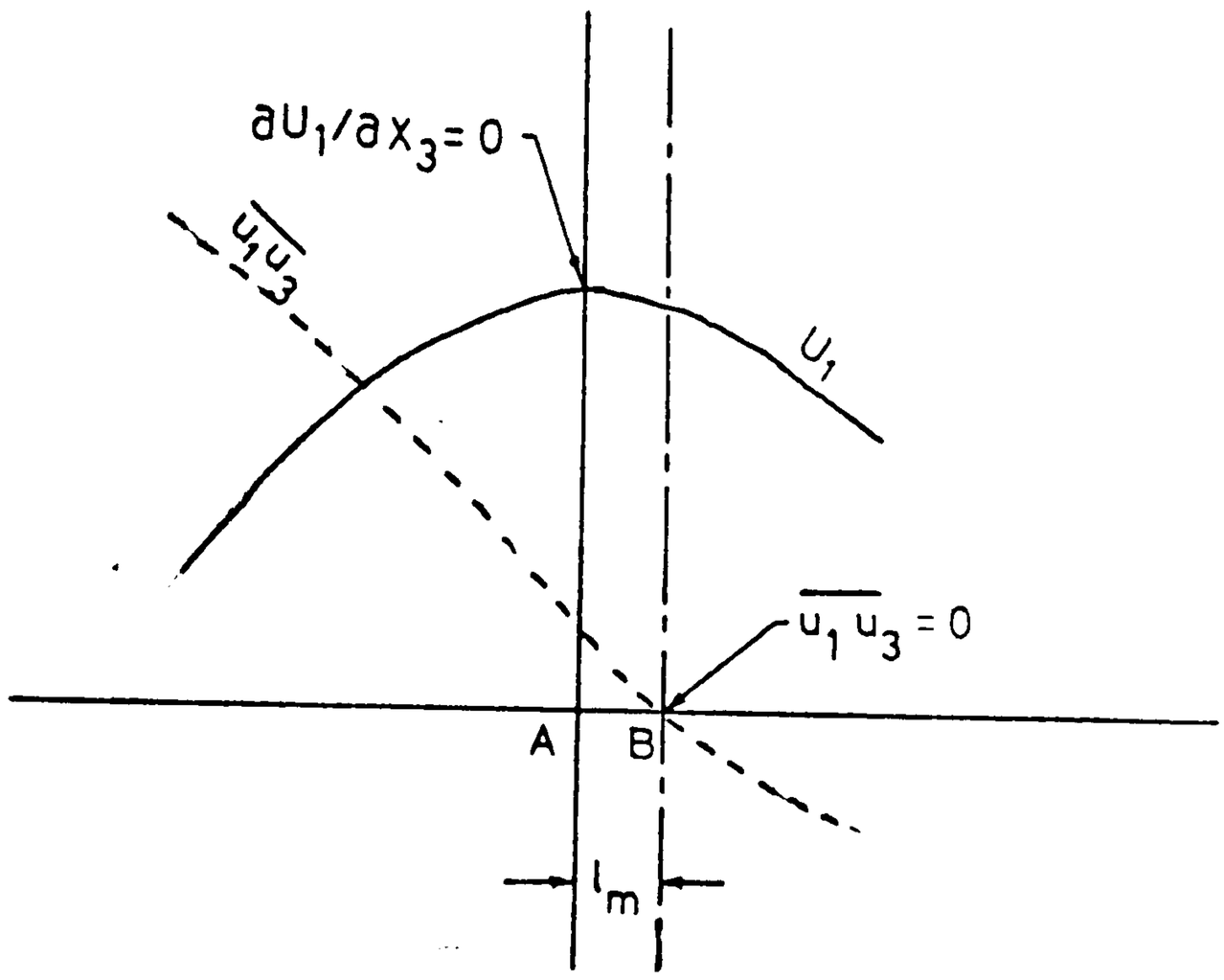

Fig. 7·7 Diagram showing the planes of zero shear stress and zero velocity gradient.

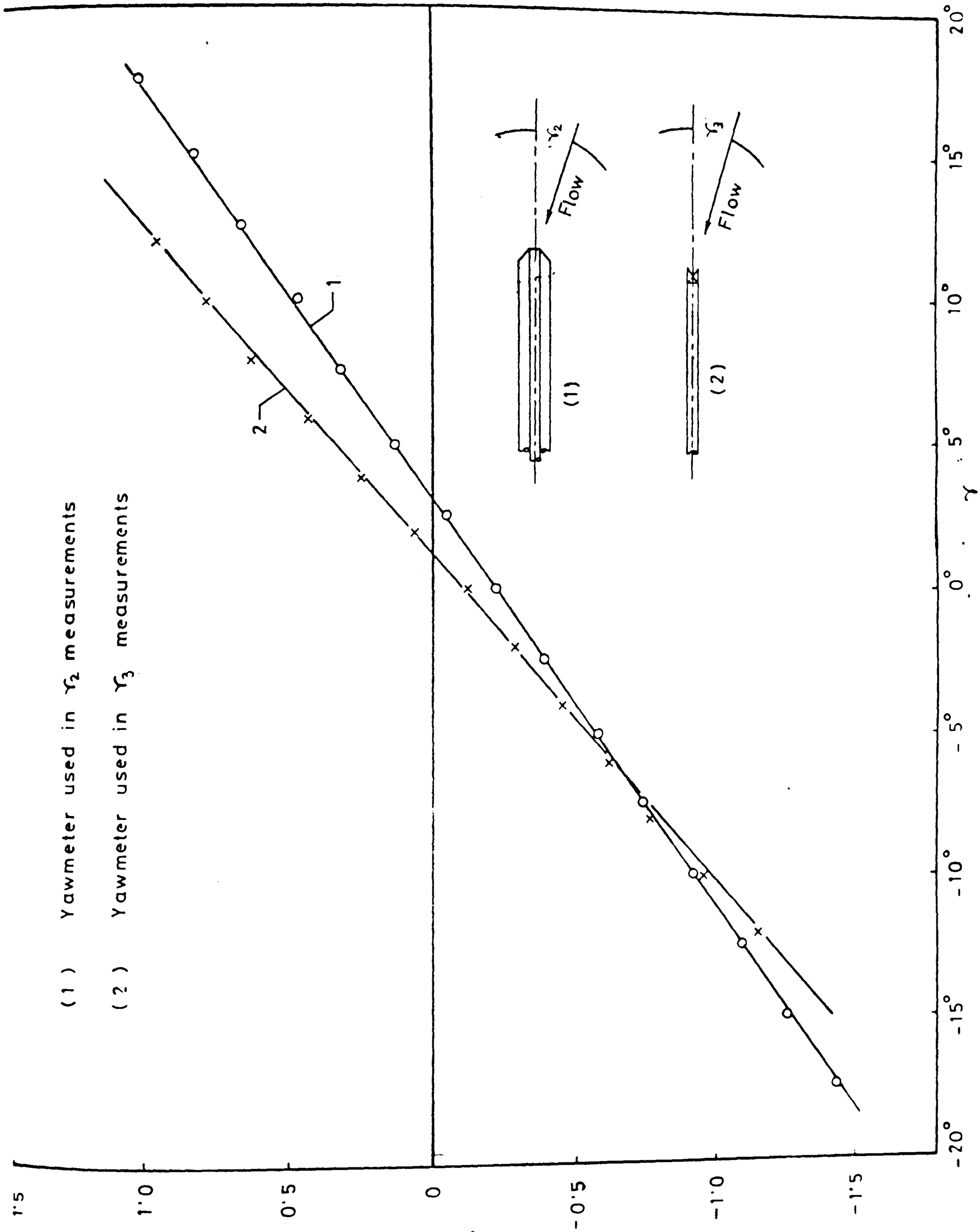

(1) Yawmeter used in γ_2 measurements

(2) Yawmeter used in γ_3 measurements

Fig. A 3·1 Calibration curves for the yawmeters.

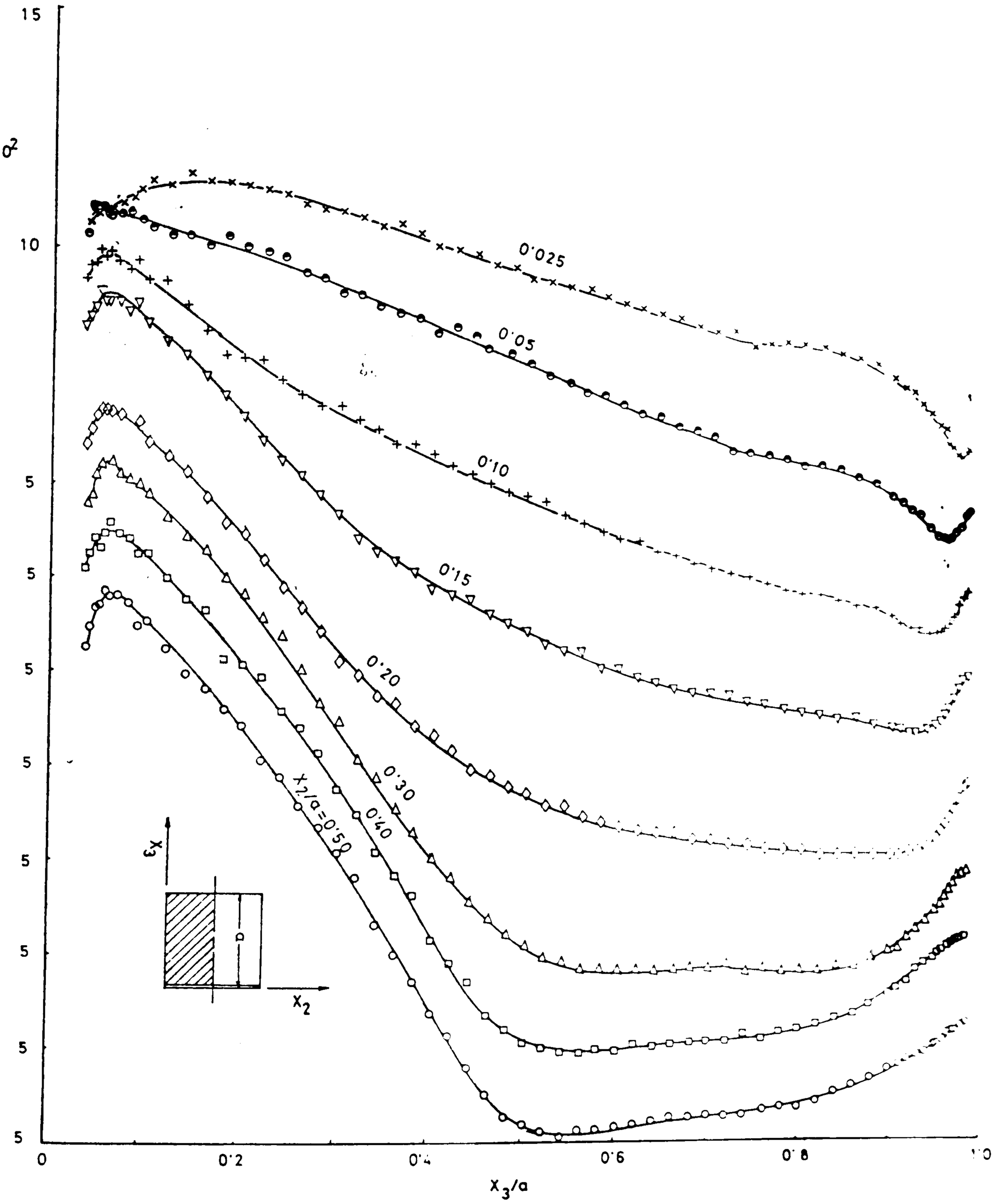

Fig. A 4·1 Profiles of $\bar{u}_1/U_c \times 10^2$.

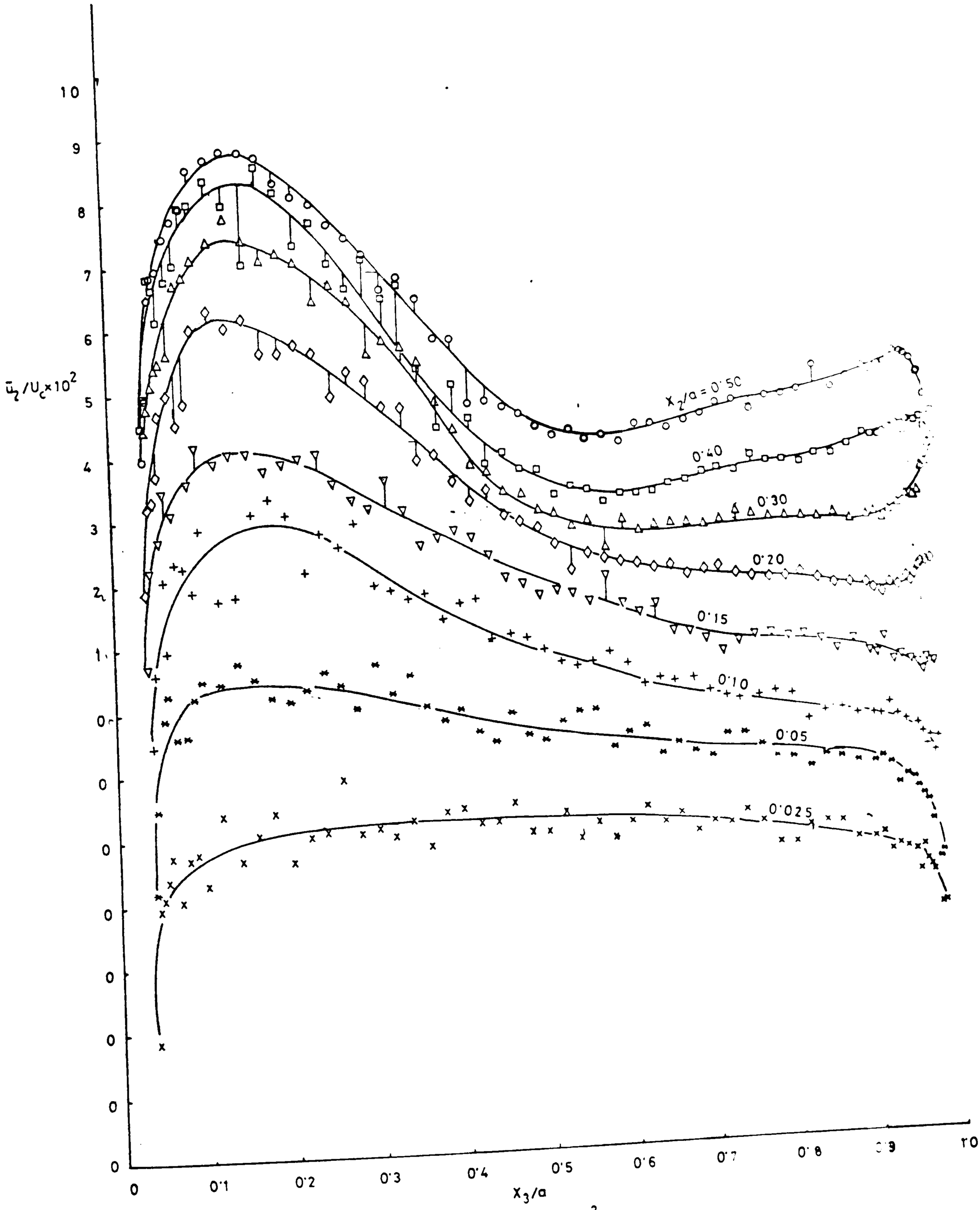

Fig. A4·2 Profiles of $\tilde{u}_2 / U_c \times 10^2$

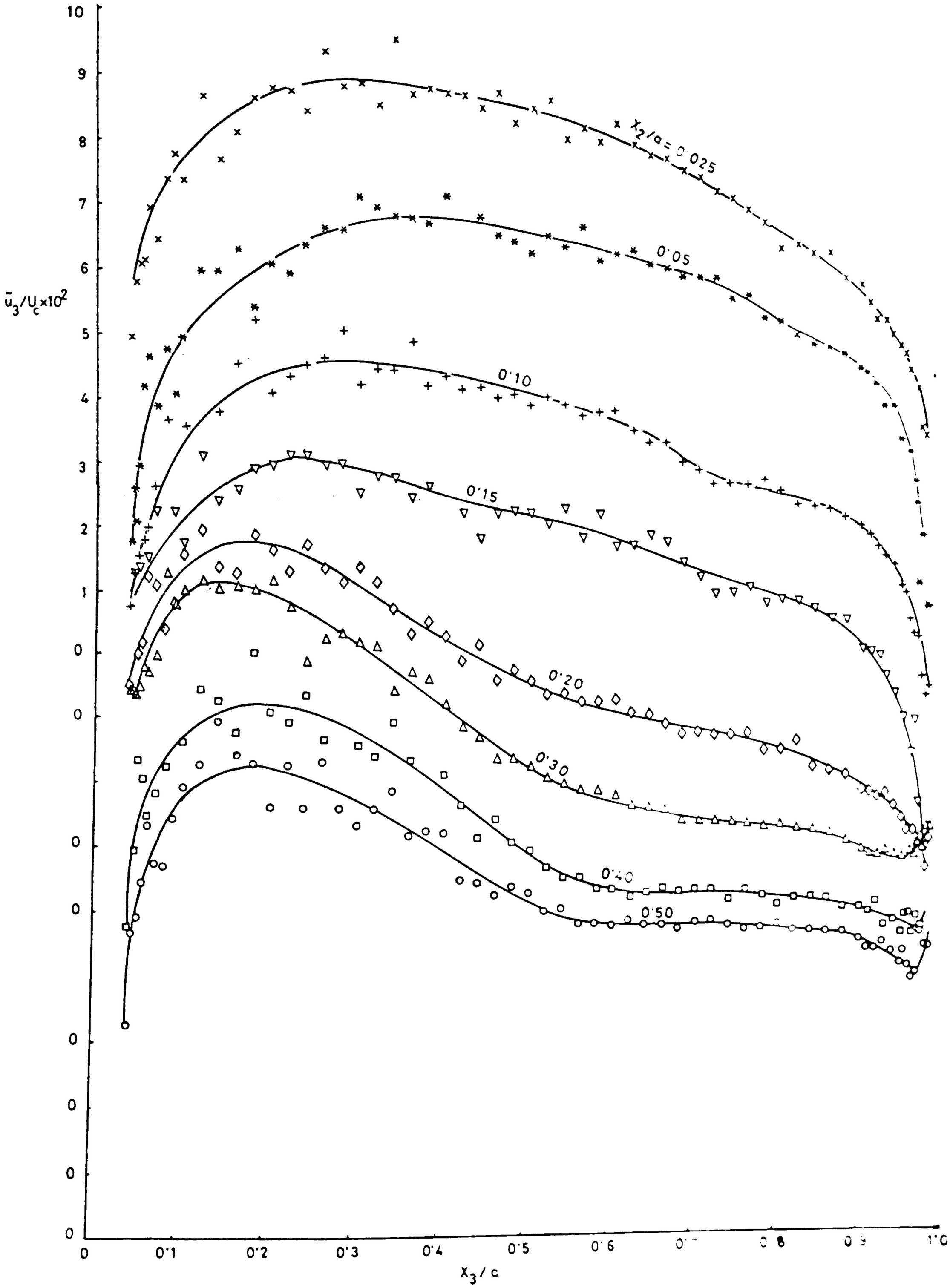

Fig. A4·3 Profiles of $\bar{u}_3/U_c \times 10^2$.

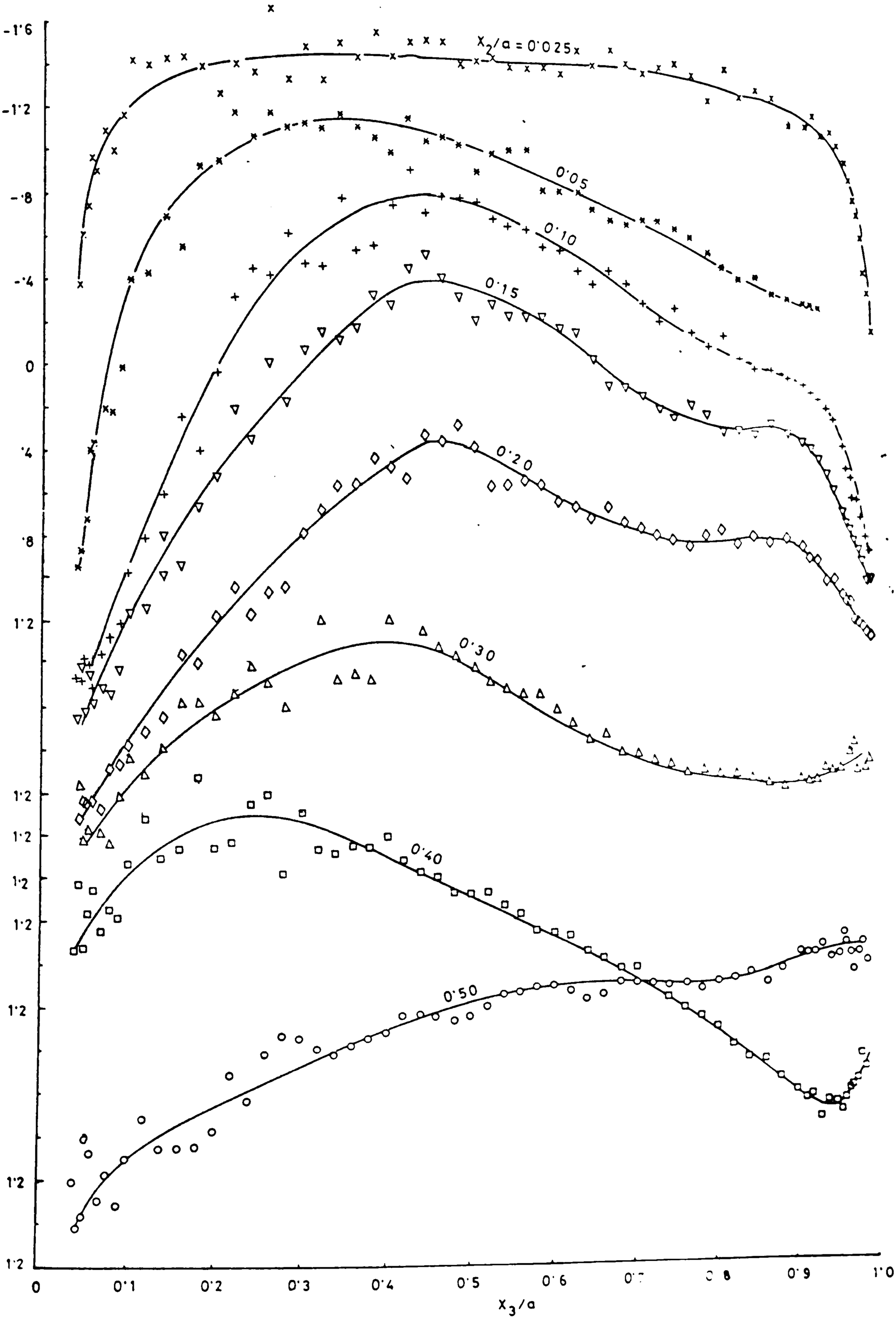

Fig.A 4.4 Profiles of $\overline{u_1 u_2}/U_c^2 \times 10^3$

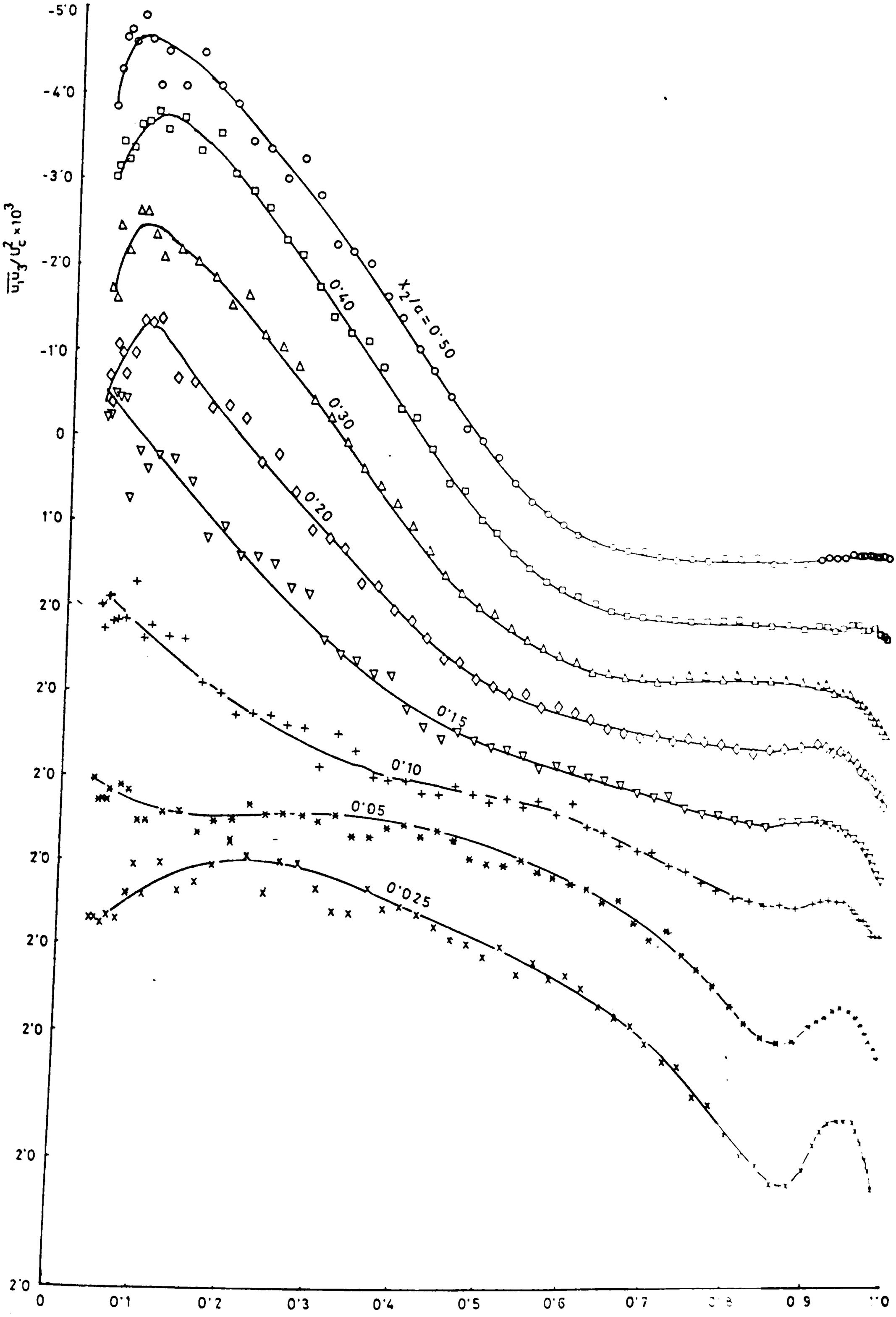

Fig.A4·5 Profiles of $\overline{u_1u_3}/U_c^2 \times 10^3$.

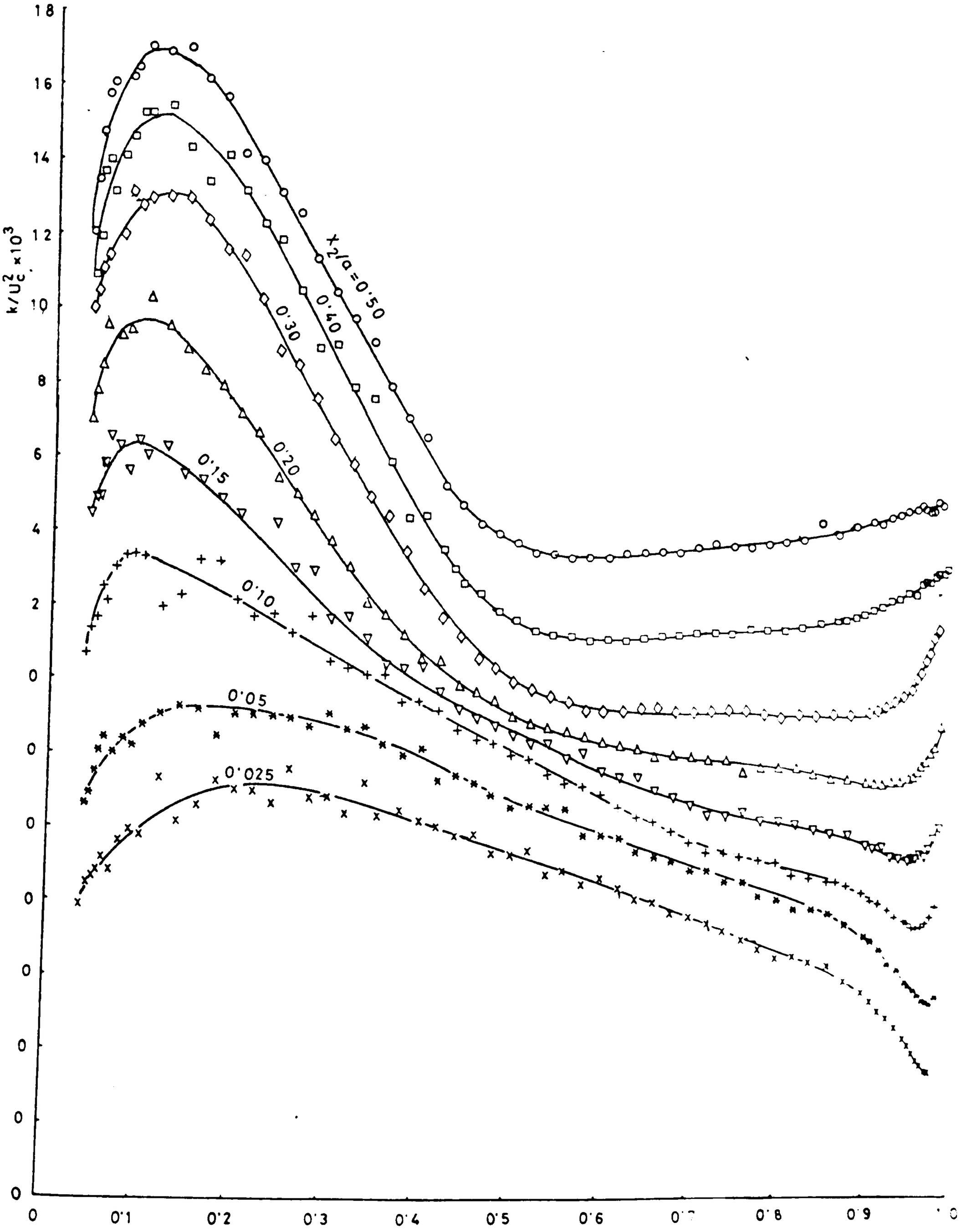

Fig. A 4.6 Profiles of $k / U_c^2 \times 10^3$.

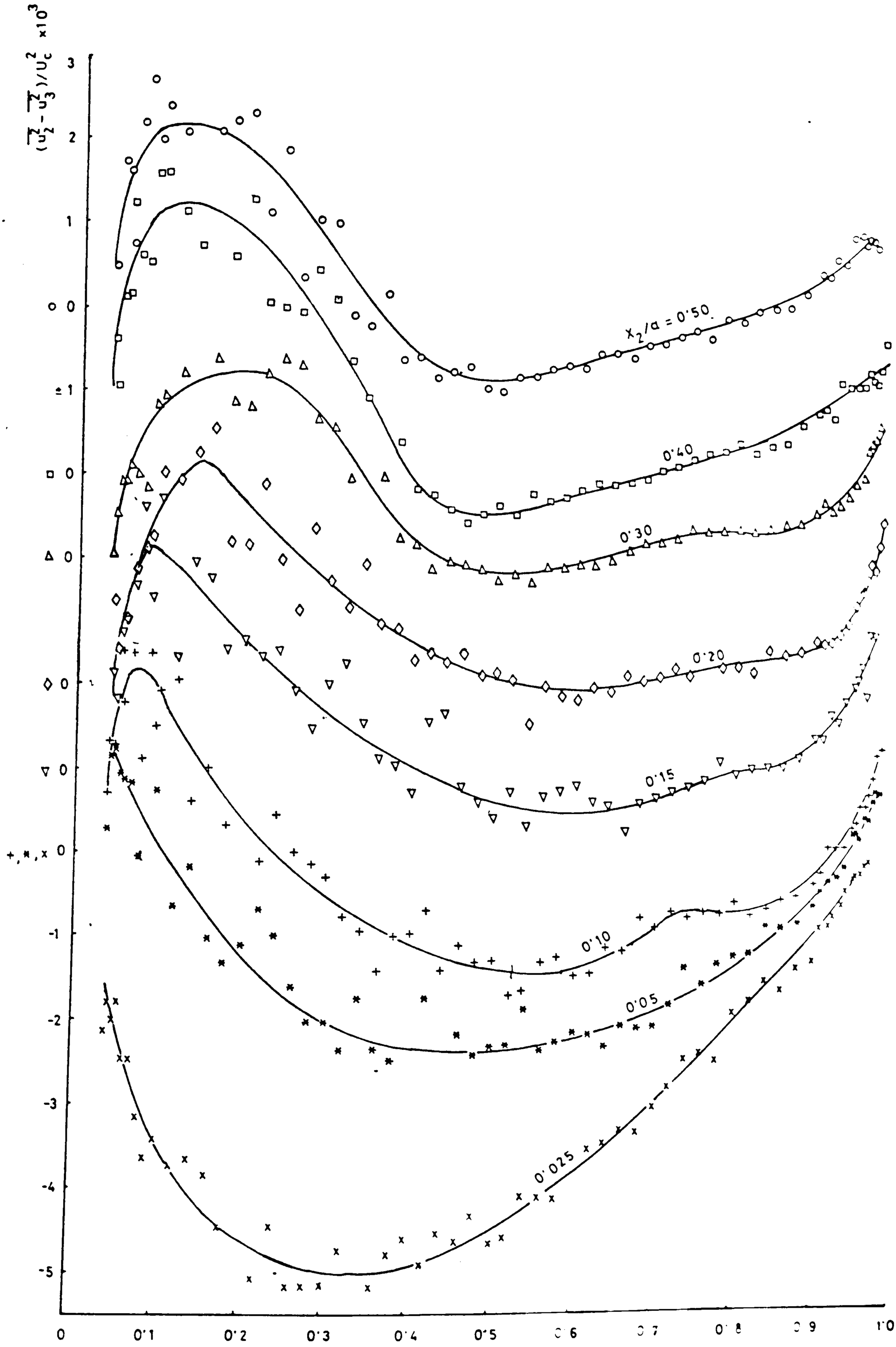

Fig. A4·7 Profiles of $(\overline{u_2^2} - \overline{u_3^3})/U_c^2 \times 10^3$.

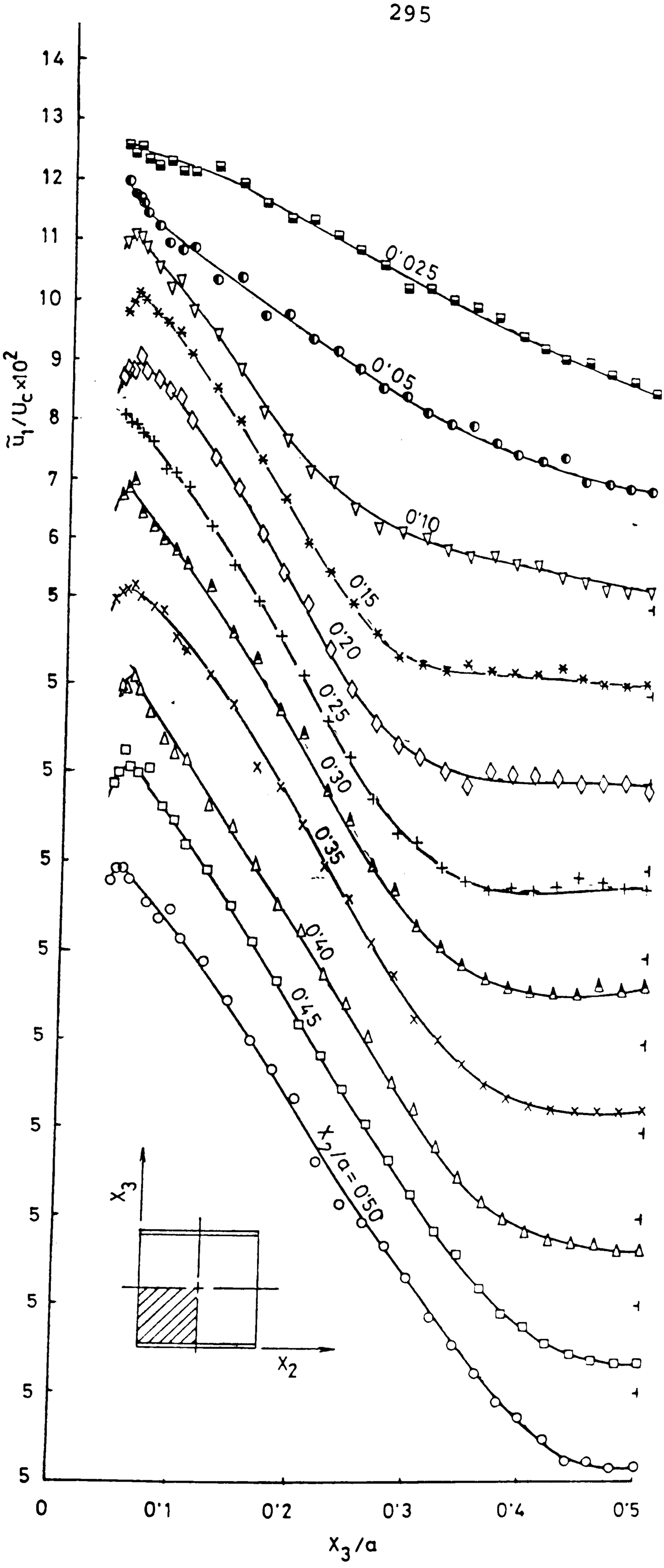

Fig. A5·1 Profiles of $\tilde{u}_1/U_c \times 10^2$.

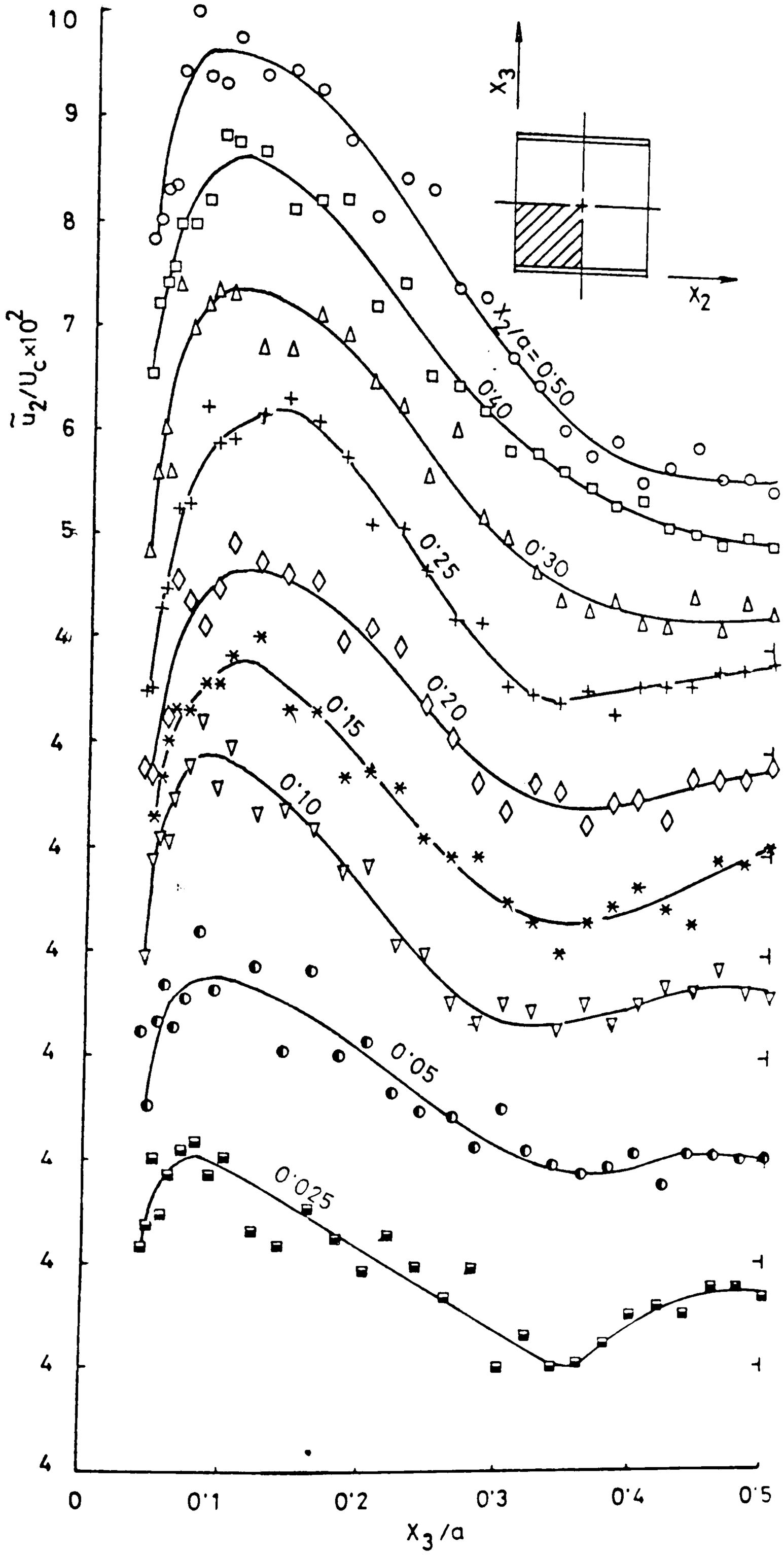

Fig. A 5·2 Profiles of $\bar{u}_2 / U_c \times 10^2$.

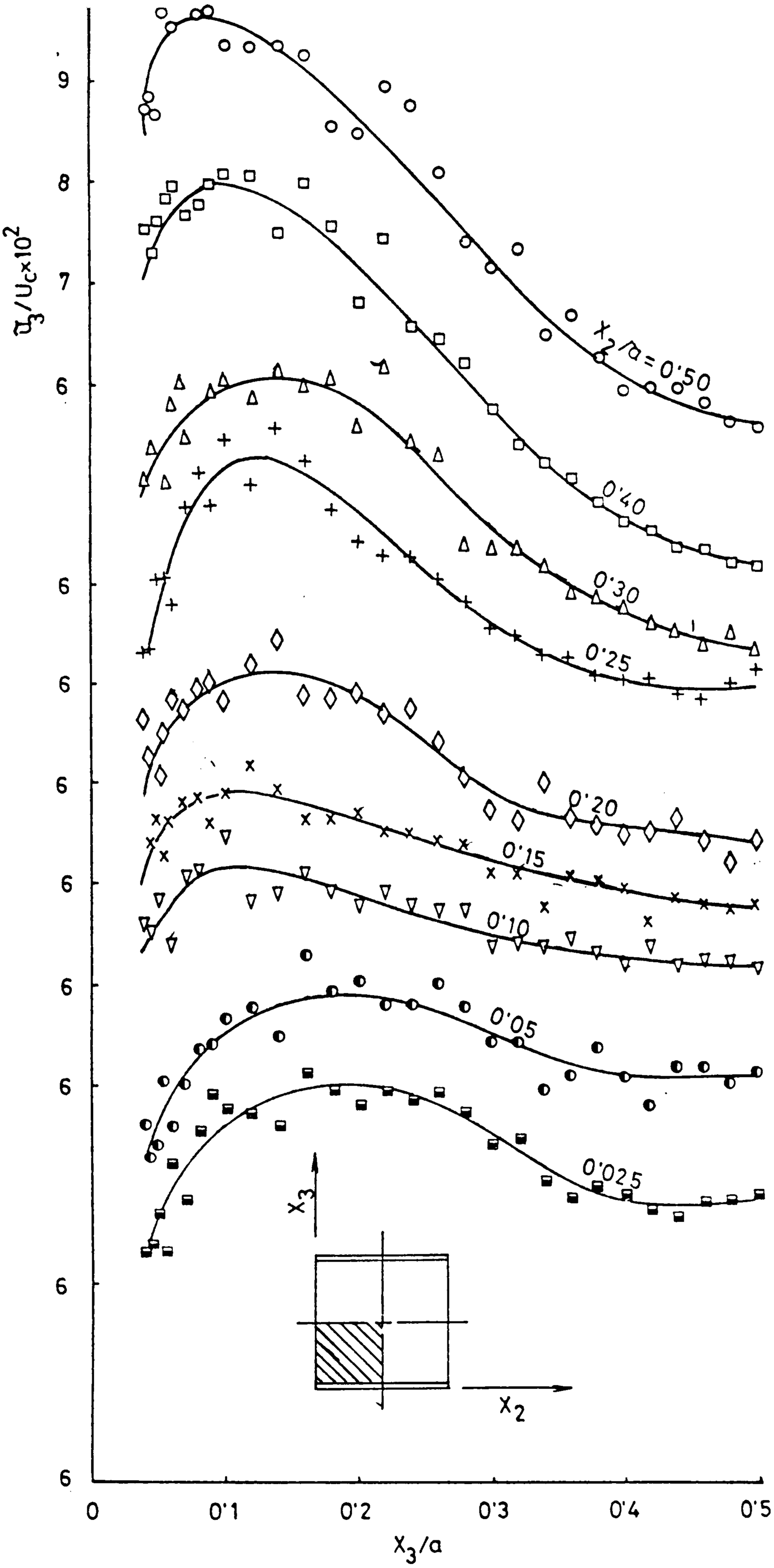

Fig. A5·3 Profiles of $\tilde{u}_3/U_c \times 10^2$

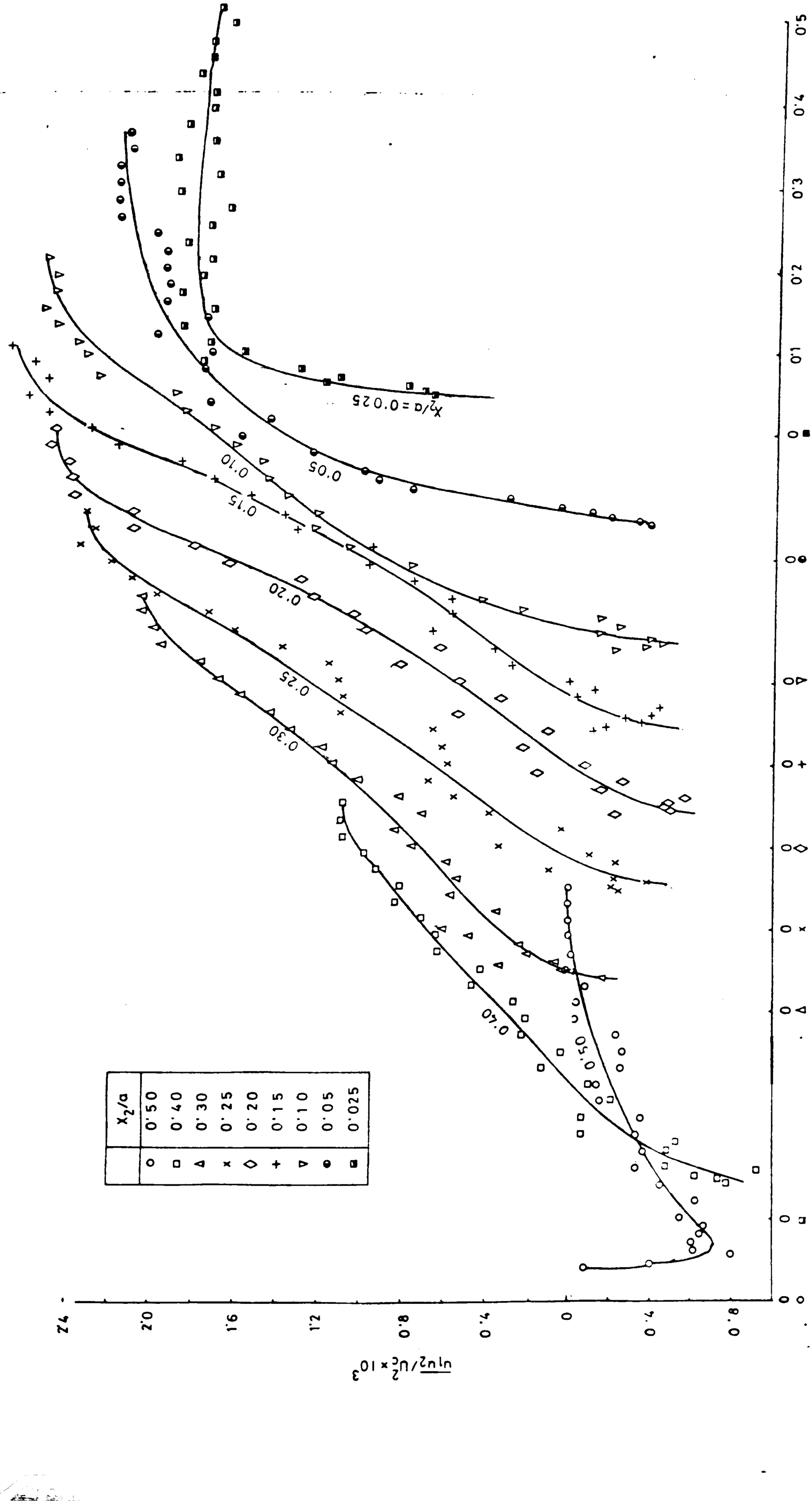

Fig. A5'4 Profiles of $\overline{u_1u_2}/U_c^2 \times 10^3$.

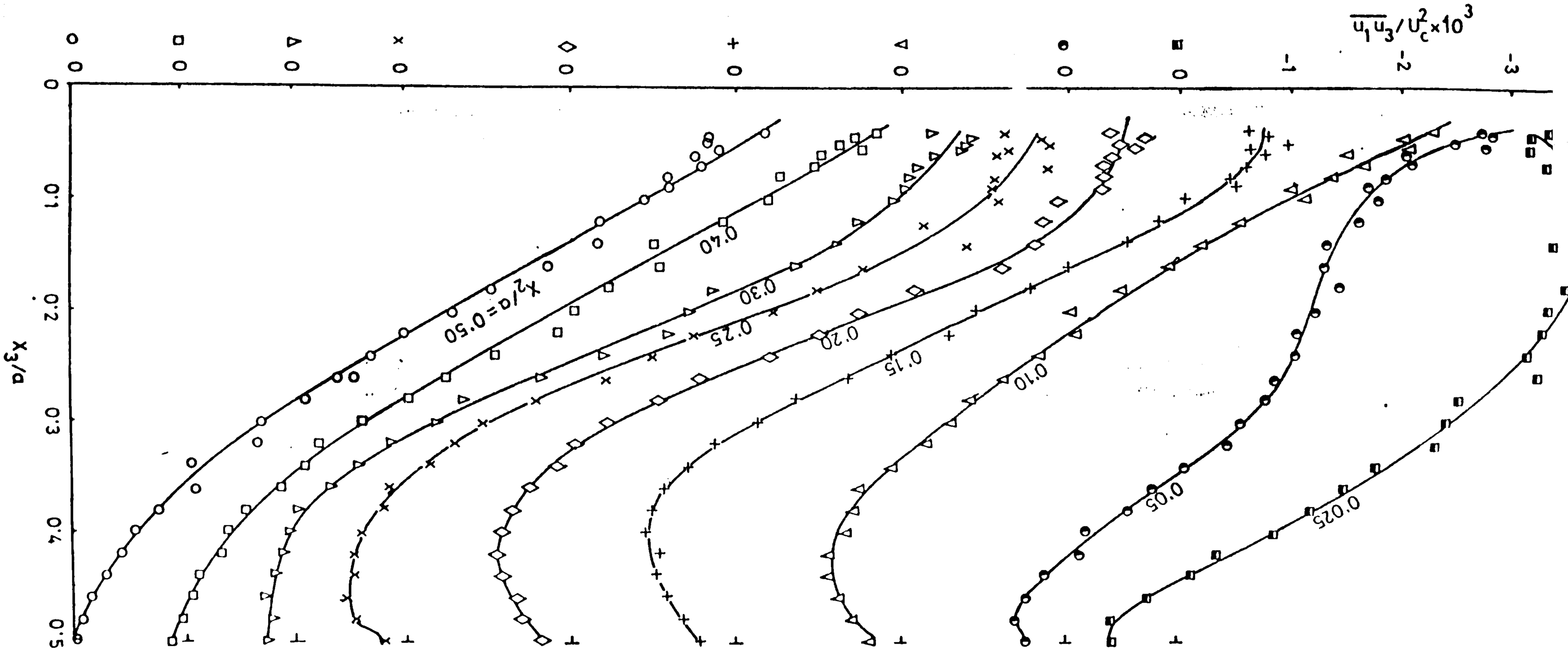

Fig.A5'5 Profiles of $\overline{u_1u_3}/U_c^2\times10^2$.

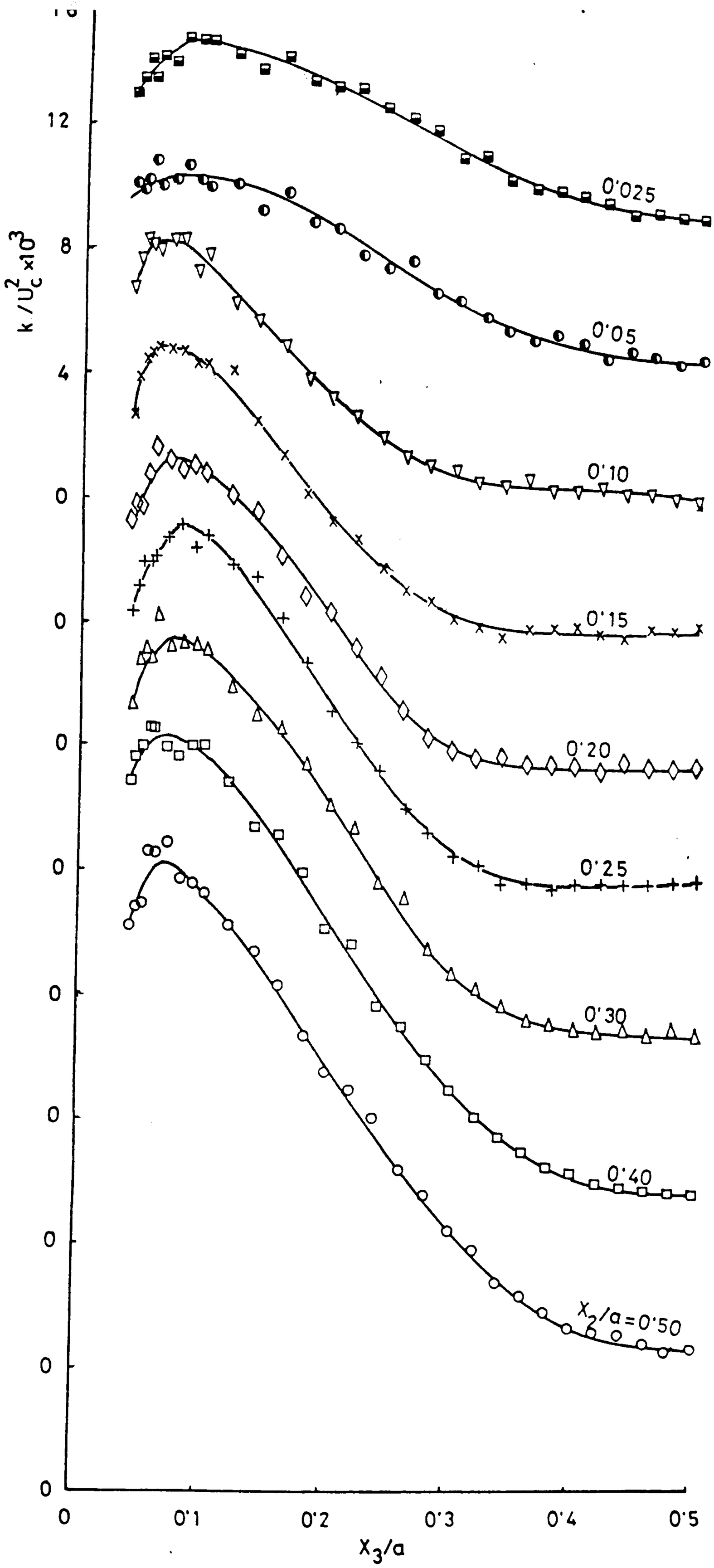

Fig. A 5'6 Profiles of $k / U_c^2 \times 10^3$

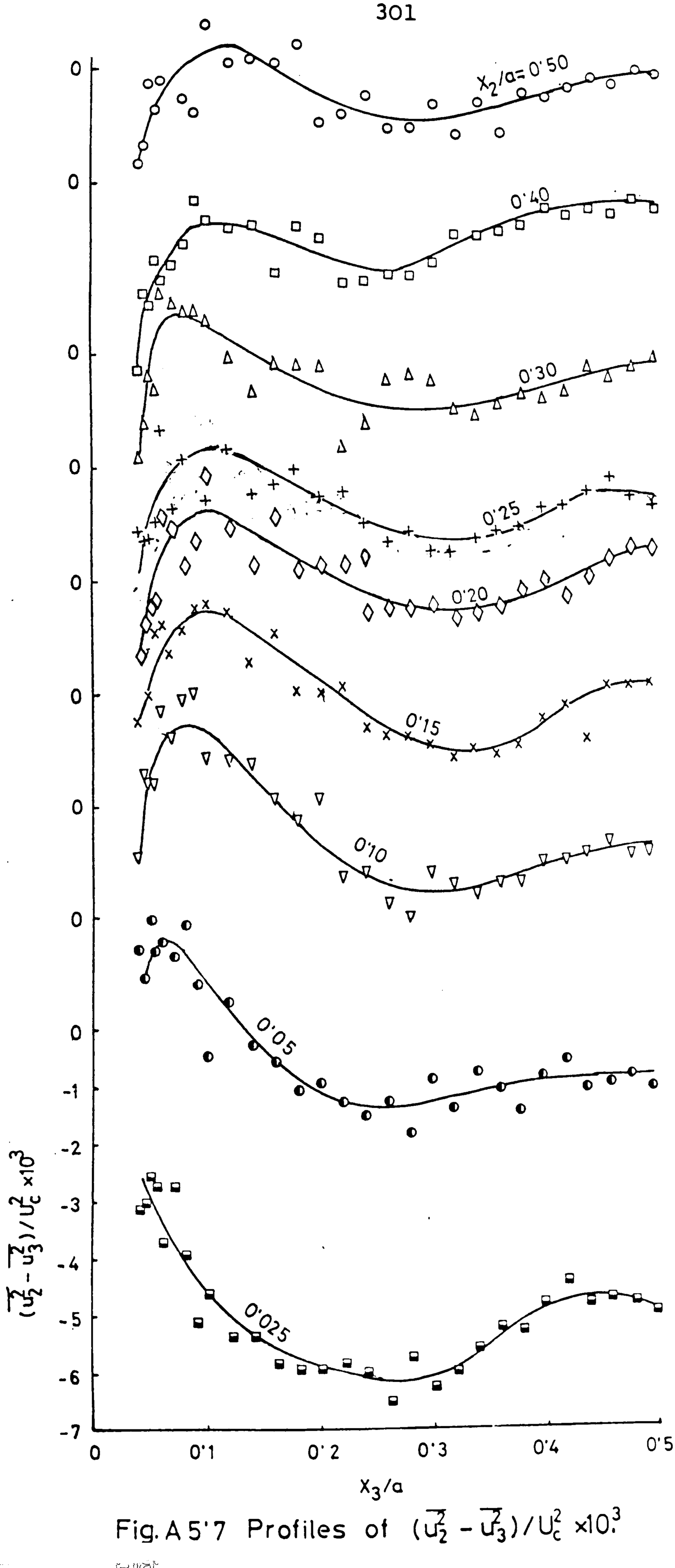

Fig. A 5'7 Profiles of $(\overline{u_2^2} - \overline{u_3^2})/U_c^2 \times 10^3$